"Coupled Thermo-Hydro-Mechanical Processes in Geothermal Reservoirs: a Multiphysic and Multiscale Approach Linking Geology and 3D Numerical Modelling"

Von der Fakultät für Georessourcen und Materialtechnik

der Rheinisch-Westfälischen Technischen Hochschule Aachen

zur Erlangung des akademischen Grades eines

Doktors der Ingenieurwissenschaften

genehmigte Dissertation
vorgelegt von **M.Sc.**

Antoine Baptiste Jacquey

aus Castres, Frankreich

Berichter: Univ.-Prof. Dr. rer. nat. Magdalena Scheck-Wenderoth
Prof. Florian Wellmann, Ph.D.

Tag der mündlichen Prüfung: 21. Juli 2017

Table of contents

List of figures

List of tables

Nomenclature

Scalar symbols

E	Young's modulus [Pa].
ν	Poisson's ratio [-].
L	First Lamé modulus [Pa].
G	Second Lamé or shear modulus [Pa].
K_ϕ	Unjacketed pore bulk modulus [Pa].
K_d	Drained bulk modulus [Pa].
K_p	Drained pore modulus [Pa].
K_s	Solid bulk modulus [Pa].
ϵ_v	Volumetric strain [-].
p_c	Confining pressure [Pa].
p'	Effective pressure [Pa].
p_f	Pore pressure [Pa].
J_1	First invariant of the stress tensor [Pa].
J_2	Second invariant of the stress tensor [Pa^2].
$\mathcal{F}$	Plastic yield stress [Pa].
$\mathcal{G}$	Plastic potential [Pa].
γ	Plastic multiplier [-].

σ'_N Normal stress [Pa].

τ Shear stress [Pa].

μ_s Sliding coefficient [-].

T_s Slip tendency [-].

ϕ Porosity [-].

α Biot-Willis coefficient [-].

ρ_f Fluid density [$\mathrm{kg} \cdot \mathrm{m}^{-3}$].

μ_f Fluid viscosity [$\mathrm{Pa} \cdot \mathrm{s}$].

M_b Biot modulus [Pa].

T Temperature [K].

β Volumetric thermal expansion coefficient [K^{-1}].

c Heat capacity [$\mathrm{J} \cdot \mathrm{kg}^{-1} \cdot \mathrm{K}^{-1}$].

λ Thermal conductivity [$\mathrm{W} \cdot \mathrm{m}^{-1} \cdot \mathrm{K}^{-1}$].

Vector symbols

$\boldsymbol{g}$ gravity vector [$\mathrm{m} \cdot \mathrm{s}^{-2}$].

$\boldsymbol{q}_D$ Specific discharge or Darcy's velocity [$\mathrm{m} \cdot \mathrm{s}^{-1}$].

$\boldsymbol{u}$ Displacements vector [m].

Tensor symbols

$\mathbb{C}$ Rank-four elasticity tensor [Pa].

$\boldsymbol{\epsilon}$ Strain tensor [-].

$\boldsymbol{\sigma}$ Cauchy stress tensor [Pa].

$\boldsymbol{\sigma}'$ Effective stress tensor [Pa].

$\boldsymbol{k}$ Permeability tensor [D] or [m^2].

Chapter 1

Introduction

1.1 Rationale

In the last two decades, there has been a growing interest to develop more accurate multiphysics approaches for problems related to environmental and energy issues. With the term multiphysics, I hereby denote an analysis of certain natural phenomena, which include disparate physico-chemical processes, and where each process has its own physical description, which is usually expressed in terms of proper conservative mathematical laws. Multiphysics problems are indeed common in Earth science studies due to the natural heterogeneity of all geomaterials and their complex transient responses to changing thermodynamic conditions. All geomaterials, including soil and porous rocks, are naturally Discontinuous, Inhomogeneous, Anisotropic and Non-Elastic (DIANE after Hudson and Harrison (1997)). They consist of a composite of mineral phases that have aggregated through geological times and under different tectono-thermal ambient conditions, which finally has resulted in a specific arrangement of the solid grains forming the rigid skeleton of a rock volume. Among the grains, voids (pores) are also found, the dimension, geometry and level of interconnectivity of which play a prominent role in determining the stiffness and thermomechanical stability of a certain rock under differential loading conditions. Usually, such pores are also filled by one or more wetting/non wetting fluid phases (water, gas or a brine mixture) which kinetically interact with the solid phase thus giving rise to a complex and nonlinear multiphasic system. Indeed, interactions between the solid skeleton and the dynamics of the fluid filling the pores increase the level of coupling complexity of the multiphysics problem. An example that also lies at the core of this thesis is represented by the investigation and prediction in time and space of reservoirs' performances. Such a study must rely on an accurate representation of the multicomponent and multiscale fractured porous rock-fluid system as well as of all physical processes responsible for groundwater flow, heat and solute mass transfer, mechanical deformation of the solid rock, and, ultimately, chemical feedbacks from fluid-to-solid interactions. An additional aspect is the need to consider non-linear variations among the different natural components and physical processes as they do occur across disparate temporal and spatial scales.

First motivated by practical problems in civil engineering on the stability of soil under constant loading (Terzaghi, 1943), the quantification of the nature and level of coupling among different physical processes as they interact within a complex medium has now become increasingly popular among almost all geoscientific and geotechnical applications (Carrol and Katsube, 1983; Lockner, 2002; Soltanzadeh et al., 2009; Mehrabian and Abousleiman, 2014). The current need for a secure provision of natural resources under an ever-growing population has inspired studies aiming at a deeper understanding of the geomechanical behaviour of porous rocks under diverse thermodynamic conditions. The goal here is to maximise exploitation scenarios while minimising potential detrimental environmental effects. A number of studies have been focusing among the oil and gas community (industry and academia) on studying causative processes responsible for the induced land subsidence due to fluid withdrawal from reservoirs (Verruijt, 1969; Schiffman, 1989), and later on the mechanical stability of pressurised boreholes and their productivity (Haimson and Fairhurst, 1969; Peška and Zoback, 1995; Yew, 1997; Legarth et al., 2005). In more recent years, the search for alternative, carbon-free sources of energy has motivated an increasing interest towards a better understanding of the physical and chemical states of porous reservoirs under operational conditions (1) for geothermal energy production via proven concepts for enhanced geothermal systems (Gérard et al., 2006; Genter et al., 2010; Blöcher et al., 2016) or (2) for the assessment of the stability of potential storage sites for CO_2, methane and more recently nuclear waste disposal (Rinaldi et al., 2014; McCartney et al., 2016). Common to all the above-mentioned applications, there is the need to improve the production from a reservoir, by maintaining its stability through time and by reducing the hazards from operational activities as induced seismicity, fault reactivation, slip and rupturing processes, all aspects that do require a multiphysics and across scale description of the porous medium (Deichmann and Giardini, 2009; Cappa and Rutqvist, 2011; Rinaldi et al., 2014).

1.2 Objectives

In this thesis, I will focus on thermal, hydraulic and mechanical (THM hereafter) coupled processes as applied specifically to geothermal reservoirs. Geothermal operations aim to harvest the heat energy stored in the underground (reservoirs) both for direct usage (e.g. private and/or district heating) and for electricity conversion. Usually one or more borehole doublets are drilled to reach the targeted geological horizon where the heat stored within the rock can be extracted by injecting and producing operational fluid in the reservoir. In the majority of cases, the natural productivity of a reservoir

is enhanced by the creation of secondary permeability via induced fracturing of the reservoir rock (Zimmermann et al., 2010; Genter et al., 2010). Typical examples are petrothermal, hot and dry (HDR) systems which typically lack primary permeability, though engineering a reservoir has become standard practice also while targeting medium to low enthalpy sandy reservoirs. The main results of geothermal operations is to alter the thermodynamic conditions of the reservoir due to imposed gradients in pore pressure, temperature and deformation. Production and injection of geothermal fluid is responsible for varying the pore pressure distribution in the reservoir and for affecting the stress distribution especially in the nearby area of the open section of the wells, possibly leading to borehole failure (Moeck and Backers, 2006; Blöcher et al., 2009). Injecting fluid at lower temperature than reservoir conditions leads to the onset of thermal gradients, which form at the front of the moving fluid and therefore propagate in the porous domain. These thermal gradients generate stress on the solid matrix of the reservoir, which in turn can modify the hydrodynamic of the operational fluid (Geertsma, 1957; Norris, 1992; Zimmerman, 2000). In addition, all these aspects have an additional effect, which induces variations in the transport properties of the reservoir rock (Fatt and Davis, 1952; Al-Wardy and Zimmerman, 2004; Ghabezloo et al., 2009a). This is especially of relevance when the sustainability of the operations is to be considered. Induced fractures are sensitive to variations in the THM state, and therefore efforts are towards finding a best practice to sustain these features during the whole lifetime of an operational campaign. Variations of the in-situ stress field induced by injection and production are also a major source of environmental concern, since they can trigger possible (re)activation of pre-existing fault zones even at some distance from a well, thus inducing seismic slip movements along their rupture planes (Morris et al., 1996; Cappa and Rutqvist, 2011; Rutqvist et al., 2013). From what stated above, it appears clear that in order to guarantee a productive, sustainable and environmental safe geothermal operational campaign, it is of extreme importance to be able to quantify in time and space the dynamics of the relevant physical processes and their interactions with the geological environment where they occur. It is the principal aim of this thesis to provide with a flexible working framework combining laboratory and field data to numerical dynamic models to address the aforementioned issues. In the following, I will specifically focus in carrying out an analysis of THM coupled processes. Nevertheless, the developed scientific framework can be easily redirect to integrate additional effects related to other processes including transport of chemically reactive minerals, their dissolution and biological feedbacks.

1.2.1 Motivations behind the study

To make reliable predictions of reservoirs' performances, as well as to better engineer such systems by improving their productivity in a sustainable way there is a number of interconnected issues that must be taken into account. I hereafter make use of these aspects to help phrasing the main motivations (challenges, goals and open questions) behind my doctoral research.

Coupling among the different processes

THM coupling in porous reservoirs can be organised in distinct categories if based on the processes considered, which are hydromechanical, thermomechanical and hydrothermal couplings. The hydromechanical behaviour of porous media involves two major processes, which are, (1) differential changes in pore pressure, which induce deformation of the solid skeleton (fluid-to-solid coupling); and (2) variations in the stress applied to the solid skeleton of a rock volume, which in turn induce a change in pore pressure and consequently in the fluid dynamics inside the porous matrix (solid-to-fluid coupling). These phenomena, which are nowadays well established, are observed during all operation activities in reservoirs (Carrol and Katsube, 1983; Moeck et al., 2009b), and are well studied in laboratory experiments (Mandel, 1953; Ghabezloo et al., 2009b; Blöcher et al., 2009).

Thermomechanical coupling describes also a two-way coupled physical system. Changes in the thermal state of the rock induce a volumetric deformation (contraction or dilation) (Geertsma, 1957; McTigue, 1986). Shear deformation as observed during major slip events along faults' planes can result in an increase in the thermal energy of the system (often referred as shear heating). While the former coupling is an essential component of any reservoir operational campaign, the latter is usually considered relevant when addressing issues related to origin and evolution of sedimentary basins and their interactions with the crustal and mantle dynamics (Souche et al., 2013).

When considering hydrothermal coupling, heat advection by a moving fluid can be considered by far as the most well studied of all couplings both at the reservoir scale, as well as at the scale of a whole basinal system (Blöcher et al., 2010; Cherubini et al., 2014). Less investigated and understood is the feedback effect that changes in the temperature conditions have on the resulting pore pressure field. So far, thermal pressurisation has been regarded more as having a secondary effect, and it has been mainly investigated at the laboratory scale on selected samples under smooth and controlled conditions (Ghabezloo and Sulem, 2009).

Additionally, the existence of nonlinear dependencies among geological structures, material properties and state variables increases the complexity of reservoirs' applications. These include for example the evolution of transport properties such as porosity and permeability in response to variations in the in-situ hydraulic, thermal and mechanical states of the porous material (Fatt and Davis, 1952; Walder and Nur, 1984; Han and Dusseault, 2003; Blöcher et al., 2014). Increase in the pore fluid pressure during injection in a reservoir can induce an expansion of the porous space and therefore lead to an increase in the effective porosity. Production from a well will reduce pore pressure and therefore induce an increase in the compressive effective stress state. It can therefore tend to reduce the porosity of the matrix. Changes in temperature may alter the material porosity by initiating a volumetric deformation leading to the contraction or dilation of the pores and grains and resulting in the development of differential stresses within the porous matrix (Zimmerman, 2000; Ghabezloo et al., 2009b). It follows that it is essential to capture and quantify these phenomena, since they can alter the productivity of a reservoir.

In addition, variations in the thermodynamic state of the system might have an effect on the basic properties of the fluid contained in the pores and they can give rise to additional buoyant components to the flow. Changes in temperature, pore pressure or mineral composition can trigger fluid density and viscosity anomalies, the onset and development of which might lead to unstable convective flow patterns thus affecting the reservoir's dynamics (Elder, 1967).

Geological heterogeneities

A common aspect of Earth science applications is to deal with a complex, heterogeneous and multicomponent natural system. Porous rocks are complex by definition. At the microscopic level, rocks are an aggregate of differently packed minerals. The composition, arrangement, as well as the presence of interlocking materials can alter the macroscopic appearance and behaviour of a rock. However, quantification of the micro-macro structural dependency in porous rocks is a challenging and still unresolved topic. Field observations and laboratory experimental results strongly suggest that the macroscopic behaviour of a rock is highly dependent on the presence of microstructural defects (microcracks and fissures) and their degree of connectivity (Morlier, 1971; Mura, 1987; Blöcher et al., 2009; Dautriat et al., 2009).

Also major fault zones exhibit a complex structure, mainly consisting of a ultracataclasite gouge, fault core, surrounded by an area characterised by intensively jointed rock materials and dilation breccias (damage zone) which can have been also chemically

altered (Caine et al., 1996; Faulkner et al., 2010). Depending on its internal structure, the degree of fault-inherited fracture nucleation and propagation within the major damaged area, a fault can act as a drain or as an area of preferential flow. Therefore, it can locally alter the groundwater dynamics, and, due to hydromechanical coupling, also the in-situ stress field. Fractures, whether natural or engineered often act as flow preferential pathways (Barton et al., 1997; Cherubini et al., 2013). The density of fractures and their interconnectivity can give rise to secondary permeability and porosity which may drastically modify the hydraulic conditions and the flow dynamics in the reservoir (Walder and Nur, 1984; Cacace et al., 2013). In the particular case of low porosity and low permeability geothermal reservoirs, stimulation treatments are often used to create hydraulic fractures in order to gain access to the target formation fluids, drain the geothermal fluid and therefore increase the overall productivity of the geothermal reservoir. Understanding the interactions between the host rock and the processes occurring within these induced fractures is therefore of interest for any reservoir application.

Multiscale modelling

Coupled THM processes span a relatively large spectrum of temporal and spatial scales and they interact in a highly non-linear fashion. In natural and engineered systems, onset conditions and the evolution in time and space of a particular process are affected by the initiation and evolution of all the other processes. Therefore, monitored variations of rock masses to natural and anthropogenic perturbations cannot be fully reconciled by considering the causative processes independently. This is particularly the case for reservoir applications which demand for a complete understanding of the multi-component (fractured) porous rock-fluid system and its multiphysics dynamics to predict the reservoir's behaviour and/or to improve its productivity and sustainability. To recognise that the majority of geological observations are the results of non-linear interactions among classes of physical processes have justified the recent development and massive use of so-called multiphysics and multiscale computer simulators as complementary tools to classical experimental and theoretical analyses (Clauser, 2003; Wang and Kolditz, 2007; Watanabe, 2011; Blöcher et al., 2015). Numerical simulations are particularly adapted to the study of a multi-component physical system since they allow a systematic analysis of the dynamics of single processes and their interactions (i) under proper time and length scales, (ii) within complex geometries, and (iii) also considering changing loading conditions. In addition, given their predictive capabilities,

numerical modelling techniques can assist studies aiming at estimating performances and potential risks related to different operational scenarios.

1.2.2 Open questions to be addressed

Inspired by the above described motivations, in this paragraph I summarise the main open questions, as I intend to address in my thesis. In line with the aspects highlighted in the above chapter, I conceived as major goal of this study to provide a workflow which can help improving our fundamental understanding of the multiphysics and across-scale nature of porous media. In such a workflow, I make extensive use of data obtained from laboratory experiments, which are used to constrain the derived theoretical framework describing the system. The latter is then consistently integrated into a numerical simulator which captures both the geological complexity of natural examples, and the complex, non-linear dynamics of the evolution of structure-properties relationships. The result is a robust workflow that can assist scientists in the making of time efficient and reliable predictions of reservoirs' performances.

I conceive therefore the following three mayor open questions to be addressed by the present work:

- What are the dominant physical processes affecting, if not controlling the thermo-hydro-mechanical behaviour of reservoir rocks? And, how can these processes be integrated in a numerical simulator to make reliable predictions at the field scale?

- How to effectively quantify and represent the non-linear dependencies between geological structures, material properties and reservoirs' state variables? Is it possible to make use of information derived from laboratory experiments to constrain the dynamics of processes occurring at the mesoscale of a reservoir? Can we develop a unique framework to predict micro- and macroscale processes and their interactions?

- How can details of the main heterogeneous characteristics of geological systems, including faults and fractures be captured in a dynamic model? And, how, once integrated, can such a model help to quantify the impact of these natural discontinuities on the thermo-mechanical and hydraulic state of a reservoir?

1.3 Establishing a workflow

In this section, I describe in some details how such a workflow has been realised. In the following chapters, I present and discuss applications of the same workflow to address specific problems of interest for reservoir applications.

The basic outline of the workflow, as schematically depicted in Figure 1.1 is to combine information and data derived from experiments conducted on rock samples in the laboratory (cm scale) and operational data (km scale) into a multicomponent physical framework, by which the physics can be described and the interactions among the different processes quantified. Implementing such a theoretical framework into a numerical simulator permits to capture not only the overall coupling complexity, but also to crosslink the feedbacks among the different processes along relevant scales (from the microscale of the pores and grains to the macroscale of field applications) by taking into account the details of the heterogeneous nature of natural geological systems.

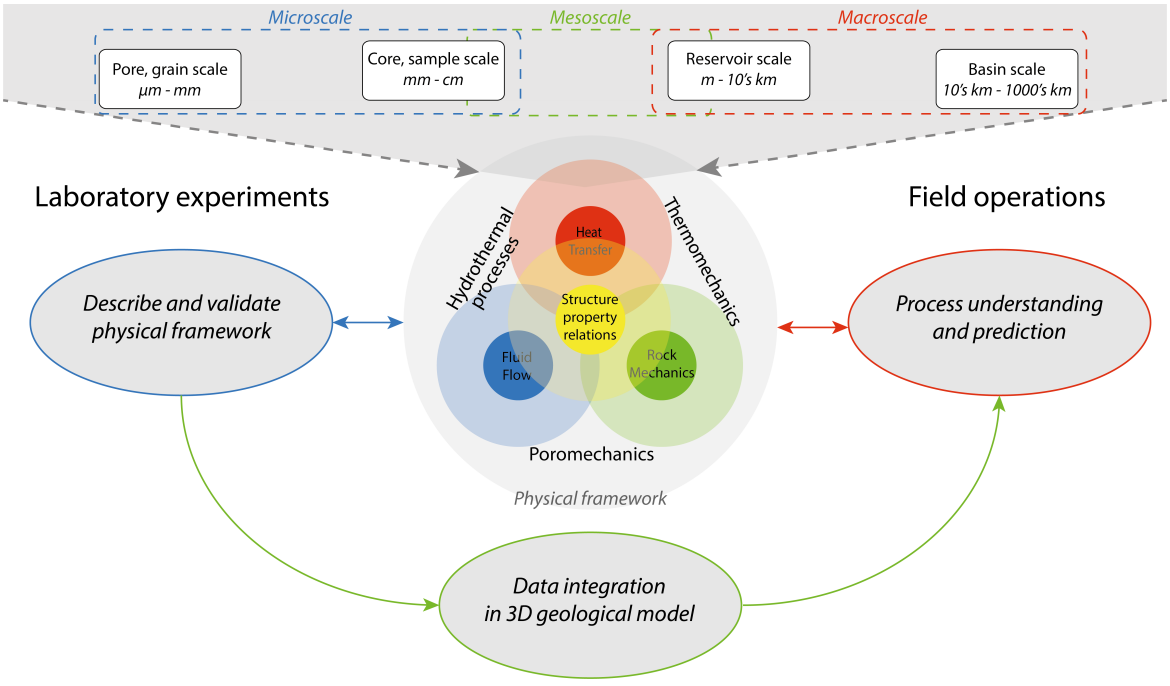

Fig. 1.1 Conceptual scheme describing the developed workflow.

Developing a new numerical simulator with a strong focus on non-linear coupling and on flexible implementation was therefore highly motivated. In the framework of this thesis, I developed a numerical simulator for modelling coupled THM processes in reservoir rocks called GOLEM, based on the MOOSE (Multiphysics Object Oriented Simulation Environment) framework (Gaston et al., 2009). The MOOSE framework

provides a powerful and flexible platform to solve multiphysics problems implicitly and in a tightly coupled manner on unstructured meshes which is of interest for the non-linear context introduced in this thesis.

Data integration into numerical models is a key issue for treating increasingly realistic scenarios, which include complex geometries and data-based property relations. Technical difficulties are not only limited to the processing of geological data as they come from diverse sources, but mainly, for numerical applications, in how to discretise the continuous representation of the geology on a format that can be handled successfully by a simulator. Most discretisation tools (meshing software) provide only generic and simplified model representations limited by the degree of assumptions made to represent the actual geometry of geological systems. In establishing the present workflow, efforts have been made to minimise uncertainties in the geological representation and to capture the complexity of the subsurface in a consistent manner. This was achieved by interfacing the dynamic simulator to an open-source meshing software developed at the GFZ Potsdam (MeshIt, Cacace and Blöcher (2015)) that permits the integration of non-planar and intersecting interfaces bounding geological formations as also disconnected by major fault zones and fractures into a consistent discrete mesh for FEM and/or FVM modelling.

An additional issue stems from how to best establish, derive and integrate, adequate structure property relationships which are consistent with observations collected in the field and in the laboratory. These state equations, not only enable to consider and therefore quantify the results from interactions among physical processes and the geological environment where they occur, but also offer, if based on data, the possibility to link the diverse spatial and temporal scales of interest. Conceptual models dealing with porous media are usually based on a volume statistical average of the properties and variables, the Representative Elementary Volume (REV) concept after Bear (1988). Introduction of the REV is used to substitute a multiphase problem dealing with the fluid/solid mixture of porous media by a continuum medium in which state variables (effective stress, pore pressure, temperature) and properties (elastic moduli, bulk density, etc...) are statistically defined. However, in the majority of reservoir applications, establishing a REV is particularly challenging. The main problematic aspect relates to the choice of a statistically meaningful volume based on which the system can be homogenised. This in turn translates in finding a length scale that can be representative of the system as a whole. However, for all geological systems, where feedbacks among the microstructural components strongly interact with the macro structures, it is not possible to unequivocally define such a scale of interest.

Throughout this study, the assumption is made that such a reference length scale is given by the length of discrete fractures. I make then use of data from laboratory experiments to realistically, though in a statistical sense quantify the feedback effects of microstructural defects on the resulting material properties.

In the laboratory, predefined and monitored conditions can be applied to core samples and it is possible to observe a specific physical or chemical process which can be also recognised as relevant at the reservoir scale. Therefore, the results obtained from such experiments can be used to improve a conceptual model and to constrain the evolution of the rock properties. In this regard, I present in Chapter 3 a detailed practical example of how to make use of such data to develop proper state equations which quantitatively account for the feedbacks of the microstructural heterogeneous composition of rocks onto their macroscopic mechanical behaviour. An extension of this approach to include additional processes, including for example grain crushing and pore collapse in a more systematic manner is also presented in Chapter 7 at the end of this thesis.

As a concluding remark I would like to stress what I consider as a key characteristic of this workflow, that is, its flexible structure. Indeed, this aspect not only permits to easily integrate novel observations and data as soon as they are available. In addition, relying only on open-source and modular numerical tools offers the unique chance to easily incorporate new data and to improve the physical modules in order to represent more complex scenarios.

1.4 Overview over the thesis

The chapters of this thesis present in details how and to which degree all of the open questions introduced before are addressed separately. Chapter 2 presents the mathematical descriptions and their underlying assumptions (as well as their numerical implementation) adopted for modelling coupled thermo-hydro-mechanical processes in porous rocks throughout the thesis. Chapter 3 focuses on the physical description of hydromechanical coupling and on the definition and validation of non-linear relations between the porous structure and the mechanical and transport properties of a porous medium. Chapters 4 and 5 consider an extension of the physical framework to a complete thermo- and poroelastic description of porous media. Chapter 4 is focused on the implications of such framework for transport properties' relations as applied to a field case whereas Chapter 5 describes the potential (re)activation of natural major fault zones by geothermal operations, as a result from a tight coupling among hydraulic, thermal and mechanical processes. Chapter 6 investigates further the hydromechanical

coupling, (especially the solid to fluid coupling) as illustrated at the reservoir scale with field observations. In Chapter 7, I end the results part of this thesis by outlining first efforts to extent the current physical and numerical framework to include additional feedback effects of fracture mechanics onto the micro- and macroscale state of rocks. I conclude this thesis with a final discussion on the results from the applications described in the previous chapters and their relevance in the context of geothermal reservoir applications, as well as on outlooks for future activities as inspired by the work accomplished this far in Chapter 8.

This thesis contains a collection of papers published or under review in peer-reviewed ISI-journals. Chapters 3, 4 and 5 are based on three published manuscripts in *Transport in Porous Media*, *Tectonophysics* and *Energy Procedia* respectively whereas Chapter 6 is based on a manuscript under review in *Journal of Geophysical Research: Solid Earth*.

It is worth noticing that numerical results presented in Chapters 3, 4 and 5 were obtained with the "OpenGeoSys" numerical simulator initially for the submission of the manuscripts in peer-reviewed ISI-journals. However these results were successfully reproduced using the numerical simulator GOLEM, which was developed in the frame of this thesis.

In the following, some information about these publications are given, including the publication details and the main scientific contributions for each chapter.

Chapter 2: Governing equations for coupled Thermo-Hydro-Mechanical processes in porous rocks and their numerical implementation: introduction to the GOLEM numerical simulator

This chapter describes the derivation and numerical implementation of the thermo-hydro-mechanical processes as occurring within porous media. Starting from balance equations (fluid and solid mass and momentum and energy), the governing equations for fluid flow, heat transport and deformation are derived in a general manner. This chapter provides some insights into the approximations used for the implementation. These governing equations were implemented in a newly developed open-source simulator called GOLEM based on the MOOSE framework (Gaston et al., 2009). Basic concepts behind the GOLEM simulator are presented in this part as well as a few application examples to illustrate its main features.

This chapter is based on a manuscript in preparation that I wrote together with M. Cacace.

Chapter 3: Hydro-Mechanical Evolution of Transport Properties in Porous Media: Constraints for Numerical Modelling

This paper focuses on the hydromechanical response of two different sandstones subjected to isotropic compaction under drained conditions. It presents a general poroelastic model capturing the non-linear mechanical response and the evolution of transport properties of the rocks which are porosity and permeability, and its implementation into the open-source simulator "OpenGeoSys" (Kolditz et al., 2012a). Particular attention is given to the use of available laboratory observations (Blöcher et al., 2014) to constrain the poroelastic models. The results presented in this chapter show that non-linearities in the stress-strain relation and porosity evolution can be well captured by the extended poroelastic framework. The crack-closure theory is used to deal with the non-linear stress-strain response at low confinement. Three different porosity models are evaluated by comparing to the experimental data. This study emphasises that similar sandstones at the macroscale can have significantly different poroelastic behaviours (non-linear and absolute decrease of porosity due to compaction) due to the difference in elastic properties and in the density of microcracks.

As the first author, I was the main contributing author to this study. I implemented several models (crack-closure theory, three hydro-mechanical porosity models and a Kozeny-Carman-like permeability model) in the open-source simulator "OpenGeoSys" (Kolditz et al., 2012a). I also carried out the different numerical simulations and compared the results to the experimental data provided by a co-author (G. Blöcher). I drafted the manuscript including the figures and tables which was completed with minor contributions of the co-authors.

Chapter 4: Thermo-poroelastic numerical modelling for enhanced geothermal system performance: case study of the Groß Schönebeck reservoir

In this paper, the previous poroelastic framework was extended for thermal feedbacks, including a thermoelastic model. The impacts of temperature changes on the mechanical behaviour and as well as on the porosity and permeability distributions were analysed and quantified by means of a generic model and a field case application, the Groß Schönebeck geothermal research facility, located north of Berlin, Germany. It was chosen to assess a geothermal system for this study as large temperature changes can occur in such reservoir resulting from cold brine injection in comparison to the in-situ temperature. This chapter indicates that thermal stresses can be as large as poroelastic stresses in the vicinity of a geothermal injection well. It also asserts the propagation of increased porosity and permeability together with the thermal front due to temperature changes. The numerical simulations were conducted with the open-source simulator "OpenGeoSys".

As for the previous chapter, I was the first and main contributing author to this manuscript. I extended the previous poroelastic implementation to thermo-poroelasticity in "OpenGeoSys" and designed the generic model to illustrate and quantify the thermal effects. I carried out the numerical simulations for both the generic and the field case applications. I drafted the manuscript and prepared all included elements (figures and tables). The draft manuscript was improved by comments from the co-authors. It is worth noticing that this manuscript was published as part of the special issue in *Tectonophysics* on *GeoMod 2014 – Modelling in Geoscience*.

Chapter 5: Numerical investigation of thermoelastic effects on fault slip tendency during injection and production of geothermal fluids

This chapter studies the impacts of temperature changes on the fault slip behaviour within deep faulted geothermal reservoirs. Based on the thermo-poroelastic model presented in the previous chapter, this study shows that temperature changes can induce an increase in the slip tendency when the cold fluid front reaches the fault. The influence of the temperature difference and the dip angle of the fault on the slip tendency are analysed and quantified. This manuscript therefore provides valuable insight to understand how thermal stresses can influence the slip behaviour of faults and points out that thermoelastic stresses can often exceed poroelastic stresses in the context of deep geothermal reservoirs.

As a first and main contributor to this manuscript, I designed the setup of the generic numerical models, conducted the simulations and drafted the manuscripts including tables and figures. The co-authors helped to improve the quality of the manuscript with their comments.

Chapter 6: Poroelastic response of geothermal reservoirs to hydraulic stimulation treatment: theory and application to the Groß Schönebeck geothermal research facility

This chapter deals with poroelastic effects as occurring during cyclic hydraulic stimulation of wells. It illustrates an effect resulting from a solid to fluid hydromechanical coupling, similar to a Mandel-Cryer effect (Mandel, 1953; Cryer, 1963) triggered by cyclic injection of fluid. Cyclic injection schedule leads to a cyclic opening of the hydraulic fracture which allows to control the growth of the fracture shape. However, the opening of the fracture induces also compression in the surrounding rocks which leads to an additional pore pressure build-up as controlled by poroelasticity. The results presented in this chapter illustrate a poroelastic effect falling in the family of the Mandel-Cryer effect by means of a generic model together with its analytical solution. This study also includes an illustration at the field scale for the Groß Schönebeck

geothermal facility for which an unexpected pore pressure response was monitored during cyclic hydraulic stimulation.

As the first author of this manuscript, I also was the main contributor. I implemented all the governing equations into the open-source GOLEM simulator presented in Chapter 2, which is based on the MOOSE framework (Gaston et al., 2009). I setup the model and numerical simulations and also developed the analytical solution for the generic problem. The field data were provided by two co-authors (G. Zimmermann and G. Blöcher) and I post-processed them in order to be used in the numerical simulations. Together with the second author (L. Urpi), I worked on the parametrisation of the numerical simulations. Finally, I conducted the numerical simulations and drafted the manuscripts including figures and tables. The co-authors provided minor comments to improve the quality of the manuscript.

Chapter 7: Fracture mechanics, localised deformation and hydrothermal processes: an outline of preliminary results based on a multiscale coupling approach

In this chapter, I describe in some details more recent, and still ongoing activities aiming at integrating in the current formulation a thermodynamic description of the mechanics of fracturing and faulting. More specifically, the aim is to arrive at considering (1) how the level of microdefects might influence the macroscopic behaviour of a rock, possibly leading to enhanced local weakening of the rock fabric and consequent initiation of localised deformation, and (2) the feedback effects of these dynamics on the poroelastic rock properties. I will therefore concentrate more on presenting the basic working hypothesis, a combination of laboratory derived observations and thermodynamically consistent physical modelling by also giving some, though preliminary at this stage, results.

Chapter 8: Summarising discussions, outlook and conclusions

This chapter contains a discussion of the overall results of the thesis with respect to the open questions raised in this introduction. The results are set into the global context of the thesis. The main focus is on the coupling among the considered THM processes occurring in geothermal reservoirs and on the multiscale approach adopted to overcome the scale paradox arising from modelling porous media. Finally, an outlook on further extensions of the physical framework is presented to capture the mechanical feedbacks of geological discontinuities at different scales but also a description of the next steps I envisage for future activities.

Appendix A: Appendix related to Chapter 3

Appendix B: Appendix related to Chapter 6

Appendix C: Experimental study

This appendix contains the description and results from laboratory experimental studies conducted in the framework of this thesis. The aim of these experimental studies is to provide observations of the processes controlling microcracking, strain localisation and their hydraulic and poroelastic impacts. It consists of three axial loading experiments in a triaxial setting on Bentheim sandstone samples and a micro-structure analysis of the samples post-experiment. The three laboratory experiments were conducted at different confining pressures under drained conditions (constant pore pressure) leading to different poro-mechanical responses. Continuous porosity measurements during the experiments were conducted. Localised deformation was observed in the form of shear failure and shear-enhanced compaction bands. The micro-structure analysis consists of electron micro-probe (EMP) as well as X-ray powder diffraction (XRD) images. This appendix provides an experimental base for the discussion on modelling the initiation of localised deformation presented in Chapter 7.

Appendix D: List of publications and conferences attendances related to this thesis

Chapter 2

Governing equations for coupled Thermo-Hydro-Mechanical processes in porous rocks and their numerical implementation: introduction to the GOLEM numerical simulator

2.1 Introduction

The goal of this chapter is not to summarise the state of the art computational methods for problems that are relevant for reservoir applications. My interest herein is rather toward computational reliability and performances when simulating the behaviour of a particular reservoir in a way that can be of help to improve scenario-oriented analysis of such systems. In this context, I address issues related on how (i) to quantify the non-linear feedbacks among the different physical processes, and (ii) to represent into a computational model the porous rock-fracture-fluid system by capturing its discontinuous, anisotropic, inhomogeneous and non-elastic nature. At this purpose, I give an overview of the methods implemented into a novel, yet robust and efficient multiphysics and multi-component porous media open-source modelling simulator called GOLEM (available at https://github.com/ajacquey/Golem) which can deal with all these aspects. The emphasis throughout this chapter is to simulate thermal-hydraulic-mechanical (THM) processes of relevance for hydrothermal and geothermal systems. Though GOLEM can also simulate the transport of non-reactive chemical species, I do not discuss this aspect in the present chapter. At the same time, to consider additional chemical (fluid-solid) interactions is the subject of future work.

Throughout this chapter, fractures and faults are represented as single-nodded, zero-thickness, lower dimensional elements as illustrated in Figure 2.1 from Cacace and Blöcher (2015).

2.2 Mathematical formulation of the problem

In the following the main equations are derived. The problem variables considered are the pore fluid pressure p_f, the temperature T, and the solid displacement vector $\boldsymbol{u}$. Pore pressure is defined as compression positive for the fluid phase, while stress is defined as tension positive for the solid phase.

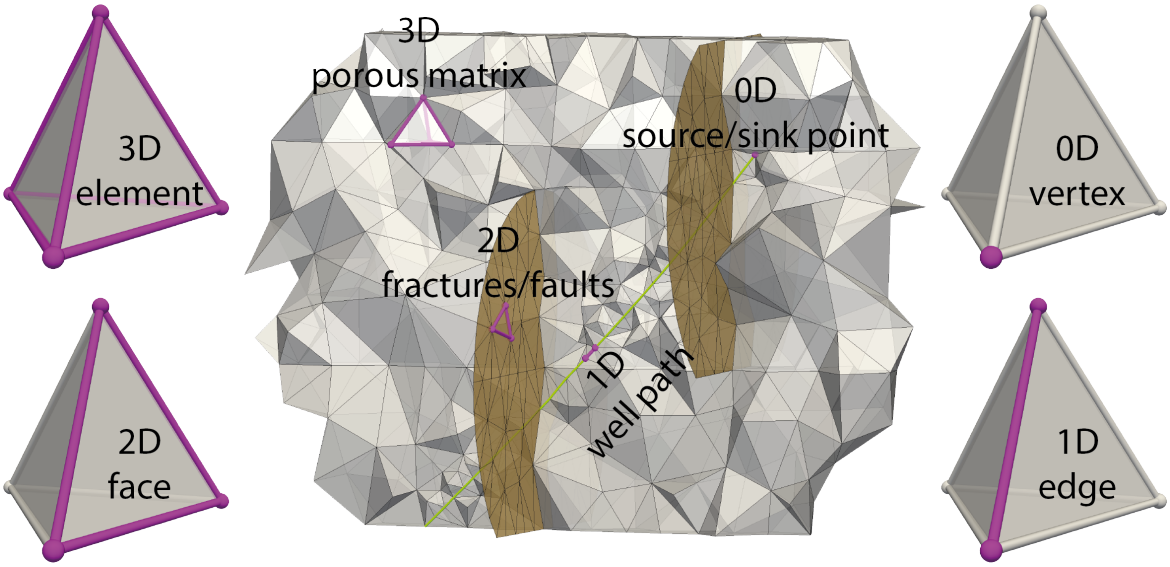

Fig. 2.1 Schematic representation of the approach to model fracture rock masses as based on a superposition of lower and higher dimensional geometric elements, after Cacace and Blöcher (2015): 0D vertex (point-like sources/sinks), 1D edge (well paths), 2D face (fractures an faults) and 3D element (porous matrix)

The mass balance equation for a deformable, saturated porous medium is described in terms of volumetric averaged mass conservation equations for the fluid and solid phases. Mass conservation therefore requires that for the fluid phase,

$$\frac{\partial \left(\phi \rho_f\right)}{\partial t} + \nabla \cdot \left(\phi \rho_f \boldsymbol{v}_f\right) = Q_f \tag{2.1}$$

where ρ_f is the density of the fluid phase, ϕ is the porosity and Q_f is a sink/source term considered null hereafter for the sake of simplicity. In a similar way, for the solid phase, one can obtain:

$$\frac{\partial \left(\left(1-\phi\right) \rho_s\right)}{\partial t} + \nabla \cdot \left(\left(1-\phi\right) \rho_s \boldsymbol{v}_s\right) = Q_s \tag{2.2}$$

where ρ_s is the density of the solid phase and Q_s is a sink/source term also considered as null hereafter. Darcy's law describes the conservation of momentum of the fluid phase, which can be expressed in terms of fluid velocity relative to the solid velocity as:

$$\boldsymbol{q}_D = \phi \left(\boldsymbol{v}_f - \boldsymbol{v}_s\right) = -\frac{\boldsymbol{k}}{\mu_f} \cdot \left(\nabla p_f - \rho_f \boldsymbol{g}\right) \tag{2.3}$$

where $\boldsymbol{q}_D$ is a volumetric flow rate per unit of surface area (Darcy velocity), $\boldsymbol{k}$ is the permeability tensor of the porous medium and μ_f the fluid viscosity.

Substituting Equation 2.3 into 2.1 yields:

$$\frac{\partial\left(\phi\rho_f\right)}{\partial t} + \nabla\cdot\left(\rho_f\boldsymbol{q}_D\right) + \nabla\cdot\left(\phi\rho_f\boldsymbol{v}_s\right) = 0. \tag{2.4}$$

The equations of mass conservations can be rewritten by applying the concept of the Lagrangian total derivative with respect to a moving solid, e.g. $\frac{D^s(\bullet)}{Dt} \equiv \frac{\partial(\bullet)}{\partial t} + \nabla(\bullet)\cdot\boldsymbol{v}_s$, and $\frac{D^f(\bullet)}{Dt} \equiv \frac{\partial(\bullet)}{\partial t} + \nabla(\bullet)\cdot\boldsymbol{v}_f$ for a moving fluid. By expanding the fluid mass conservation equation and noting that $\nabla\cdot[(\bullet)\boldsymbol{v}_f] = (\bullet)\nabla\cdot\boldsymbol{v}_f + \nabla(\bullet)\cdot\boldsymbol{v}_f$, Equation 2.4 can be rewritten as:

$$\frac{\phi}{\rho_f}\frac{D^f\rho_f}{Dt} + \frac{D^s\phi}{Dt} + \phi\nabla\cdot\boldsymbol{v}_s + \nabla\cdot\boldsymbol{q}_D = 0. \tag{2.5}$$

In a similar way it is possible to rework the solid mass balance equation (Equation 2.2) to obtain:

$$\frac{1}{\rho_s}\frac{D^s\rho_s}{Dt} - \frac{1}{(1-\phi)}\frac{D^s\phi}{Dt} + \nabla\cdot\boldsymbol{v}_s = 0. \tag{2.6}$$

From Equation 2.6, it can be noticed that even by considering both the solid skeleton and the pore fluid to be incompressible, the porous rock material will deform (contract or dilate) when fluid is expelled from or injected into the pore space.

Equation 2.6 can be used to express the evolution of the porosity in terms of the Lagrangian derivative with respect to the solid deformation velocity as:

$$\frac{D^s\phi}{Dt} = \frac{(1-\phi)}{\rho_s}\frac{D^s\rho_s}{Dt} + (1-\phi)\,\nabla\cdot\boldsymbol{v}_s. \tag{2.7}$$

Substituting Equation 2.7 into Equation 2.5, one obtains:

$$\frac{\phi}{\rho_f}\frac{D^f\rho_f}{Dt} + \frac{(1-\phi)}{\rho_s}\frac{D^s\rho_s}{Dt} + \nabla\cdot\boldsymbol{v}_s + \nabla\cdot\boldsymbol{q}_D = 0. \tag{2.8}$$

The first term in the left hand side of Equation 2.8 can be expressed in terms of the fluid pore pressure and temperature by thermodynamic differentiation as:

$$\frac{\phi}{\rho_f}\frac{D^f\rho_f}{Dt} = \phi\left(\frac{1}{K_f}\frac{D^f p_f}{Dt} - \beta_f\frac{D^f T}{Dt}\right) \tag{2.9}$$

where $\frac{1}{K_f} = \frac{1}{\rho_f}\left(\frac{\partial\rho_f}{\partial p_f}\right)_T$ is the inverse of the fluid bulk modulus and $\beta_f = -\frac{1}{\rho_f}\left(\frac{\partial\rho_f}{\partial T}\right)_{p_f}$ the fluid volumetric thermal expansion coefficient.

The second term in the left hand side of Equation 2.8 can also be cast in terms of the problems variables, e.g. pore pressure, temperature and solid skeleton displacement, by defining a proper constitutive mechanical model. The linear momentum balance

equation of the mixture in terms of the effective Cauchy stress tensor $\boldsymbol{\sigma}'(\boldsymbol{x}, t)$ takes the form:

$$\nabla \cdot (\boldsymbol{\sigma}' - \alpha p_f \mathbb{1}) + \rho_b \boldsymbol{g} = 0 \tag{2.10}$$

where $\mathbb{1}$ is the rank-two identity tensor, and $\alpha = 1 - \frac{K_d}{K_s}$ is the Biot's elastic coefficient, with K_d being the drain bulk modulus of the solid skeleton and K_s the bulk modulus of the solid grains. The geometrical compatibility condition gives the following strain-displacement relation:

$$\boldsymbol{\epsilon} = \frac{1}{2}\left(\nabla \boldsymbol{u} + \nabla^T \boldsymbol{u}\right) = \nabla^s \boldsymbol{u}. \tag{2.11}$$

Deformation of the solid skeleton is described in terms of thermo-poro-elastic response (Biot's consolidation theory) and dissipative plastic behaviour. To simplify the presentation of the constitutive mechanical model, in the following I will consider only small strain conditions, but the theory has been also extended to account for finite deformation. In addition, due to strain history dependence, I detail the formulation in incremental form. Following Biot's theory, (effective) stresses are always related to elastic strains via the following relationship:

$$\dot{\boldsymbol{\sigma}}' = \dot{\sigma}'_{ij} = \mathbb{C}_{ijkl}\dot{\epsilon}^e_{kl} = \mathbb{C} : \dot{\boldsymbol{\epsilon}}^e \tag{2.12}$$

where $\mathbb{C} = \mathbb{C}_{ijkl} = L\delta_{ij}\delta_{kl} + G\left(\delta_{ik}\delta_{jl} + \delta_{il}\delta_{jk}\right)$ is the rank-four elastic stiffness tensor, with L and G being the first and second (shear) Lamé moduli respectively.

The stress-strain constitutive relation given by Equation 2.12, can be then used to find an expression of the material derivative of the solid density in terms of the problem variables (Equation 2.6) as:

$$\frac{(1-\phi)}{\rho_s}\frac{D^s\rho_s}{Dt} = \frac{(\alpha-\phi)}{K_s}\frac{D^s p_f}{Dt} - (1-\phi)\,\beta_s\frac{D^s T}{Dt} + \frac{1}{K_s}\frac{D^s p'}{Dt} \tag{2.13}$$

where p' indicates the effective pressure ($p' = -\frac{\boldsymbol{\sigma}'_{kk}}{3}$) and β_s the volumetric thermal expansion coefficient of the solid grains.

Substituting Equation 2.9 and Equation 2.13 into Equation 2.8, one obtains:

$$\frac{\phi}{K_f}\frac{D^f p_f}{Dt} - \phi\beta_f\frac{D^f T}{Dt} + \frac{(\alpha-\phi)}{K_s}\frac{D^s p_f}{Dt} - (1-\phi)\,\beta_s\frac{D^s T}{Dt} + \frac{1}{K_s}\frac{D^s p'}{Dt} + \dot{\epsilon}_{kk} + \nabla \cdot \boldsymbol{q}_D = 0 \tag{2.14}$$

where I have expressed the gradient of the solid deformation velocity in terms of the volumetric component of the total stain rate tensor, $\nabla \cdot \boldsymbol{v}_s = \nabla \cdot \dot{\boldsymbol{u}} = \dot{\epsilon}_{kk}$.

By making use of the definition of the total derivative and given the stress-strain constitutive equation (Equation 2.12), Equation 2.14 can be recast as:

$$\begin{aligned}\frac{1}{M_b}\frac{\partial p_f}{\partial t} - \beta_b \frac{\partial T}{\partial t} - (1-\alpha)\,\dot{\epsilon}^e_{kk} + \dot{\epsilon}_{kk} + \nabla \cdot \boldsymbol{q}_D + \frac{\phi}{K_f}\nabla p_f \cdot \boldsymbol{v}_f + \frac{(\alpha-\phi)}{K_s}\nabla p_f \cdot \boldsymbol{v}_s \\ - \left(\phi\beta_f \nabla T \cdot \boldsymbol{v}_f + (1-\phi)\,\beta_s \nabla T \cdot \boldsymbol{v}_s\right) + \frac{1}{K_s}\nabla p' \cdot \boldsymbol{v}_s = 0\end{aligned} \tag{2.15}$$

where $\frac{1}{M_b} = \frac{\phi}{K_f} + \frac{(\alpha-\phi)}{K_s}$ is the specific storage of the porous medium and $\beta_b = \phi\beta_f + (1-\phi)\,\beta_s$ is the specific thermal compressibility of the porous medium.

It is possible to rewrite Equation 2.15 in terms of the solid deformation velocity only, by integrating the momentum balance equation (Equation 2.3) as:

$$\begin{aligned}\frac{1}{M_b}\frac{\partial p_f}{\partial t} - \beta_b \frac{\partial T}{\partial t} - (1-\alpha)\,\dot{\epsilon}^e_{kk} + \dot{\epsilon}_{kk} + \nabla \cdot \boldsymbol{q}_D \\ + \boldsymbol{q}_D \cdot \left(\frac{1}{K_f}\nabla p_f - \beta_f \nabla T\right) + \boldsymbol{v}_s \cdot \left(\frac{1}{M_b}\nabla p_f - \beta_b \nabla T + \frac{1}{K_s}\nabla p'\right) = 0\end{aligned} \tag{2.16}$$

where the last two terms can be considered as second order correction terms taking into account non-linear (non-Boussinesq) advective effects.

To quantify any permanent (irreversible) deformation of the material due to inelastic processes I make use of the concept of eigenstrain ($\boldsymbol{\epsilon}^*$) as derived from micromechanics (Mura, 1987). By assuming small strain approximation, the total strain of the material $\boldsymbol{\epsilon}$ can be decomposed as the sum of the elastic strain component ($\boldsymbol{\epsilon}^e$) and eigenstrain parts ($\boldsymbol{\epsilon}^*$) as:

$$\boldsymbol{\epsilon} = \boldsymbol{\epsilon}^e + \boldsymbol{\epsilon}^*. \tag{2.17}$$

Therefore, Equation 2.16 can be written as:

$$\begin{aligned}\frac{1}{M_b}\frac{\partial p_f}{\partial t} - \beta_b \frac{\partial T}{\partial t} + \alpha\dot{\epsilon}_{kk} + (1-\alpha)\,\dot{\epsilon}^*_{kk} + \nabla \cdot \boldsymbol{q}_D \\ + \boldsymbol{q}_D \cdot \left(\frac{1}{K_f}\nabla p_f - \beta_f \nabla T\right) + \boldsymbol{v}_s \cdot \left(\frac{1}{M_b}\nabla p_f - \beta_b \nabla T + \frac{1}{K_s}\nabla p'\right) = 0\end{aligned} \tag{2.18}$$

In the present study I focus on two major kinds of residual deformation, that is thermal expansion and plastic flow, i.e. $\boldsymbol{\epsilon}^* = \epsilon^*_{ij} = \epsilon^{*T}_{ij} + \epsilon^{*p}_{ij} = \boldsymbol{\epsilon}^{*T} + \boldsymbol{\epsilon}^{*p}$, though additional processes including for example swelling, fatigue or phase transformations can be easily integrated in the current formulation.

Thermal strains are related to deformation induced by temperature changes inside the material, and can be therefore expressed by:

$$\dot{\boldsymbol{\epsilon}}^{*T} = \frac{1}{3}\beta_b \dot{T} \mathbb{1} \tag{2.19}$$

where $\beta_b = \phi\beta_f + (1-\phi)\,\beta_s$ is the bulk volumetric thermal expansion coefficient, and $\dot{T}$ is the relative temperature rate.

We determine the plastic component of the strain tensor (Equation 2.17) by making use of the normality rule as:

$$\dot{\boldsymbol{\epsilon}}^{*p} = \dot{\gamma}\frac{\partial \mathcal{Q}}{\partial \boldsymbol{\sigma}'} \tag{2.20}$$

where $\dot{\gamma} = \dot{\gamma}(\boldsymbol{\sigma}', \kappa)$ is the plastic multiplier satisfying the classical Kuhn-Tucker conditions ($\dot{\gamma} \geq 0, \mathcal{F} \leq 0, \dot{\gamma}\mathcal{F} = 0$) with $\mathcal{F}(\boldsymbol{\sigma}', \kappa)$ being the yield surface, and $\mathcal{Q} = \mathcal{Q}(\boldsymbol{\sigma}', \kappa)$ is the plastic potential function giving the direction of the plastic strain increment, and κ represents the vector of internal variables that modify the yield surface during loading and unloading of the material.

Therefore, Equation 2.18 can be finally written for thermal and plastic eigenstrain as:

$$\begin{aligned} &\frac{1}{M_b}\frac{\partial p_f}{\partial t} - \alpha\beta_b\frac{\partial T}{\partial t} + \alpha\dot{\epsilon}_{kk} + (1-\alpha)\,\dot{\epsilon}^{*p}_{kk} + \nabla\cdot\boldsymbol{q}_D \\ &+\boldsymbol{q}_D\cdot\left(\frac{1}{K_f}\nabla p_f - \beta_f\nabla T\right) + \boldsymbol{v}_s\cdot\left(\frac{1}{M_b}\nabla p_f - \beta_b\nabla T + \frac{1}{K_s}\nabla p'\right) = 0. \end{aligned} \tag{2.21}$$

Equation 2.21 can be simplified by neglecting the advective (non-Boussinesq) terms as:

$$\frac{1}{M_b}\frac{\partial p_f}{\partial t} - \alpha\beta_b\frac{\partial T}{\partial t} + \alpha\dot{\epsilon}_{kk} + (1-\alpha)\,\dot{\epsilon}^{*p}_{kk} + \nabla\cdot\boldsymbol{q}_D = 0. \tag{2.22}$$

Similarly, the evolution of porosity can therefore be expressed using Equations 2.7 and 2.13 as well as the strain decomposition as:

$$\frac{\partial \phi}{\partial t} = \frac{(\alpha - \phi)}{K_s}\frac{\partial p_f}{\partial t} - \left[(1-\phi)\,\beta_s - (1-\alpha)\,\beta_b\right]\frac{\partial T}{\partial t} + (\alpha - \phi)\,\dot{\epsilon}_{kk} + (1-\alpha)\,\dot{\epsilon}^{*p}_{kk} + \boldsymbol{v}_s \cdot \left(\frac{(\alpha - \phi)}{K_s}\nabla p_f - (1-\phi)\,\beta_s \nabla T + \frac{1}{K_s}\nabla p' - \nabla \phi\right) \tag{2.23}$$

where the last term can be considered as second order term as well and by neglecting it, Equation 2.23 can be simplified as:

$$\frac{\partial \phi}{\partial t} = \frac{(\alpha - \phi)}{K_s}\frac{\partial p_f}{\partial t} - \left[(1-\phi)\,\beta_s - (1-\alpha)\,\beta_b\right]\frac{\partial T}{\partial t} + (\alpha - \phi)\,\dot{\epsilon}_{kk} + (1-\alpha)\,\dot{\epsilon}^{*p}_{kk}. \tag{2.24}$$

The balance of energy for the fluid-rock mixture, assuming local thermal equilibrium between the two phases, and neglecting the dissipation of mechanical energy due to deformation of the solid phase reads as:

$$(\rho c)_b \frac{\partial T}{\partial t} + \nabla \cdot (\rho_f c_f \boldsymbol{q}_D T - \lambda_b \nabla T) - \dot{H} = 0 \tag{2.25}$$

where $(\rho c)_b = \phi \rho_f c_f + (1-\phi)\,\rho_s c_s$ is the bulk specific heat of the porous medium, $\lambda_b = \phi \lambda_f + (1-\phi)\,\lambda_s$ is the bulk thermal conductivity, and $\dot{H}$ is a rate of energy production. Equation 2.25 can also be extended to take into account secondary, non-Boussinesq dissipative effects related to the pressure temperature dependency of the bulk storage as:

$$T\frac{\partial (\rho c)_b}{\partial t} + (\rho c)_b \frac{\partial T}{\partial t} + \nabla \cdot (\rho_f c_f \boldsymbol{q}_D T - \lambda_b \nabla T) - \dot{H} = 0 \tag{2.26}$$

where the first term (non-Boussinesq) is usually rewritten only considering variable fluid and solid density as:

$$T\frac{\partial (\rho c)_b}{\partial t} = (1-\phi)\,\rho_s c_s T \left(\frac{1}{K_s}\frac{\partial p_f}{\partial t} - \beta_s \frac{\partial T}{\partial t}\right) + \phi \rho_f c_f T \left(\frac{1}{K_f}\frac{\partial p_f}{\partial t} - \beta_f \frac{\partial T}{\partial t}\right) \tag{2.27}$$

The use of a conservative finite element formulation in Equation 2.25 ensures the balance of the fluid enthalpy ($\rho_f c_f T$) both at element and node levels. Therefore it guarantees avoiding accumulating in time unbalances in the intercell fluxes as it is usually the case when relying on non-conservative formulations for convective-type problems.

The energy conservation equation as given by Equation 2.25 is valid for a porous medium in the absence of any thermoelastic coupling. Following Biot consolidation theory, it is possible to consider the effects of the solid elastic deformation on the temperature distribution by augmenting Equation 2.25 with a thermoelastic dissipation rate term, as:

$$(\rho c)_b \frac{\partial T}{\partial t} + T_0 \beta_b \dot{\epsilon}^e_{kk} + \nabla \cdot (\rho_f c_f \boldsymbol{q}_D T - \lambda_b \nabla T) - \dot{H} = 0 \tag{2.28}$$

where T_0 represents the absolute temperature of the porous medium in a stress-free state. Equation 2.25 can be easily modified to take into account additional thermal effects from fluid dilation and shear heating stresses.

2.3 Numerical implementation

In order to solve the system of coupled and non-linear equations as described above, a number of interconnected issues must be taken into account. These include for example the choice of the spatial discretisation adopted, the time stepping scheme and temporal integration, iterative solvers and preconditioners. In what follows, I describe the methods adopted in the simulator in order to tackle these issues. In the next section, I also present some numerical applications that serve as code benchmarking and illustrate the capability of the simulator to solve for problems of different degree of difficulty at optimal cost.

GOLEM is an open source simulator specifically developed for Thermo-Hydraulic-Mechanical coupled applications in fractured geological systems, supporting 1D, 2D, and 3D computations in a single code implementation. It builds on the object-oriented numerical framework MOOSE (Multiphysics Object Oriented Simulations Environment) developed at the Idaho National Laboratory (Gaston et al., 2009). MOOSE provides a flexible, massive parallel (including both MPI and multi-threading) platform to solve for multiphysics and multi-component problems in an implicit manner. It relies on state of the art and extensively tested libraries developed both at universities and national laboratories, as the libMesh library (Kirk et al., 2006) developed at the University of Austin in Texas for capabilities related to parallel finite element method, and a suite of scalable parallel nonlinear and linear solvers (PETSc, Trilinos, Hypre) (Balay et al., 2016). The use of different open-source libraries provides a modular structure to the framework, which permits the developer of an application to only concentrate on the high level description of the multiphysics problem and to maintain the code relatively compact. Following the basic structure of the MOOSE framework, GOLEM

has also been developed as a modular application, where each module is responsible for the solution of a specific physical process. This aspect makes easy any further modification, adjustment and improvement of the program with limited efforts from the user's side. GOLEM is available under the GNU General Public License version 3.0 from the hosting GitHub repository https://github.com/ajacquey/Golem and it comes together with a suite of relatively simple benchmark problems.

2.3.1 Variational formulation and its numerical solution

The finite element discretisation is based on the weak form, in an integral sense, of the system of partial differential equations as derived in the previous paragraph. At this purpose, I consider the porous matrix to be described by a close domain of volume $\Omega \subset \Re^n$ bounded by a boundary $\Gamma \subset \Re^{(n-1)}$. Given the length to width ratio typical of fractures, a discrete fracture is represented by a lower dimensional element of volume $\Omega_f \subset \Re^{(n-1)}$ and surface area $\Gamma_f \subset \Re^{(n-2)}$. The corresponding weak form of the governing equations are then derived by applying the method of the weighted residuals as:

$$\begin{aligned}\int_\Omega \omega \frac{1}{M_b}\frac{\partial p_f}{\partial t} d\Omega - \int_\Omega \omega \alpha \beta_b \frac{\partial T}{\partial t} d\Omega \int_\Omega \omega \left(\alpha \dot{\epsilon}_{kk} + (1-\alpha)\dot{\epsilon}^{*p}_{kk}\right) d\Omega - \int_\Omega \nabla \boldsymbol{\omega} \cdot \boldsymbol{q}_D d\Omega \\ + \int_{\Gamma_{q_H}} \omega \left(\boldsymbol{q}_D \cdot \boldsymbol{n}_{\Gamma_{q_H}}\right) d\Gamma = 0\end{aligned} \tag{2.29}$$

$$\begin{aligned}\int_\Omega \omega (\rho c)_b \frac{\partial T}{\partial t} d\Omega - \int_\Omega \nabla \omega \cdot \left((\rho c)_f \boldsymbol{q}_D T - \lambda_b \nabla T\right) d\Omega \\ + \int_{\Gamma_{q_T}} \omega \left((\rho c)_f \boldsymbol{q}_D T - \lambda_b \nabla T\right) \cdot \boldsymbol{n}_{\Gamma_{q_T}} d\Gamma + \int_\Omega \omega \dot{H} d\Omega = 0\end{aligned} \tag{2.30}$$

$$\int_\Omega \nabla^s \boldsymbol{\omega} : (\boldsymbol{\sigma}' - \alpha p_f \mathbb{1})\, d\Omega - \int_\Omega \boldsymbol{\omega} \cdot \rho_b \boldsymbol{g} d\Omega - \int_\Gamma \boldsymbol{\omega} \cdot (\boldsymbol{\sigma}' - \alpha p_f \mathbb{1}) \cdot \boldsymbol{n}_{\Gamma_{q_M}} d\Gamma = 0 \tag{2.31}$$

where in Equation 2.29, Equation 2.30, and Equation 2.31 all supra-(sub)scripting are omitted and the advective (non-Boussinesq) terms were considered negligible for easiness in the notation.

The equations derived above describe an initial and boundary value problem, for which proper boundary and initial conditions need to be assigned. These can be set by

either prescribing the value of the problem variables along or its flux across a portion of the boundary. More precisely, the model discussed in the previous paragraph, must satisfy the following set of boundary conditions:

- Equilibrium of boundary stresses and external loads (last two terms in Equation 2.31).
- Prescribed displacement, pore pressure and temperature, i.e. $\boldsymbol{u} = \bar{\boldsymbol{u}}$, $p_f = \bar{p_f}$, $T = \bar{T}$ on Γ_u, Γ_{p_f} and Γ_T respectively.
- Continuity of the fluid flux across the imposed boundary, i.e. $\boldsymbol{q}_D \cdot \boldsymbol{n}_{\Gamma_{q_H}} = \bar{q}_H$ on $\partial\Omega_{q_H}$ where $\bar{q}_H$ is the rate of in/out-flow per unit of area across the boundary surface.
- Continuity of the total (diffusive plus advective) heat flow, i.e. $\Big((\rho c)_f \boldsymbol{q}_D T - \lambda_b \nabla T\Big) \cdot \boldsymbol{n}_{\Gamma_{q_T}} = \bar{q}_T$ on Γ_{q_T} where $\bar{q}_T$ is the rate of in/out-heat flow per unit of area across the boundary surface.

The resulting system of equations together with a proper choice of boundary and initial conditions is discretised spatially by the Finite Element Method, while the temporal discretisation is done by traditional finite difference techniques. The nodal values of the primary variables of the problem, temperature (T^n), pore pressure (p_f^n), and the deformation vector of the solid skeleton ($\boldsymbol{u}^n$) are approximated by linear Lagrangian interpolation polynomial functions as:

$$\begin{aligned} T^n &= \sum_{i=1}^{i=N_T} T_i^n w_i^T(\boldsymbol{x}) \\ p_f^n &= \sum_{i=1}^{i=N_{p_f}} {p_f}_i^n w_i^{p_f}(\boldsymbol{x}) \\ \boldsymbol{u}^n &= \sum_{i=1}^{i=N_u} u_i^n \boldsymbol{w}_i^u(\boldsymbol{x}) \end{aligned} \tag{2.32}$$

Though higher order polynomials are also available through the libMesh library, I rely on linear finite element approximation for all variables. Indeed, I have found that, for the kinds of problems as those that will be presented in the next paragraph, higher order approximations do not necessarily guarantee higher order of convergence in the solution, being subjected at the same time to severe under-(over)shooting numerical effects in the presence of sharp gradients.

Single-nodded, zero thickness finite elements are used to explicitly represent individual fractures, the latter assumed to be clean and fully saturated (i.e. $\alpha = 1$ and $M_b = K_f$). It follows that fractures can be parametrised as based on the concept of their effective aperture, the latter giving a quantitative measure of the geometric width of the fracture surface. The use of single-nodded finite elements imposes continuity of gradients in both pressure and temperature across the fracture width, as well as the absence of any shear and normal strain acting on the fracture plane. While the latter assumption simplifies the problem formulation, it prevents to include the effects of local fracture mechanics in the current formulation. Therefore, fractures are only considered as having a distinct hydraulic and thermal behaviour with respect to the porous domain. In Chapter 7, I discuss how to extend the current formulation to include mechanical feedback effects from localised deformation, nucleation and fracture propagation via XFEM techniques.

The mass balance equation for a discrete fracture then reads as:

$$\begin{aligned}\int_{\Omega_f}\int_{-\frac{b}{2}}^{\frac{b}{2}} \omega \frac{1}{K_f}\frac{\partial p_f}{\partial t} dy' d\Omega_f - \int_{\Omega_f}\int_{-\frac{b}{2}}^{\frac{b}{2}} \bar{\nabla}\omega \cdot \boldsymbol{q}_D dy' d\Omega_f \\ + \int_{\Gamma_f}\int_{-\frac{b}{2}}^{\frac{b}{2}} \omega \boldsymbol{q}_D \cdot \hat{\boldsymbol{n}} dy' d\Gamma + \Lambda_H^+ + \Lambda_H^- = 0\end{aligned} \tag{2.33}$$

where $\Lambda_H^{\pm}$ are leakage terms (weak form) across each of the two sides of the fracture surface into the surrounding porous domain.

In a similar manner, the energy balance equation for a fracture element reads as:

$$\begin{aligned}\int_{\Omega_f}\int_{-\frac{b}{2}}^{\frac{b}{2}} \omega \left(c_f \rho_f \frac{\partial T}{\partial t} + H\right) dy' d\Omega_f - \int_{\Omega_f}\int_{-\frac{b}{2}}^{\frac{b}{2}} \nabla_f^T \omega \cdot \rho_f \left(c_f \boldsymbol{q}_D T - \lambda_f \nabla_f T\right) dy' d\Omega_f + \\ \int_{\partial\Omega}\int_{-\frac{b}{2}}^{\frac{b}{2}} \omega \left(\rho_f c_f \boldsymbol{q}_D T - \lambda_f \nabla_f T\right) \cdot \hat{\boldsymbol{n}} dy' d\Omega_f + \Lambda_T^+ + \Lambda_T^- = 0\end{aligned} \tag{2.34}$$

where $\Lambda_T^{\pm}$ quantify the amount of heat leaking from the fracture surfaces into the porous medium domain.

In Equations 2.33 and 2.34 integration is done in the local coordinates system of the fracture tangential and normal directions respectively. This enables to superimpose the discretised conservative equations for the porous medium and the fractures at the

nodal location shared by the two elements, where the fluid mass and heat fluxes also cancelled out. Therefore the weak form of the conservation equations can be simplified as:

$$\int_{\Omega_f} b\omega \frac{1}{K_f} \frac{\partial p_f}{\partial t} d\Omega_f - \int_{\Omega_f} b \nabla_f \omega^T \cdot \boldsymbol{q}_D d\Omega_f + \int_{\partial\Omega_f} b\omega \boldsymbol{q}_D \cdot \hat{\boldsymbol{n}} dS_f = 0 \tag{2.35}$$

and

$$\begin{aligned} \int_{\Omega_f} b\omega \left(\rho_f c_f \frac{\partial T}{\partial t} + H \right) d\Omega_f - \int_{\Omega_f} b \nabla_f^T \omega \cdot \rho_f \left(c_f \boldsymbol{q}_D T - \lambda_f \nabla_f T \right) d\Omega_f + \\ \int_{\partial\Omega_f} b\omega \left(\rho_f c_f \boldsymbol{q}_D T - \lambda_f \nabla_f T \right) \cdot \hat{\boldsymbol{n}} dy' dS_f = 0 \end{aligned} \tag{2.36}$$

where no distinction between the effective hydraulic aperture (b_h) and the mechanical aperture (b_m) were made.

Derivatives of the test functions and of direction-dependent material properties with respect to the system of global coordinates are computed by standard coordinate transformation, i.e. $\frac{\partial N_i}{\partial x_i} = J_{ij}^{-1} \frac{\partial N_i}{\partial \psi_i}$ where J_{ij} is the Jacobian matrix of the mapping between global (x_i) and local (ψ_i) coordinates. Transformation in local coordinates for lower dimensional elements is achieved by computing the rotational matrix, $\boldsymbol{R} = \begin{bmatrix} \cos(x', x) & \cos(x', y) & \cos(x', y) \\ \cos(y', x) & \cos(y', y) & \cos(y', y) \\ \cos(z', x) & \cos(z', y) & \cos(z', y) \end{bmatrix}$ with $\cos(x_i', x_i)$ being the directional cosines. Coordinate transformation is applied to all direction-dependent (i.e. tensorial) material properties as well as to the directional derivatives as:

$$\boldsymbol{N} = \boldsymbol{R} \boldsymbol{I}_f \boldsymbol{N}' \boldsymbol{I}_f^T \boldsymbol{R}^T \tag{2.37}$$

where $\boldsymbol{N}$ and $\boldsymbol{N}'$ are direction-dependent material properties in global and local coordinates respectively, and $\boldsymbol{I}_f$ is the unit tangent vector of local coordinates.

The above system of coupled equation can be rewritten in a more concise form as:

$$\bar{\boldsymbol{S}} \frac{d\bar{\boldsymbol{x}}}{dt} + \bar{\boldsymbol{K}} \bar{\boldsymbol{x}} - \bar{\boldsymbol{F}} = \boldsymbol{R}(\hat{\boldsymbol{u}}) \tag{2.38}$$

where $\bar{\boldsymbol{S}}$ is the nodal coefficient storage matrix, $\bar{\boldsymbol{K}}$ denotes the stiffness matrix of the problem, $\bar{\boldsymbol{F}}$ is the load vector and $\bar{\boldsymbol{x}}$ is the vector of the problems variables, and $\boldsymbol{R}(\hat{\boldsymbol{u}})$

is the residual from the discrete approximation. I make use of an unconditionally stable, backward Euler method to integrate Equation 2.38 in the time domain, and to arrive at the monolithic form of the coupled system. The monolithic form of Equation 2.38 is then solved iteratively by classical Newton's method, where different linear solvers (e.g. GMRES and its flexible variant, FGMRES) and preconditioners (including also Newton-Krylov-Schwartz domain decomposition techniques) are available from the open source algebraic libraries.

2.3.2 Nonlinearities and their stabilization

The coefficient matrices in Equation 2.38 contain off diagonal components, thus giving rise to a highly-nonlinear problem to be solved for. Non-linearities arise due the non-linear constitutive relationship between problem variables and material properties, as well as to the presence of internal feedback effects among the different processes. The constitutive relation linking structure properties and primary variables considered include equation of states for fluid density, thermal compressibility and expansivity and fluid viscosity with respect to the p-T state of the system (IAPWS, 2008a,b), as well as poro-perm relationships relating porosity and permeability evolution as a function of variation in the thermal, mechanical an hydraulic state of the system, see Figure 2.2 as an example.

For problems involving heat transport, if the convective term dominates over the diffusive term, the solution of the energy transport equation typically contains interior and boundary layers and its solution by the Galerkin finite element technique is usually globally unstable. Numerical instabilities in the forms of spurious oscillations around sharp gradients and boundary layers and which likely lead to non convergent solutions, have been observed to occur independent of the level of mesh refinement. In such situations, in order to enhance the stability and accuracy of the finite element solution, some sort of stabilisation has to be added to the discrete formulation. In GOLEM, I have opted for the Streamline Upwind Petro/Galerkin (SUPG) method, which can be conceived as adding an upwind perturbation along computed streamlines to the standard Galerkin formulation (Brooks and Hughes, 1982). The SUPG discretisation of Equation 2.25 is obtained by making use of an 'enriched' weighting functions, ω^*, as:

$$\omega^* = \omega + p \tag{2.39}$$

where ω is the continuous weighting function and $p = \tau \nabla\omega \nabla \boldsymbol{q}_D \|\boldsymbol{q}_D\|$ is a discontinuous streamline upwind correction. Note that by its definition, ω^* is no longer continuous

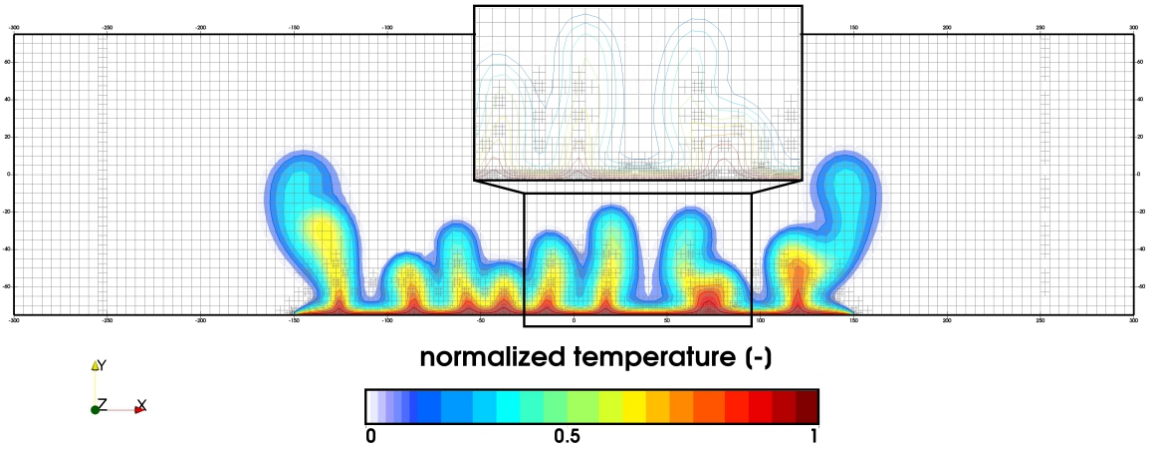

Fig. 2.2 Example of a non-linear convective flow problems after Elder (1967). An homogeneous, isotropic and saturated porous medium is heated from below with fluid density and viscosity being a function of temperature and pressure (IAPWS, 2008a,b). Due to the temporal evolution in fluid property gradients, thermal buoyant forces develop thus giving rise to an unstable convective flow regime as illustrated by the temperature isolines. H-mesh adaptive refinement with local error estimate based on the L-2 norm projection of the intercell thermal flux vectors and a two-refinement cycle per time step has been enforced in order to guarantee numerical stability even in the presence of sharp thermal gradients (see close up).

across inter-element boundaries. A critical question is related to the choice of the upwind parameter τ, which might influence the stability and accuracy of the discrete solution. In the current formulation, it has been chosen to use the following definition (Galeão et al., 2004):

$$\tau = \frac{h}{2\|\boldsymbol{q}_D\|p}\left(\coth(P_e) - \frac{1}{P_e}\right) \tag{2.40}$$

where h is the diameter of the finite element adopted along the direction of $\boldsymbol{q}_D$, p is the order of approximation considered in the interpolation, $\|\cdot\|$ is the Euclidean norm, and $P_e = \frac{\|\boldsymbol{q}_D\|h}{2\lambda_b p}$ is the local Péclet number. A major disadvantage of the SUPG method is to add numerical diffusion to all elements characterised by a high Péclet number, even in the absence of sharp thermal gradients. I leave as a subject of future studies the implementation of more recent and more sophisticated damping methods, such as entropy viscosity methods.

2.3.3 Plasticity and return-map algorithm

I consider plastic deformation in terms of a Drucker-Prager frictional plastic yield criterion in which the onset of yield is a function of the first and second invariants of the effective stress tensor $J_1 = \boldsymbol{\sigma}'_{kk}, \quad J_2 = \frac{1}{2}(\boldsymbol{\tau}_{ij}\boldsymbol{\tau}_{ij})$ respectively where τ_{ij} is the deviatoric part of the effective stress tensor ($\boldsymbol{\tau}_{ij} = \boldsymbol{\sigma}'_{ij} - \frac{1}{3}J_1\delta_{ij}$):

$$\mathcal{F} = \sqrt{J_2 + \epsilon_0^2} + \frac{\sin(\varphi)}{3}J_1 - C\cos(\varphi) \tag{2.41}$$

where φ and C are the Mohr-Coulomb friction angle and cohesion respectively and ϵ_0 is a small non-hardening parameters here introduced to relax the singularity at the cone's tip of the Drucker-Prager yield envelope. An important aspect relates to the form of plastic potential function adopted. It has been shown that associated flow rule might lead to overestimate the dilation of the rocks and it generally results in a overly weaker response of the rock to loading (Vermeer and de Borst, 1984). I avoid these issues by implementing a non-associated form of Drucker-Prager, in which the plastic potential function $\mathcal{G}$, is considered to depend on the dilation angle, ψ as:

$$\mathcal{G} = \sqrt{J_2} + \frac{\sin(\psi)}{3}J_1 \tag{2.42}$$

and, in consequence, the unnormalised flow directions can be derived as:

$$\frac{\partial \mathcal{G}}{\partial \boldsymbol{\sigma}'_{ij}} = \frac{1}{2\sqrt{J_2}}\frac{\partial J_2}{\partial \boldsymbol{\sigma}'_{ij}} + \frac{\sin(\psi)}{3}\delta_{ij} \tag{2.43}$$

Note that in the formulation, I take also into account possible degradation of the strength of the rock subjected to loading in terms of hardening (and softening) of the internal parameters (friction angle, cohesion and dilation angle) as a function of the accumulated plastic strain.

The stress update procedure is conducted with a return-map algorithm based on the closest point projection on the yield surface (Simo and Hughes, 1998) with a Newton-Raphson procedure. Conceptually, this algorithm is presented in incremental form in the following. Subscript n refers to a value at the time t_n, that is $\sigma_n = \sigma(t_n)$ and superscript (k) refers to the k^{th} iteration in the Newton-Raphson procedure. We use the following notation for sake of simplicity: $\partial_{\boldsymbol{\sigma}'}\cdot = \frac{\partial \cdot}{\partial \boldsymbol{\sigma}'}$.

1. Assume plastic loading, $\mathcal{F}_{n+1}^{trial} > 0$ so the increment of plastic multiplier is also positive according to the Kuhn-Tucker conditions, $\Delta\gamma > 0$. Define the system of equations with the residuals to minimise, the plastic flow residual $\boldsymbol{R}_{\boldsymbol{\epsilon},n+1}$, the internal parameter residuals $\boldsymbol{R}_{\boldsymbol{\kappa},n+1}$ and the yield condition for this time step

$\mathcal{F}_{n+1}$ as:

$$\begin{cases} \boldsymbol{R}_{\boldsymbol{\epsilon},n+1} &= -\boldsymbol{\epsilon}^{*p}_{n+1} + \boldsymbol{\epsilon}^{*p}_{n} + \Delta\gamma\partial_{\boldsymbol{\sigma}'}\mathcal{G} \\ \boldsymbol{R}_{\boldsymbol{\kappa},n+1} &= \boldsymbol{\kappa}_{n+1} + \boldsymbol{\kappa}_{n} - \Delta\gamma\mathcal{H} \\ \mathcal{F}_{n+1} &= \mathcal{F}\left(\boldsymbol{\sigma}'_{n+1}, \boldsymbol{\kappa}_{n+1}\right) \end{cases}$$

where $\mathcal{H}$ is the hardening flow rule for the internal parameter $\boldsymbol{\kappa}$, that is $\dot{\boldsymbol{\kappa}} = -\dot{\gamma}\mathcal{H}$.

2. This system of equation is then linearised as follow:

$$\begin{cases} \boldsymbol{R}^{(k)}_{\boldsymbol{\epsilon},n+1} + \partial_{\boldsymbol{\sigma}'}\boldsymbol{R}^{(k)}_{\boldsymbol{\epsilon},n+1} : \Delta\boldsymbol{\sigma}'^{(k)}_{n+1} + \partial_{\boldsymbol{\kappa}}\boldsymbol{R}^{(k)}_{\boldsymbol{\epsilon},n+1} : \Delta\boldsymbol{\kappa}^{(k)}_{n+1} &= 0 \\ \boldsymbol{R}^{(k)}_{\boldsymbol{\kappa},n+1} + \partial_{\boldsymbol{\sigma}'}\boldsymbol{R}^{(k)}_{\boldsymbol{\kappa},n+1} : \Delta\boldsymbol{\sigma}'^{(k)}_{n+1} + \partial_{\boldsymbol{\kappa}}\boldsymbol{R}^{(k)}_{\boldsymbol{\kappa},n+1} : \Delta\boldsymbol{\kappa}^{(k)}_{n+1} &= 0 \\ \mathcal{F}^{(k)}_{n+1} + \partial_{\boldsymbol{\sigma}'}\mathcal{F}^{(k)}_{n+1} : \Delta\boldsymbol{\sigma}'^{(k)}_{n+1} + \partial_{\boldsymbol{\kappa}}\mathcal{F}^{(k)}_{n+1} : \Delta\boldsymbol{\kappa}^{(k)}_{n+1} &= 0 \end{cases}$$

which can be expressed as a matrix system as follow:

$$\begin{bmatrix} \left(\mathbb{C}^{-1} + \Delta\gamma^{(k)}_{n+1}\partial^2_{\boldsymbol{\sigma}'\boldsymbol{\sigma}'}\mathcal{G}^{k}_{n+1}\right) & \Delta\gamma^{(k)}_{n+1}\partial^2_{\boldsymbol{\sigma}'\boldsymbol{\kappa}}\mathcal{G}_{n+1}(k) & \partial_{\boldsymbol{\sigma}'}\mathcal{G}^{(k)}_{n+1} \\ \Delta\gamma^{(k)}_{n+1}\partial_{\boldsymbol{\sigma}'}\mathcal{H}^{(k)}_{n+1} & \mathbb{1} + \Delta\gamma^{(k)}_{n+1}\partial_{\boldsymbol{\kappa}}\mathcal{H}^{(k)}_{n+1} & \mathcal{H}^{(k)}_{n+1} \\ \partial_{\boldsymbol{\sigma}'}\mathcal{F}^{(k)}_{n+1} & \partial_{\boldsymbol{\kappa}}\mathcal{F}^{(k)}_{n+1} & 0 \end{bmatrix} \begin{bmatrix} \Delta\boldsymbol{\sigma}'^{(k)}_{n+1} \\ \Delta\boldsymbol{\kappa}^{(k)}_{n+1} \\ \Delta^2\gamma^{(k)}_{n+1} \end{bmatrix} = \begin{bmatrix} -\boldsymbol{R}^{(k)}_{\boldsymbol{\epsilon},n+1} \\ -\boldsymbol{R}^{(k)}_{\boldsymbol{\kappa},n+1} \\ -\mathcal{F}^{(k)}_{n+1} \end{bmatrix}$$

3. The aforementioned matrix system of equation is solved at each k^{th} iteration using routines from the PETSc library (Balay et al., 2016) for the increment of stress, internal parameter and plastic multiplier ($\Delta\boldsymbol{\sigma}'^{(k)}_{n+1}$, $\Delta\boldsymbol{\kappa}^{(k)}_{n+1}$ and $\Delta^2\gamma^{(k)}_{n+1}$).

4. The variables are updated at the end of the k^{th} iteration:

$$\begin{aligned} \boldsymbol{\sigma}'^{(k+1)}_{n+1} &= \boldsymbol{\sigma}'^{(k)}_{n+1} + \Delta\boldsymbol{\sigma}'^{(k)}_{n+1} \\ \boldsymbol{\epsilon}^{*p(k+1)}_{n+1} &= \boldsymbol{\epsilon}^{*p(k)}_{n+1} - \mathbb{C}^{-1} : \Delta\boldsymbol{\sigma}'^{(k)}_{n+1} \\ \boldsymbol{\kappa}^{(k+1)}_{n+1} &= \boldsymbol{\kappa}^{(k)}_{n+1} + \Delta\boldsymbol{\kappa}^{(k)}_{n+1} \\ \Delta\gamma^{(k+1)}_{n+1} &= \Delta\gamma^{(k)}_{n+1} + \Delta^2\gamma^{(k)}_{n+1} \end{aligned}$$

5. Steps 1 to 4 are repeated until the residuals reached minimum threshold values

2.4 Benchmarks

In this section, I present three different applications of the numerical simulator. These applications are intended to test the ability of the simulator to deal both with single processes and their coupling.

2.4.1 Heat transport in a fracture

The first application deals with groundwater flow and (diffusive and advective) heat transport in a fracture, i.e. TH application. We assume a fracture which is fully saturated with water ($\phi = 1$), having homogeneous and isotropic properties. Groundwater flow in the fracture is assumed to be unidirectional and the average velocity is considered constant throughout the length of the flow field. The initial temperature is set to zero. At time $t = 0$, a sudden increase in temperature is imposed along the inlet boundary of the medium ($T = T_0$). The problem can be formulated as a semi-infinite medium with a point source at the inlet boundary ($T = T_0 H(x = 0, t)$ with $H(t)$ being the Heaviside function). Under these assumptions, Ogata and Banks (1961) gave an analytical solution for the variation of the temperature as a function of the position and time as:

$$T(x,t) = \frac{T_0}{2}\left(erfc\left(\frac{(x - v_x t)}{\sqrt{4kt}}\right) + \exp\left(\frac{v_x x}{k}\right) erfc\left(\frac{(x + v_x t)}{\sqrt{4kt}}\right)\right) \tag{2.44}$$

where k is the thermal diffusivity ($k = \frac{\lambda_f}{\rho_f c_f}$). For the numerical simulation, I consider a fracture of length $L = 100\,\mathrm{m}$, which has been discretised into line elements of equal length and subjected to an imposed pressure gradient of $\nabla p_f = 3\,\mathrm{Pa} \cdot \mathrm{m}^{-1}$. All material properties are listed in Table 2.1.

Table 2.1 Fluid properties for the example of heat transport in a fracture

Property name	Symbol	Value	SI unit
Fluid density	ρ_f	1000	$\mathrm{kg} \cdot \mathrm{m}^{-3}$
Fluid thermal conductivity	λ_f	0.65	$\mathrm{W} \cdot \mathrm{m}^{-1} \cdot \mathrm{K}^{-1}$
Fluid heat capacity	c_f	4000	$\mathrm{J} \cdot \mathrm{kg}^{-1} \cdot \mathrm{K}^{-1}$
Fluid viscosity	μ_f	1.0×10^{-3}	$\mathrm{Pa} \cdot \mathrm{s}$
Fluid permeability	k	1.0×10^{-10}	m^2

Given the parameters considered, a constant fluid velocity ($v_x = 3.0 \times 10^{-7}\,\mathrm{m} \cdot \mathrm{s}^{-1}$) is obtained. Initial conditions for the pressure and temperature are $p_f = 0.1\,\mathrm{MPa}$ and $T = 0\,^{\circ}\mathrm{C}$ respectively. In this benchmark, I compare the evolution of the temperature field (normalized by the inlet temperature value) at four different points along the length of the fracture with the analytical solution as given by Equation 2.44. Figure 2.3 shows the comparison between model results (red curves) and the corresponding analytical solutions (black circles) during the entire simulation time. There is a general good

fit in terms of the temporal evolution of the advected front at all location along the fracture plane, with the modelled thermal moving slightly faster as visible from the earlier stepping of the temperature at the observation points. I have investigated the influence of the spatial discretisation on the resulting thermal front evolution, by gradually increasing the resolution of the mesh. The results from this analysis are shown in Figure 2.3b where the curves obtained from three different mesh refinements are plotted against the analytical results. From Figure 2.3b it can be notice that the discretisation error converges relatively fast, a resolution of 0.1 m being sufficient to saturate the relative errors (continuous curves). Based on the obtained results, one can conclude that the TH numerical implementation is accurate for practical applications.

2.4.2 Flow in a fractured porous medium

The purpose of this application is to test the numerical implementation of the formulation in the presence of discrete fractures. At this purpose, I refer to a relative common benchmark dealing with uniform, steady-state flow in a porous medium locally disturbed by the presence of a fracture (Strack, 1982; Watanabe, 2011; Watanabe et al., 2012). The original problem formulation considers a semi-infinite two-dimensional horizontal section with an embedded fracture located symmetrically at its centre. Uniform flow is maintained by imposing a specific discharge (q_0) from the left boundary inside the domain, the value of which is kept constant and equal to $q_0 = 1.0 \times 10^{-4}\,\mathrm{m \cdot s^{-1}}$. The fracture is consider to extend infinitely along the direction normal to the plane, while being of finite along-plane length (L), with its middle point located exactly at the centre of the domain. It has a width which can be varied along its length (though it is assumed to remain constant in the following), an it is inclined with respect to the model boundary by a constant angle (α).

Table 2.2 Material properties the example of flow in a fractured porous medium

	Property name	Symbol	Value	SI unit
Fracture	Angle	α	45	$^\circ$
	Length	L	2	m
	Aperture	h	0.05	m
	Permeability	k^f	1.0×10^{-10}	$\mathrm{m^2}$
	Viscosity	μ_f^f	1.0×10^{-3}	$\mathrm{Pa \cdot s}$
Porous medium	Porosity	ϕ	0.15	-
	Permeability	k	1.0×10^{-12}	$\mathrm{m^2}$
	Viscosity	μ_f	1.0×10^{-3}	$\mathrm{Pa \cdot s}$

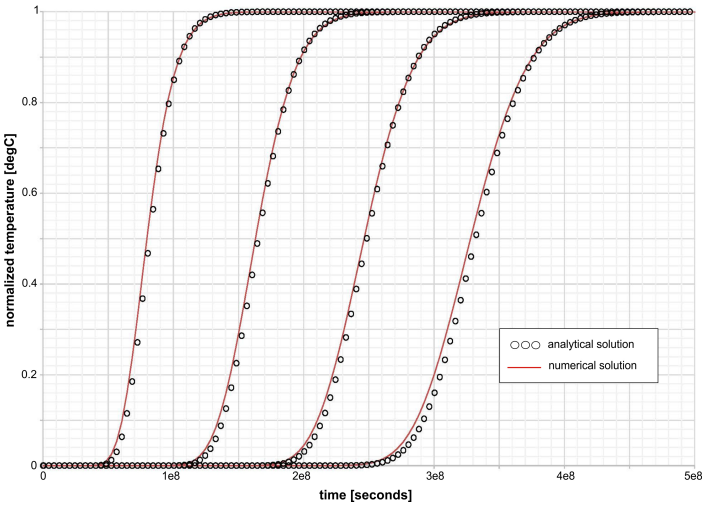

(a)

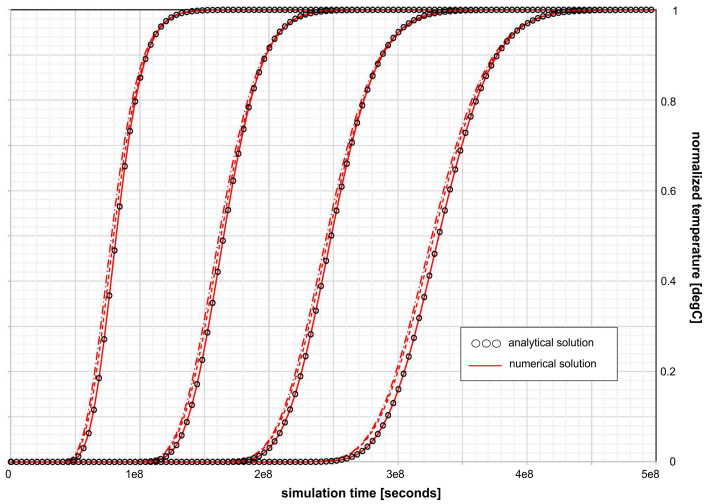

(b)

Fig. 2.3 Comparison of numerical results (red curves) and analytical solutions (black circles) for heat transport in a fracture. Panel 2.3a shows the temperature evolution at different positions along the fracture as a function of time. The mesh resolution was kept constant and equal to 0.2 m. Panel 2.3b illustrates the same results but considering a refinement in the discretisation (mesh resolution of 0.1 m).

I have extended the original formulation to a three dimensional case, see Figure 2.4 for the model geometry and boundary conditions. The setup of the problem comprises a three dimensional, quadrilateral box ($10 \times 10 \times 1$ m in x-y-z-directions respectively) representing the porous medium. The fracture is implemented as a two dimensional surface cutting entirely the model along the vertical direction and having a finite horizontal length of $L = 2$ m. It is inclined by an angle α =45° with respect to the model boundaries. In order to maintain a constant discharge from the left to the

right of the model, constant pressure boundary conditions are imposed along the same boundaries thus resulting in a constant pressure gradient along the x-axis. The value of the imposed pressure gradient ($\Delta p = 1\,\mathrm{MPa}$) has been enforced so to match the value of specific discharge of the original problem, thus permitting a direct comparison between the analytical and numerical solution. No flow conditions are imposed along the other boundaries. Laminar flow is assumed in the fracture plane, and pressure variations across its width are neglected. All relevant parameters are summarised in Table 2.2.

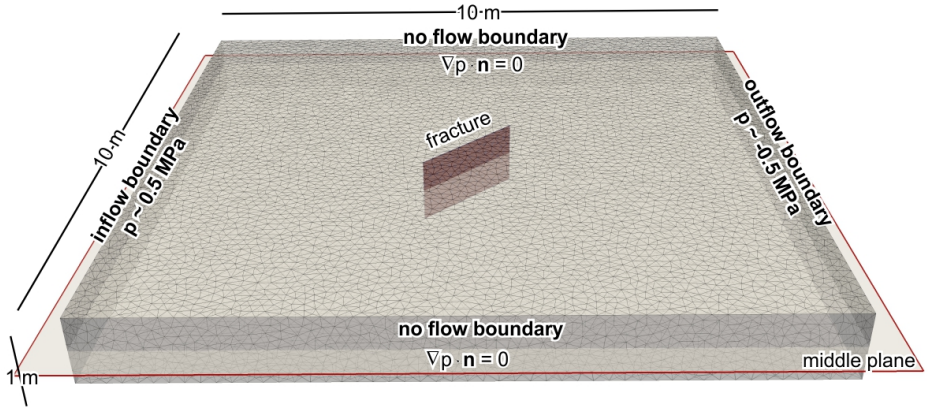

Fig. 2.4 Geometry and boundary condition for the benchmark case of groundwater flow in a fractured porous medium.

Strack (1982) provided an analytical solution for the one dimensional version of the problem derived in terms of a complex potential flow as:

$$\Omega = -A\sqrt{(Z-1)(Z+1)} + AZ - \frac{1}{2}q_0 L e^{i\alpha} Z \tag{2.45}$$

where q_0 is the magnitude of the flow occurring within the model domain (assumed uniform), $Z = \frac{z-\frac{1}{2}(z_1+z_2)}{\frac{1}{2}(z_2-z_1)}$ is the fracture-related dimensionless variable (z_1 and z_2 being the endpoints of the fracture), and $A = \frac{\frac{1}{2}k_f h}{kL+k_f h} q_0 L \cos\alpha$.

The numerical solution of the three dimensional problem has been obtained by solving a steady state flow problem within the matrix-fracture domain. The computed pressure distribution together with the outline of the geometry of the fracture are plot in Figure 2.5.

The presence of the discrete fracture disturbed the uniform horizontal flow in a close domain around its location. There, the isolines of constant pressure are distorted, and results in a faster flow preferentially oriented parallel to the fracture plane. In order to test the reliability of the numerical solution, I compare the computed pore pressure

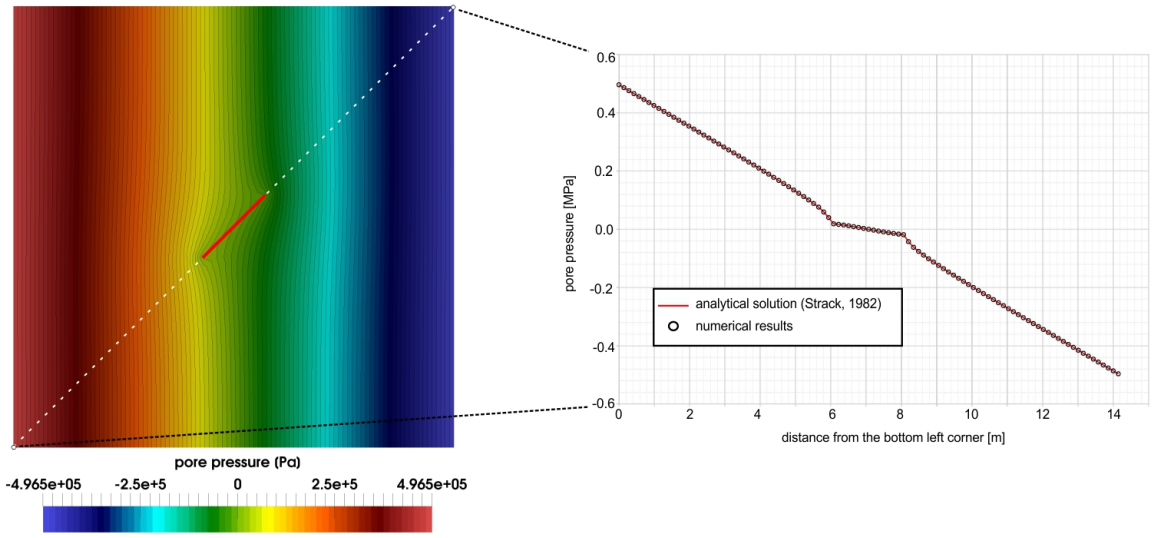

Fig. 2.5 Isolines of pressure computed from the 3D numerical simulation extracted along a horizontal plane cutting the model domain. Comparison between simulated (empty black circles) and analytical derived (continuous red curve) pressure distribution along a line through the model.

extracted along a diagonal cross section cutting the model domain along its bottom left-top right corners with the pore pressure derived from analytical solution. The comparison shows a perfect fit between the two results, thus proving the applicability of the discrete fracture approach as implemented in the current formulation.

2.4.3 3D oedometer test

In the following test, I consider a cube of porous medium with edges of 1 m. The cube is subjected to axial loading with constant velocity v_x under the conditions of an oedometer test (see setup in Figure 2.6a). The porous material undergoes elastic loading until the strength of the material is reached and then undergoes plastic loading. The elastoplastic constitutive laws adopted for this simple problem formulation is the Drucker-Prager plasticity model. The Drucker-Prager yield envelope is a smoother version of the classical Mohr-Coulomb failure criterion. Under these conditions, an analytical solution for the stress state of the porous material can be derived as described in the next section and serves here as verification of the numerical implementation of the elastoplastic constitutive laws. The physical properties used for this benchmark are summarised in Table 2.3.

Figure 2.6b shows the evolution of stress and plastic strain for an associative (red dots) and two non-associative (dilation angle different from friction angle) plastic

Table 2.3 Mechanical properties for the oedometer benchmark.

Property name	Symbol	Value	Unit
Bulk modulus	K	2.0×10^3	MPa
Shear modulus	G	2.0×10^3	MPa
Cohesion	C	1	MPa
Friction angle	φ	20	°
Dilation angle	ψ	0, 10 or 20	°
Velocity	v_x	1.0×10^{-5}	$\mathrm{m} \cdot \mathrm{s}^{-1}$
Edge of the cube	l	1	m

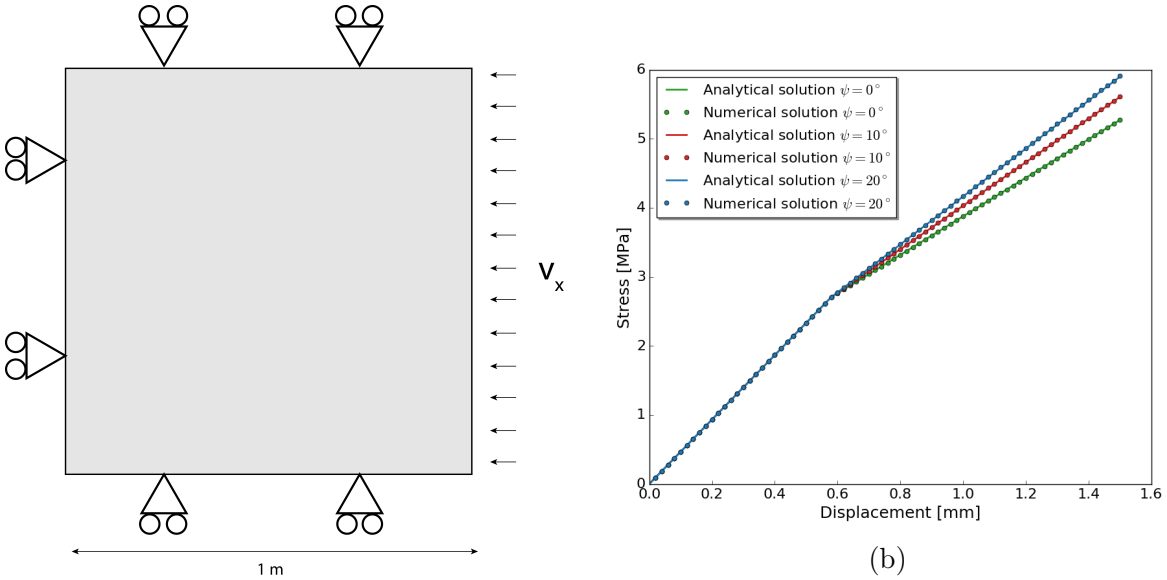

(a) (b)

Fig. 2.6 Problem formulation and results of the oedometer benchmark. Panel 2.6a shows the problem formulation. Panel 2.6b illustrates the results for different dilation angles with the stress-displacement curves.

potentials (blue and green dots). The results exhibit a perfect agreement between analytical solution and numerical prediction.

Analytical solution for the oedometer benchmark During elastic loading with constant velocity v_x, the strain evolves as:

$$\epsilon_{xx} = \frac{v_x t}{l}, \quad \epsilon_{yy} = \epsilon_{zz} = 0 \tag{2.46}$$

because of the no displacement boundary conditions in the y- and z-directions. The stress during elastic loading therefore reads:

$$\sigma_{xx} = (L + 2G)\,\frac{v_x t}{l}, \quad \sigma_{yy} = \sigma_{zz} = L\frac{v_x t}{l}. \tag{2.47}$$

With these expressions of stress, the invariants of the stress tensor, J_1 and J_2 can be written as:

$$J_1 = (3L + 2G)\,\frac{v_x t}{l}, \quad J_2 = \frac{4}{3}\left(G\frac{v_x t}{l}\right)^2. \tag{2.48}$$

The onset of plastic strain accumulation is reached when the yield function reaches 0 at a time noted t_y, that is $\mathcal{F}(t_y) = 0$. By using the expressions of the stress invariants in Equation 2.41, the time for onset of yielding can be expressed as:

$$t_y = \frac{lC\cos\varphi}{|v_x|\left(\frac{2}{\sqrt{3}}G - \sin(\varphi)(L + \frac{2}{3}G)\right)}. \tag{2.49}$$

The increment of plastic strain accumulation can be expressed by reinjecting the expressions of the stress invariants and Equation 2.47 into Equation 2.20:

$$\begin{aligned}
\Delta\epsilon^{*p}_{xx} &= \frac{\Delta\gamma}{\sqrt{3}}\left(-1 + \frac{\sin(\psi)}{\sqrt{3}}\right),\\
\Delta\epsilon^{*p}_{yy} &= \frac{\Delta\gamma}{\sqrt{3}}\left(\frac{1}{2} + \frac{\sin(\psi)}{\sqrt{3}}\right),\\
\Delta\epsilon^{*p}_{zz} &= \frac{\Delta\gamma}{\sqrt{3}}\left(\frac{1}{2} + \frac{\sin(\psi)}{\sqrt{3}}\right).
\end{aligned} \tag{2.50}$$

The increment of stress during plastic accumulation can therefore be written:

$$\begin{aligned}
\Delta\sigma_{xx} &= (L + 2G)\,\frac{v_x\Delta t}{l} + \Delta\gamma\left[\frac{2}{\sqrt{3}}\left(1 - \frac{\sin(\psi)}{\sqrt{3}}\right)G - L\sin(\psi)\right],\\
\Delta\sigma_{yy} &= L\frac{v_x\Delta t}{l} - \Delta\gamma\left[\frac{2}{\sqrt{3}}\left(\frac{1}{2} + \frac{\sin(\psi)}{\sqrt{3}}\right)G + L\sin(\psi)\right],\\
\Delta\sigma_{zz} &= L\frac{v_x\Delta t}{l} - \Delta\gamma\left[\frac{2}{\sqrt{3}}\left(\frac{1}{2} + \frac{\sin(\psi)}{\sqrt{3}}\right)G + L\sin(\psi)\right].
\end{aligned} \tag{2.51}$$

Furthermore, the Kuhn-Tucker conditions imply that the derivative over time of the yield function remains 0 during plastic accumulation, that is, in incremental form:

$$\Delta\mathcal{F} = 0 \Leftrightarrow \frac{-1}{\sqrt{3}}\left(\Delta\sigma_{xx} - \Delta\sigma_{yy}\right) + \frac{\sin(\varphi)}{3}\left(\Delta\sigma_{xx} + 2\Delta\sigma_{yy}\right) = 0. \tag{2.52}$$

By injecting Equation 2.51 into Equation 2.52, one finally obtains the value for the increment of plastic multiplier as:

$$\Delta\gamma = \frac{\frac{2}{\sqrt{3}}G - \sin(\varphi)\left(L + \frac{2}{3}G\right)}{G + \frac{2}{3}(L+G)\sin(\varphi)\sin(\psi)}\frac{|v_x|\Delta t}{l}. \tag{2.53}$$

The solution for plastic strain and stress can therefore be integrated as:

$$\begin{aligned}
\epsilon^{*p}_{xx}(t) &= \frac{\gamma(t)}{\sqrt{3}}\left(-1 + \frac{\sin(\psi)}{\sqrt{3}}\right),\\
\epsilon^{*p}_{yy}(t) &= \frac{\gamma(t)}{\sqrt{3}}\left(\frac{1}{2} + \frac{\sin(\psi)}{\sqrt{3}}\right),\\
\epsilon^{*p}_{zz}(t) &= \frac{\gamma(t)}{\sqrt{3}}\left(\frac{1}{2} + \frac{\sin(\psi)}{\sqrt{3}}\right),
\end{aligned} \tag{2.54}$$

$$\begin{aligned}
\sigma_{xx}(t) &= (L+2G)\frac{v_x t}{l} + \gamma(t)\left[\frac{2}{\sqrt{3}}\left(1 - \frac{\sin(\psi)}{\sqrt{3}}\right)G - L\sin(\psi)\right],\\
\sigma_{yy}(t) &= L\frac{v_x t}{l} - \gamma(t)\left[\frac{2}{\sqrt{3}}\left(\frac{1}{2} + \frac{\sin(\psi)}{\sqrt{3}}\right)G + L\sin(\psi)\right],\\
\sigma_{zz}(t) &= L\frac{v_x t}{l} - \gamma(t)\left[\frac{2}{\sqrt{3}}\left(\frac{1}{2} + \frac{\sin(\psi)}{\sqrt{3}}\right)G + L\sin(\psi)\right],
\end{aligned} \tag{2.55}$$

with the plastic multiplier as:

$$\gamma(t) = \frac{\frac{2}{\sqrt{3}}G - \sin(\varphi)\left(L + \frac{2}{3}G\right)}{G + \frac{2}{3}(L+G)\sin(\varphi)\sin(\psi)}\frac{|v_x|t}{l}. \tag{2.56}$$

2.5 Conclusion

In this chapter, I have presented a novel but robust simulator for modelling coupled thermo-hydro-mechanical processes within fractured rocks, with specific focus on reservoir applications. The code, GOLEM, relies on an open-source massive parallel finite-element-based numerical framework (MOOSE) to solve for the coupled problem. It makes use of a fully implicit approach to treat the nonlinear coupling among the different processes and their feedback effects on fluid and rock properties, thus providing higher numerical stability in the context of nonlinear problems. Geological heterogeneities, i.e. discrete fractures and fault zones, are taken into account in the current formulation. The latter are represented as finite element of lower geometrical

dimension, which allows to model focused fluid and heat flows on fractures and faults planes or well paths. The capability and robustness of the simulator has been illustrated by means of benchmark examples covering the different processes in the considered problem formulations.

Chapter 3

Hydro-Mechanical Evolution of Transport Properties in Porous Media: Constraints for Numerical Modelling[1]

3.1 Introduction

Quantifying rates and magnitudes of variations of flow and transport properties of saturated porous materials is of interest for different branches of geo-energy related studies, including geothermal, energy storage, petroleum and gas applications. Indeed, variations in space and time of these properties can strongly affect, if not control reservoir productivity and recovery (Walder and Nur, 1984; Raghavan and Chin, 2004; Blöcher et al., 2010; Cacace et al., 2013). Coupled deformation and thermal processes occurring within a geological reservoir can give rise to alteration of its basic transport properties, that is porosity and permeability. Previous studies have shown that reduction of porosity and permeability is dominated by deformation processes (Zimmerman, 2000). Therefore, understanding the coupling between elastic deformation of the porous material and alteration of its transport properties is of interest for any natural systems study. Correlations between pore pressure changes as those induced by injection or production of fluid and the in-situ stress field within a reservoir play a major role in coupled hydraulic and deformation processes (Terzaghi, 1943; Carrol and Katsube, 1983; Soltanzadeh et al., 2009). Stress-dependent permeability relations have also been developed in experimental reservoir engineering for the past 60 years. However, these phenomena at the field scale are in most cases hard to quantify due to practical limitations of available methods and tools. Therefore, scientists often turn to observations conducted at the laboratory scale where the impacts of the phenomena involved can be measured. Based on such observations, it is then possible to formulate quantitative expressions for these parameters. These theoretical formulations can be integrated into mathematical models, which can be used to analyse their impacts on the reservoir performance (Fatt and Davis, 1952; Bernabe, 1986; Han and Dusseault, 2003).

Numerical simulations provide a powerful tool for analysing hydraulic and mechanical processes for geological systems and predict reservoir productivity. This is specially

[1]This chapter is published in the journal *Transport in Porous Media* (Jacquey et al., 2015b).

the case since progresses in hardware and software technologies for natural systems simulations have been made along the past decade (O'Sullivan et al., 2001; Turner, 2005; Kolditz et al., 2012a,b). Using calibration parameters as defined at the laboratory scale, numerical simulations provide a tool to make quantitative predictions at the field scale. Often, processes like plastic deformation, creep and elastic deformation cannot be separated or distinguished during experiments or analytically. Numerical simulations provide therefore a useful tool to quantify these different processes.

The presence of a stress-sensitive structure such as fault zones can also have significant impacts on the hydraulic and mechanical properties of the hosting rocks. Different domains can be identified within a faulted region such as a low permeable fault core, surrounded by a highly fractured damage zone where permeability significantly increases and poorly fractured or intact rocks situated far away from the fault core (Faulkner et al., 2010). The degree of fracturing, the fractures apertures and their interconnectivity can play a major role in affecting mechanical and transport properties of the porous material and are therefore key interests for any fluid-induced reservoir applications (Cherubini et al., 2013).

Numerical description of the physics involved in the deformation of porous medium and the evolution of its transport properties requires to account for the coupling between the different processes and to integrate relations between different scales. The aim of this study is to deepen the current understanding of fluid-rock interactions as occurring in generic fractured or faulted reservoirs by developing thermal-hydraulic-mechanical (T-H-M) numerical formulations of their behaviour. As the first step, this chapter focuses on implementing H-M numerical formulations capable of describing evolutions of the hydraulic and mechanical properties of intact rocks affected by the in-situ stress and pore pressure changes. Such formulations are integrated in the open-source finite element method based software for thermal-hydraulic-mechanical and chemical coupled processes (T-H-M-C) "OpenGeoSys" which includes a hybrid approach combining discrete fractures and continua models for simulating fluid flow through fractured reservoirs (Kolditz et al., 2012a).

The phenomena involved in these coupled processes are easily observed in the laboratory (David et al., 1994; Ghabezloo et al., 2009b; Blöcher et al., 2014). Simulations of drained hydrostatic compression tests at the laboratory scale are performed to test the validity and performance of different numerical formulations for porosity and drained bulk modulus evolutions. Impacts of these formulations are discussed by analysing the permeability changes induced by porosity decrease using a Kozeny-Carman-like relation. This study provides therefore relevant insights in understanding hydro-mechanical

behaviour of porous materials which are of relevance for any fluid-induced operations on geological systems.

3.2 Approach

Deformation of porous media as formulated in the theory of poroelasticity has been first introduced by Terzaghi (1943) and Biot (1956, 1973). It considers a porous material with a connected network of pores saturated with fluid. A main variable in poroelastic theory is the effective pressure p', which is here defined after Carrol and Katsube (1983) as a function of the confining pressure p_c (positive in compression), the Biot's coefficient α and the pore pressure p_f (positive in compression):

$$p' = p_c - \alpha p_f. \tag{3.1}$$

Poroelastic theory considers different states which correspond to experimental setups: drained, undrained and unjacketed conditions. Under drained conditions, when a deformation of a porous volume occurs, fluid is free to flow in or out of the confining volume. Therefore pore pressure is in thermodynamic equilibrium with the surrounding ($\Delta p_f = 0$). Under unjacketed conditions, external load is equal to pore pressure and effective pressure remains therefore equal to zero ($p' = 0$). Undrained conditions relate an impossibility of the fluid to flow out of the sample and fluid volume is therefore compressed as well.

For a continuous non-porous material, applied stress only induces elastic changes of its volume. The latter can be described by one elastic modulus, the bulk modulus. For a porous material, effective pressure and pore pressure can change, and both can induce changes in pore and bulk volumes. Four different elastic moduli K_d, K_p, K_s and K_ϕ can therefore be defined as (Zimmerman, 1991):

$$\frac{1}{K_d} = \frac{-1}{V_b}\left(\frac{\partial V_b}{\partial p'}\right)_{p_f} \quad , \quad \frac{1}{K_p} = \frac{-1}{V_\phi}\left(\frac{\partial V_\phi}{\partial p'}\right)_{p_f} \tag{3.2}$$

$$\frac{1}{K_s} = \frac{-1}{V_b}\left(\frac{\partial V_b}{\partial p_f}\right)_{p'=0} \quad , \quad \frac{1}{K_\phi} = \frac{-1}{V_\phi}\left(\frac{\partial V_\phi}{\partial p_f}\right)_{p'=0} \tag{3.3}$$

where K_d and K_p are the drained bulk and pore moduli and K_s and K_ϕ are the unjacketed solid and pore moduli. Formulations in Equation 3.2 refer to drained experimental conditions whether formulations in Equation 3.3 to unjacketed experimental conditions. These four elastic moduli are necessary to describe the mechanical behaviour of a porous medium. From the two equations above, it is clear that parameters from both

drained and unjacketed states are needed to define a complete poroelastic formulation. With these moduli, the Biot's coefficient involved in Equation 3.1 can be expressed as:

$$\alpha = 1 - \frac{K_d}{K_s}. \tag{3.4}$$

Because the drained bulk modulus is always higher than the unjacketed solid modulus (Zimmerman, 1991), the Biot's coefficient is always lower than 1.

The two moduli K_d and K_s can be derived from experimental observables (volumetric strain, here negative in compression and confining/effective pressures) under drained and unjacketed conditions respectively as:

$$\frac{1}{K_d} = -\left(\frac{d\epsilon_v}{dp'}\right)_{drained} \quad , \quad \frac{1}{K_s} = -\left(\frac{d\epsilon_v}{dp_c}\right)_{unjacketed}. \tag{3.5}$$

Zimmerman (1991) showed that the drained pore modulus K_p can be expressed in term of an initial porosity ϕ^i (porosity at idle state), drained bulk modulus K_d and unjacketed solid modulus K_s as:

$$\frac{1}{K_p} = \frac{1}{\phi^i}\left(\frac{1}{K_d} - \frac{1}{K_s}\right). \tag{3.6}$$

Unjacketed pore modulus K_ϕ is relatively difficult to measure in the laboratory (Ghabezloo et al., 2009b; Blöcher et al., 2014). However, Ghabezloo et al. (2009b) have shown that for homogeneous and isotropic porous media at the microscopic scale, the unjacketed solid and pore moduli (K_ϕ and K_s) are equal to the bulk modulus of the solid phase K:

$$K_\phi = K_s = K. \tag{3.7}$$

3.2.1 Porosity

Porosity relates to the void space in a porous medium which may contain fluid. With increasing confining stress or pore pressure, pore and bulk volumes changes affect directly the porosity. The Eulerian porosity is defined by Zimmerman (1991) as the ratio of the pore volume to the current bulk volume:

$$\phi = \frac{V_\phi}{V_b} = \frac{V_\phi^i + \Delta V_\phi}{V_b^i + \Delta V_b}. \tag{3.8}$$

Three different models are here presented for calculation of porosity changes during drained hydrostatic compression which can be formulated in terms of deformation variables.

Model 1:
The first model, developed by Zimmerman (1991) relates porosity to Terzaghi effective pressure. Differentiation of the pore and bulk volumes can be expressed in terms of four elastic moduli according to Equations 3.2 and 3.3 as:

$$\frac{dV_b}{V_b} = -\frac{dp'}{K_d} - \frac{dp_f}{K_s} \quad , \quad \frac{dV_\phi}{V_\phi} = -\frac{dp'}{K_p} - \frac{dp_f}{K_\phi}. \tag{3.9}$$

A change in porosity can therefore be expressed by differentiation of Equation 3.8 depending on the four elastic moduli using Equations 3.9:

$$\frac{d\phi}{\phi} = \left(\frac{1}{K_d} - \frac{1}{K_p}\right) dp' - \left(\frac{1}{K_\phi} - \frac{1}{K_s}\right) dp_f. \tag{3.10}$$

If the material is homogeneous and isotropic at the microscopic scale, Equation 3.7 is valid. Replacing Equation 3.6 and Equation 3.7 in Equation 3.10, changes in porosity can be therefore expressed as a function of Terzaghi effective pressure as:

$$d\phi = -\left[\frac{(1-\phi^i)}{K_d} - \frac{1}{K}\right] dp'. \tag{3.11}$$

In the case of an anisotropic and heterogeneous porous medium at the microscopic scale, Equation 3.11 need to be extended to account for the full dependence of porosity on the pore and solid moduli:

$$d\phi = -\left[\frac{(1-\phi^i)}{K_d} - \frac{1}{K_s}\right] dp' + \phi^i \left(\frac{1}{K_s} - \frac{1}{K_\phi}\right) dp_f. \tag{3.12}$$

Most of rocks are composed of different minerals and are therefore heterogeneous. Therefore it seems that Equation 3.12 should be adopted to reconcile the effective changes in porosity. Unfortunately, as mentioned previously the unjacketed pore modulus K_ϕ cannot be measured directly in laboratory. Therefore, in the present study Equation 3.12 is approximated by Equation 3.11 under the assumption that Equation 3.7 is valid. As seen in Equations 3.11 and 3.12, parameters from both experimental states, drained and unjacketed are needed to calculate porosity changes.

Model 2:
Blöcher et al. (2014) presented another formulation for porosity changes based on

an evaluation of the changes in pore and bulk volumes. A change in pore volume is therefore assumed to be linked to changes in bulk volume and solid volume as:

$$\Delta V_\phi = \Delta V_b - \Delta V_s = \epsilon_v V_b^i - \epsilon_v^u \left(V_b^i - V_\phi^i\right) \tag{3.13}$$

where ϵ_v and ϵ_v^u refer to the volumetric strain under drained and unjacketed conditions respectively (both counted negatively for a reduction of volume). Substituting Equation 3.13 for Equation 3.8 gives:

$$\phi = \frac{V_\phi^i + \epsilon_v V_b^i - \epsilon_v^u \left(V_b^i - V_\phi^i\right)}{V_b^i + \epsilon_v V_b^i}. \tag{3.14}$$

Here, it is also worth noticing that both experimental setups under drained and unjacketed conditions are necessary to compute the porosity as dictated by Equation 3.14.

Model 3:
Chin et al. (2000) developed a model for porosity changes which depends only on the volumetric strain. This model has been applied initially to petroleum reservoirs applications and after has been extended for CO_2 storage problems by Cappa and Rutqvist (2011). The basic relationship between porosity and volumetric strain reads as:

$$\phi = 1 - \left(1 - \phi^i\right) e^{\epsilon_v}. \tag{3.15}$$

Here again, volumetric strain is counted negatively for a reduction of volume.

3.2.2 Drained bulk modulus evolution

As seen in Section 3.1, the drained bulk modulus is a key parameter for understanding and quantifying poroelastic behaviour of porous media. Zimmerman (1991) gives bounds for this elastic modulus:

$$K_f \leq K_d \leq K(1 - \phi) \tag{3.16}$$

where K is the bulk modulus of the solid phase and K_f of the fluid phase. Zimmerman (1991) and Hassanzadegan and Zimmermann (2013) have expressed the drained bulk modulus for fractured porous media as an exponential function depending on the Terzaghi effective pressure as:

$$\frac{1}{K_d} = \frac{1}{K_d^{\infty}} + \left(\frac{1}{K_d^{i}} - \frac{1}{K_d^{\infty}}\right) e^{-p'/\hat{p}} \tag{3.17}$$

where K_d^i and K_d^{∞} are calculated by numerical derivation of the stress-strain experimental curve and where the characteristic crack closure pressure ($\hat{p}$) is determined by crack spectrum analysis. Morlier (1971) defined the closure pressure p^* as a function of the crack aspect ratio (a) which corresponds to the pressure needed to close a crack of a given aspect ratio a as:

$$p^*(a) = \frac{3\pi K(1-2\nu)}{4(1-\nu)^2} a. \tag{3.18}$$

The characteristic closure pressure $\hat{p}$ in Equation 3.17 corresponds to the closure pressure of cracks having the more distributed aspect ratio ($p^*(\hat{a})$). The aspect ratio distribution function $h(a)$ (Morlier, 1971) which gives the distribution of the cracks depending on their aspect ratio can then be adapted to determine the characteristic aspect ratio ($\hat{a}$). This parameter corresponds to a maximum of the aspect ratio distribution function $h(a)$, given by:

$$h(a) = \left[\frac{3\pi K\,(1-2\nu)}{4\,(1-\nu^2)}\right]^2 a \left(-\frac{d^2\epsilon_v^d}{dp'^2}\right)_{p^*}. \tag{3.19}$$

The characteristic closure pressure $\hat{p}$ depends therefore on the solid and bulk properties (K and ν) and is determined by derivation of an experimental stress-strain curve, see Figure 3.3. The method presented here to model the mechanical behaviour of a porous medium during drained hydrostatic compression requires therefore one laboratory experiment to calculate the drained bulk modulus.

3.2.3 Numerical implementation

Simulations of poroelastic behaviour of porous media are conducted using the open-source finite element method-based simulator "OpenGeoSys" (Kolditz et al., 2012a). Equations 3.11, 3.14 and 3.15 have been implemented in "OpenGeoSys" to simulate porosity changes. As seen in Subsection 3.2.1, Equations 3.11 and 3.14 require variables from both drained and unjacketed conditions. These equations relates the poroelastic evolution of the hydraulic properties. In order to reproduce a complete poroelastic behaviour of porous media, characteristic mechanical behaviour needs to be implemented too.

The simulator "OpenGeoSys" does not initially handle a throughout poroelastic evolution of the bulk modulus. Therefore the computed stress-strain curve is linear. In this numerical approach, an analytical solution of the drained bulk modulus based on Equations 3.17 - 3.19 has been additionally implemented. Given that the input elastic modulus in the mechanical solver is the Young's modulus, an expression of the drained Young's modulus is therefore used. This was done by expressing the Young's modulus (referred hereafter as drained Young's modulus E_d) as a function of the drained bulk modulus as:

$$E_d = 3(1 - 2\nu)K_d \tag{3.20}$$

where K_d is calculated using Equation 3.17. The range of evolution of the Poisson's ratio is relatively narrow, it is therefore assumed that the bulk Poisson's ratio ν remains constant and that evolution of the drained Young's modulus is dominated by the drained bulk modulus changes. According to Equation 3.20, the Young's modulus is supposed to be isotropic but not necessarily homogeneous (because of its dependency on the Terzaghi effective pressure). This parameter is used to reproduce the non-linearity in the stress-strain relation. With this implementation of the mechanical behaviour, volumetric strain under drained conditions and drained bulk modulus can be directly calculated. This numerical approach takes therefore into account evolutions of hydraulic (porosity and permeability) and mechanical (drained bulk modulus) properties and describes a complete poroelastic behaviour of a porous medium.

3.2.4 Rock samples and setup for simulations

The approach presented before has been tested on two kinds of sandstones for which triaxial experimental data during drained and unjacketed hydrostatic compression in laboratory are available (Blöcher et al., 2014). The two studied sandstones are Flechtinger sandstone, a Lower Permian (Rotliegend) sedimentary rock from an outcrop near Flechtingen, Germany (Milsch et al., 2008) and Bentheim sandstone, a Lower Cretaceous sedimentary rock from an outcrop near Bentheim, Germany (Dautriat et al., 2009). Unlike the Bentheim sandstone which is very homogeneous (95 % quartz, 3 % kaolinite and 2 % orthoclase), Flechtinger sandstone is composed of quartz (55 −65 %), rock fragments of volcanic origin (20 −25 %) and feldspar (15 −20 %). Hassanzadegan et al. (2012) has estimated experimentally the Poisson's ratio for the Flechtinger sandstone as 0.31 and Dautriat et al. (2009) for the Bentheim sandstone as 0.20 · Initial porosity, permeability and mechanical constant properties for the two sandstones are

presented in Table 3.1. More information about the experimental methods and material can be found in Blöcher et al. (2014).

Rock samples used for the experimental tests are cylindrical with a diameter of 5 cm and a length of 10 cm. Simulations have been conducted on two different systems which gave similar results: on a 3-dimensional mesh representing the entire rock sample with 12 580 quadratic tetrahedral elements and on a 3-dimensional mesh simplified using the cylindrical symmetry of the sample with 4277 quadratic tetrahedral elements. Since the same results have been obtained, the system simplified by cylindrical symmetry has been adopted. This simplified mesh is obtained from the cylindrical mesh by symmetry along the horizontal plane $z = 0$ first which gives a cylinder with length $L = 5\,\text{cm}$. Then by revolution symmetry around the vertical axis z, the elementary volume illustrated on Figure 3.1 and defined by an elementary rotation angle $d\theta$ is approximated as a cuboid of size (l,d,L) where $L = 5\,\text{cm}$, $l = 2.5\,\text{cm}$ and $d \ll l$ (here $d = 1\,\text{mm}$). Drained hydrostatic compressions are simulated by increasing confining pressures up to 70 MPa with a rate of $6.0\,\text{MPa} \cdot \text{min}^{-1}$. Pore pressure is constant and equals to atmospheric pressure to represent drained conditions. Mechanical boundary conditions are illustrated on Figure 3.2.

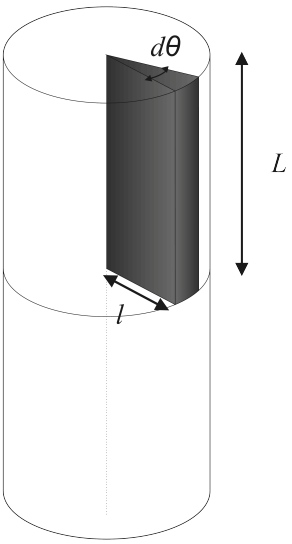

Fig. 3.1 Elementary volume obtained with revolution symmetry with vertical axis. This volume is approximated as a cuboid of size (l,d,L) to simplify the geometry of the system.

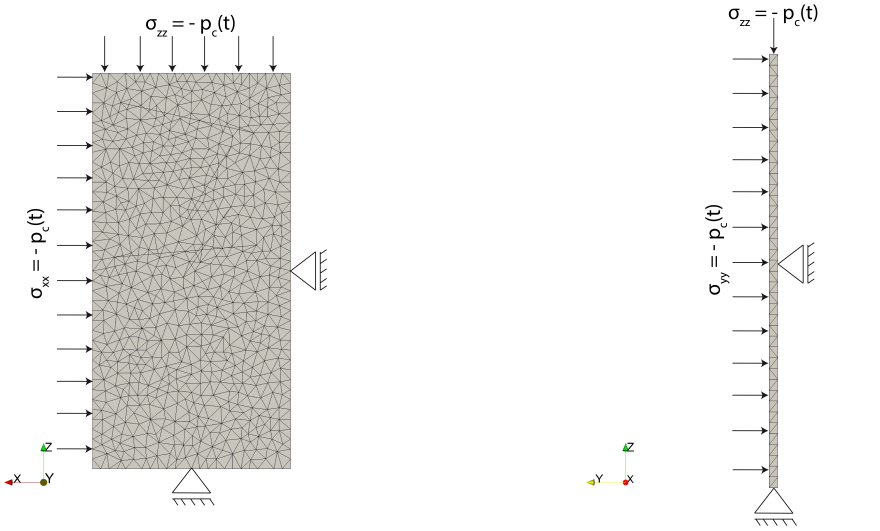

(a) (b)

Fig. 3.2 Stresses and no displacement boundary conditions used to simulate drained hydrostatic compression with "OpenGeoSys". Confining pressure function $p_c(t)$ is linear from 0 to 70 MPa with a rate of 6.0 MPa $\cdot$ min^{-1}. Minus sign is used to satisfy stresses convention used in "OpenGeoSys".

Table 3.1 Properties of the sandstones (Blöcher et al., 2014)

Sandstone	Porosity ϕ^i [-]	Permeability k^i [mD]	Poisson's ratio ν [-]	Solid bulk modulus K [MPa]
Flechtinger	$0,125$	$0.3 - 1.5$	$0,31$	41500
Bentheim	$0,236$	870	$0,20$	27000

Figure 3.3 shows the aspect ratio distribution functions for the two sandstones (see Equation 3.19). They have been obtained by numerical derivations of the stress-strain experimental curve and are used to determine the characteristic closure pressure $\hat{p}$ corresponding to the maximum of the aspect ratio distribution function $h(a)$. Based on this parameter it is then possible to use Equation 3.17 to calculate the analytical formulation of the drained bulk modulus.

Figure 3.4 shows typical evolution trend of the drained bulk modulus from experimental results. The drained bulk modulus increases strongly with low effective pressure and is almost constant for high effective pressure due to its upper bound (see Equation 3.16).

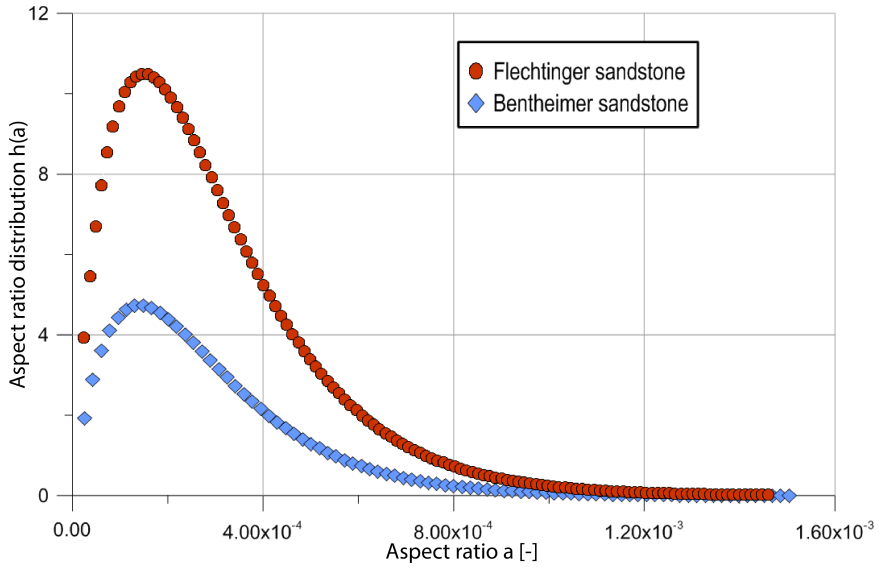

Fig. 3.3 Aspect ratio distribution functions for the Flechtinger sandstone in red and for the Bentheim sandstone in blue. The aspect ratio which corresponds to the maximum of the function $h(a)$ is linked to the characteristic closure pressure $\hat{p}$

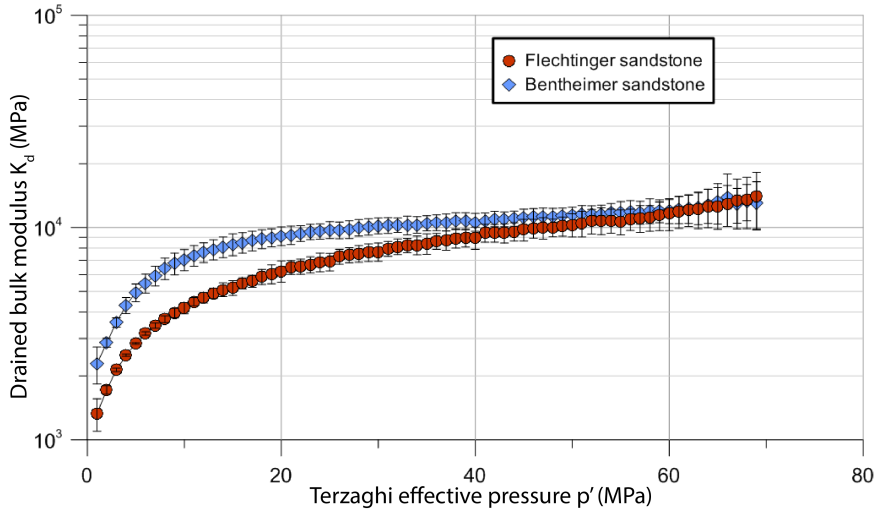

Fig. 3.4 Drained bulk modulus of Flechtinger and Bentheim sandstones. Experimental data are from Blöcher et al. (2014). In red is presented the evolution of the drained bulk modulus of the Flechtinger sandstone and in blue of the Bentheim sandstone

3.3 Results

One simulation with the setup presented in Subsection 3.2.3 for each porosity model has been conducted. The simulator solves coupled hydraulic and mechanical processes iteratively for 70 time steps of 10 s each to obtain the given rate of $6.0\,\mathrm{MPa} \cdot \mathrm{min}^{-1}$.

Initial conditions are defined as the equilibrium of confining pressure and pore pressure ($p_f = 1 \times 10^5$ Pa, atmospheric conditions). This section presents the results of these simulations conducted with "OpenGeoSys" for the mechanical behaviour and for porosity changes during drained hydrostatic compression tests of the two kinds of sandstones.

3.3.1 Poroelastic behaviour

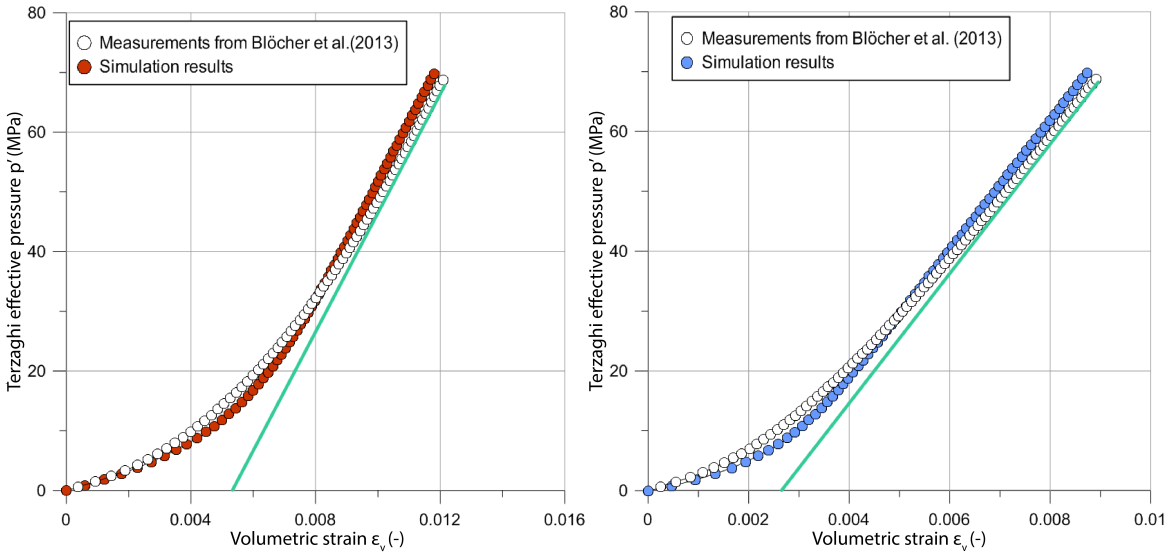

(a) Flechtinger sandstone.

(b) Bentheimer sandstone.

Fig. 3.5 Stress-strain curves for the two sandstone. In white are the experimental data from Blöcher et al. (2014) and in red/blue the simulations results obtained with "OpenGeoSys" after implementation of the evolution of the drained bulk modulus. The green lines illustrate the linear behaviour of the stress-strain curve at high effective pressure (tangent lines).

On Figures 3.5a and 3.5b are shown the stress-strain curves obtained by simulating drained hydrostatic compression of the Flechtinger and Bentheim sandstones and integrating the characteristic non-linearity of the poroelastic behaviour. Volumetric strain evolves non-linearly for low effective pressure and above 40 MPa, a classic linear stress-strain relations is noticeable. The presence of a non-linear domain at low effective pressure is a result of different phenomena: progressive closure of cracks in the porous rock, compaction of the porous space and stiffening of the rock by Hertzian contacts between solid grains (Morlier, 1971). Following this observation, it is then possible to parametrise an effective crack porosity which characterises the non-linearity of the poroelastic behaviour of a porous medium in terms of the difference of the volumetric strain (the latter given by the tangent line on Figure 3.5) and the measured value.

This crack porosity reaches its maximum at idle state and decreases with increasing effective pressure till it becomes null at 40 MPa.

As illustrated on Figure 3.5, the crack porosity, characterising non-linear poroelastic mechanical behaviour is non-negligible and can be reproduced with "OpenGeoSys" using Equation 3.17. For the Flechtinger sandstone, an error of 3.73 % is calculated for the simulated stress-strain curve compared to the experimental data and an error of 4.04 % for the Bentheim sandstone. Considering these errors, the poroelastic mechanical behaviour implemented in "OpenGeoSys" shows satisfying accuracy when compared to the experimental data. Small remaining errors derive from the determination of the characteristic closure pressure $\hat{p}$ using numerical derivation (see Subsection 3.2.2). Despite this, it can be concluded that the approach introduced allows to reproduce in simulations a key characteristic of the mechanical behaviour of the theory of poroelasticity which is expressed by the crack porosity.

3.3.2 Porosity change

As seen in Section 3.2, porosity decreases with increasing effective pressure. The three models presented previously have been tested with "OpenGeoSys" coupled with the mechanical evolution. Change in drained bulk modulus is essential since all three models depend directly (see Equation 3.11) or indirectly (volumetric strain for Equations 3.14 and 3.15) on this parameter.

Figure 3.6 shows simulations results conducted with "OpenGeoSys" and experimental measurements. The porosity evolutions of the two sandstones show similar trends when affected by hydrostatic compression. Two different domains can be identified. For low effective pressure, porosity decreases non-linearly (under 20 MPa for Flechtinger sandstone and 10 MPa for Bentheim sandstone). Within this non-linear domain, porosity is decreased by 5.4 % for the Flechtinger sandstone and by 1.4 % for the Bentheim sandstone. Above this effective pressure, porosity decreases linearly. During this linear decrease, porosity decreases slowly (2.7 % decrease between 20 and 70 MPa for the Flechtinger sandstone and 1 % decrease between 10 and 70 MPa for the Bentheim sandstone). In total, for an effective pressure of 70 MPa, a 8.1 % decrease of porosity has been observed for the Flechtinger sandstone and of 2.4 % for the Bentheim sandstone compared to idle state. These results show that porosity decreases are dominated by non-linear phenomena at low effective pressure. These phenomena, also responsible for the non-linear stress-strain curve show that compression of the porous medium is dominated by compression of pores, closure of cracks and stiffening of the rock by Hertzian contacts between the grains.

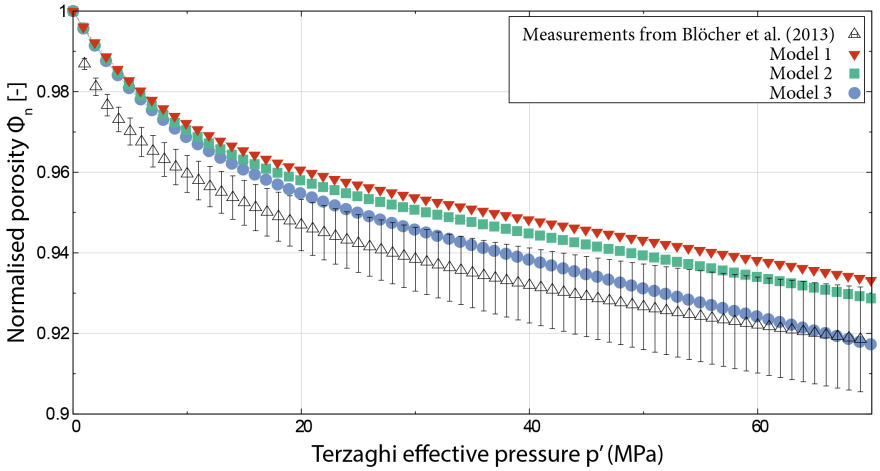

(a) Flechtinger sandstone.

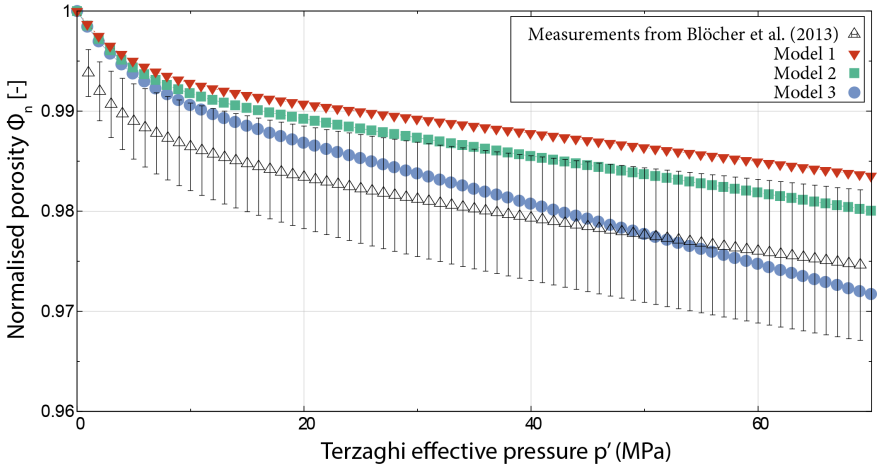

(b) Bentheimer sandstone.

Fig. 3.6 Porosity evolutions of the two sandstones considering all three models presented in Section 3.2. Simulation results are compared to laboratory measurements presented in white with error bars.

All three models can reproduce the non-linear decrease of porosity for low effective pressure and the linear one for higher effective pressure. However, the porosity calculated by Model 3 shows a more significant decrease than the experimental porosity in the linear domain of high effective pressure. Models 1 and 2 show similar and satisfying linear decreases for porosity at high effective pressure but porosity predicted by these two models tends to overestimate the porosity measured in laboratory. Blöcher et al. (2014) reported that the systematic error behaviour of models 1 and 2 appears under low effective pressure, between 0 and 15 MPa.

Table 3.2 Error on the calculated porosity for the three models compared to the direct measurements

Sandstone	Model 1	Model 2	Model 3
Flechtinger	1.58 %	1.15 %	0.60 %
Bentheim	0.81 %	0.54 %	0.24 %

Table 3.2 shows the accuracy of each model on porosity for the two considered sandstones. Errors have been calculated as the normalised sum of the absolute differences with the direct measurements.

3.4 Discussions

We have outlined an approach to quantitatively investigate the poroelastic response of porous rocks to varying stress boundary conditions, by means of a description of porosity evolution as a function of effective pressure changes. Integration of this functional behaviour in the open source software "OpenGeoSys" enabled to test the reliability of our porosity description via hydro-mechanical coupled numerical simulations. Triaxial laboratory experiments under drained hydrostatic loading performed on two different kinds of sandstones have been used to validate the numerical results. A good agreement has been found between model outcomes and observations. First, performance of the three porosity models are discussed. In the following, the obtained results are used to inspire a discussion on their implications for field scale geothermal applications and to outline future work perspectives.

3.4.1 Performance of the porosity variations models

In Section 3.3, it has been noticed that a non-linear and a linear domain can be observed for the porosity variations depending on the range of effective pressure imposed. The linear domain is similar to a non-porous material for which the compression of the solid phase is dominant and the drained bulk modulus is constant. Results of porosity changes for the two sandstones show that the Flechtinger sandstone is more sensitive to change in the effective pressure than the Bentheim sandstone. Within the linear domain, this difference can be explained by the difference in solid bulk moduli for the two sandstones (see Table 3.1) since in this range of effective pressure the deformation of the porous medium is dominated by the deformation of the solid grains. Composition of sandstones, density of micro-cracks or shape of pores can influence the impact at low effective pressure on the porosity and are therefore hard to characterise and constrain.

In the range of low effective pressure (under 20 MPa), the difference between simulation and experimental results increases and at higher effective pressure, this difference remains constant and shows a systematic error behaviour, which has been also reported in the direct measurements. This is due to some limitations in the precision of the extensometers used for such experimental tests which are influenced by the deformation of the jacket around the sample. Therefore the experimental values of volumetric strain are slightly overestimated even when a procedure to correct this phenomenon has been applied (Blöcher et al., 2014). This phenomenon, reported as jacket effect influences the experimental values and is the origin of this discrepancy observed on Figure 3.6.

The uncertainty at low effective pressure can be visualised on Figure 3.4 on the first data point for drained bulk modulus with a very long error bar compared to the next measured values (20 % error for the first data point against less than 5 % for the other data points under 20 MPa of effective pressure). In this range of effective pressure, Blöcher et al. (2014) also measured values of the Biot's coefficient higher than 1 which has no physical meaning and testifies that the measurement tools and procedure used induce significant error on the drained bulk modulus and therefore on the computed porosity. In general, Model 2 do a better job in fitting the data than Model 1. A possible explanation to this behaviour can be related to the assumptions made in deriving the latter formulation. Indeed, to derive the mathematical formulation of Model 1 described in Section 3.2, we have assumed homogeneous conditions of the rock sample at the microscopic scale. This hypothesis was used to simplify Equation 3.12 to Equation 3.11. This approach avoids to consider a formulation for the unjacketed pore compressibility, the latter being a parameter which cannot be measured and is therefore hard to constrain. However as discussed previously, the two sandstones are not completely homogeneous. Bentheim sandstone is composed of 95 % of quartz but Flechtinger sandstone of only 65 % quartz and is therefore significantly heterogeneous. This assumption, used to simplify the calculation of porosity change can induce some error, specially for the Flechtinger sandstone since its validity is questionable. This approximation of Model 1 could be one reason why it is less accurate than Model 2. The error induced by a non-linear decrease at low effective pressure can also be a result from this approximation and the term $\left(\frac{1}{K_s} - \frac{1}{K_\phi}\right)$ in Equation 3.12 can therefore be non-negligible for this range of effective pressure.

3.4.2 Porosity-permeability relation and its implications for geothermal reservoir studies

The performance of a reservoir, whether for geothermal, energy storage or enhanced oil recovery applications, is usually parametrised in terms of the permeability of the reservoir rocks as main property controlling the transport of fluid and energy. Its value depends on different characteristics of the rock comprising the geometry of its pores, their density and degree of interconnectivity (Bear, 1988). By making some assumptions on the effective geometry of the pores, it is possible to derive a relationship between porosity and permeability of a specific rock. In its more generic form, this poro-perm relationship takes the form of the Kozeny-Carman equation (Carman, 1956), which can be written as following:

$$k = \frac{c\phi^3}{\tau^2 S^2} \tag{3.21}$$

where c is a geometric factor, τ the tortuosity and S the specific surface area defined as the ratio of the wetted area to the bulk volume. Worth noticing is that Equation 3.21 is derived under the assumption of steady laminar flow through capillary tubes (Hagen-Poiseuille problem). The specific surface area is the most relevant parameter of this porosity-permeability relation. It structurally depends on the exact shapes of the pores, and it is therefore hard to calculate for porous rocks given their rather complex pore and grain geometries. When the hydraulic-radius approximation is used, it is possible to obtain a quantitative poro-perm relationship (Sisavath et al., 2000). For the particular case of packed bed of spheres with the assumption that all the pores are connected ($\tau = 1$), such relation allows to express the specific surface area parameter as ((Hassanzadegan and Zimmermann, 2013) and Appendix A.1):

$$S = \frac{3\,(1-\phi)}{r_s} \tag{3.22}$$

Where r_s is the radius of the spherical grains. By substituting Equation 3.22 in Equation 3.21, permeability can be expressed as:

$$k = A\frac{\phi^3}{(1-\phi)^2} \tag{3.23}$$

Where the coefficient A includes the geometric factor c and the grain radius r_s as: $A = c\frac{r_s^2}{9}$. For the purpose of the present description, the coefficient A is assumed to stay constant and is therefore calculated based on an initial permeability k^i and initial porosity ϕ^i: $A = \frac{k^i\left(1-\phi^i\right)^2}{\left(\phi^i\right)^3}$.

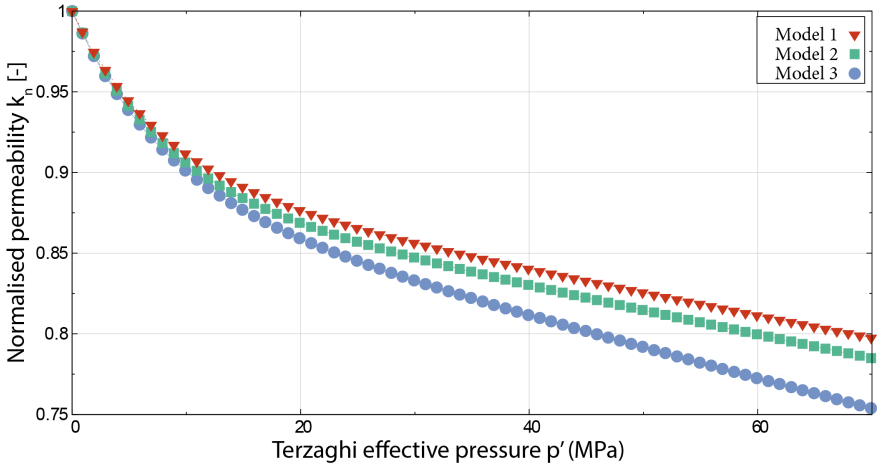

(a) Flechtinger sandstone.

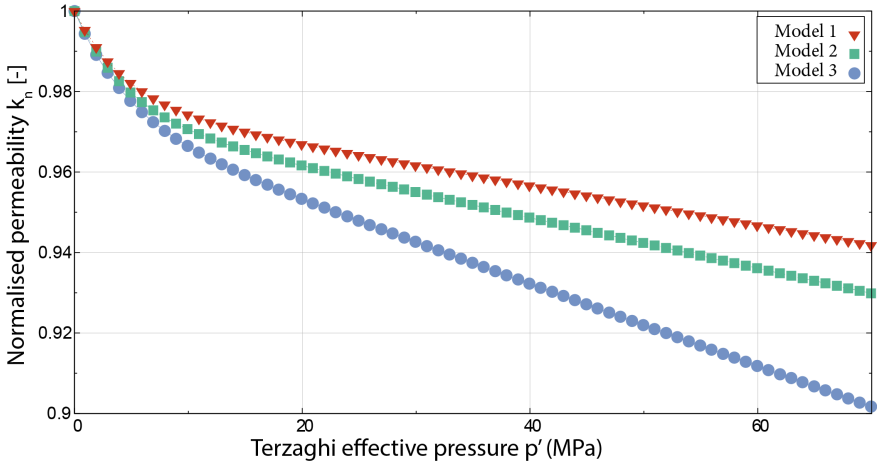

(b) Bentheimer sandstone.

Fig. 3.7 Permeability evolutions of the two sandstones considering all three models for porosity changes.

Figure 3.7 shows evolution of permeability of the Flechtinger sandstone (3.7a) and of the Bentheim sandstone (3.7b) considering the three different porosity models previously discussed. Not surprisingly, given the poro-perm relation adopted, permeability decreases when increasing effective pressure. Indeed, a drop between 20 and 25 % for permeability is observed at 70 MPa effective pressure for the Flechtinger sandstone and a drop between 6 and 10 % for the Bentheim sandstone. In the porosity-permeability relationship introduced, permeability is assumed to depend only on porosity of the sample. Changes of the shape of pores and evolution of their interconnectivity have been neglected. Further investigation on the dependencies of permeability would require information about pore deformation and pore connections during hydrostatic compres-

sion in parallel with laboratory experiments to constrain parameters of a complete permeability description (evolution of the parameter noted A in Equation 3.23).

In the present work the stress dependency of both porosity ϕ and permeability k has been constrained based on laboratory measurements thus reflecting simplified conditions than those observed in real case settings. One major simplification stems from considering hydrostatic stress conditions, which does not effectively represent reservoir working conditions. Generalisation of the mathematical formulation presented here to generic poly-axial effective stress distribution is subject of ongoing research.

3.4.3 Relevance of other processes: plasticity, thermal stresses and fractures

The present study deals exclusively with hydraulic and mechanical poroelastic coupling under isothermal conditions. However, triaxial experiments performed on sandstone samples at different temperatures have reported the occurrence of some inelastic deformation components (i.e. creeping mechanisms) which resulted in irreversible variations observed for the drained bulk modulus and the aspect ratio distribution function (Hassanzadegan and Zimmermann, 2013). This phenomenon, close to a hysteresis effect has been found to exert a direct impact on porosity changes and thus on permeability changes. Even though plastic deformation was not the focus of this study, it is experimentally hard to avoid when high effective pressure are reached. Indeed, both Figure 3.6a and Figure 3.6b illustrate a slight non-linearity between 60 and 70 MPa (Flechtinger) and between 50 and 70 MPa (Bentheim) in the porosity stress curve. It is believed that these non linear behaviour might be structurally related to the yield strength of the two rock samples, indicating either weakening by fracture nucleation or hardening due to processes occurring at the grain boundaries resulting in irreversible deformation. Opening or closure of fractures are dominant for porosity and permeability evolutions compared to deformation of the matrix system. Furthermore, dynamic processes can occur in fractured systems such as fractures propagation or nucleation which demand new mathematical formulation for plastic deformation to quantify these effects. Concerning the drained bulk modulus, its evolution can also be significantly altered by presence of fractures and deformation of fractured rocks can therefore be strongly different as the poroelastic formulation presented here. This chapter has settled the base for poroelastic numerical simulations of intact porous rocks. In the next steps, the study of damaged rocks will be performed in parallel with laboratory experiments with different fracture densities to extend the formalism to fractured rocks.

3.5 Conclusion

Poroelastic variations of porosity and drained bulk modulus for coupled hydraulic and mechanical processes have been integrated in the open-source simulator "OpenGeoSys". These formulations derived from the theories of poroelasticity and crack closure are based on characteristics of a porous medium such as the aspect ratio distribution function or the shape of pores. Evolutions of porosity and drained bulk modulus for drained hydrostatic compression at the laboratory scale are taken into account. The simulated porosity and drained bulk modulus values have shown really satisfying results in comparison to direct laboratory measurements. It has been noticed that one model for porosity changes (Model 2) has a better precision and a suitable trend. On the other hand, evolution of the drained bulk modulus allows to reproduce the non-linearity in the stress-strain curve which is a characteristic of the mechanical behaviour of porous materials. Both porosity and drained bulk modulus changes are linked and are part of the poroelastic description of porous media. These formulations have been tested on two kinds of sandstone based on laboratory observations.

The following results were obtained by simulating drained hydrostatic compressions:

- Non-linearity of the stress-strain curve has been reproduced for the two considered sandstones. For the Flechtinger sandstone, an error of 3.73 % is measured compared to the direct measurements and of 4.04 % for the Bentheim sandstone. This was possible by considering evolution of the drained bulk modulus depending on the applied effective pressure.

- Reduction of porosity: a 8.1 % decrease of porosity for the Flechtinger sandstone and a 1.4 % decrease for the Bentheim sandstone have been simulated. These results have been obtained with an error of 1.15 % and 0.54 % respectively compared to direct measurements.

- Additionally, it has been demonstrated that the modelled porosity decrease induces a reduction of the rock permeability. By means of an appropriate Kozeny-Carman relation, a reduction between 20 % and 25 % for the Flechtinger sandstone permeability has been obtained and between 6 % and 10 % for the Bentheim sandstone.

This chapter provides therefore interesting insights on the coupling between hydraulic and mechanical processes for porous media and especially on its impacts on the rock transport properties. Constraints of the parameters involved in this coupling

between different processes allow to deepen possibilities and precision of reservoir simulations for geo-energy related applications.

Chapter 4

Thermo-poroelastic numerical modelling for enhanced geothermal system performance: case study of the Groß Schönebeck reservoir[1]

4.1 Introduction

Understanding processes controlling transport properties of saturated porous media is of interest for geothermal power production, energy storage or hydrocarbon exploration. Spatial and temporal variations of porosity and permeability can indeed control reservoir productivity and recovery (Walder and Nur, 1984; Raghavan and Chin, 2004; Blöcher et al., 2010; Cacace et al., 2013). Changes of pore pressure, temperature and stress distributions during injection or production of fluid can give rise to porosity and permeability alterations which can be effectively described based on the theories of poroelasticity and thermoelasticity (Fatt and Davis, 1952; Bernabe, 1986; Han and Dusseault, 2003). Correlations between pore pressure and temperature changes as those induced by injection of cold fluid and the in-situ stress field within a reservoir impose strong and non-linear couplings between Thermo-Hydro-Mechanical physical processes (Terzaghi, 1943; Carrol and Katsube, 1983; Soltanzadeh et al., 2009). Quantification of these phenomena at the reservoir scale is difficult due to technical limitations of available methods and tools. Therefore, a common approach in the field of geomechanics is to conduct experiments in laboratory under simple and controlled reference conditions to observe and quantify the phenomena of interest. Based on these results, it is then possible to calibrate and implement these information into mathematical formulations to conduct numerical simulations at the reservoir scale.

In a previous study (Jacquey et al., 2015b), a detailed description of porosity evolution due to hydro-mechanical coupling has been introduced. The theory is based on a strong theoretical background for poroelasticity (Biot, 1956; Biot and Willis, 1957; Zimmerman, 1991). In this contribution, we describe an approach for coupled thermo-hydro-mechanical (THM) processes modelling. The mathematical formulations have been integrated in the open-source finite-element method-based software "OpenGeoSys" (Kolditz et al., 2012a) following theory of coupled thermo-poroelasticity (Zimmerman,

[1]This chapter is published in the journal *Tectonophysics* (Jacquey et al., 2016).

2000; McTigue, 1986; Ghabezloo et al., 2008; Ghabezloo and Sulem, 2009). To validate the numerical implementation, in a first stage, the distribution of porosity around an injection well with simple geometry is analysed and described. This serves as an introductory stage to the non-linear processes which are subsequently analysed by means of a real case application for the geothermal research doublet of Groß Schönebeck (40 km north of Berlin, Germany).

This research platform, which has been the subject of several studies for the past 13 years (Huenges and Hurter, 2002; Holl et al., 2005; Legarth et al., 2005; Reinicke et al., 2005; Moeck et al., 2009b; Milsch et al., 2009; Zimmermann et al., 2009, 2010) provides a rich geological dataset to analyse the impacts of transport properties evolution models at the reservoir scale. The presence of stress-sensitive structures such as natural faults and induced fractures gives furthermore new insights on characterising fluid flow and mechanical behaviour in such a geological setting.

4.2 Numerical approach

4.2.1 Balance equations

Modelling coupled THM processes requires solving the governing equations for fluid-flow, heat transport and deformation of the porous medium. These governing equations are derived from balance equations for mass, energy and momentum. In this section the governing equations for THM modelling are presented as they are implemented in the software "OpenGeoSys" (Kolditz et al., 2012a).

From the conservation of mass, flow in a porous medium is described by Equation 2.22 (here simplified by neglecting thermal pressurisation and inelastic deformation):

$$\frac{1}{M_b}\frac{\partial p_f}{\partial t} + \nabla \cdot \boldsymbol{q}_D = Q_f$$

where M_b is the Biot modulus (reciprocal of the specific storage), p_f the pore pressure, $\boldsymbol{q}_D$ the specific discharge and Q_f a source/sink term. The specific discharge $\boldsymbol{q}_D$ can be expressed from the conservation of momentum following Equation 2.3 (Darcy's law).

The equation governing heat transport is derived from heat balance under thermal equilibrium conditions between solid and fluid phase. Diffusive as well as advective heat transport processes are considered in saturated porous media following Equation 2.25.

Deformation of a fully saturated porous medium is described by the momentum balance equation which can be written in terms of effective stress following Equation 2.10.

Here, the effective stress tensor is defined after Carrol and Katsube (1983) as:

$$\boldsymbol{\sigma}' = \boldsymbol{\sigma} + \alpha p_f \mathbb{1}. \tag{4.1}$$

Equation 4.1 is an extension of Equation 3.1 in 3D with $p' = -\frac{\boldsymbol{\sigma}'_{kk}}{3}$. The terms in Equation 4.1 illustrate how deformation is coupled with the fluid flow. The primary variable solved for deformation of the porous medium is the displacement vector $\boldsymbol{u}$ which can be linked to the effective stress tensor $\boldsymbol{\sigma}'$ via the constitutive law for stress-strain behaviour following Equation 2.12.

In this work, only isotropic elastic deformation is considered, though non isothermal. Therefore, linear elasticity can be fully described via the generalized Hooke's law:

$$\mathbb{C}_{ijkl} = L\delta_{ij}\delta_{kl} + 2G\left(\delta_{ik}\delta_{jl} + \delta_{il}\delta_{jk}\right) \tag{4.2}$$

where δ is the Kronecker delta and L and G the first and second (shear) Lamé moduli respectively.

Fluid flow is therefore coupled with heat transport and deformation through dependent transport properties (porosity and permeability) and the dependent fluid properties (density and dynamic viscosity). In the next sections, the model for the modified Hooke's law used for mechanical behaviour of porous medium as well as models for evolution of transport properties (porosity and permeability) are presented.

4.2.2 Mechanical behaviour of porous media

The typical response of porous materials shows a non-linear stress-strain behaviour at low effective pressure (below 30 MPa) (Biot, 1973; Zimmerman, 1991; Blöcher et al., 2014). Therefore, Hooke's law (which follows a linear stress-strain relations) cannot be applied under these conditions. In this section, a model for stress-dependent material matrix is presented to reproduce numerically the typical non-linear stress-strain relation of porous media by making use of concepts derived from poroelasticity (Terzaghi, 1943; Biot, 1956, 1973) and crack closure theory (Morlier, 1971).

For a continuous non-porous material, applied stress only induces elastic changes of its volume. The latter can be described by one elastic modulus, the bulk modulus. In the context of deformation of a porous medium, effective pressure and pore pressure can change, and both can induce changes in pore and bulk volumes (Zimmerman, 1991). Four isothermal elastic moduli can therefore be defined corresponding to different experimental conditions (see Equations 3.2 and 3.3)

With these moduli, the Biot's coefficient involved in Equation 4.1 can be expressed after Carrol and Katsube (1983) (recall of Equation 3.4):

$$\alpha = 1 - \frac{K_d}{K_s}.$$

Since drained experimental conditions better represent in-situ reservoir conditions, isothermal drained bulk modulus is a key parameter to understand the mechanical behaviour of a porous medium (Zimmerman, 1991). In this study, the expression for stress-dependent bulk modulus of porous media based on the crack closure theory (Morlier, 1971) is used. This theory relates non-linearity in the stress-strain relation of low effective pressure to closure of micro-cracks within the porous medium. The stress-dependent isothermal drained bulk modulus is then expressed after Zimmerman (1991); Hassanzadegan and Zimmermann (2013) (recall of Equation 2.17):

$$\frac{1}{K_d} = \frac{1}{K_d^\infty} + \left(\frac{1}{K_d^i} - \frac{1}{K_d^\infty}\right) e^{-p'/\hat{p}}$$

This model has been tested against experimental data for two different sandstones with 4 % relative error on the stress-strain relation (Jacquey et al., 2015b).

4.2.3 Transport properties

As seen in Subsection 4.2.1, coupling between THM processes can be increased by considering stress- or temperature-dependent transport properties such as porosity and permeability. The theory of thermo- and poroelasticity gives some theoretical bases to consider porosity evolution.

Porosity

Variations in the bulk and pore volumes result in porosity changes.

If porosity evolves only due to poroelastic effects, changes in porosity can be expressed by making use of appropriate definitions for the elastic moduli as well as of relations between them (Zimmerman, 1991) (recall of Equation 3.11):

$$d\phi = -\left[\frac{(1-\phi^i)}{K_d} - \frac{1}{K_s}\right] dp'.$$

Considering thermoelastic effects in addition requires to define the volumetric drained and pore thermal expansion coefficients. Those parameters describe changes of bulk and pore volumes due to temperature changes (Ghabezloo et al., 2008):

$$\beta_b = \frac{1}{V_b}\left(\frac{\partial V_b}{\partial T}\right)_{p_f,p'} \quad , \quad \beta_\phi = \frac{1}{V_\phi}\left(\frac{\partial V_\phi}{\partial T}\right)_{p_f,p'}. \tag{4.3}$$

By combining Equation 3.11 with thermoelastic effects using thermal expansion coefficients introduced in Equation 4.3, one arrives at the following constitutive equation for porosity taking both poroelastic and thermoelastic effects into account (Ghabezloo et al., 2008):

$$d\phi = -\left[\frac{(1-\phi^i)}{K_d} - \frac{1}{K_s}\right] dp' - \phi^i \left(\beta_b - \beta_\phi\right) dT. \tag{4.4}$$

In the case of an ideal porous medium, McTigue (1986) and Ghabezloo et al. (2008) reported that $\beta_b = \beta_\phi = \beta_s$, a hypothesis which is not assumed in this study. The relation between the three thermal expansion coefficients (mean algebraic mixing rule) is: $\beta_b = \phi\beta_\phi + (1-\phi)\beta_s$. The drained expansion coefficient β_b can be measured during drained heating test (slope of the volumetric strain - temperature curve). The pore thermal expansion coefficient β_ϕ can also be derived during this experiment by measuring the amount of fluid escaping from the sample.

Equations 3.11 and 4.4 relate therefore the porosity evolution due to poroelastic effects and due to coupled thermo- and poroelastic effects respectively.

Permeability

Permeability is a key transport property characterising reservoir performance whether for geothermal, energy storage or hydrocarbon exploration. Several studies have investigated the evolution of permeability for geological reservoirs (Bernabe, 1986; Doyen, 1988; David et al., 1994; Zhao et al., 2011). Theoretical expressions are often difficult to formulate since permeability depends on different parameters such as void space ratio or evolution of the pores shape during deformation. The challenge in this context is to address a model which is in accordance with experimental data on permeability evolution and which can deal with an anisotropic permeability tensor (often the case for reservoir conditions).

Bai et al. (2002) have adapted an expression of isotropic permeability changes based on Hertz's elastic contact theory (Hertz, 1985) to anisotropic conditions:

$$dk_i = k_i^0 \left[\sum_{j=1, j\neq i}^{3} \left(1 - \frac{1}{2}\left[\frac{9(1-\nu^2)^2}{2}(\pi\Delta\epsilon_j)^2\right]^{\frac{1}{3}}\right)^2 - 1\right] \tag{4.5}$$

where k_i^0 is the permeability along the i^{th} direction at idle state, ν the Poisson's ratio and $\Delta\epsilon_i$ the change of strain along the i^{th} direction. This formulation states that reduction of permeability is explained by the reduction of the flow cross-sectional area ($(\pi\Delta\epsilon_j)^2$).

The approach presented in this section does not describe undrained effects such as mechanical and thermal pressurisation (increase of pore pressure due to stress and temperature changes). Formulations are first applied to a single stimulated injection well model within an uniform and homogeneous reservoir. Based on this geometry, impacts of injection on the porosity and permeability distribution are analysed. In the final application, the presented approach is applied to the Groß Schönebeck geothermal reservoir to analyse the reservoir performance.

4.3 Single injection test case

In this section, a single injection well within an uniform and homogeneous reservoir with a hydraulically induced fracture is considered. This simple geometry allows to describe and analyse the impacts of transport properties evolution models on the thermo-hydro-mechanical processes modelling. The injection depth and physical properties of the reservoir are considered as representative for those encountered within the target sandstone formation in the Groß Schönebeck geothermal reservoir (see Section 4.4). Injection temperature is 70 °C and a reservoir temperature of 145 °C is applied initially.

The model is 1 km large in horizontal directions and 500 m in the vertical direction with an injection point in its centre. The hydraulically induced fracture is 100 m high and large and orthogonal to the x-horizontal direction. Isotropic stress conditions are considered in this test case ($\sigma_{xx} = \sigma_{yy} = \sigma_{zz}$). The main focuses of this application are:

- Quantify impacts of poroelastic and thermoelastic effects on porosity distribution.
- Analyse the impacts of increase in injection rate on porosity and permeability distributions.

Physical properties as used for the homogeneous reservoir are listed in Table 4.1.

Table 4.1 Properties of the homogeneous reservoir and the virtual induced fracture (initial porosity ϕ^i and permeability k^i, solid density ρ_s, solid thermal capacity c_s, solid thermal conductivity λ_s, Young's modulus E, Poisson's ratio ν and fracture aperture a).

	ϕ^i [%]	k^i [m^2]	ρ_s [kg $\cdot$ m^{-3}]	c_s [J $\cdot$ kg^{-1} $\cdot$ K^{-1}]	λ_s [W $\cdot$ m^{-1} $\cdot$ K^{-1}]	E [GPa]	ν [-]	a [m]
Reservoir	12.5	1.30×10^{-15}	2650	920	3.1	55	0.2	–
Fracture	100	4.33×10^{-9}	–	–	–	–	–	2.28×10^{-4}

4.3.1 Contribution of poroelastic effects and thermoelastic effects

In Subsection 4.2.3, porosity has been formulated as a function of effective pressure and temperature. Two different models are presented, one considering only poroelastic effects (Equation 3.11) and another considering both thermo- and poroelastic effects (Equation 4.4). At the injection point, increase of pore pressure (leading to decrease of effective pressure) and decrease of temperature are observed as illustrated in Figure 4.1. Depending on the reservoir rock properties and the hydraulic and thermal configuration, contributions of poroelastic effects (due to effective stress changes) and thermoelastic effects (due to temperature changes) on porosity can strongly vary and quantifying each contribution can be therefore not trivial. Furthermore, since physical processes controlling pressure and temperature distributions are different, poroelastic and thermoelastic effects on porosity can have different behaviours.

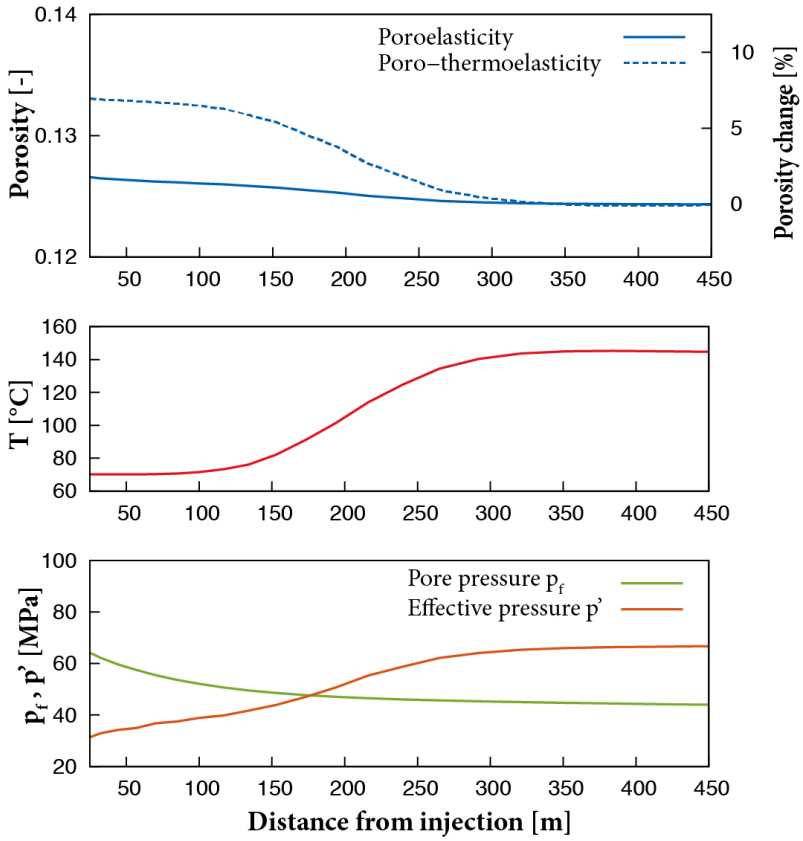

Fig. 4.1 Porosity, temperature, pore pressure and effective pressure profiles after 30 years of injection at 75 $m^3.h^{-1}$ with the two different porosity models considered. Horizontal axis is the distance from the injection well in the horizontal direction. Temperature, pore pressure and effective pressure have same profiles for both cases.

Figure 4.1 shows porosity, temperature, pore pressure and effective pressure profiles from the injection well to the border of the domain along the x-direction after 30 years of injection at $75\,\mathrm{m}^3 \cdot \mathrm{h}^{-1}$ of 70 °C water (initial target production rate for the Groß Schönebeck research project). Results from the two porosity models are presented. From the pure poroelastic model (solid line), a 2 % increase of porosity at the injection point is observed as due to effective pressure and pore pressure changes which is in accordance with observations (Blöcher et al., 2009). Since pore pressure is controlled by diffusion (see governing Equations 2.22 and 2.3), this increase of porosity is also diffused from the injection fracture. Poroelastic impacts are therefore localised at the injection point and depend only on the localised pressure build-up. The combined thermo- and poroelastic model (dashed line) presents a different behaviour. As seen in Equation 4.4, poroelastic and thermoelastic effects add linearly. Temperature changes (70 °C at injection and initially 145 °C within the reservoir) induce a porosity increase of about 5 % for the given temperature difference ($\Delta T \sim$75 °C) and 7 % increase in total at the injection for both thermo- and poroelastic effects. In such context, thermoelastic effects are dominating over porosity changes. Furthermore, the temperature distribution is not only controlled by diffusion but also by thermal advection which is the most effective process around the injection. Therefore the absolute increase of porosity due to thermoelastic effects is not only localised at the injection point, as for the case where only poroelastic effects are considered.

4.3.2 Injection rate dependency

As described in the previous paragraph, pressure build-up at the injection point is responsible for a poroelastic increase of porosity and controls fluid flow which governs thermal advection and thus rates porosity increase due to thermoelastic effects. The injection rate is therefore a key variable for studying porosity distribution around one injection well since it affects both pressure and temperature distributions. Porosity model with both thermo- and poroelastic effects has been tested for two different injection rates, $Q_f = 30\,\mathrm{m}^3 \cdot \mathrm{h}^{-1}$ and $Q_f = 75\,\mathrm{m}^3 \cdot \mathrm{h}^{-1}$. The latter was the expected production rate for the geothermal doublet of Groß Schönebeck and the former represents an average value taken from field measurements.

Figure 4.2 shows porosity and temperature profiles after 30 ·years of injection for the two different injection rates (solid lines for $Q_f = 30\,\mathrm{m}^3 \cdot \mathrm{h}^{-1}$ and dashed lines for $Q_f = 75\,\mathrm{m}^3 \cdot \mathrm{h}^{-1}$). As seen on the temperature profiles, the thermal front is 75 m ahead with an injection rate of $75\,\mathrm{m}^3 \cdot \mathrm{h}^{-1}$ compared to an injection rate of $30\,\mathrm{m}^3 \cdot \mathrm{h}^{-1}$. Concerning the porosity profile, the increase in injection rate results in a slight increase

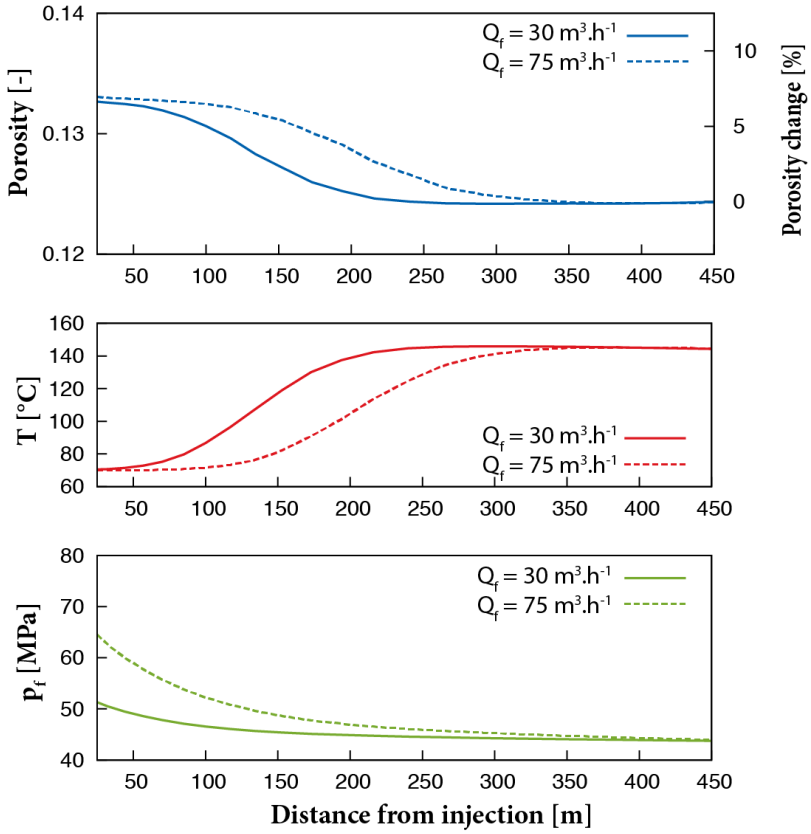

Fig. 4.2 Porosity, temperature and pore pressure profiles after 30 ·years of injection for two different injection rates.

of porosity at the injection point (7 % increase for $Q_f = 75\,\mathrm{m}^3 \cdot \mathrm{h}^{-1}$ against 6.5 % increase for $Q_f = 30\,\mathrm{m}^3 \cdot \mathrm{h}^{-1}$) due to pore pressure build-up. Pore pressure changes depend indeed linearly on the injection rate around an injection well. Therefore, poroelastic changes in porosity depend also linearly on the injection rate as described by Equation 3.11, due to their dependency on the effective stress. Furthermore, changes in injection rate do not impact the absolute increase of porosity due to thermoelastic effects since temperature differences are the same in both situations. However, the fluid velocity profile (depending on pore pressure distribution) impacts the temperature distribution due to thermal advection and therefore impacts also thermoelastic changes in porosity. As seen in Figure 4.2 the porosity front propagates together with the thermal front.

4.4 Application to the Groß Schönebeck geothermal reservoir

4.4.1 Characterization of the Groß Schönebeck reservoir

Geological context and target formations

The Groß Schönebeck reservoir (about 40 km north of Berlin, Germany) is located within the Lower Permian sedimentary sequence of the Northeast German Basin (NEGB), between −3815 and −4247 m below sea level. Two different categories of reservoir rocks can be identified: Upper Rotliegend siliciclastics ranging from conglomerates to fine-grained sandstones, siltstones and mudstones and Lower Rotliegend volcanics. The first category can be subdivided into five formations depending on their lithological properties after Blöcher et al. (2010): Hannover formation, Elbe alternating sequence, Elbe base sandstone II, Elbe base sandstone I and Havel formation.

The Elbe base sandstones I and II have been identified as target formations for future geothermal energy supply based on their promising hydraulic properties (local permeability up to 100 mD or $1.0 \times 10^{-13}\,\mathrm{m}^2$ after Trautwein and Huenges (2005) and porosity up to 10 % after Huenges and Hurter (2002)) and temperatures between 145 °C and 150 °C. These two formations are located between −4000 and −4100 m below sea level with a total averaged thickness of 100 m.

Natural faults and in-situ stress regime

The reservoir is crossed by a set of natural faults dominated by major NW-SE and minor NE-SW trending faults. The NNE- to NE-oriented minor faults bear the highest ratio of shear to normal stress which results in a critically stressed state in the sandstones and a highly stressed state in the volcanic layer (Moeck et al., 2009b; Kwiatek et al., 2010). Based on studies dealing with relation between fluid flow and fault stress state (Barton et al., 1995, 1997), NNE- to NE-striking faults are expected to act as hydraulically conductive structures and the NW-oriented major faults as drains.

According to Holl et al. (2005), the maximum horizontal stress (σ_H) is oriented NNE-SSW in the Rotliegend section of the Groß Schönebeck reservoir based on borehole breakout experiments. This direction also correlates with the World Stress Map database (Heidbach et al., 2016). To evaluate present-day stress magnitudes, the concept of limiting stress ratios on frictional sliding on critically stressed faults (Jaeger et al., 2007) is applied:

$$\frac{\sigma_1 - p_f}{\sigma_3 - p_f} = \left(\sqrt{m^2 + 1} + m\right)^2 \tag{4.6}$$

with $\sigma_{1,3}$ maximum and minimum principle stresses and p_f pore pressure. A frictional coefficient of $m = 0.85$ is assumed after Byerlee (1978) which better defines shear failure at shallow crustal depth (from 1 to 5 km). Considering hydrostatic pore pressure conditions with an average rock density of the overburden of $\rho = 2500\,\mathrm{kg \cdot m^{-3}}$ (Moeck et al., 2009b) and fresh water conditions ($\rho_f = 1000\,\mathrm{kg \cdot m^{-3}}$) leads to:

$$p_f = 0.43\sigma_v. \tag{4.7}$$

Substituting Equations 4.7 in 4.6 leads therefore to the following relation between the maximum, minimum and effective vertical stress:

$$\sigma_1 + 1.58\sigma_v = 4.68\sigma_3. \tag{4.8}$$

Equation 4.8 yields an upper and lower bound of any possible stress regime with the given reservoir conditions (depth, pore pressure and friction coefficient) as illustrated in Figure 4.3 (Peška and Zoback, 1995; Moeck et al., 2009b):

$$\begin{aligned} \sigma_H &\leq \quad 3.10\sigma_v \quad (\sigma_h = \sigma_v) \\ \sigma_h &\geq \quad 0.55\sigma_v \quad (\sigma_H = \sigma_v). \end{aligned} \tag{4.9}$$

However, Moeck et al. (2009b) reported downward displacement of the hanging walls from fault throw analysis limiting possible stress regimes to normal or strike-slip faulting (including transitional types between the two given regimes). Furthermore, hydraulic stimulations of the wells (Legarth et al., 2005; Reinicke et al., 2005; Zimmermann et al., 2010) gave estimates of the minimum horizontal stress ($\sigma_h = 53 \pm 3\,\mathrm{MPa}$) excluding pure strike-slip faulting regime. Therefore, the previous bounds given by Equation 4.9 can be further reduced to the two following stress regimes:

- Normal faulting regime, case II in Figure 4.3 ($\sigma_v > \sigma_H > \sigma_h$) with:

$$\begin{aligned} \sigma_H &\leq \quad 0.78\sigma_v \\ \sigma_h &\geq \quad 0.55\sigma_v. \end{aligned} \tag{4.10}$$

- Transitional stress regime between normal and strike slip faulting, case III in Figure 4.3 ($\sigma_v = \sigma_H > \sigma_h$) with:

$$\begin{aligned} \sigma_H &= \quad 1.00\sigma_v \\ \sigma_h &\geq \quad 0.55\sigma_v \end{aligned} \tag{4.11}$$

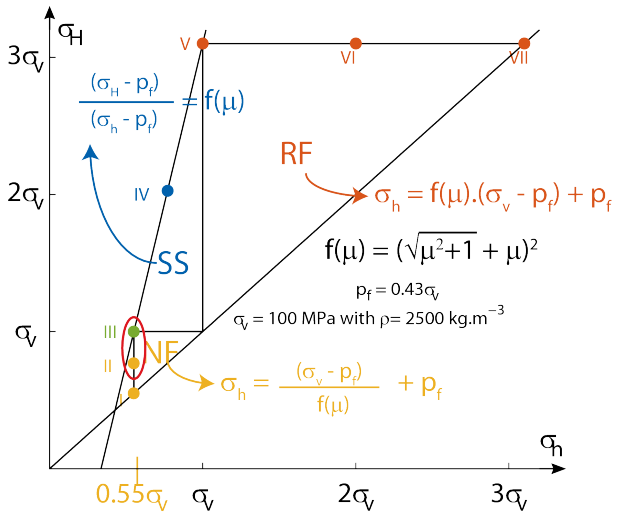

Fig. 4.3 Possible stress field at depth of the Groß Schönebeck reservoir based on frictional equilibrium (Peška and Zoback, 1995). A friction coefficient of $\mu = 0.85$ is assumed. NF refers to normal faulting, SS to strike slip faulting and RF to reverse faulting. Cases I to VII refer to: I radial extension, II normal faulting, III transition normal-strike slip faulting, IV strike slip faulting, V transition strike slip-reverse faulting, VI reverse faulting and VII radial compression. Different relations between stress magnitudes for each regime are derived from Equation 4.6.

Doublet system and hydraulically induced fractures

The well doublet system consists of an injection well (E GrSk 3/90) and a production well (Gt GrSk 4/05). The injection well is an abandoned gas exploration well reopened in 2001. The production well was successfully drilled in 2007. The injection well reaches the sandstone formations and the volcanics (−4100 m below see level) and the production well consists of an open hole section into these same two formations (between −3799 to −4228 m below sea level). Hydraulic stimulation has been performed in the wells resulting in four induced hydraulic fractures to increase the productivity. Seven fracture treatments and eight perforation treatments were performed. Two gel-proppant fractures and two waterfractures were induced at the injection well to stimulate the sandstone sections (Zimmermann et al., 2009). A waterfracture treatment in the low permeable volcanic rocks as well as two gel-proppant treatments in the sandstone sections were applied at the production well (Zimmermann et al., 2010; Zimmermann and Reinicke, 2010). These induced fractures are mainly tensile and are therefore oriented parallel to the maximum horizontal stress direction σ_H. Geological formations, geometry of the wells and of the induced fractures are structurally illustrated in Figure 4.4.

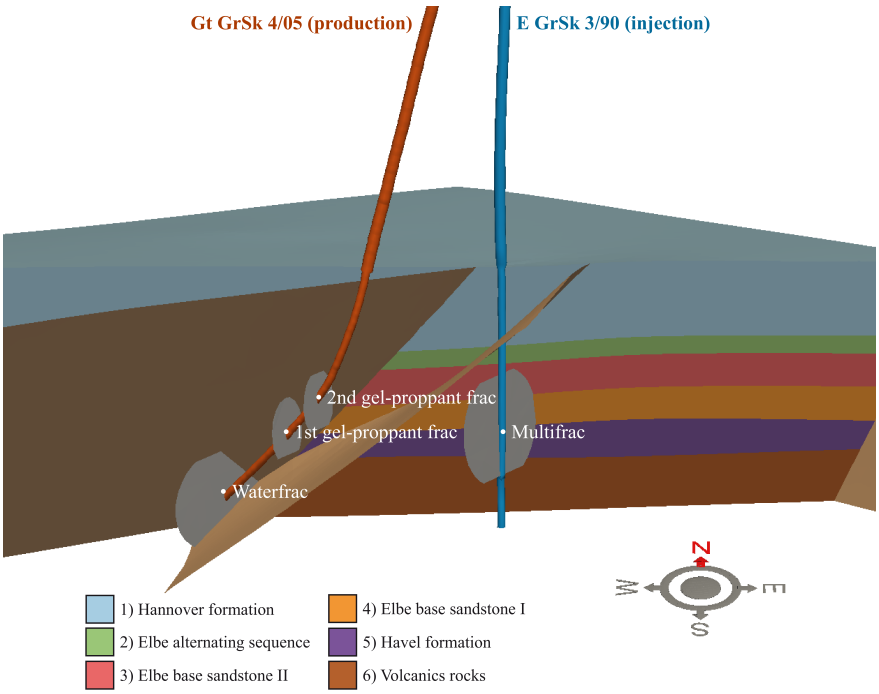

Fig. 4.4 Geological formations, doublet wells and induced hydraulic fractures in the Groß Schönebeck reservoir. White points represent injection (multifrac) or production points.

Physical properties of the reservoir

Hydraulic and thermal properties of the reservoir units can be found in published data (Legarth et al., 2005; Zimmermann et al., 2009; Blöcher et al., 2010). Mechanical properties were determined by ultrasonic and density logs (Zimmermann et al., 2010). All properties of the reservoir units are summarised in Table 4.2. Furthermore, cores samples from the Groß-Schönebeck reservoir formations have constrained an anisotropic permeability tensor Trautwein and Huenges (2005) with a ratio between vertical and horizontal permeability of $k_z/k_{xy} = 0.25$ as reported by Blöcher et al. (2010).

Dimensions of the induced fractures were computed and verified by field experiments (Zimmermann and Reinicke, 2010; Zimmermann et al., 2010) and are summarised in Table 4.3.

A 3-dimensional structural model of the reservoir has been developed by Moeck et al. (2009b) including the presented geological formations, faults and hydraulically induced fractures. Geometrical discretisation of the model has been done using an in house open-source meshing software allowing the transfer of the geometrical complexity of the model to the Finite-Element solver (Cacace and Blöcher, 2015).

Table 4.2 Properties of the reservoir formations (initial porosity ϕ^i permeability k^i, solid thermal capacity c_s, solid thermal conductivity λ_s, Young's modulus E and Poisson's ratio ν). Solid density of all the units is $\rho_s = 2650\,\mathrm{kg}\cdot\mathrm{m}^{-3}$

.

Unit	Height [m]	ϕ^i [%]	k^i [m^2]	c_s [$\mathrm{J}\cdot\mathrm{kg}^{-1}\cdot\mathrm{K}^{-1}$]	λ_s [$\mathrm{W}\cdot\mathrm{m}^{-1}\cdot\mathrm{K}^{-1}$]	E [GPa]	ν [-]
1) Hannover formation	159	1	4.9×10^{-17}	920	1.91	55	0.18
2) Elbe alternating sequence	30	3	3.2×10^{-16}	920	1.94	55	0.18
3) Elbe base sandstone II	55	8	6.4×10^{-16}	920	3.1	55	0.18
4) Elbe base sandstone I	52	15	1.3×10^{-15}	920	3.18	55	0.18
5) Havel formation	36	0.1	9.9×10^{-17}	1000	3.0	55	0.18
6) Volcanic rocks	100	0.5	9.9×10^{-17}	1380	2.31	55	0.2

Table 4.3 Properties of the hydraulically induced fractures (porosity ϕ, permeability k and aperture a).

	ϕ [%]	k [m^2]	half-length [m]	height [m]	a [m]
Water-fracture	100	4.33×10^{-9}	190	175	2.28×10^{-4}
Gel/proppant fracture	100	4.33×10^{-9}	60	95	2.28×10^{-4}
Multi-fracture	100	4.33×10^{-9}	160	185	2.28×10^{-4}

Simulation configurations

Based on the possible in-situ stress states as described in Subsection 4.4.1 and to allow evaluation of the transport properties evolution models, two different scenarios have been simulated: (1) a Thermo-Hydro-Mechanical model within a normal faulting regime (case II in Figure 4.3) and (2) a Thermo-Hydro-Mechanical model within a transitional regime between normal and strike slip faulting (case III in Figure 4.3). The two cases have the following stress magnitudes at reservoir depth (-4100 m meters below sea level) using an average density of $\rho = 2500\,\mathrm{kg}\cdot\mathrm{m}^{-3}$ for the entire rock column derived from weight variations (Moeck et al., 2009b):

- Case 1:
  - ⋆ $\sigma_v = 100$ MPa.
  - ⋆ $\sigma_H = 78$ MPa.
  - ⋆ $\sigma_h = 55$ MPa.
- Case 2:
  - ⋆ $\sigma_v = 100$ MPa.

⋆ $\sigma_H = 100$ MPa.

⋆ $\sigma_h = 55$ MPa.

For the two given scenarios, steady-state simulations have been first conducted to calculate pressure, temperature and stress natural distributions before any injection/production of fluid. For these steady-state simulations, a hydrostatic distribution of pressure is assumed as well as a heat flow of $72\,\mathrm{mW \cdot m^{-2}}$ at the bottom of the reservoir (Norden et al., 2008). Distributions of pressure, temperature and stress obtained as results of the steady-state simulations are then used as initial conditions for the transient simulations when injection and production of fluid start. An injection rate of $30\,\mathrm{m^3 \cdot h^{-1}}$ is considered and production rates of $10\,\mathrm{m^3 \cdot h^{-1}}$ at each of the three production points are considered for a total production rate of $30\,\mathrm{m^3 \cdot h^{-1}}$.

A total operation time of 100 years has been simulated. In a first step, the evolution of the pressure at the wells and the evolution of the production temperatures are described to provide an overview of the performance of the geothermal system. Then, the distribution of porosity and the evolution of the anisotropy factor for permeability are described. In a last step, the two different cases in terms of regional stress field are investigated for the stress distribution around the wells.

4.4.2 Life time of the system and productivity

Thermal breakthrough of the doublet is here defined as the time when production temperature at one of the three fractures of the production well drops by 1 °C. Furthermore, life time of the geothermal system is defined as the time when one of the production temperature drops below 127 °C (~ 400 K). As seen on Figure 4.3, the two possible stress regimes are quite similar and all results presented in this sub-section are mostly identical for both cases. Results of the normal faulting case are therefore only presented here. Figure 4.5 shows the evolution of the production temperature at the three fractures of the production well (Figure 4.5a) and the evolution of pore pressure changes at the fractures of the production well and at the injection well (Figure 4.5b). As seen on Figure 4.5a, initial production temperatures are different according to the geothermal gradient in the reservoir calculated during the steady-state initial simulation. They are evaluated at 145 , 146 and 149 °C at the second and first and second gel proppant fractures and the water fracture respectively. The production temperatures remain mostly constant until the cold water front reaches the upper fracture (2^{nd} proppant gel fracture) after 11 years, and then the 1^{st} proppant gel fracture after 16 years of injection. Production temperature at these two fractures

drops significantly reaching 125 and 141 °C after 54 years. After 100 years of production simulated, thermal breakthrough in the lower waterfracture in the volcanic layer is not observed. Thermal breakthrough (illustrated by the blue square in Figure 4.5a) is predicted after 18 years of injection. The life time of the system (illustrated by the red square) is evaluated as 50 years.

On Figure 4.5a, a transient draw down phase of pore pressure is illustrated at the production points as well as the pore pressure build up at the injection well resulting from constant production rates (three times $Q_p = 10\ \mathrm{m}^3 \cdot \mathrm{h}^{-1}$) and constant injection rate ($Q_i = 30\,\mathrm{m}^3 \cdot \mathrm{h}^{-1}$) respectively. After 1 year of injection, pore pressure increase at the injection is 7 MPa and pressure draw down at the fractures of the production well are comparable between -6 and -8 MPa. Such pore pressure draw down can be used to estimate a productivity index (PI) with a total production rate of $30\,\mathrm{m}^3 \cdot \mathrm{h}^{-1}$ of about $5\,\mathrm{m}^3 \cdot \mathrm{h}^{-1} \cdot \mathrm{MPa}^{-1}$ which is consistent with field measurements ($6\,\mathrm{m}^3 \cdot \mathrm{h}^{-1} \cdot \mathrm{MPa}^{-1}$, Blöcher et al. (2015)).

Figure 4.6 shows the evolutions of the thermal breakthrough isotherm ($T = 144\,°\mathrm{C}$ in red) and of the life time isotherm ($T = 127\,°\mathrm{C}$) during injection and production of fluid. These two isotherms are shown after 10 , 20 , 50 and 100 years of operation. The volume occupied by the cold water increases through time in the preferable direction from the injection fracture to the production well. It is clearly shown that thermal breakthrough occurs first at the 2nd gel proppant fracture at 18 years (red isotherm in Figure 4.6b). Furthermore, in Figure 4.6c, the blue isotherm reaches the 2nd gel proppant fracture, corresponding to the life time of the system. These two isotherms are not influenced by the permeable fault in between the wells. The permeability difference between the fault and the matrix as well as the pressure gradient influence the fluid flow. Since the permeable fault does not act as a preferable fluid pathway, the magnitude of the pressure gradient (which is the highest between the injection and the production well) is the dominant variable controlling the fluid flow in the reservoir. These results show that the reservoir behaviour is not controlled by the hydraulic properties of the permeable fault in between the two wells but by the pressure gradient resulting from the injection and production of fluid.

4.4.3 Porosity distribution and permeability anisotropy

The increase of pore pressure and the decrease of temperature result in porosity and permeability enhancement at the injection well due to poroelastic and thermoelastic effects respectively. Figure 4.7 shows the porosity and anisotropy factor for permeability (k_z/k_{xy}) distributions in the Elbe base sandstone 1 layer after 30 years of injection.

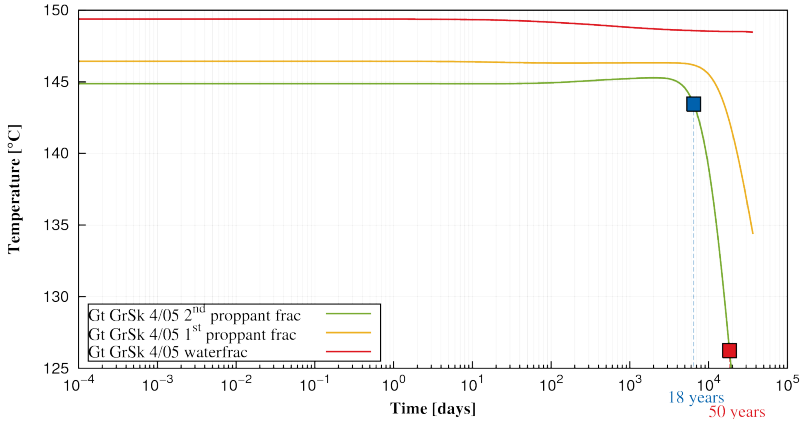

(a) Production temperature.

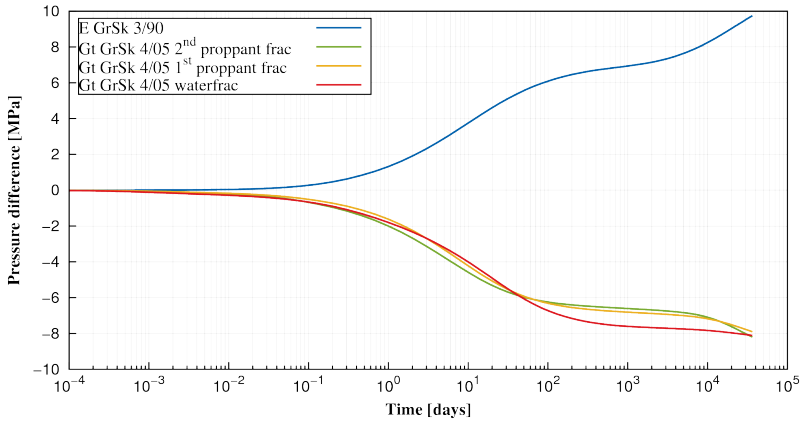

(b) Pressure difference.

Fig. 4.5 Production temperature (a) and pressure difference (b) evolutions at the injection and production wells over simulated time. Blue square correspond to thermal breakthrough and red square to life time of the system.

Initial porosity in this formation is 15 % and an increase of porosity of 5.5 % is observable at the injection well on Figure 4.7a. Furthermore, as described in Section 4.3, the porosity front due to thermoelastic effects propagates from the injection. However, no significant changes at the production fractures can be noticed in term of porosity. Indeed, the magnitude of the effective pressure around the injection well is not strongly altered. According to Equation 4.1, a decrease in pore pressure leads to an increase in effective stress. However, the initial effective pressure ($p' \sim 60\,\text{MPa}$) obtained by Equation 4.10 gives a Biot's coefficient close to 0 as described by Equations 3.4 and 3.17. Coupling between Equations 4.10, 3.4 and 3.17 tends to limit the increase in effective pressure due to a decrease in pore pressure. Therefore, the porosity remains mostly constant around the production well.

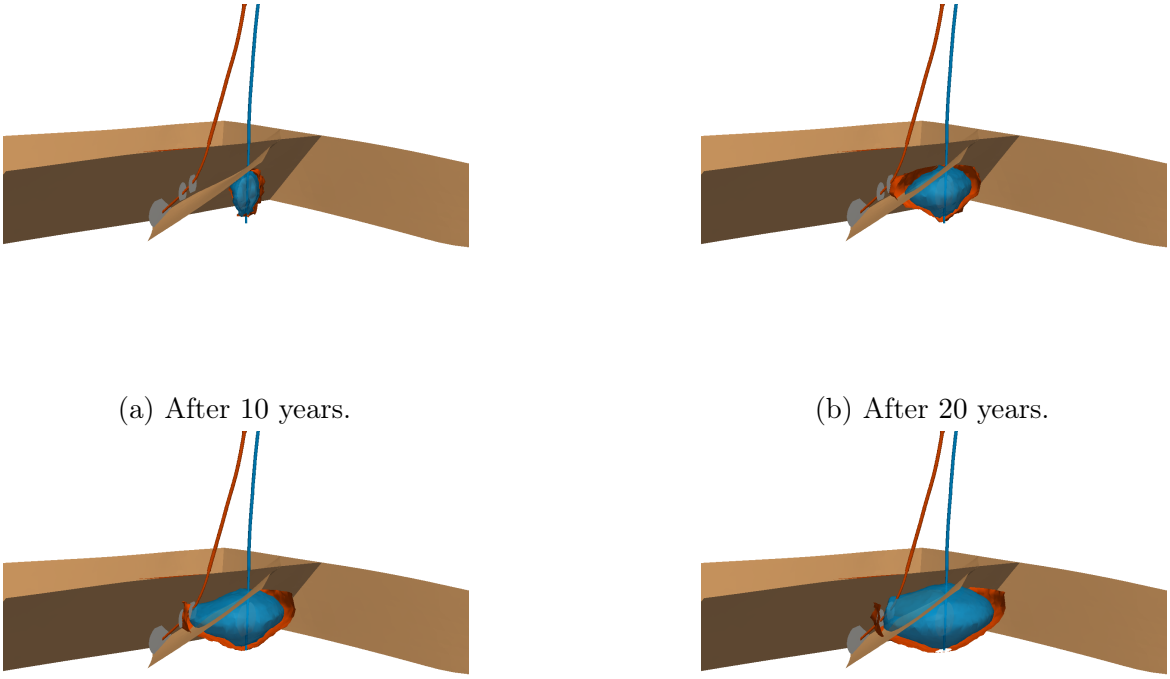

(a) After 10 years.

(b) After 20 years.

(c) After 50 years.

(d) After 100 years.

Fig. 4.6 Evolution of two isotherms during geothermal operation after 10 , 30 , 50 and 100 years of injection. Red surface is the 144 °C isotherm (thermal breakthrough) and blue surface the 127 °C (life time of the system).

Figure 4.7b shows the anisotropy factor of the permeability tensor. As seen in Subsection 4.4.1, an initial anisotropy factor of 0.25 has been identified within the Groß Schönebeck geothermal reservoir. On this figure, an increase of the anisotropy factor controlled by Equation 4.5 is observed around the injection fracture. Maximum values of anisotropy can be found at the border of the thermal front, suggesting that it originates from build-up of thermal strain.

Enhancement of the transport properties which are porosity and permeability contributes to accelerating the thermal front and therefore reduces the thermal breakthrough time (further discussed in the next sub-section). Quantifying these transport properties changes are therefore of relevance for analysing reservoir performance and sustainability.

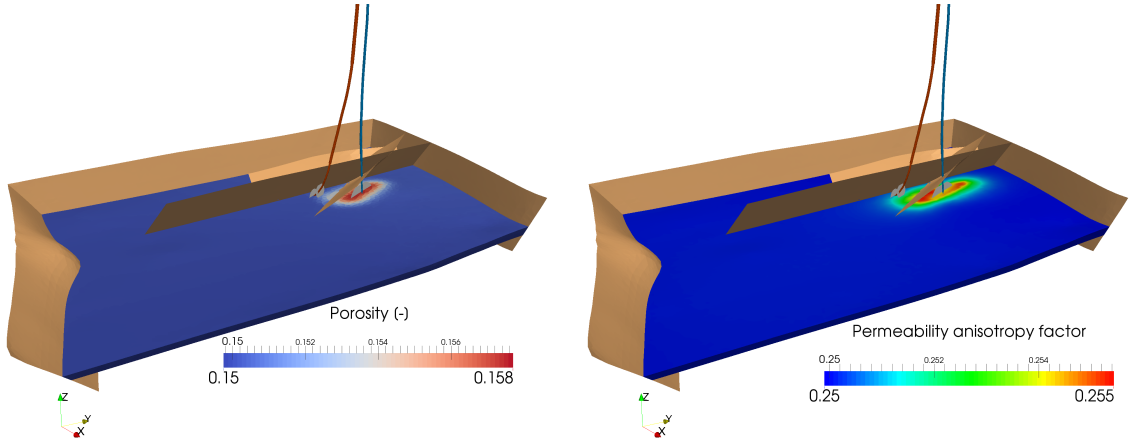

(a) Porosity distribution.

(b) Anisotropy factor in permeability.

Fig. 4.7 Porosity and anisotropy factor for permeability (k_z/k_{xy}) distributions in the Elbe base sandstone I after 30 years of injection.

4.4.4 Impact of the regional stress field

Two different regional stress field possibilities have been presented in Section 4.4, a normal faulting regime and a transitional regime between normal and strike slip faulting. To compare these regimes, stress distributions are observed at the wells where stress changes are mostly concentrated due to pore pressure and temperature evolutions.

Figure 4.8 shows the effective pressure evolution at the injection (Figure 4.8a) and at the production well (Figure 4.8b). Differences in the initial values of effective pressure ($\Delta p' \sim 8\,\mathrm{MPa}$) on Figure 4.8a comes from the initial steady-state distribution of stress according to the two cases configuration. In both cases, mean effective stress increases slightly due to pore pressure decrease. A significant drop of effective pressure is also observed for the two gel proppant fractures when thermal breakthrough (blue squares) is reached.

At the injection well, the decrease of compressional stresses starting after a few days (in Figure 4.8b) can be directly correlated with an increase of pore pressure as illustrated in Figure 4.5b. Pore pressure changes induced by injection and production of fluid have the same effects in both cases. The only noticeable difference comes from the initial stress distribution.

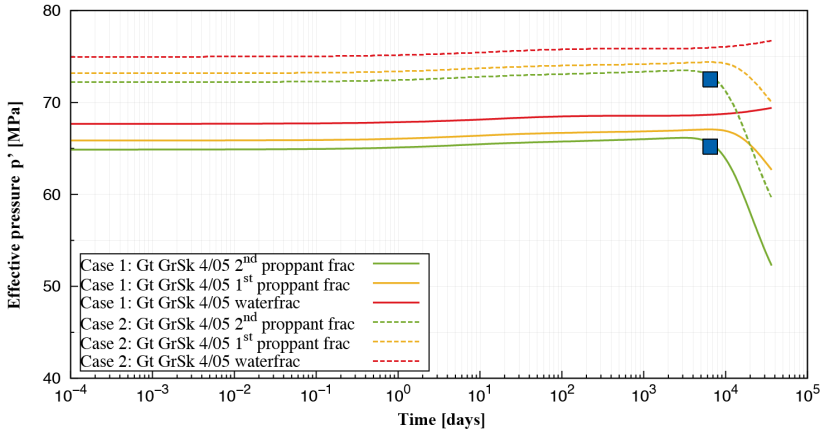

(a) Effective pressure at the production fractures.

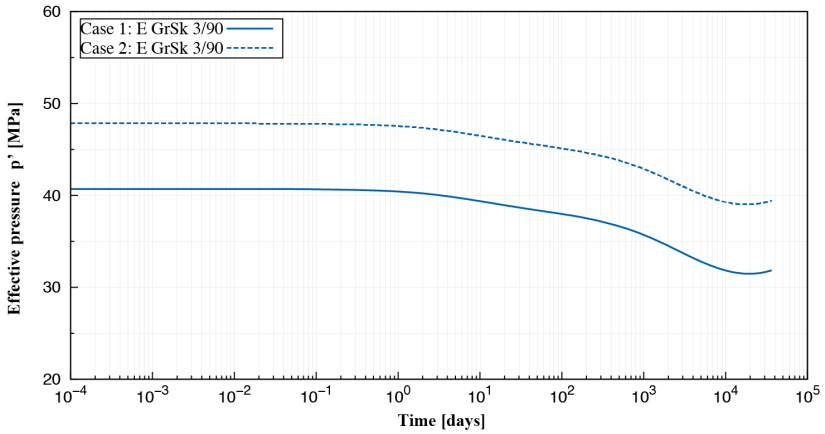

(b) Effective pressure at the injection well.

Fig. 4.8 Effective pressure evolution at the production (a) and at the injection well (b). Positive stress relates to a compressional regime.

4.5 Discussion

4.5.1 Impacts of mechanical processes on reservoir performance and sustainability

As reported in Subsection 4.4.3, injection of cold water results in porosity and permeability enhancements propagating together with the thermal front. This in turn leads to an increase in cold water propagating within the reservoir rocks. One classic Thermal-Hydraulic simulation with constant porosity and permeability (other parameters are kept the same) has been performed to compare with the current results for fully THM simulations. Without transport properties evolution models, a 1 °C reduction of the production temperature (here defined as thermal breakthrough) after 19 years of injection and production temperature under 127 °C (400 K) (here defined as life time of

the doublet) after almost 59 years of injection are predicted. Table 4.4 compares results from TH and THM simulations. Considering transport properties evolution models reduce therefore the thermal breakthrough time by more than 1 year (−8 %) and the life time of the system by 8 years (−14 %). Integrating the mechanical evolution of the geothermal reservoir gives therefore a better evaluation of these characteristic times controlling the reservoir sustainability for geothermal operations.

Table 4.4 Comparison of thermal breakthrough and life time of the doublet and impacts of transport properties evolutions.

	Thermal breakthrough [years]	Life time [years]
TH simulations (constant ϕ and k)	19.23	58.61
THM simulations (present study, evolution of ϕ and k)	17.75	50.46

Furthermore poroelastic and thermoelastic processes for the reservoir rocks can give information about the sustainability of the induced fractures during geothermal operations. Indeed, the increase in the effective stress at the production well (Section 4.4.4) could contribute to closure of the production fractures and decrease in the effective stress at the injection well could lead to propagation of the injection fracture. However, current results can only give trends for the induced fractures sustainability and point out that fracture related processes need to be considered to properly quantify production fractures sustainability and injection fracture propagation. Processes related to fracture mechanics are not yet implemented in "OpenGeoSys" but their integration is part of ongoing work and will be considered in the next future.

Chemical precipitation and corrosion are often observed at the production well due to pressure changes. These processes (often summarised in the term scaling) can also alter well and fracture sustainability in addition to the mechanical processes related to fractures. These phenomena are not modelled in this approach and should be considered to study well sustainability.

4.5.2 Geomechanical effects with thermo- and poroelastic coupling

As described in the balance equations in Section 4.2, the total stress tensor depends on pressure and temperature changes. An increase of pore pressure will lead to dilatation of the rock and a decrease of temperature leads to build-up of compressional stresses. The ratio between thermoelastic and poroelastic stresses can be evaluated after Segall and Fitzgerald (1998) as:

$$\frac{\sigma^{Thermo}}{\sigma^{Poro}} = \frac{K_d \beta_b \Delta T}{\alpha \Delta p_f}. \tag{4.12}$$

This ratio increases with rock mechanical stiffness which could be related to an increase of confining stress and therefore to an increase in depth. In the case of the Groß Schönebeck reservoir, thermoelastic stress exceeds poroelastic stresses by a factor of 10.

Thermoelastic coupling is therefore a key process to model which also influences fluid-flow by mean of porosity. In this study, porosity changes due to temperature changes (Equation 4.4) result from the difference between drained and pore thermal expansion coefficients. Under the assumption of an ideal porous medium, these coefficients are assumed to be the same (McTigue, 1986; Ghabezloo et al., 2008). However, the validity of such approximation for real case systems application is questionable. Drained heating laboratory experiments can be conducted to better constrain these two parameters (especially the pore thermal expansion coefficient). The drained thermal expansion coefficient is also described as linearly dependent on temperature (Somerton, 1992) which requires experimental constrains to describe the phenomenon in simulations.

However, detailed information about the reservoir rock properties are often simplified when upscaling from laboratory to reservoir conditions. Measurements for drained and pore thermal expansion coefficients obtained in the laboratory will not necessarily describe the effects of reservoir heterogeneities. Thermoelastic effects on porosity could therefore behave differently if reservoir heterogeneities could be taken into account. Such studies require therefore both experimental information to constrain models and techniques to better integrate reservoir heterogeneities and their impacts on the physical processes. This is part of ongoing activities.

4.5.3 Faults and in-situ stress field in the Groß Schönebeck reservoir

The approach used here for solving deformation processes is based on continuum mechanics and does not consider frictional contacts which could occur along the plane of the fault. Faults are only considered for hydraulic and thermal processes. This is due to current technical limitation of the software used.

Considering mechanical processes for reservoirs with natural faults such as the Groß Schönebeck geothermal reservoir can give useful information about slip tendency of the faults during geothermal operations. Figure 4.9 shows the initial computed slip tendency of the faults based on formulations after Moeck et al. (2009a). Faults parallel to the maximum horizontal stress have a higher slip tendency than those perpendicular

to the maximum horizontal stress. A general observable trend is a decrease of slip tendency with depth.

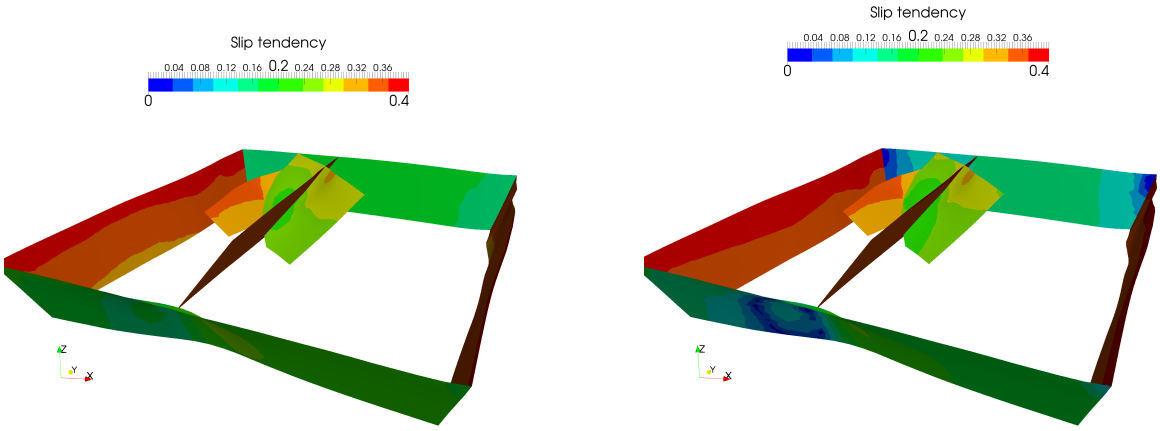

(a) Initial slip tendency for case 1: normal faulting ($\sigma_H/\sigma_v = 0.78$, $\sigma_h/\sigma_v = 0.55$).

(b) Initial slip tendency for case 2: transitional regime between normal and strike slip faulting ($\sigma_H/\sigma_v = 1.00$, $\sigma_h/\sigma_v = 0.55$).

Fig. 4.9 Initial slip tendency of the faults within the Groß Schönebeck reservoir before geothermal application. Left figure corresponds to case 1, normal faulting regime and right figure to case 2, transitional regime between normal and strike slip faulting.

Changes in pore pressure have been identified as origin of possible fault reactivation (Cappa and Rutqvist, 2011) due to poroelastic effects. In the present context, thermally induced stresses have non negligible impacts since the difference between in-situ temperature and injected temperature is significant ($\Delta T \sim 70\,°C$). Analysing contributions of poroelastic and thermoelastic stresses separately with respect to slip tendency of the faults and to the magnitude of possible induced seismic events could therefore give valuable insight concerning the thermal state of faults and their possible reactivation during geothermal energy applications (Jacquey et al., 2015a). This phenomenon could also be the origin of the microseismicity measured during hydraulic stimulations of the Groß Schönebeck reservoir (Kwiatek et al., 2010).

The work presented here is therefore a first step in considering faults as stress-sensitive structures and not only as hydraulically active. The mechanical behaviour of the surrounding rocks has been described and implemented. Background deformation and related transport property evolutions give a complete behaviour description of the rocks, the next step of the project is to consider new physical processes related to frictional contacts and plasticity models which could give more information on the reservoir and faults behaviour. Indeed, considering frictional contacts related processes

for faults could lead to stress and strain localisation along the fault planes and could help to better describe the in-situ stress field within the reservoir.

The in-situ stress field could also be better described by mean of the vertical stress distribution, which is of great importance in the stress regimes considered ($\sigma_1 = \sigma_v$). To calculate the magnitude of the vertical stress acting on the reservoir, the weight of the overburden was derived after Moeck et al. (2009b) using an average density for the upper major lithostratigraphic units of the Northeast German Basin. This approach leads to an homogeneous vertical stress distribution at the top of the reservoir since the distribution of the lithostratigraphic units is assumed to be homogeneous at the scale of the reservoir. However, heterogeneities in the lithostratigraphic units can occur and alter the vertical stress distribution. To better describe the mechanical behaviour of the geothermal reservoir, description of spatial changes in term of vertical stress due to heterogeneities in density distribution of the overburden need to be constrained from regional models. A possible way to improve the present results would be using the 3D regional model developed by Moeck et al. (2009b) to extract the stress field of the reservoir from the computed stress field at the regional scale. The stress field at the scale of the reservoir thus obtained would better describe the present day stress regime and could be used as initial condition.

4.6 Conclusions

The present study describes a new way of physically coupling transport properties for Thermo-Hydro-Mechanical process modelling within fluid-bearing reservoirs relevant for several applications, including geothermal energy, energy storage and hydrocarbon exploration. This theoretical background has been tested on the Groß Schönebeck research geothermal doublet. Based on the results, a thermal breakthrough time of 18 years and a life time of the system of 50 years are predicted. Due to porosity and permeability enhancements, these results show a reduction of the thermal breakthrough time ($-7.72\,\%$) and the life time of the system ($-14\,\%$) compared to classic Thermo-Hydraulic simulations with constant transport properties. These results may therefore guide geothermal reservoir management by raising the importance of appropriate coupling between thermo-hydro and mechanical processes.

Chapter 5

Numerical investigation of thermoelastic effects on fault slip tendency during injection and production of geothermal fluids[1]

5.1 Introduction

Understanding processes controlling slip behaviour of faults as induced by man-made activities is of interest for several geo-energy related studies such as geothermal power production, energy storage and enhanced oil and gas recovery. Injection-induced reactivation of faults or fracturing can indeed lead to notable micro-earthquakes (Moeck et al., 2009a; Deichmann and Giardini, 2009; Rutqvist et al., 2013, 2015). Correlations between pore pressure changes as those induced by injection and production of fluid and the in-situ stress field within a reservoir play a major role in coupled hydraulic and deformation processes (Terzaghi, 1943; Carrol and Katsube, 1983; Soltanzadeh et al., 2009). These poroelastic effects have been identified as part of the processes controlling faults slip behaviour (Jaeger et al., 2007; Cappa and Rutqvist, 2011; Rutqvist et al., 2013, 2015). Furthermore, changes in temperature can also affect the in-situ stress-field (Geertsma, 1957; Lord and Shulman, 1967; McTigue, 1986; Zimmerman, 2000). Although the ratio between thermoelastic and poroelastic stresses ($\sigma^{Thermo}/\sigma^{Poro} = K_d\beta_b\Delta T/\alpha\Delta p_f$) has been reported to increase with rock stiffness and therefore depth (Segall and Fitzgerald, 1998), thermoelastic effects are often not considered when analysing slip tendency and possible reactivation of faults in geothermal reservoirs.

This contribution presents a numerical evaluation of the impacts of thermoelastic stresses on the slip behaviour of faults within deep geothermal reservoirs as based on a frictional sliding resistance formulation. A coupled approach for thermo-hydro-mechanical process modelling has been integrated in the open-source finite element method based simulator "OpenGeoSys" (Kolditz et al., 2012a) following theory of coupled thermo- and poroelasticity.

The reactivation potential of a fault is evaluated during injection and production of geothermal fluid as a function of the ratio of shear to normal stress on the fault plane. First, a simple geometry model is considered with different configurations, by

[1]This chapter is published in the journal *Energy Procedia* (Jacquey et al., 2015a).

changing the dip angle of the fault. Thermoelastic stress enhancement comes from the temperature anomaly of the cold injected geothermal fluid propagating within the relative warmer fluid-bearing reservoir. This simple model serves as an introduction to a real-case application of the Groß Schönebeck geothermal research site, which is discuss further in the manuscript.

5.2 Approach

5.2.1 Governing equations for thermo-hydro-mechanical process modelling

Governing equations for fluid-flow, heat transport and elastic deformation as required to solve coupled thermo-hydro-mechanical (THM) processes are derived from balance equations of mass, heat and momentum.

Governing equation for fluid flow results from conservation of mass in a fully saturated porous medium as described by Equations 2.22 and 2.3.

Heat transport governing equation is derived from heat balance considering conductive and advective heat transport processes following Equation 2.25, assuming thermal equilibrium between fluid and solid.

Deformation of the porous medium in a context of poro-and thermoelasticity (McTigue, 1986; Zimmerman, 2000) is governed by the momentum balance equation in terms of effective stress following Equation 2.10.

Effective stress tensor is related to strain via the generalised Hooke's law extended for non-isothermal deformation, as described in Equation 2.12.

It is worth noticing that the approach adopted here does not describe undrained effects such as mechanical and thermal pressurisation (increase of pore pressure due to stress and temperature changes).

5.2.2 Slip tendency

Slip tendency is the ratio of resolved shear stress to normal stress acting on the fault plane (Morris et al., 1996; Lisle and Srivastava, 2004). If the shear stress exceeds the frictional sliding resistance (here parametrised in terms of a sliding coefficient μ_s after Byerlee (1978)), slip is likely to occur on the fault plane, which can be described as:

$$T_s = \frac{\tau}{\sigma'_N} \leq \mu_s \tag{5.1}$$

where T_s denotes the slip tendency. Here, it is assumed a sliding coefficient μ_s of 0.85 which better defines shear failure at shallow crustal depth (from 1 to 5 km) (Byerlee,

1978). Equation 5.1 is only valid for normal stress smaller than 200 MPa (Jaeger et al., 2007). Orientation of the plane can be defined by means of the three angles between the plane normal and each of the principal stress axes. In all simulations presented, principle stress axes match coordinate axes. The direction cosines of these angles (n_x, n_y and n_z) are related with the following relation (Pythagoras theorem):

$$n_x^2 + n_y^2 + n_z^2 = 1. \tag{5.2}$$

Shear and normal stresses acting on a plane the orientation of which is defined by the three previous direction cosines can be calculated after Ramsay and Lisle (2000); Jaeger et al. (2007); Moeck et al. (2009a) as:

$$\sigma'_N = n_x^2\sigma'_{xx} + n_y^2\sigma'_{yy} + n_z^2\sigma'_{zz}. \tag{5.3}$$

$$\tau = \sqrt{n_x^2 n_y^2(\sigma_{xx} - \sigma_{yy})^2 + n_y^2 n_z^2(\sigma_{yy} - \sigma_{zz})^2 + n_x^2 n_z^2(\sigma_{xx} - \sigma_{zz})^2}. \tag{5.4}$$

5.2.3 Model setup

The approach presented in the previous sections is applied on a simple geometry model. The model consists of a homogeneous reservoir (target depth 4000 m below sea level) with a fault discretised in 3 dimensions (20 m width) with a dip angle noted γ ($\gamma = \pi/4 = 45°$). Two hydraulically induced fractures from each side of the fault are integrated in the model where injection and production of the geofluid occur. The model is 1 km large in horizontal direction and 200 m high in vertical direction. The geometry of this model is schematically illustrated in Figure 5.1.

Geometrical discretisation of the model has been done using an in house open-source meshing software MeshIt (Cacace and Blöcher, 2015), allowing the transfer of the geometrical configuration of the model to the Finite-Element solver. A normal faulting stress regime is considered ($\sigma_1 = \sigma_{zz}$, $\sigma_2 = \sigma_{yy}$ and $\sigma_3 = \sigma_{xx}$) characterised by the following stress magnitudes:

- $\sigma_1 = -95$ MPa
- $\sigma_2 = -75$ MPa
- $\sigma_3 = -70$ MPa

Initial conditions for pore pressure, temperature and stress distributions are obtained from a steady-state simulation, for which a hydrostatic distribution of pore pressure

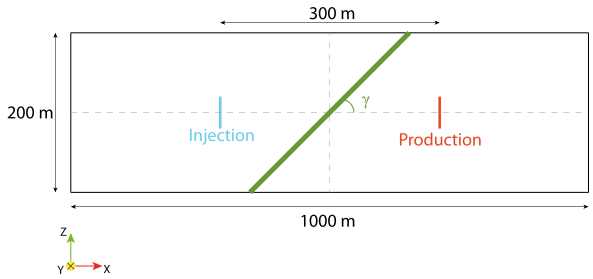

Fig. 5.1 Geometry of the 3-dimensional model used for the simulations. Here, a vertical cross-section is shown for a constant plane at $Y = 0$. Model is 1 km large in horizontal direction (X and Y directions) and 200 m height in vertical direction (Z). The geometry of the fault plane (in green) is characterised by its dip angle (γ). Injection and production fractures (in blue and red respectively) are orthogonal to the X direction and are 100 m large squares. Distance between the injection and the production fractures is 300 m.

(43.5 MPa at 4 km depth) and a geothermal gradient of ($33\,°\mathrm{C} \cdot \mathrm{km}^{-1}$) are assumed (Figure 5.2).

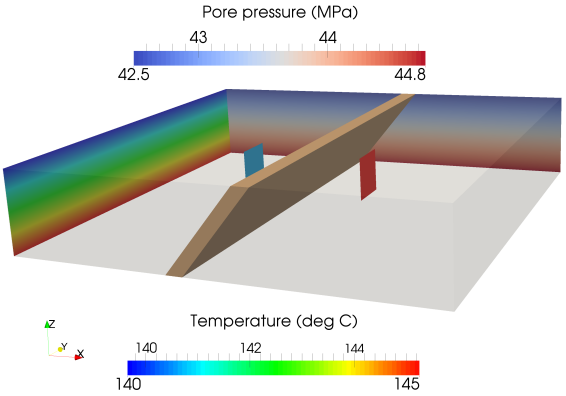

Fig. 5.2 Initial pore pressure and temperature distributions within the reservoir.

Water is injected with a temperature of 70 °C at $75\,\mathrm{m}^3 \cdot \mathrm{h}^{-1}$ at the injection fracture (in blue in Figures 5.1 and 5.2). Symmetrically, $75\,\mathrm{m}^3 \cdot \mathrm{h}^{-1}$ of warm water (in-situ temperature) is produced at the production fracture (in red in Figures 5.1 and 5.2). Physical properties of the reservoir and the fault are listed in Table 5.1.

Table 5.1 Properties of the homogeneous reservoir and the fault (solid density ρ_s, porosity ϕ, permeability k, solid thermal capacity c_s, solid thermal conductivity λ_s, drained thermal expansion coefficient β_b, drained bulk modulus K_d, solid bulk modulus K_s and Poisson's ratio ν).

	ρ_s [kg · m^{-3}]	ϕ [%]	k [m^2]	c_s [J · kg^{-1} · K^{-1}]	λ_s [W · m^{-1} · K^{-1}]	β_b [K^{-1}]	K_d [GPa]	K_s [GPa]	ν [-]
Reservoir	2650	12.5	1.28×10^{-14}	920	3.1	1.0×10^{-5}	60	70	0.31
Fault	2650	43	1.28×10^{-14}	1000	3.0	1.0×10^{-5}	20	41.5	0.1

5.3 Results

5.3.1 Initial slip tendency

Initial slip tendency can be evaluated using Equations 5.1, 5.2, 5.3 and 5.4 and as a function of the dip angle γ. Analytically, the initial slip tendency is evaluated as 0.28. However, this value is obtained by assuming a homogeneous stress distribution within the reservoir, conditions that are not met within the model domain which is characterised by a fault having different mechanical properties than the hosting reservoir (Table 5.1). Initial mean effective stress distribution (negative for compression) and vertical displacement computed from the steady-state simulation are illustrated on Figure 5.3. Highest values of the mean effective stress are localised at the interface between the fault and the reservoir while lowest values are within the fault, where also the lowest values for the vertical displacement localise.

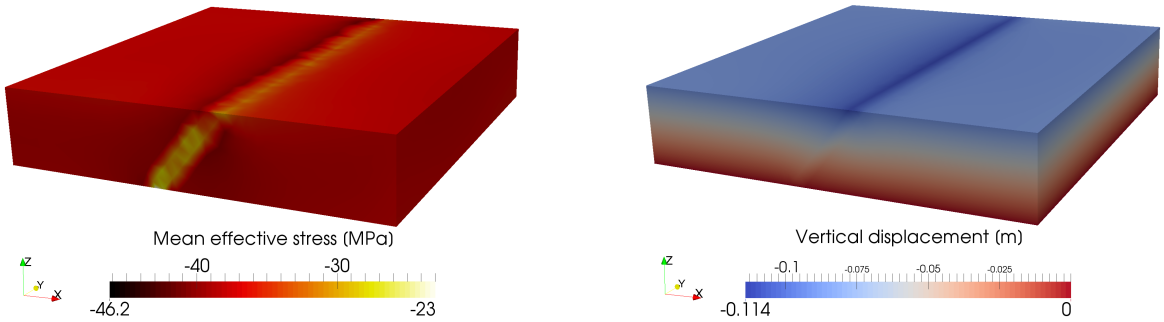

(a) (b)

Fig. 5.3 Initial mean effective stress distribution (a) and vertical displacement (b) computed from the steady-state simulation using the regional stress field. Negative effective stress relates compressive regime

Under the given stress distribution as initial condition, the slip tendency is calculated to be in average 0.3. This higher value than the analytical one comes from stress

localisation at the reservoir/fault interface. The fault acts as a heterogeneity in terms of mechanical properties. This leads to build up of stresses along the contact surface area with the reservoir thus explaining the higher slip tendency observed within this domain.

5.3.2 Dynamic evolution of slip tendency

Injection of cold fluid induce poroelastic and thermoelastic stresses within the reservoir. Unlike the temperature distribution which is governed by conduction and advection (Equation 2.25), the pressure distribution is only governed by diffusion (Eq.2.22 and 2.3). Therefore pore pressure changes are mostly localised at the injection and production fractures. No significant pore pressure changes are noticeable on the fault plane. Only thermoelastic stress changes have therefore an impact on the slip behaviour of the fault.

When the cold water front reaches the fault, normal and shear stress acting on the fault plane are enhanced by thermal effects. In this section, dynamic evolution of the slip tendency is analysed, as a function of temperatures changes modelled during geothermal operations.

Figure 5.4 shows the obtained results after 15 years of injection, including the 3-D model and the 130 °C isotherm reaching the fault (Figure 5.4a), the slip tendency T_s on the fault plane (Figure 5.4b), the temperature difference dT from the initial state (Figure 5.4c) and the slip tendency difference dT_s from the initial state (Figure 5.4d).

As seen in Figure 5.4c and Figure 5.4d, a 30 °C decrease in temperature lead to an increase of about 0.6 in slip tendency due to a thermally induced increase in shear stress and decrease in normal stress. This results in a total slip tendency reaching almost 1 at the hitting point of the cold fluid. Assuming a frictional coefficient of $\mu_s = 0.85$ (Byerlee, 1978), it follows from Equation 5.1 that under these conditions the fault is likely to be reactivated. However, this high slip value is localised and not homogeneously distributed within the entire fault plane.

It is worth noticing that the small increase of slip tendency (+0.2 in light blue) localised in the upper part of the fault is due to poroelastic effects. Indeed, a slight pore pressure increase (0.1 MPa) is predicted at this location on the fault plane.

5.3.3 Influence of the fault dip angle

Changing the dip angle of the fault influences the initial slip tendency, as well as its dynamic evolution. Under a normal faulting regime as specified in the previous section, decreasing the dip angle of the fault decreases the slip tendency ($\sigma_1 = \sigma_{zz}$).

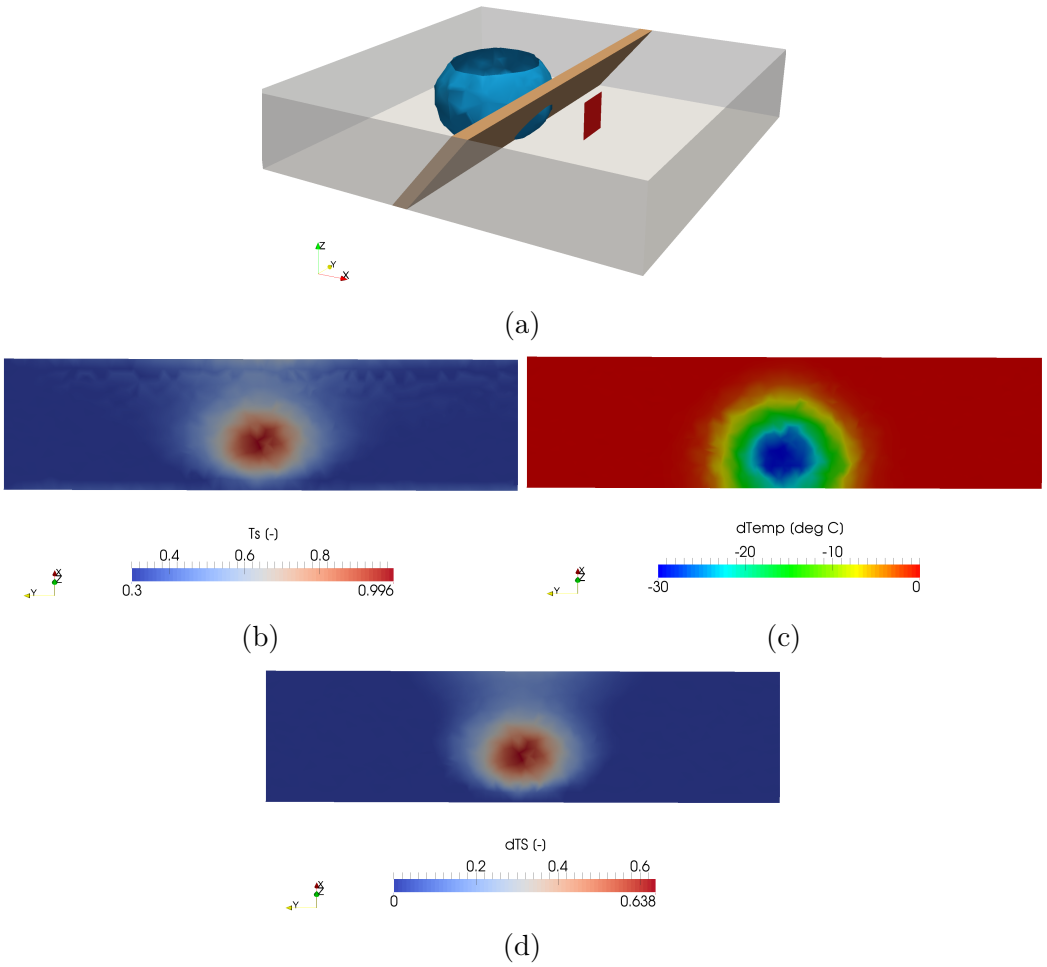

Fig. 5.4 Results after 15 years of injection. (a) The 3-D model with the 130 °C isotherm (in blue). (b) 2-D view of a cross-section on the fault place showing the slip tendency T_s distribution. (c) On the same cross-section, distribution of the temperature difference with initial conditions. (d) On the same cross-section, distribution of the slip tendency difference with initial conditions ($dT_s = T_s - T_s^i$).

To quantify these effects, two additional scenarios are investigated as shown in Figure 5.4. These two scenarios corresponds to two different values of the dip angle of the fault γ (see Figure 5.5.):

- Reference dip angle: $\gamma = \pi/4 = 45°$ (results presented on Figure 5.4).
- Low dip angle: $\gamma = \pi/8 = 22.5°$.
- High dip angle: $\gamma = 3\pi/8 = 67.5°$.

Calculated initial slip tendency is 0.2 for the low dip angle case (Figure 5.5a) and 0.4 for the high dip angle case (Figure 5.5b). After 15 years of injection, these two

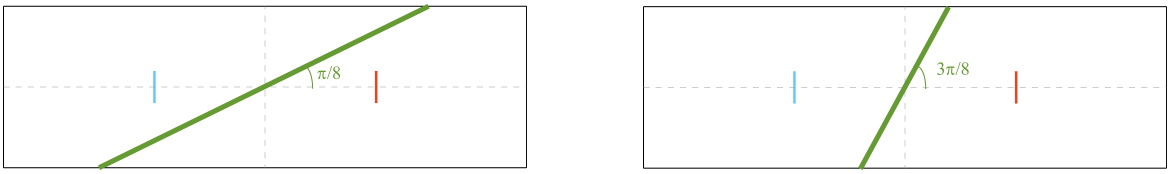

(a) Low dip angle case. (b) High dip angle case.

Fig. 5.5 Two additional scenarios in terms of dip angle of the fault. (a) Low dip angle model with $\gamma = \pi/8$. (b) High dip angle model with $\gamma = 3\pi/8$.

additional fault configurations give interesting insights on the thermoelastic response of the slip tendency. For the low dip angle case, a 60 °C decrease in temperature is observable on the fault plane with a similar distribution as for the reference case (see Figure 5.4c). However the observed 60 °C decrease in temperature leads to a +0.3 increase in slip tendency. Furthermore, for the high dip angle case, a 20 °C decrease in temperature leads to a +1 increase in slip tendency. These results are summarised in Figure 5.6. Differences in the temperature distribution for the two cases result from differences in the geometry of the model. As seen on Figure 5.5, if the dip angle is lowered, the cold water front will hit the fault at earlier stages and coldest temperatures will be observed in the lower part of the fault.

For a given in-situ stress field (here normal faulting), the dip angle of the fault has a significant influence on the increase in slip tendency resulting from thermoelastic effects (from +0.3 to +1 increase in slip tendency).

5.4 Discussion: real-case application of the Groß Schönebeck geothermal reservoir

The approach presented in this contribution has been applied on a real-case application: the geothermal research site of Groß Schönebeck (40 km north of Berlin, Germany). This site consists in a geothermal doublet (target depth of −4100 m) drilled with a faulted reservoir. Geological context of this reservoir, stimulation treatments as well as dynamic modelling of thermo-hydraulic processes are well described in the literature (Moeck et al., 2009b,a; Zimmermann and Reinicke, 2010; Blöcher et al., 2010, 2012). An approach for coupled thermo-hydro-mechanical processes similar to the one presented in Section 5.2 with transport properties evolution models has been applied to a 3-dimensional discretised model of the Groß Schönebeck reservoir (Cacace and Blöcher, 2015). 70 °C fluid is injected in the reservoir with a rate of $30\,\mathrm{m}^3 \cdot \mathrm{h}^{-1}$. The in-situ temperature within the reservoir ranges from 145 to 150 °C. The in-situ stress-field

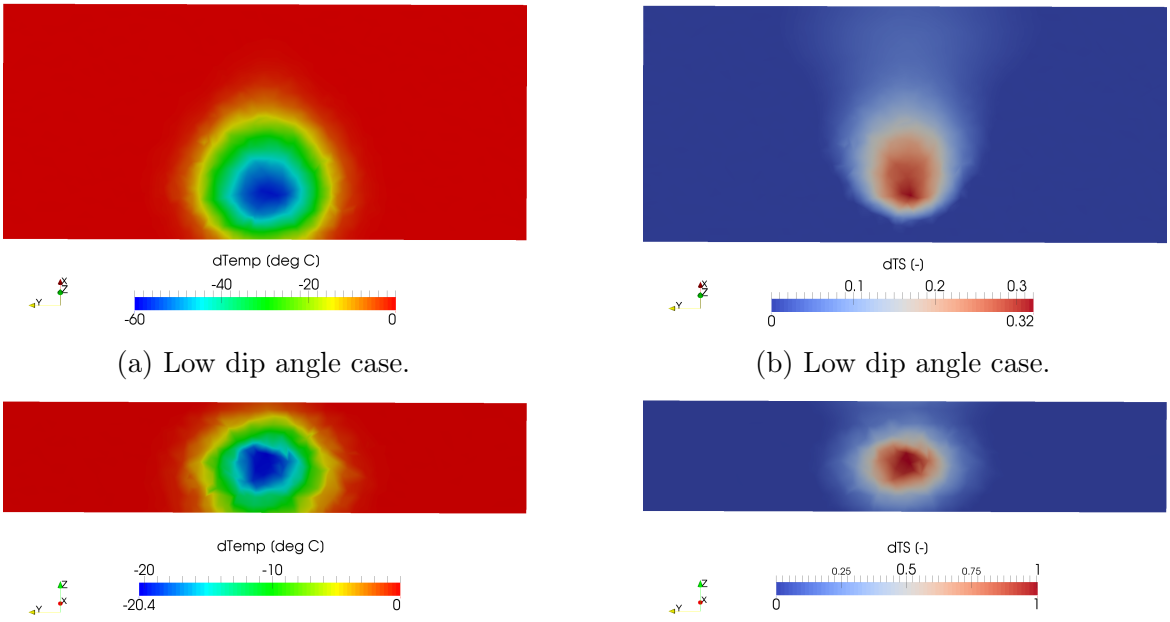

(a) Low dip angle case.

(b) Low dip angle case.

(c) High dip angle case.

(d) High dip angle case.

Fig. 5.6 Results after 15 years of injection. (a) Distribution of the temperature difference with initial conditions on the fault plane for the low dip angle case. (b) Distribution of the slip tendency difference with initial conditions (dT_s) on the fault plane for the low dip angle case. (c) Distribution of the temperature difference with initial conditions on the fault plane for the high dip angle case. (d) Distribution of the slip tendency difference with initial conditions (dT_s) on the fault plane for the high dip angle case.

is transitional regime between normal faulting and strike-slip faulting (Moeck et al., 2009b).

Figure 5.7 shows the temperature distribution (Figure 5.7a) and the slip tendency (Fig 5.7b) distribution along the major faults within the reservoir after 100 years of simulated operation time. A temperature decrease of about 70 °C leads to an increase in slip tendency of about +0.6 on two different faults. This increase in slip tendency is localised on the faults around the injection well (blue line on Figure 5.7) as well behind the production well (red line on Figure 5.7). The magnitude of slip tendency could lead to alteration of the slip behaviour of the fault and in extreme case, to reactivation of the fault (if $T_s \geq \mu_s$) and therefore to the generation of seismic events. Microseismicity activity has been recorded during water frac treatment of the production well drilled in 2007 (Kwiatek et al., 2010). These microseismic events have been related to pressure diffusion effects (rapid injection of fluid) and have shown that the faults around the well have a high reactivation potential. The present study supports the idea that these faults are initially critically stressed (in accordance with Moeck et al. (2009a))

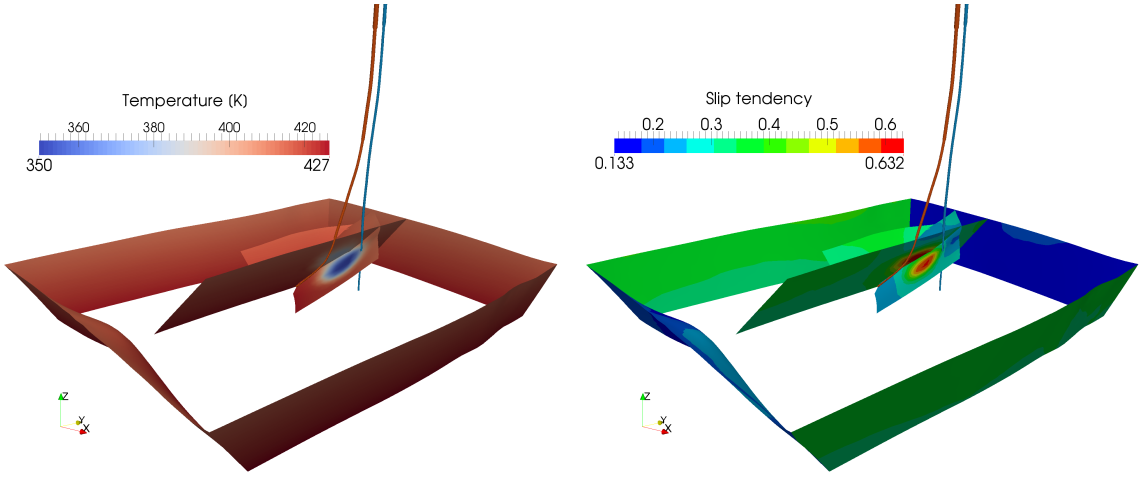

(a) (b)

Fig. 5.7 Results of fully coupled THM process modelling for the Groß Schönebeck geothermal reservoir. Here only the faults in the reservoir are shown after 100 years of injection of cold fluid (70 °C) at $30\,\mathrm{m}^3 \cdot \mathrm{h}^{-1}$. (a) Temperature distribution. (b) Slip tendency. The blue line represent the path of the injection well and the red one the path of the production well.

and that they also present high reactivation potential, here caused by thermal stress enhancement. However, whether such a dynamic relation between these processes exists and what implications it imports in terms of reservoir sustainability remains only speculative at this stage.

As reported by several studies, formulations of the theory of thermoelasticity show strong similarities to formulations adopted to describe poroelastic phenomena (Geertsma, 1957; Lord and Shulman, 1967; McTigue, 1986; Zimmerman, 2000). Where an effective stress law has been introduced in the theory of poroelasticity (Terzaghi, 1943; Carrol and Katsube, 1983) to correct the effect of pore pressure on deformation, the results presented in the present study suggest the need of an extended effective stress law correcting also for temperature changes effects, taking the form:

$$\boldsymbol{\sigma'} = \boldsymbol{\sigma} + \alpha p_f \mathbb{1} + K\beta\,(T - T_0)\,\mathbb{1}. \tag{5.5}$$

This new formulation for the effective stress tensor would also induce an increase in normal stress acting on the fault plane (Equation 5.3) which could contribute to correct the increase of slip tendency due to temperature decrease. Validation of the new formulation is part of ongoing work.

In this approach, a one way coupling for thermo-mechanical processes has been discussed, that is, the temperature distribution has an impact on the deformation (thermal strain and stress) but deformation has no influence on the temperature field. This assumption, though valid in most materials may not be considered realistic for coupled thermo-hydro-mechanical processes modelling in such applications. Indeed, in the case of faulted reservoir, processes such as shear heating can occur and influence the temperature distribution along a fault plane. This contribution therefore raises the need of a stronger coupling between thermal, hydraulic and mechanical processes taking into account all dynamic feedbacks to better describe changes in the in-situ stress field acting on faults which are of relevance for the studying of their potential reactivation during man-made activities.

5.5 Conclusion

For deep geothermal reservoirs, thermoelastic stress often exceeds poroelastic stress (by a factor of 10 for the given configuration). Changes in temperature induced by injection of cold fluid control therefore the in-situ stress field. Such phenomenon has a direct impact on slip tendency of major fault zones. In the present study, it has been shown that injection temperature and geometry of the fault (dip angle) play an important role in evaluating the fault reactivation potential. In general, slip is more likely to occur when the cold fluid front hit the fault plane. Similar conclusions have been derived for a real-case study based on the geothermal facility of Groß Schönebeck. These preliminary studies elucidate the importance of thermal effects on the mechanical stability of major fault zones during geothermal reservoir activities and raises the importance of deepening the coupling among thermo-hydro-mechanical processes affecting the reservoir.

Chapter 6

Poroelastic response of geothermal reservoirs to hydraulic stimulation treatment: theory and application to the Groß Schönebeck geothermal research facility[1]

6.1 Introduction

Understanding the hydromechanical behaviour of fluid-saturated porous rocks has gained great relevance over the last decades for a number of different applications including geothermal energy production, radioactive waste disposal or enhanced oil recovery from deep and high-pressure reservoirs. In these reservoirs, interactions between hydraulic and mechanical processes are indeed common due to the presence of deformable pores within the solid matrix. Therefore the hydromechanical state of such systems is likely to be controlled by the stiffness of the porous rocks but also by the behaviour of the fluid-filled pores. Studying the coupling among processes governing the deformation of a porous material and the dynamics of the circulating fluid (theory of consolidation or poroelasticity) has been first introduced by Terzaghi (1943) for a one-dimensional case. It was later extended to three dimensions by Biot (1956, 1973). This theory has been the subject of several studies ever since (Lockner, 2002; Mehrabian and Abousleiman, 2014; Segall and Lu, 2015; Jacquey et al., 2015b) and has now reached a level of general consortium in the community concerning its governing equations. Several critical observations associated with nonlinear pore pressure responses provided relevance of hydromechanical coupling both at the laboratory scale (with the so-called Mandel-Cryer effect (Mandel, 1953; Cryer, 1963)) and at the field scale ((Verruijt, 2010; Slack et al., 2013; Vinci et al., 2014), including the Noordbergum effect (Rodrigues, 1983; Kim and Parizek, 1997)).

In this study, we aim at understanding and quantifying the effects of poroelastic coupling as occurring during cyclic hydraulic stimulation treatments. Such stimulation treatments are usually conducted to gain access to low permeability and low porosity geological formations by inducing artificial fluid pathways, i.e. hydraulic fractures. During these treatments, high pressure fluid is injected into the reservoir target formation thus leading to the generation of new fractures or to an enhancement of

[1]This chapter is under review in the journal *Journal of Geophyscial Research: Solid Earth.*

existing ones. Fluid injection leads to pore pressure increase, therefore decreasing the effective principal stress, which finally might lead to a tensile failure of the rock (Yew, 1997; Guéguen and Boutéca, 2004). By alternating high and low flow rates it is possible to influence the aperture and length grow of the fracture (Zimmermann et al., 2010). Other concepts of stimulation treatments have been developed to enhance the permeability or a reservoir, including thermally induced fracturing and chemical/acid stimulation (Ecomides and Nolte, 2000). Several studies in the literature improved the current understanding of the fracturing process both from a theoretical but also from a more applied point of view (Warren and Smith, 1985; Wu et al., 2007; Moore and Glaser, 2007). However, these studies often focused on processes responsible for fractures development and/or their sustainability while they generally neglected the impacts of such stimulations on the hydromechanical state of the surrounding reservoir rocks.

The opening of a hydraulic fracture likely induces compression of the surrounding reservoir rocks preferably in the direction orthogonal to the fracture plane. Since high flow rates are injected into the reservoir, rates of induced deformation can build up and propagate at some distances throughout the porous matrix. This in terms entails, that in such situations the pore pressure response to the stimulation observed in the surrounding rocks is not only controlled by a diffusive process but it likely involves a poroelastic component as well. In this study, we therefore perform a number of 3D numerical tests in order to demonstrate and quantify how such poroelastic processes built up during hydraulic stimulation treatments affect the hydromechanical state of the surrounding rocks.

This contribution is organised as follow. In a first part, the governing equations for fully-coupled hydromechanical behaviour of porous rocks are introduced. A simplified generic model is then presented to highlight induced pore pressure variations following poroelastic deformation within a porous medium. In a second part, field measurements from a cyclic hydraulic stimulation treatment conducted in August 2007 at the Groß Schönebeck geothermal platform are used to illustrate the impacts of this poroelastic effect at the reservoir scale.

6.2 Model implementation and benchmark test case

6.2.1 Governing equations

Modelling of coupled hydromechanical processes requires solving for the governing equations for fluid-flow and deformation of the porous medium. These equations are

derived from balance equations of fluid and solid mass and momentum. In this section, the governing equations for hydromechanical modelling are presented based on the Biot's theory of consolidation. From the conservation of mass, fluid flow within a porous medium is described by (isothermal version of Equation 2.22 without inelastic deformation).

$$\frac{1}{M_B}\frac{\partial p_f}{\partial t} + \alpha\frac{\partial \boldsymbol{\epsilon}_{kk}}{\partial t} + \nabla \cdot \boldsymbol{q}_D = Q_f$$

where p_f is the pore pressure, α the Biot's coefficient, $\boldsymbol{\epsilon}_{kk}$ the volumetric strain, Q_f a sink or source term and M_B is the Biot's modulus (reciprocal of the storage coefficient) defined as:

$$\frac{1}{M_B} = \frac{\phi}{K_f} + \frac{(\alpha - \phi)}{K_s}$$

where K_f is the bulk modulus of the fluid and K_s the bulk modulus of the solid grains. The specific discharge $\boldsymbol{q}_D$ can be expressed from the conservation of fluid momentum (within the limits of Darcy's approximation) following Equation 2.3.

Deformation of a fully saturated porous medium is described by the momentum balance equation in terms of effective stress following Equation 2.10

The effective stress tensor is here defined after Carrol and Katsube (1983) as a function of the Cauchy's stress tensor $\boldsymbol{\sigma}$, the pore pressure p_f and the Biot's coefficient (Equation 3.5).

The primary variable solved for deformation of a porous medium is the displacement vector $\boldsymbol{u}$ which is linked to the effective stress tensor via the constitutive stress-strain laws defined as (isothermal case of Equation 2.12). In this study, only linear elasticity is considered to describe the deformation of the reservoir rocks. Therefore, the elastic material tensor can be described via the generalised Hooke's law.

6.2.2 Implementation

The governing equations for deformation and fluid flow have been implemented in a fully-coupled finite-element-method based framework called MOOSE (Gaston et al., 2009). The MOOSE framework provides a powerful and flexible platform to solve multiphysics problems implicitly and in a tightly coupled manner on unstructured meshes. This framework is based on two main libraries, the finite element library libMesh (Kirk et al., 2006) and the solver library PETSc (Balay et al., 2016). Based on these two libraries, the MOOSE framework allows the users to develop models with

high flexibility and to deal with realistic scenarios, including complex geometries and non-linear physics by maintaining computational efficiency and code portability.

The weak forms of the governing equations presented in the previous section were implemented in the in-house developed branch of the MOOSE framework. These equations are therefore solved in a tightly coupled manner, which means the fully coupled system of equations is solved without external iterations among the different processes.

6.2.3 Synthetic model setup

This section presents a synthetic problem formulation characterised by a relative simplistic geometry and loading setting. It aims at illustrating the poroelastic response of a porous medium subjected to a cyclic hydraulic stimulation treatment. The domain considered is a three-dimensional rectangular beam consisting of a fully-saturated porous medium of length $L = 10\,\mathrm{m}$ extending along the positive x-axis. The domain is discretised in 100 hexahedral elements. Gravity terms are neglected in this configuration. Furthermore, solid grains and fluid are considered incompressible (which leads to a Biot's coefficient of $\alpha = 1$). All synthetic physical properties adopted for the simulation are listed in Table 6.1.

Table 6.1 Synthetic material properties for the simplified porous material.

Property	Notation	Unit	Value
Solid grains compressibility	$\frac{1}{K_s}$	GPa^{-1}	0.0
Fluid compressibility	$\frac{1}{K_f}$	GPa^{-1}	0.0
Young's modulus	E	GPa	7.2
Poisson's ratio	ν	-	0.2
Permeability	$\boldsymbol{k}$	m^2	1.5×10^{-15}
Fluid viscosity	μ_f	$\mathrm{Pa} \cdot \mathrm{s}$	1.0×10^{-3}

On the face $x = 0$, constant pore pressure (drained conditions $p = p_0$) and displacement in the form of a dependent function ($u_x(x = 0, t) = f(t)$) representing the opening of the hydraulic fracture due to a synthetic cyclic stimulation treatment are applied. All other faces of the domain are impermeable and sliding faces. For the sake of simplicity, injection is not taken into account for this problem formulation. Instead it has been chosen to use a sinusoidal function to represent the idealised cyclic behaviour of the fracture opening, as:

$$u_x(x = 0, t) = f(t) = a(1 - \cos(\omega t)) \tag{6.1}$$

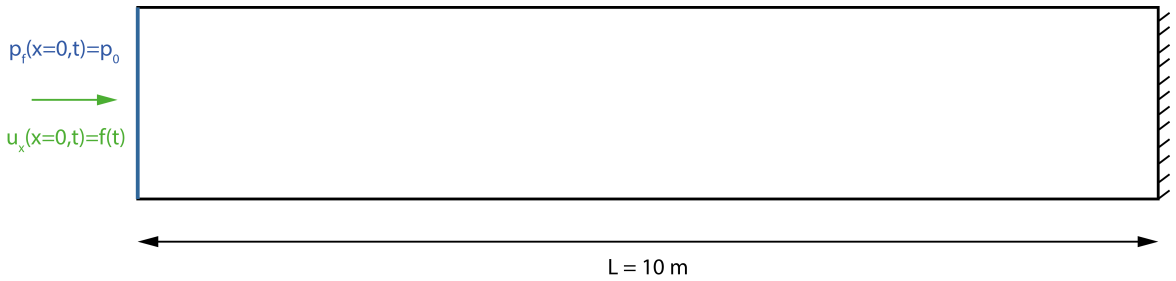

Fig. 6.1 Model geometry and boundary conditions for the simplified problem formulation. All faces except the left one are sliding faces. Horizontal displacement is applied on the left face in the form of a time dependent function. Across the same boundary face, pore pressure is kept constant ($p_f = p_0$).

where $a = 5.0\,\text{mm}$ and $\omega = \frac{\pi}{10}$. Initial pore pressure is denoted as $p_0 = 1\,\text{MPa}$ and no initial displacements is considered. The configuration of this simplified problem is illustrated in Figure 6.1. The three-dimensional problem configuration can be simplified in a one-dimensional problem, for which it is possible to obtain an analytical solution as detailed in Appendix B.1.

An overview on the results for this problem configuration is presented in Figure 6.2. Figure 6.2-a illustrates the evolution of the displacement u_x, pore pressure change Δp_f and effective stress σ_{xx} at the point $x = \frac{L}{2} = 5$ m located in the middle of the beam. It can be clearly seen that a maximum in displacement corresponds to a minimum in effective stress, as known from the classical elasticity theory. Pore pressure evolution is affected by the deformation history of the porous medium thus leading to a time dependent evolution of the pore pressure. Furthermore, it can also be observed that the maxima in the pore pressure response lag in time behind with respect to the maxima of the displacement field. Maximum values of pore pressure changes are indeed reached before the maxima in displacement: a maximum or minimum of effective stress corresponds to a negligible (approximatively 0 MPa) pore pressure change. The observed time gap between the changes in pore pressure and displacement can be directly related to the poroelastic coupling between fluid flow and deformation. Figure 6.2-b illustrates the distributions of displacement, pore pressure change and effective stress along the x-axis at the time when a maximum value of pore pressure change is obtained ($t = 46\,\text{s}$). At this specific time, it can again be seen that the value of displacement applied on the left boundary face does not approach its maximum value (10 mm) whereas the induced pore pressure change reaches its maximum. Furthermore, the distribution of displacement and effective stress show clear non linear behaviours which illustrates again the full coupling between fluid flow and deformation. The

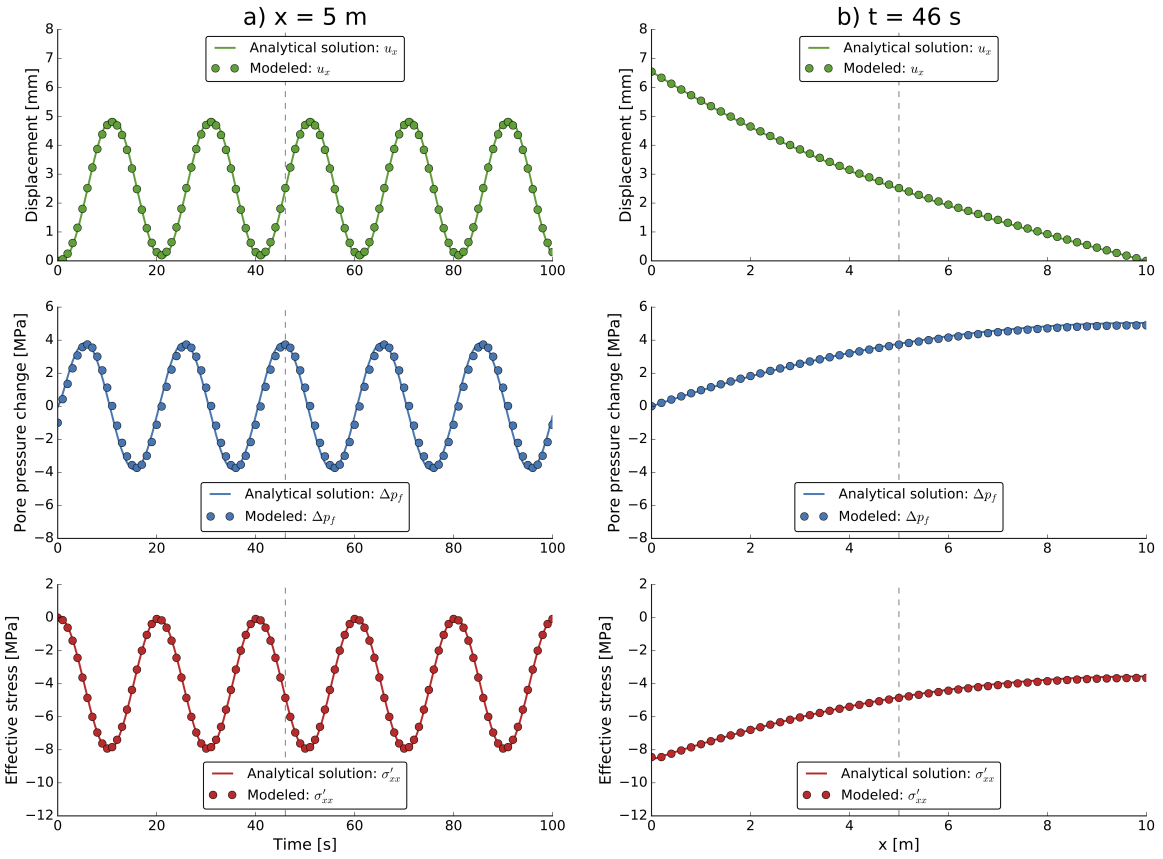

Fig. 6.2 Overview on the results of the synthetic model configuration. On the left, a) illustrates evolutions of the horizontal displacement, pore pressure change and effective stress at the middle of the beam. On the right, b) illustrates the distributions of horizontal displacement, pore pressure change and effective stress at the time $t = 46\,\mathrm{s}$ which corresponds to a maximum in pore pressure change.

effective stress distribution is indeed influenced by the pore pressure distribution, which results in a different mechanical response than by considering a classic elastic model.

The results briefly discussed above, despite the relative simplicity of the formulation nicely illustrate the importance of the hydromechanical coupling in the context of cyclic deformation of porous materials. Considering such coupling leads to the onset of a nonlinear poroelastic effect in which pore pressure build-up attains a maximum predating the applied maximum of displacement. In the next section, the relevance of this poroelastic effect for geothermal reservoir applications is quantified by means of field measurements of a cyclic hydraulic stimulation treatment which took place at the Groß Schönebeck geothermal research facility (Germany) in August 2007.

6.3 Field application: cyclic hydraulic stimulation at the Groß Schönebeck geothermal facility

6.3.1 Geology of the Groß Schönebeck area

The geothermal research site of Groß Schönebeck consists of a well doublet targeting a geothermal reservoir at depth between 3815 and 4247 m below sea level. This reservoir is located within the Lower Permian sedimentary sequence of the North East German Basin (NEGB) and comprises sandstones (Upper Rotliegend) and volcanic andesitic rocks (Lower Rotliegend) (Zimmermann et al., 2010). The sandstone sedimentary sequence can be subdivided into five different formations depending on their lithological properties after Blöcher et al. (2010): Hannover formation, Elbe alternating sequence, Elbe base sandstone II, Elbe base sandstone I and Havel formation. The target formations for geothermal energy production are the permeable sandstones (Elbe sandstone I and II) based on their promising hydraulic properties (local permeability up to 100 mD after Trautwein and Huenges (2005) and porosity up to 10 % after Huenges and Hurter (2002)). The underlying volcanic sequence has also been targeted for its relatively higher temperature conditions. Within this formation permeability is mainly associated with secondary fractures. In the reservoir section, two sets of natural faults have been identified based on interpretation of 2D seismic profiles. They consist of minor NE-SW trending faults considered to be critically stressed and therefore expected to act as hydraulically conductive structures and major NW-SE less critically stressed therefore considered to act as drains (Moeck et al., 2009b; Kwiatek et al., 2010).

The in-situ horizontal maximum stress (σ_H) is oriented NNE-SSW in the Rotliegend section of the Groß Schönebeck reservoir based on borehole breakout experiments (Holl et al., 2005). This direction correlates with the World Stress Map database (Heidbach et al., 2016). Hydraulic stimulations at the two wells (Legarth et al., 2005; Reinicke et al., 2005; Zimmermann and Reinicke, 2010) and a leak-off test (Moeck et al., 2009a) provided some estimates of the minimum horizontal stress in the sandstones ($\sigma_h \sim 55\,\mathrm{MPa}$) and in the volcanics ($\sigma_h \sim 72\,\mathrm{MPa}$) respectively. Furthermore, an estimate of the maximum horizontal stress was derived from borehole breakouts in the sandstones ($\sigma_H \sim 95\,\mathrm{MPa}$) (Moeck and Backers, 2006). The stress magnitudes in the reservoir at 4100 m below sea level (sandstones) were therefore determined to be $\sigma_v = 100$ MPa, $\sigma_H = 95$ MPa and $\sigma_h = 55$ MPa. This stress field within the reservoir is equivalent to a normal faulting regime with a trend towards a transitional regime between normal faulting and strike-slip faulting.

An abandoned gas exploration well (E GrSk 3/90) was reopened in 2001 and deepened to 4294 m below sea level. To complete the doublet system serving as an in-situ geothermal research laboratory, a deviated well (Gt GrSk 4/05) was drilled in 2006 reaching as deep as the volcanic rocks. The well path of the Gt GrSk 4/05 well is parallel to the minimum horizontal stress direction in order to make use of the porous reservoir (enhanced by fractures in the near wellbore area).

To increase the overall hydraulic conductivity of the doublet system, several stimulation treatments have been carried out (Legarth et al., 2005; Zimmermann and Reinicke, 2010; Zimmermann et al., 2010; Blöcher et al., 2016):

(a) Two hydraulic proppant fracture stimulation treatments in the well E GrSk 3/90 in 2002.

(b) Two waterfrac stimulation treatments in the whole open hole section of the well E GrSk 3/90 in 2003.

(c) One waterfrac stimulation treatment in the volcanic section of the well Gt GrSk 4/05 (bottom of the well) in August 2007.

(d) Two gel-proppant stimulation treatments in the sandstone section of the well Gt GrSk 4/05 in August 2007.

For some of these stimulation treatments, proppant was used to maintain the fractures permeability. This study focuses on the cyclic waterfrac stimulation treatment in the volcanic section of the well Gt GrSk 4/05 (c). This stimulation treatment, the first in the well Gt GrSk 4/05 was carried out between the 9^{th} and the 14^{th} of August 2007. The well was entirely cased except for the bottom 20 m to stimulate the volcanic rock section. Consecutive injection cycles at flow rates ranging from 25 up to $150\,\text{L}\cdot\text{s}^{-1}$ were applied. Low concentrations of quartz-rich sand were also injected at high flow rates in order to sustain the fracture permeability by maintaining its opening and to support the self-propping effect (Durham and Bonner, 1994). In total, $13\,170\,\text{m}^3$ of fluids and 24.4 t of quartz-rich sand were injected in the volcanic rocks during this stimulation treatment. The well head pressure reached 586 bar at the maximum flow rate. Figure 6.3 shows the evolution of the flow rate and the observed change in bottom hole pressure during the whole cyclic waterfrac treatment.

In a previous study, a three-dimensional simulator (FRACPRO) has been used to model the opening behaviour of the induced hydraulic fracture during the waterfrac treatment in well Gt GrSk 4/05 (Zimmermann et al., 2010). Assuming a tensile fracture (mode I failure), which propagates perpendicular to the minimum principal stress, the

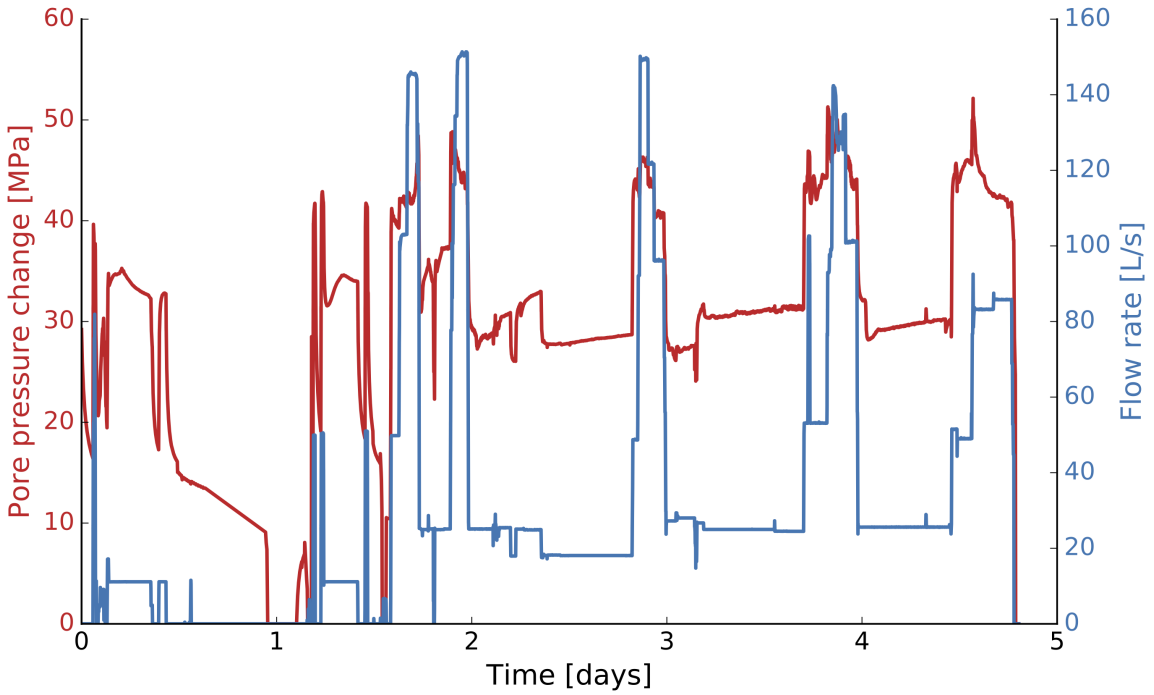

Fig. 6.3 Injection schedule of the cyclic waterfrac treatment in the volcanic rock section of the well Gt GrSk 4/05. The red curve indicates the change in bottom hole pressure in MPa and the blue one is the flow rate in $L \cdot s^{-1}$ after Zimmermann et al. (2010).

average width of the fracture has been considered to reach a maximum of 20 mm during the whole stimulation treatment. The induced fracture at the end of the stimulation was modelled to have a total height of 90 m, a length of 180 m and a maximum width of 19.5 mm.

Figure 6.4 shows the average width of the hydraulic fracture computed using the FRACPRO simulator (red curve) as a function of time and in relation to the applied injection flow rate (blue curve in Figure 6.3) after Zimmermann et al. (2010). By inspecting Figure 6.4, local maxima in the average width of the fracture coincide with peaks in injection rates. It is worth noticing that the total height of the fracture is limited by the geometry of the volcanic rock sequence, that is it does not propagate into the overlying permeable sandstones due to fluid pressure leak-off processes at the tip of the fracture. In a similar way, downward propagation of the hydraulic fracture was also limited by the presence of an underlying sequence of folded Carboniferous sedimentary rocks which would have required higher pressure than those applied.

As reported by Zimmermann et al. (2010), pressure increase was monitored during the stimulation treatment of Gt GrSk 4/05 in the adjacent well E GrSk 3/90. After 5 days of stimulation, the pore pressure in the monitoring well E GRSk 3/90 increased

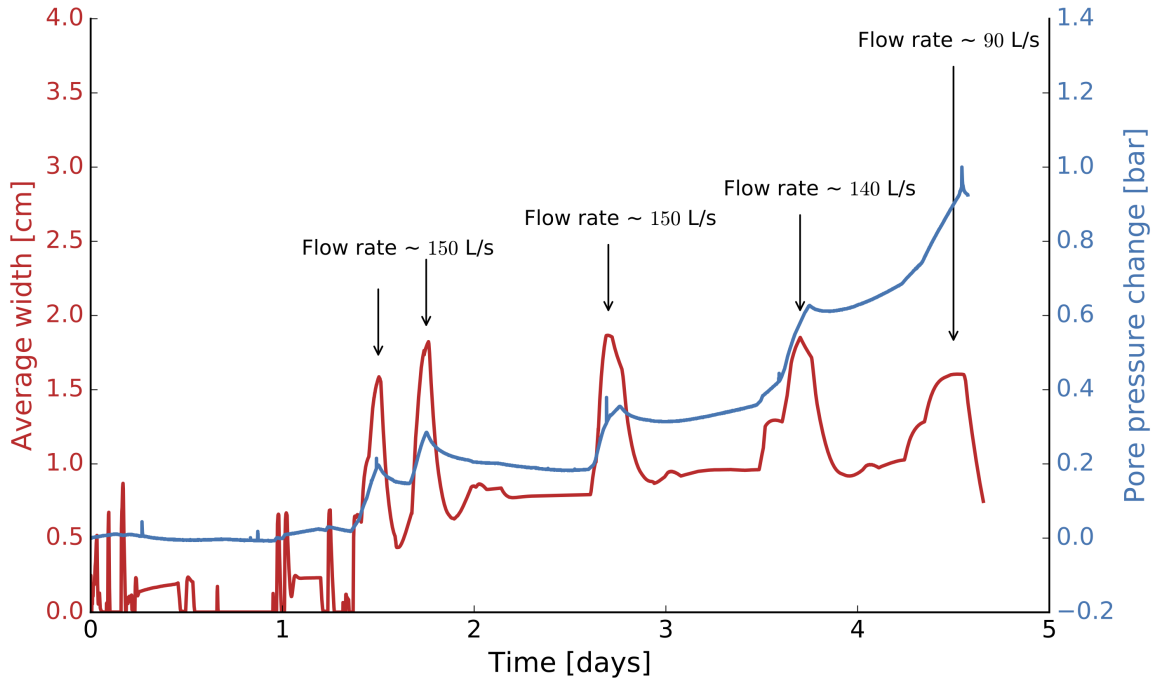

Fig. 6.4 Modelled average width of the hydraulic fracture during waterfrac treatment in well Gt GrSk 4/05. The red curve, showing the modelled average width of the induced fracture is superposed on the observed increase in pore pressure in the well E GrSk 3/90 (blue curve) after Zimmermann et al. (2010). For each local maximum in the average fracture width, the corresponding injection flow rate is indicated.

up to 1 bar. In addition to a general diffusion-controlled pore pressure increase, field measurement also highlight unexpected pore pressure variations as depicted in Figure 6.4. After the first massive injection cycle (around one and a half day after the beginning of the stimulation treatment), the pore pressure in the monitoring well E GrSk 3/90 started to increase and showed local maxima corresponding to the cyclic injection schedule. Considering the distance at reservoir depth between the two wells (475 m), such a pore pressure response propagated almost instantaneously. Therefore, pore pressure diffusion could not be considered responsible for these observations. Several hypothesis have been put forward by Zimmermann et al. (2011) in order to provide a plausible explanation to the field measurements, considering the increase in pore pressure to be possibly related to the existence of a conductive fault zone extending in the vicinity of the two wells. Fault zones can indeed act as fluid pathways and therefore accelerate pore pressure diffusion. Based on a sensitivity analysis on the fault permeability using measurements of inflow inside the well Gt GrSk 4/05, a more recent study by Blöcher et al. (2015) showed that such a fault do not act as flow

pathway. We therefore here hypothesise that these observations could be explained by considering the hydromechanical coupling of the reservoir rocks.

6.3.2 Model description

In order to carry out the numerical study, a 3-dimensional finite-element-method model has been generated consistent with respect to the reservoir units as derived from an existing 3-dimensional geological model (Moeck et al., 2009b). It comprises six different geological formations (five for the Upper Rotliegend sandstones and siltstones and one for the Lower Rotliegend volcanic rocks). The model has been discretised by using the in-house developed software MeshIt (Cacace and Blöcher, 2015). As illustrated in Figure 6.5, the coordinate axes have been chosen to match the direction of the principal stresses. This allows to remove the shear components for the background stress field in agreement with the assumption of tensile (mode I) opening of the fracture. The model extends by 1.6 km in the x direction (minimum horizontal stress direction) and by 2.3 km in the y direction (maximum horizontal stress direction). As indicated on the side view of Figure 6.5, the hydraulic fracture induced by the stimulation at the well Gt GrSk 4/05 is located on one border of the model, which is used to apply boundary conditions later described. The monitoring well E GrSk 3/90 is located within the model.

Hydraulic properties of the geological formations are based on published works (Legarth et al., 2005; Zimmermann et al., 2009; Blöcher et al., 2010). The mechanical properties were derived from ultrasonic and density logs (Zimmermann et al., 2010). Anisotropic permeability has been observed in core samples of the Groß Schönebeck reservoir with a ratio between horizontal and vertical permeability of $k_z/k_{xy} = 0.25$ as reported by Trautwein and Huenges (2005) and Blöcher et al. (2010). All hydromechanical properties are summarised in table 6.2.

The natural state of the reservoir was obtained by solving steady-state conditions with relevant boundary conditions for pore pressure distribution and in-situ stress field. Dirichlet hydraulic boundary conditions are assigned across the reservoir boundary faces to obtain a hydrostatic pore pressure distribution. Neumann and Dirichlet boundary conditions in terms of deformation are used together for obtaining the in-situ stress field within the reservoir formations. The results obtained for steady-state conditions are then used as initial conditions for the transient evolution of the reservoir during hydraulic stimulation.

For the transient stimulation, additional boundary conditions adopted represent the injected flow rate and the opening of the hydraulic fracture as previously described (see

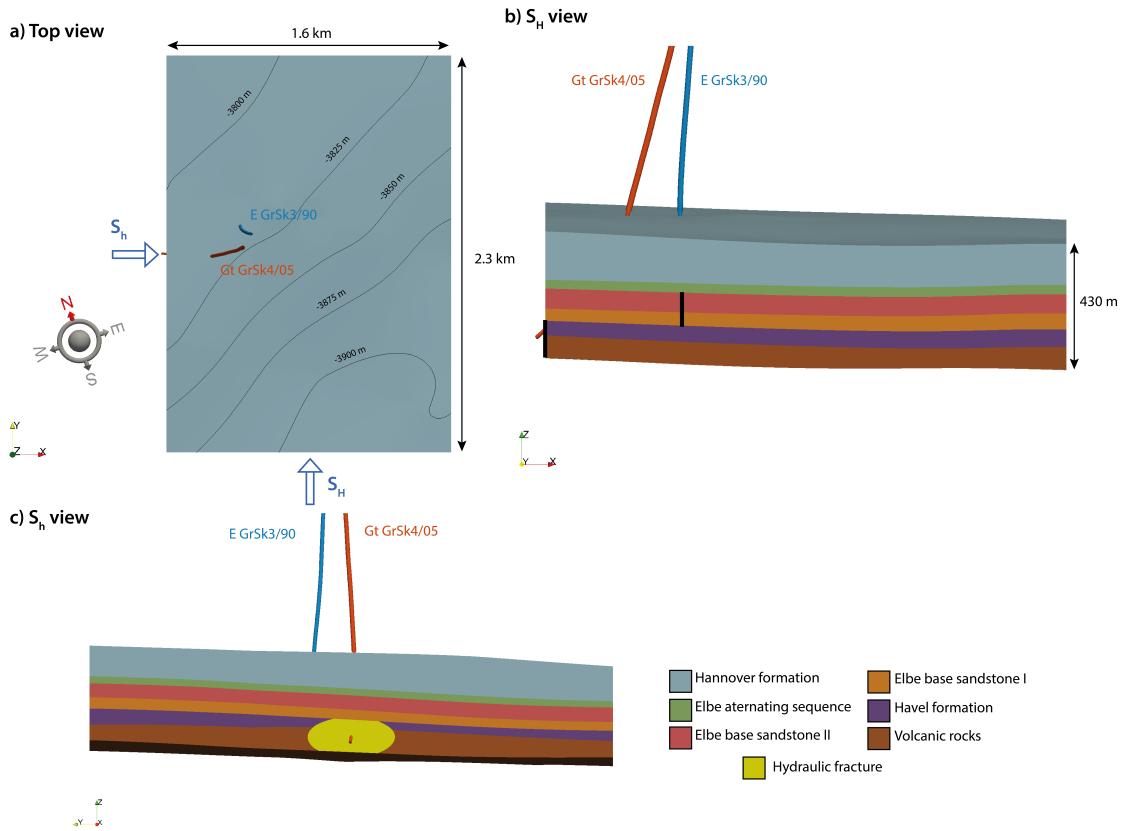

Fig. 6.5 Geometry of the Groß Schönebeck reservoir model. The coordinate axes have been chosen to match the in-situ stress orientation. a) Top view of the domain with stress field orientation. b) Side view of the domain with the wells. c) Side view of the domain with the final geometry of the hydraulic fracture in yellow after stimulation.

Table 6.2 Physical properties and thicknesses of the reservoir formations (porosity ϕ, horizontal and vertical permeability k_xy and k_z, storage coefficient $\frac{1}{M_B}$, Biot's coefficient α, Young's modulus E and Poisson's ratio ν).

Unit	Avg. thickness [m]	ϕ [%]	k_{xy} [m^2]	k_z [m^2]	$\frac{1}{M_B}$ [Pa^{-1}]	α [-]	E [GPa]	ν [-]
1- Hannover formation	159	1	4.9×10^{-17}	1.225×10^{-17}	1.00×10^{-11}	0.6	55	0.18
2- Elbe alternating sequence	30	3	3.2×10^{-16}	8.0×10^{-17}	1.42×10^{-11}	0.6	55	0.18
3- Elbe base sandstone II	55	8	6.4×10^{-16}	1.6×10^{-16}	2.47×10^{-11}	0.6	55	0.18
4- Elbe base sandstone I	52	15	1.3×10^{-15}	3.25×10^{-16}	3.93×10^{-11}	0.6	55	0.18
5- Havel formation	36	0.1	9.9×10^{-17}	2.475×10^{-17}	8.18×10^{-12}	0.6	55	0.18
6- Volcanic rocks	100	0.5	9.9×10^{-17}	2.475×10^{-17}	9.02×10^{-12}	0.6	55	0.2

Figure 6.3 and 6.4). The opening of the hydraulic fracture is therefore not modelled here but rather imposed. Furthermore, the values for the fluid injection boundary condition

are based on the field measurements illustrated in Figure 6.3. Figure 6.5-c shows the geometry of the final hydraulic fracture used to apply the boundary conditions for fluid injection and fracture opening. Time is discretised in time steps of the size of a minute, resulting in approximatively 7200 time steps to cover the whole five days of the injection period.

6.3.3 Modelled versus monitored increase in pore pressure in the well E GrSk 3/90

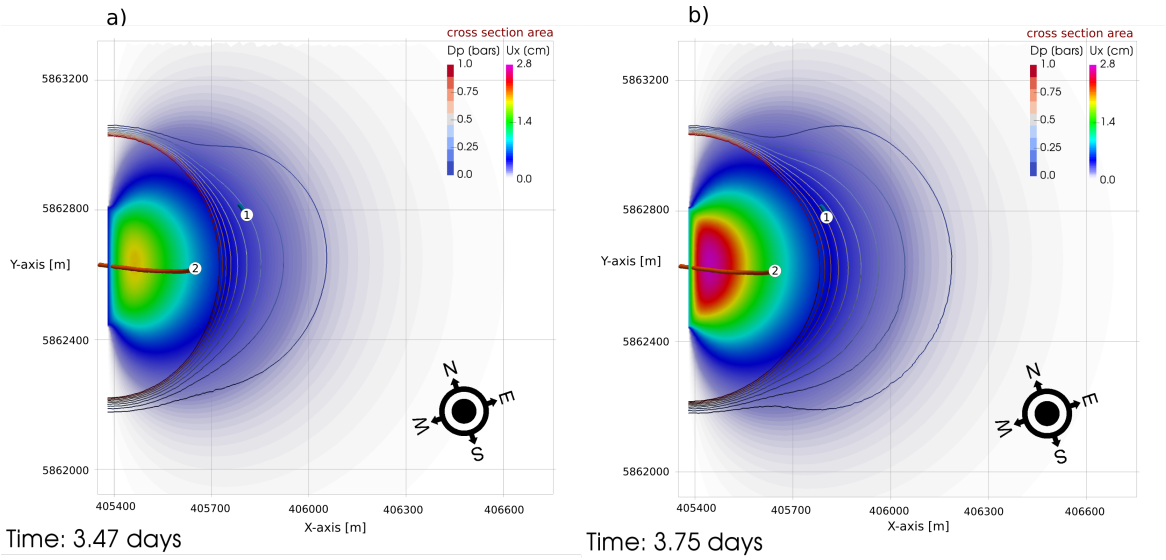

Fig. 6.6 Horizontal cross sections of the three-dimensional model at 4200 m depth within the volcanic rocks section. Simulated isolines of the pore pressure changes as well as the horizontal displacement distribution are shown after approximatively 3.47 days of stimulation just before a peak of injected flow rate (a) and after approximatively 3.75 days of stimulation just after a peak of injected flow rate (b). These times at which the snapshots were taken are indicated in Figure 6.8.

Figures 6.6 and 6.7 represent an overview on the three-dimensional results obtained during the modelled transient evolution of the reservoir 3.47 and 3.75 days after the beginning of the hydraulic stimulation schedule. Both the cross section area representations (Figure 6.6) and the overall view (Figure 6.7) show the isosurfaces of the pore pressure changes up to 1 bar and the horizontal displacement (orthogonal to the fracture plane) distribution within the volcanic and sandstone sections. These snapshots, taken soon before and after a peak of injected flow rate (see Figure 6.8) illustrate how fluid pressure and solid rock deformation are coupled. A 1 bar pore pressure change has propagated within the reservoir formations approximatively 400 m around the hydraulic

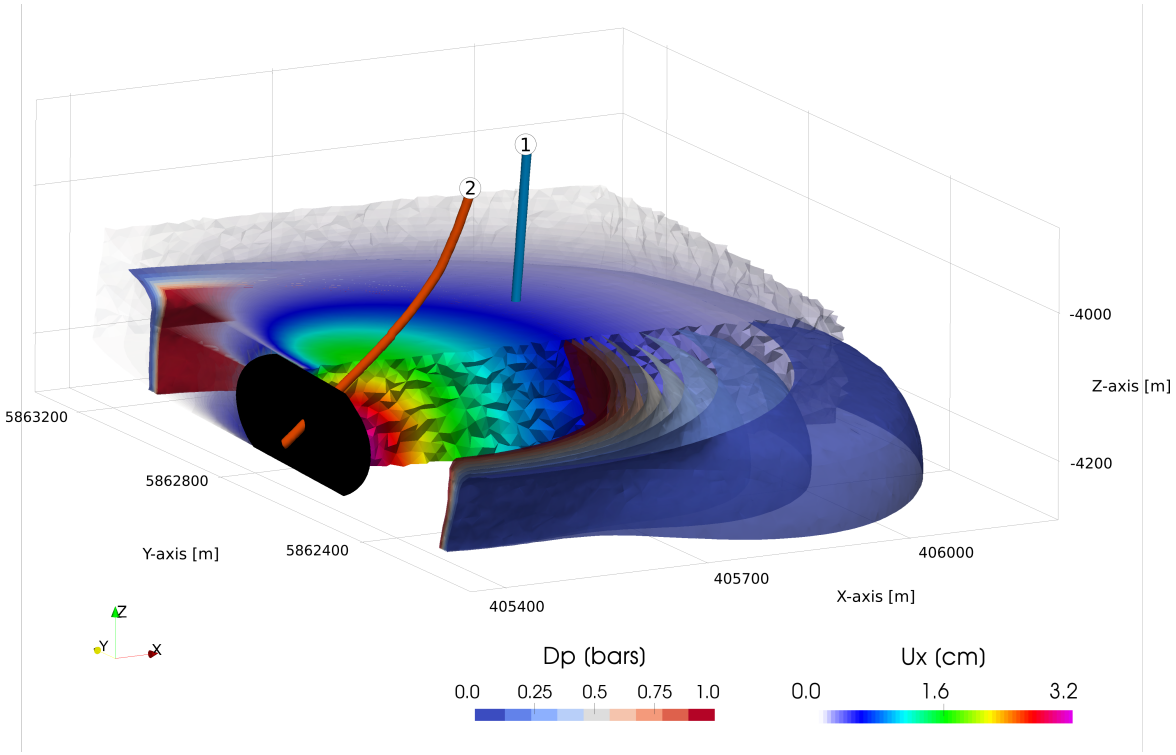

Fig. 6.7 Overview on the results of the hydromechanical simulation after approximatively 3.75 days of stimulation. Simulated isosurfaces of the pore pressure changes as well as the horizontal displacement are shown in the reservoir section.

fracture at reservoir depth. Highest values of horizontal displacement are not found on the plane of the fracture but in its vicinity. This effect illustrates that deformation history and pore pressure distribution impact the deformation distribution by means of the hydromechanical coupling.

Figure 6.8 shows the pore pressure response at the monitoring well E GrSk 3/90 extracted from the three-dimensional model (in red) as compared to the field measurements (in blue). In general, a good agreement is found between model results and field data both with respect to the short and long term behaviours. A long term increase of pore pressure resulting from pore pressure diffusion is observed. The local peaks of increase in pore pressure are also seen in the modelling results. Small deviations are found in terms of magnitudes of local maxima as well as for the evolution of the pore pressure changes following each peak. The modelled maxima usually underestimate the field measurements data. Furthermore, the evolution of the pore pressure changes following a local maximum differs from the observed data. The modelled results show some undershooting behaviour (fast decrease followed by a small increase) while the field measurements show a slow and continuous decrease of pore pressure changes after

a local maximum. The existence of local pore pressure maxima arises indeed in both cases due to the applied cyclic deformation in terms of displacement representing the opening of the hydraulic fracture.

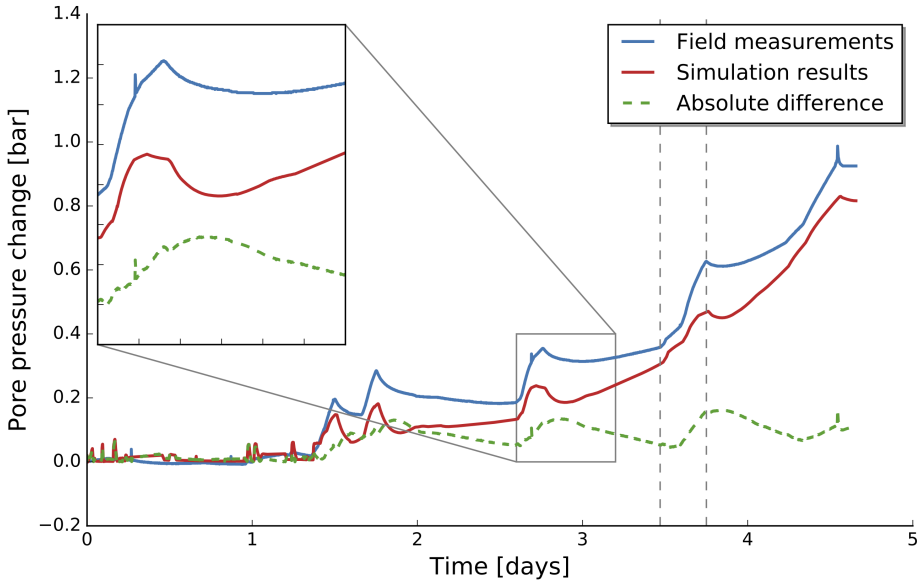

Fig. 6.8 Measured (blue curve) and modelled (red curve) pore pressure response in the well Gt GrSk 3/90 during the hydraulic stimulation of the well Gt GrSk 4/05. The green curve represents the absolute difference between observed and modelled pore pressure changes. The times at which the snapshots in Figure 6.6 were taken are indicated by two dashed lines.

These results therefore strongly indicate that the general increase of the pore pressure in the monitoring well E GrSk 3/90 might be considered as a result of pore pressure diffusion due to the injected flow rate in the stimulated well Gt GrSk 4/05, and that peaks in the pore pressure changes can be explained only by a poroelastic response of the reservoir due to the stimulation. The cyclic opening of the hydraulic fracture during the stimulation induces a rapid compression within the reservoir porous units. These changes in volumetric strain are followed by an almost instantaneous pressure build-up according to the second term of Equation 6.1. This effect, resulting from the three-dimensional Biot's consolidation theory is in full agreement with the results presented for the synthetic model configuration presented in Section 6.2.

6.4 Discussion

We have investigated and quantified the effects on the hydromechanical state of a porous reservoir due to poroelastic effects as occurring during cyclic hydraulic

stimulation treatment. Such effects lead to a rather nonintuitive pore pressure evolution characterised by an instantaneous response arising from a cyclic deformation. By means of a synthetic model configuration, the impacts and characteristics of this pore pressure response have been explained in some details. This example, due to its simplistic nature was intended as a benchmark to illustrate the direct impacts of tight hydromechanical coupling. In a second stage, the approach has been applied to a field application. Despite an overall agreement between modelling results and observations, some disparities have been found.

Figure 6.8 shows the evolution of the absolute difference between observed and modelled pore pressure changes during the stimulation treatment. The values of this difference are in general low (less than 0.15 bar difference). In addition, the evolution of the difference values does not increase in the long-term therefore indicating that the long-term diffusive behaviour has been well taken into account by the modelling results. However, modelled magnitudes of the local peaks are usually smaller than those observed. The evolution of the overpressure after each maximum induced by poroelastic effect is not perfectly modelled in the simulation results on Figure 6.6. Where a rapid decrease in the modelling results is observed with undershooting behaviour, the field measurements present a more diffuse evolution after high injection. The reason behind these disparities seems to be the behaviour of the fracture closing when flow rate is shut down at the end of every high injection cycle. The same undershooting behaviour is indeed recognisable in the modelled fracture width presented on Figure 6.4. The undershooting behaviour observed in Figure 6.8 is therefore likely to arise from the similar undershooting behaviour in the input data used to model the hydraulic fracture opening (red curve in Figure 6.4). Our understanding of the fracture closing may therefore not be complete. From the field observations of overpressure, it can be expected that the closing of the hydraulic fracture is slower than the one modelled by the 3D fracture simulator (FRACPRO).

The disparities between field observations and modelled results could also be considered as indicating the existence of potential additional physical processes occurring in the reservoir which might have an impact on its hydromechanical state. In this study, only the poroelastic behaviour was indeed taken into account and in this focus can be considered the main controlling process responsible for the pore pressure response in the monitoring well. However, some inelastic deformation is likely to accumulate in the vicinity of the hydraulic fracture, mainly at the tip of the fracture. This inelastic behaviour may impact the overall elastic deformation of the surrounding reservoir rocks and thus also its poroelastic response. Furthermore, the hypothesis of a pure tensile

opening of the hydraulic fracture may also not be completely valid. Whereas it was shown (Zimmermann et al., 2010) that shear components may be negligible, neglecting this contribution may have contributed to the discrepancies between observed and modelled pore pressure changes. Finally, previous studies (Jacquey et al., 2015b, 2016) also demonstrated that depending on the in-situ pore pressure and temperature conditions and the injection schedule, thermoelastic stresses may be as effective as poroelastic stresses. In the case presented in this study, large pore pressure changes were applied which may indicate that the reservoir response is mainly controlled by poroelastic behaviour. However, due to gradient between the in-situ reservoir temperature and that of the injected fluid, thermoelastic stresses may have build-up which could have induced an additional compressive component around the fracture surface. This added deformation would have lead to an increase in the pore pressure and thus could explain the misfit found between modelling results and field data.

This study demonstrated that the poroelastic response of a geothermal reservoir is relevant and characterised by a quasi-instantaneous propagation of the increase in pore pressure due to cyclic deformation induced by a cyclic stimulation treatment. This unexpected pore pressure response could be undesirable as a potential trigger of fault reactivation. An increase of pore pressure can indeed reduce the normal stresses acting on an existing fault plane, which might finally lead to slip and associated seismicity. For the field application considered here (the Groß Schönebeck geothermal facility) only minor micro-seismicity was recorded during the stimulation treatment (Kwiatek et al., 2010). However, depending on the geological setting in which a stimulation treatment takes place (presence of critically stressed fault zones in the vicinity of the stimulated well) potential fault reactivation via instantaneous poroelastic pore pressure increase should be considered when designing the injection campaign. It was indeed shown in this study that magnitudes of the pore pressure peaks are related to the opening of the hydraulic fracture and therefore to the injection rates. In order to avoid undesirable effects, the design of the injection campaign should therefore focus on avoiding fast changes of deformation around the well. This can be achieved for example by using a step-wise stimulation treatment, that is, by increasing the pore pressure build up around the well in a step-wise manner therefore avoiding abrupt changes of injections rate.

In this contribution, we have settled the base for understanding and quantifying poroelastic pore pressure response during hydraulic stimulation. Future work is therefore needed to integrate non-elastic deformation in the poroelastic framework as

presented in this study and to correctly quantify thermal effects in the particular case of hydraulic stimulation treatments.

6.5 Conclusions

Using numerical modelling of the hydromechanical state of a geothermal reservoir, this study emphasises the effects of cyclic hydraulic stimulation treatments on the surrounding reservoir rocks. Opening of a large hydraulic fracture inducing compression in the vicinity of the stimulated well leads to a counter-intuitive pore pressure response. A generic model with idealised cyclic evolution of the fracture opening was used to emphasise the characteristics of such poroelastic effect. The results show that the evolution of the pore pressure distribution is related to the rate of deformation leading to time-shifting effects between the maximum of pore pressure and the maximum of deformation. Field observations of a stimulation treatment conducted at the Groß Schönebeck geothermal facility in August 2007 have been used to quantify the impacts of poroelasticity at the field scale. This approach allowed us to explain an unexpected pore pressure response in a monitoring well during hydraulic stimulation, characterised by a quasi-instantaneous pore pressure increase 475 m away from the stimulated well.

This study provides therefore interesting insights on the relevance of poroelastic coupling at the field scale. It also shows that observations of poroelastic behaviour can help to improve our understanding of the fracture nucleation and propagation processes.

Chapter 7

Fracture mechanics, localised deformation and hydrothermal processes: an outline of preliminary results based on a multiscale coupling approach

7.1 Introduction

An adequate understanding and quantification of the dynamics responsible for fracture nucleation and evolution and associated fluid related transport processes is of great relevance in reservoir applications (Min et al., 2004; Cacace et al., 2013). This is because the massive hydraulic fractures produced during stimulations of a volume of rock exert a profound influence on key mechanical and transport properties, such as elastic moduli, anisotropy of the rock fabric, elastic wave velocity and permeability, and therefore they can drastically impact on the final success of any operational campaign. Based on the outcomes of the above described work as well as on earlier studies, a clear picture starts to evolve in which the macroscopic behaviour of faults and fractures can be linked to the background deformation setting, being at the same time influenced by the local thermomechanical state and deformation history of the host rock. In addition, investigations done at the microscopic scale in sample rocks have also highlight that fracture evolution in rock is a process of progressive damage accumulation and release (David et al., 1994; Baud et al., 2004). These studies pointed on how fracturing likely results from processes occurring at the microscopic scale in a rock, comprising initiation, growth and coalescence of microcracks or organisation of microdefects in the lattice due to variations in the external load or in the internal pore fluid pressure and/or thermal state. These last aspects clearly indicate the complexity and across-scale characteristic of fracturing processes and the need to develop approaches which may enable to capture, reproduce and quantify how these microscopic mechanisms evolve to reproduce the macroscopic behaviour of a rock as observed in a laboratory or in the field.

It is the aim of this chapter to discuss recent efforts done to extent the workflow presented as far to address these aspects. However, it is worth mentioning that these activities, though initiated within the framework of this thesis and thanks to the results obtained in the course of my PhD, are ongoing. Therefore, the results should be taken

as preliminary rather than conclusive. More specifically, I organise this chapter as follows. In a first part, I describe how to include the macroscale fracture dynamics into the current numerical formulation, in a way that could be amenable to describe the interactions among the mechanical aspects related to fracture evolution on the resulting hydrodynamics and thermal state of rocks. In a second part, I will then focus on describing and simulating microscopic processes deemed responsible for localised brittle deformation, leading to fracture formation and their inelastic propagation in the rock and their effects on the macroscopic phenomenological constitutive relationships.

7.2 Macroscopic behaviour of discrete geological structures

The methodology described so far, represents fractures and faults as lower dimensional finite element of zero thickness which are embedded into the discrete domain of the host rock. While such an approach has been shown to be flexible for modelling the hydrothermal behaviour of geological discontinuities at reasonable computational efforts, it comes with some limitations when trying to include their mechanical description. The main assumption of no differential displacements across the fault/fracture plane prevents to account for the initiation of local gradients in the deformation as induced by the presence of a clear discontinuity. In addition, such an approach, while requiring continuity in the pore pressure and temperature at the global nodal level, prevents to model fault and fracture acting as internal drains. In this section, I will present the basic concepts behind the XFEM and show why this method is a good candidate for modelling the macroscopic thermo-hydro-mechanical behaviour of faults and fractures by means of simplistic examples.

The idea behind the XFEM is to enrich by discontinuous functions the FEM polynomial approximation at nodes which are in the vicinity of the discontinuity. By increasing the degree of freedom while solving for the mechanics of fracture elements, it is then possible to consider discontinuous, i.e. jump-like, behaviour of the displacement vector across and along the two sides of the discontinuity interface. An additional interesting feature of the XFEM method is that it does not require to efficiently resolve by mesh refinement any localised feature of interest. Therefore, it is well suited to model fractures in a material since it requires to enrich the local basis functions of the nodes intersected by a fracture by including an additional crack opening displacement. In addition, an advantage of such a method is that for simulations dealing with a propagating discontinuity (when modelling hydraulic fracturing), it does not require the mesh to track the singularity path, thus avoiding the need for updating the mesh size and geometry at each time step. The main differences between the single nodded, zero

thickness FEM method as used so far in this thesis and the XFEM representation of a discontinuity are illustrated by a conceptual scheme in Figure 7.1. More information on the XFEM approach can be found in the relevant literature (Khoei, 2014; Richardson et al., 2011; Hansbo and Hansbo, 2004). In the following I will focus on demonstrating by simplistic examples the advantages of extending the numerical framework by the XFEM method.

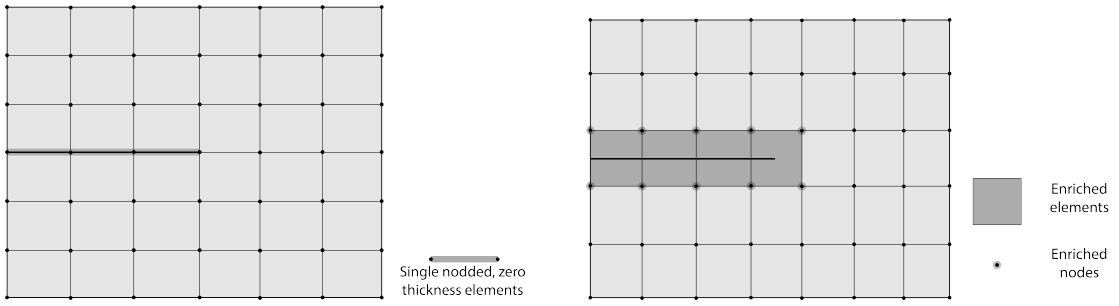

(a) Single nodded, zero thickness elements. (b) XFEM.

Fig. 7.1 Conceptual schemes for fracture representation: single nodded, zero thickness element (7.1a) and XFEM concept (7.1b).

7.2.1 XFEM problem formulation for deformable porous media

In Chapter 2, the governing equations for a deformable porous medium were derived. I recall here the three-dimensional equations governing fluid flow (Equation 2.22), heat transfer (Equation 2.25) and elastic deformation (Equation 2.10) of the porous medium (without second order terms):

$$\frac{1}{M_b}\frac{\partial p_f}{\partial t} - \alpha\beta_b\frac{\partial T}{\partial t} + \alpha\dot{\epsilon}_{kk} + (1-\alpha)\,\dot{\epsilon}^{*p}_{kk} + \nabla\cdot\boldsymbol{q}_D = 0. \tag{7.1}$$

$$(\rho c)_b\frac{\partial T}{\partial t} + \nabla\cdot(\rho_f c_f \boldsymbol{q}_D T - \lambda_b\nabla T) = 0 \tag{7.2}$$

$$\nabla\cdot(\boldsymbol{\sigma}' - \alpha p_f \mathbb{1}) + \rho_b\boldsymbol{g} = 0 \tag{7.3}$$

This set of equations is solved over a closed domain Ω with its boundary noted Γ with appropriate boundary conditions. The existence of a discontinuity Γ_d within the domain Ω leads to a modification of the weak forms of the sets of equations described before. The divergence theorem is indeed modified in the presence of a discontinuity.

Consider a discontinuous function $\boldsymbol{F}$ and a test function ω, the divergence theorem with a discontinuity reads:

$$\int_{\Omega} \omega \nabla \cdot \boldsymbol{F} d\Omega = \int_{\Gamma} \omega \boldsymbol{F} \cdot \boldsymbol{n}_{\Gamma} d\Gamma - \int_{\Gamma_d} [\![\omega \boldsymbol{F}]\!] \cdot \boldsymbol{n}_{\Gamma_d} d\Gamma - \int_{\Omega} \nabla \omega \cdot \boldsymbol{F} d\Omega \tag{7.4}$$

where $[\![\boldsymbol{F}]\!] = \boldsymbol{F}^{+} - \boldsymbol{F}^{-}$ represents a jump in the function $\boldsymbol{F}$, with $\boldsymbol{F}^{+}$ and $\boldsymbol{F}^{-}$ denoting the values of $\boldsymbol{F}$ on the two sides of the discontinuity Γ_d^{+} and Γ_d^{-} respectively.

Using the modified divergence theorem, the weak forms of the equations for fluid flow, temperature and deformation can be derived as:

$$\begin{aligned} \int_{\Omega} \omega \frac{1}{M_b} \frac{\partial p_f}{\partial t} d\Omega - \int_{\Omega} \omega \alpha \beta_b \frac{\partial T}{\partial t} d\Omega + \int_{\Omega} \omega \left(\alpha \dot{\epsilon}_{kk} + (1-\alpha) \dot{\epsilon}_{kk}^{*p} \right) d\Omega + \int_{\Omega} \nabla \boldsymbol{\omega} \cdot \boldsymbol{q}_D d\Omega \\ + \int_{\Gamma_{q_H}} \omega \left(\boldsymbol{q}_D \cdot \boldsymbol{n}_{\Gamma_{q_H}} \right) d\Gamma - \int_{\Gamma_d} [\![\delta p_f \boldsymbol{q}_D]\!] \cdot \boldsymbol{n}_{\Gamma_d} d\Gamma = 0 \end{aligned} \tag{7.5}$$

$$\begin{aligned} \int_{\Omega} \omega (\rho c)_b \frac{\partial T}{\partial t} d\Omega - \int_{\Omega} \nabla \omega \cdot \left((\rho c)_f \boldsymbol{q}_D T - \lambda_b \nabla T \right) d\Omega \\ + \int_{\Gamma_{q_T}} \omega \left((\rho c)_f \boldsymbol{q}_D T - \lambda_b \nabla T \right) \cdot \boldsymbol{n}_{\Gamma_{q_T}} d\Gamma + \int_{\Omega} \omega \dot{H} d\Omega - \int_{\Gamma_d} [\![\omega \boldsymbol{q}_T]\!] \cdot \boldsymbol{n}_{\Gamma_d} d\Gamma = 0 \end{aligned} \tag{7.6}$$

$$\begin{aligned} \int_{\Omega} \nabla^s \boldsymbol{\omega} : (\boldsymbol{\sigma}' - \alpha p_f \mathbb{1}) \, d\Omega - \int_{\Omega} \boldsymbol{\omega} \cdot \rho_b \boldsymbol{g} d\Omega - \int_{\Gamma} \boldsymbol{\omega} \cdot (\boldsymbol{\sigma}' - \alpha p_f \mathbb{1}) \cdot \boldsymbol{n}_{\Gamma} d\Gamma \\ + \int_{\Gamma_d} [\![\omega \left(\boldsymbol{\sigma}' - \alpha p_f \mathbb{1} \right)]\!] \cdot \boldsymbol{n}_{\Gamma_d} d\Gamma = 0 \end{aligned} \tag{7.7}$$

The additional terms related to the jump in Darcy velocity and heat flow (conductive and advective) across the discontinuity interfaces can be constrained by the governing equations for fluid flow and temperature within the discontinuity (similar to the ones presented in Chapter 2). The term related to the XFEM discontinuity in the momentum balance equation (Equation 7.7) of the solid skeleton vanishes for weak or strong discontinuity in a pure mechanical formulation. For hydromechanical coupling, this terms can be expressed by considering the effective stress concept and a stiffness of the fracture.

7.2.2 Mechanical response of an infinite plate with an inclined fracture

This first example considers a two-dimensional infinite plate containing a single inclined fracture subjected to uniform far-field tension. It is inspired from an example introduced in Broek (1986). The geometry and boundary conditions for this simple problem setup are shown in Figure 7.2a. The discontinuity is 2 m long, has an aperture of 5 cm and is inclined with an angle of 45°. The Young's modulus of the plate is $E = 2\,\text{GPa}$ and the Poisson's ratio is $\nu = 0.3$. The far-field tension stress is equal to $\sigma = 2\,\text{MPa}$ and applied on the top of the domain (vertical direction).

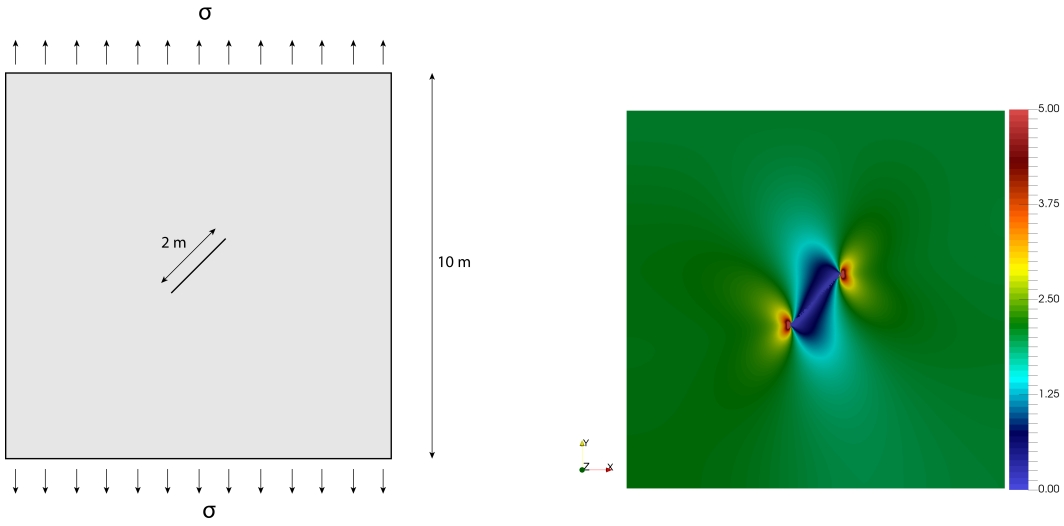

(a) Problem formulation.

(b) Stress σ_{yy} [MPa] distribution.

Fig. 7.2 Setup (7.2a) and stress distribution (7.2b) for the infinite plate with an inclined fracture subjected to uniform tension.

Figure 7.2b shows the distribution of the vertical stress (σ_{yy}) within the plate. Largest values of stress (5 MPa) are located at the two tips of the inclined fracture. The regions at the tips of the fracture, called cohesive zones and bearing the maximal stress ratio, are process zones where microcracks are likely to occur. When microcracks aggregate, they can drive the propagation of the macroscopic fracture. These processes were not considered in this simple example but could be integrated in the current formulation. This example nicely illustrates the impacts of a XFEM discontinuity on the deformation distribution. Extension of the current mechanical implementation should therefore focus on describing the microscopic processes responsible for this cohesive zone, driving the non-elastic deformation and the propagation of the macroscopic fracture.

7.2.3 Hydrothermal flows in a plate with an inclined fracture

The second example considers a similar domain, a plate with a single inclined fracture for analysing the hydrothermal processes around the discontinuity. This example is an extension (thermal flow) of the application presented in Chapter 2. A pressure gradient ($q_0 = 1.0 \times 10^{-4}\,\mathrm{m \cdot s^{-1}}$) is imposed horizontally as described in Figure 7.3a. Temperature is fixed as 10 °C at the left boundary and as 0 °C at the right boundary. Heat is transferred therefore via conductive and advective processes. The material properties adopted for this example are summarised in Table 7.1.

Table 7.1 Material properties the example of hydrothermal flow in a plate with an inclined fracture

	property name	symbol	value	SI unit
Fracture	Angle	α	45	$^\circ$
	Length	L	2	m
	Aperture	h	0.05	m
	Permeability	k^f	1.0×10^{-10}	$\mathrm{m^2}$
	Viscosity	μ_f^f	1.0×10^{-3}	$\mathrm{Pa \cdot s}$
Porous medium	Porosity	ϕ	0.15	-
	Permeability	k	1.0×10^{-12}	$\mathrm{m^2}$
	Viscosity	μ_f	1.0×10^{-3}	$\mathrm{Pa \cdot s}$
	Fluid thermal conductivity	λ_f	0.65	$\mathrm{W \cdot m^{-1} \cdot K^{-1}}$
	Solid thermal conductivity	λ_s	3.0	$\mathrm{W \cdot m^{-1} \cdot K^{-1}}$
	Fluid heat capacity	c_f	4180	$\mathrm{J \cdot kg^{-1} \cdot K^{-1}}$
	Solid heat capacity	c_s	980	$\mathrm{J \cdot kg^{-1} \cdot K^{-1}}$

Figure 7.3 shows the distribution of pore pressure and temperature around the inclined fracture. The presence of the discrete fracture disturbs the uniform horizontal flow in the vicinity of the fracture. The pore pressure isolines indicate that the flow is concentrated along the two sides of the fracture. The temperature distribution exhibits a noticeable jump across the discontinuity which is well revealed by the temperature isolines. Since the fluid flow is mainly focused along the fracture, heat transport by advection is dominant within the fracture. However, heat transport across the fracture remains dominated by conduction (within the water in the fracture) and has a significantly higher characteristic time than heat transport by advection but also than conduction in the surrounding porous rocks since the bulk thermal conductivity is significantly higher than the one of the fluid. This explains why the temperature distribution is not continuous across the fracture.

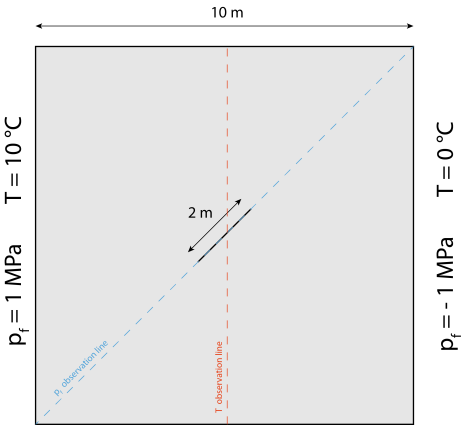

(a) Problem formulation.

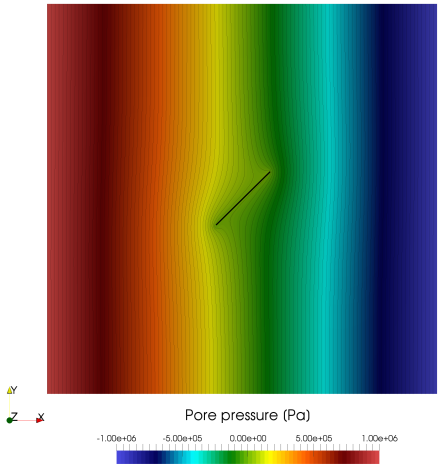

(b) Pore pressure distribution and isolines.

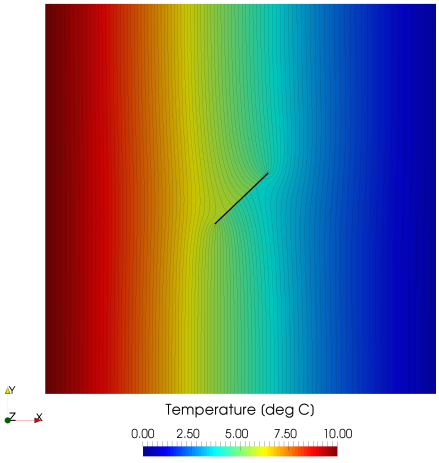

(c) Temperature distribution and isolines.

Fig. 7.3 Problem formulation (7.3a) and pore pressure (7.3b) and temperature (7.3c) distributions for a domain containing an inclined fracture.

Figure 7.4 shows the distribution of pore pressure and temperature along two lines of the domain as illustrated on Figure 7.4a. The pore pressure distribution is in perfect accordance with the analytical solution presented in Chapter 2. In Figure 7.4b, the jump in temperature across the discontinuity is well noticeable and controls the temperature distribution in a large area around the discontinuity as seen before. This example nicely illustrates the advantages of using the XFEM to model hydrothermal flow in domains including a discontinuity. The main advantages relies in the fact that the XFEM can model local flow barriers and discontinuous temperature distributions which was not possible with the single nodded, zero thickness elements approach.

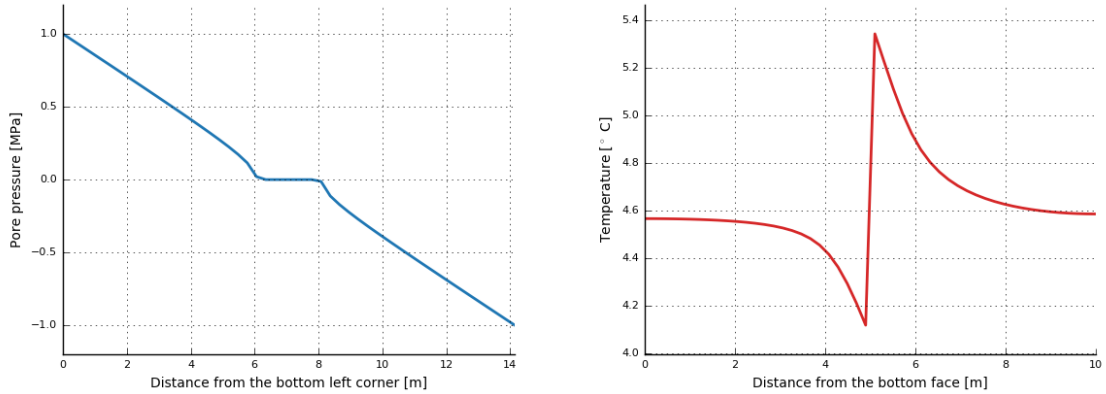

(a) Pore pressure.

(b) Temperature.

Fig. 7.4 Pore pressure (7.4a) and temperature (7.4b) along the observation lines presented in Figure 7.3.

The two examples described above have served to illustrate the basic ideas behind extending the current formulation by relying on the XFEM method. The main advantage of such an approach can be summarised in the following two points: (1) It will offer the possibility to account for localised deformation in addition to pore pressure and temperature along and around the discontinuity; and by doing so, (2) it will enable to model internal no-flow barriers in a more flexible and efficient way than the current formulation (Cacace et al., 2013). The implementation of the full thermo-hydro-mechanical feedbacks for discontinuities in XFEM is still subject to ongoing work, especially the hydromechanical coupling, considering the effective stress concept within the discontinuity and therefore a possible opening and closing of the fracture due to changes in pore pressure. This is usually achieved by introducing an anisotropic stiffness for the discontinuity (normal and tangent to the plane) which allows to model frictional contacts and slip along the discontinuity. The hydromechanical behaviour of XFEM fracture can therefore be of major interest for the issue of modelling hydraulic fracturing and reactivation of faults. Such a method can provide additional flexibility in addressing problems involving also a microscopic component as those responsible for the evolution of the deformation front at the tips of an evolving fracture as will be detailed in the next section.

7.3 From diffused to localised deformation in porous rocks

This section presents an outlook on recent and ongoing efforts to include into the current formulation a description of inelastic processes, including microcracking and strain localisation which are relevant to constrain the deformation of geological discontinuities and their hydraulic and poroelastic implications. To observe the process of localisation, three axial loading laboratory experiments in a triaxial setting were conducted on Bentheim sandstone at three different confining pressures which are presented in Appendix C. These experimental results were then used as a framework to define a modelling strategy and to constrain numerical models.

To model the mechanical response of Bentheim sandstone during triaxial loading under different confinements, the Drucker-Prager plasticity model was adopted. The yield surface of the Drucker-Prager model is a smooth version of the well-known Mohr-Coulomb failure criterion and is often used to model the elastoplastic behaviour of porous rocks (Vermeer and de Borst, 1984). For a description of the elastoplastic constitutive laws, I refer to Chapter 2.

7.3.1 Data-derived hardening and softening rules

Experimental results obtained during axial loading (stage 3) can be used to derive the values of deviatoric and mean stress at different characteristic times:

- Onset of microcracking: deviation from linear elasticity is an indication of the initiation of microcracks within the sample.
- Macroscopic failure: stress drops are an indication of the localisation of the microcracks and formation of a macro-shear plane of failure. Peak values of stress are reached before the stress drop.
- Residual strength: after macroscopic failure, the stress response indicate the residual strength of the rock.

These results are summarised in Figure 7.5 with the evolution with time of the deviatoric stress for the 40 MPa confined sample (Figure 7.5a) and in the J_1-$\sqrt{J_2}$ space (invariants of the effective stress tensor) (Figure 7.5b).

A linear interpolation for each of the three stages mentioned before allows to evaluate the evolution of the friction angle and the cohesion. At the onset of plasticity (microcracking), the friction angle is close to 0° and the cohesion is around 72 MPa.

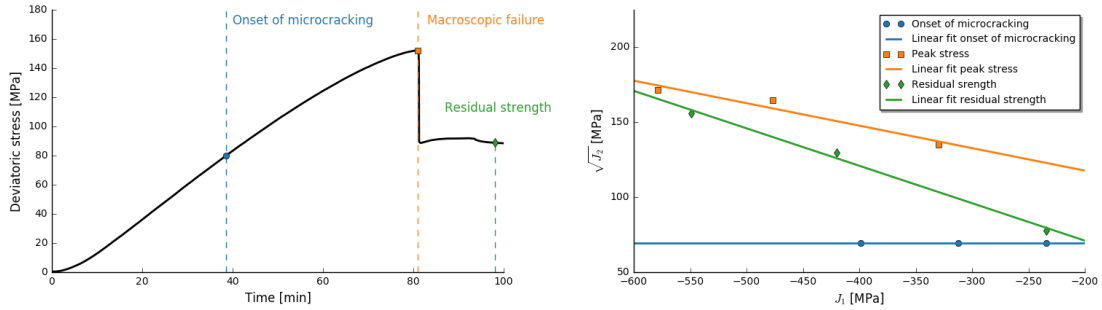

(a) 40 MPa confinement experiment. (b) Stress values for the three experiments.

Fig. 7.5 The stages of: onset of microcracking, macroscopic failure and residual strength are illustrated for the experiment at 40 MPa confining pressure (a). Square root of the second invariant versus the trace of the effective stress tensor (b). Experimental data for the onset of microcracking, peak stress and residual strength are illustrated as is a linear interpolation for each stage.

During the inelastic deformation prior to macroscopic failure, the hardening behaviour is considered as an indication of microcracking within the sample, increasing the frictional strength of the rock and the cohesion. Before macroscopic failure, a maximum of cohesion is reached with 98 MPa as well as a value of 27° for the friction angle. During macroscopic failure, the frictional strength still increases while the cohesion decreases, reaching values of 48° for the friction angle and 32 MPa for the cohesion.

The overall increase in frictional strength is modelled using an exponential function depending on the effective plastic strain used here as a plastic internal variable. The evolution of cohesion is modelled using a combination of an exponential function for the pre-failure increase and a cubic function for the decrease during macroscopic failure. The cubic function is used for smoothing the sharp decrease to provide numerical stability.

7.4 Modelling results

Figure 7.6 shows the evolution with time of the modelled and observed axial deviatoric stress (Figure 7.5a) and porosity (Figure 7.5b). In general, a good agreement was found between experimental and modelling results for the evolution of the deviatoric stress. The sharp stress drop in the experimental data is reproduced by a smooth stress drop in the modelling results which insures numerical stability. The evolution trend for porosity is reproduced with satisfying agreement for the 40 MPa confining pressure experiment. The porosity linearly decreases in the elastic regime and progressively starts

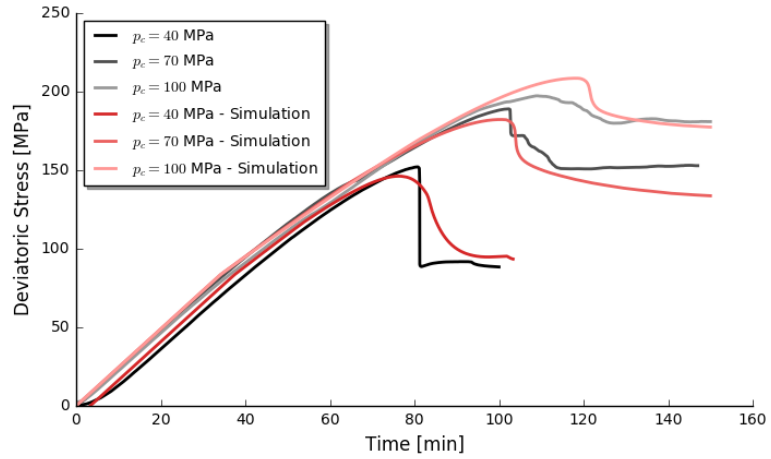

(a)

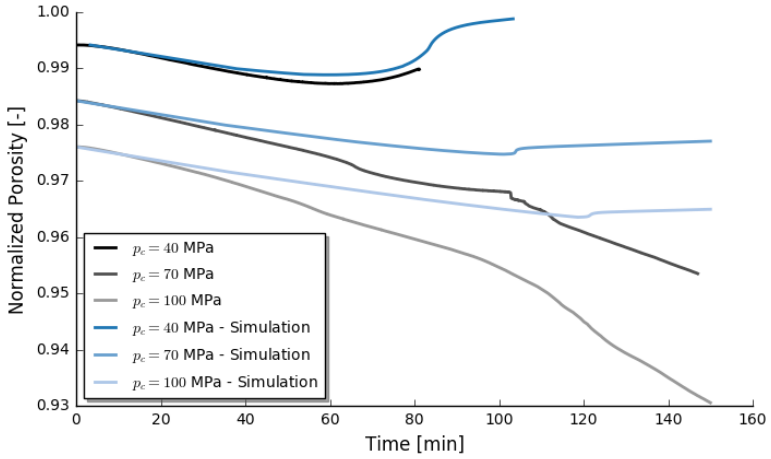

(b)

Fig. 7.6 Evolution of the observed and modelled deviatoric stress (a) and of the porosity (b) for the three different confining pressures.

to increase after the onset of microcracking. However, this approach fails to reproduce the enhanced reduction in porosity during microcracking and macroscopic failure for the two experiments conducted at 70 and 100 MPa confining pressure, respectively.

The porosity evolution predicted by the modelling approach failed to reproduce the enhanced porosity reduction observed during microcracking and macroscopic failure for the two experiments at 70 and 100 MPa confining pressures as specified before. We suggest that these observations are an indication for a possible additional physical process controlling the porosity evolution which was not considered in the present physical framework. Process candidates are grain crushing and pore collapse which

are likely to occur in Bentheim sandstone at these effective pressure ranges (Dautriat et al., 2009; Baud et al., 2004, 2006). These processes can indeed reduce considerably the size of the pores but also their connectivity, resulting in a large porosity decrease. Using microstructural observations of the samples post-failure helped to identify these processes and better understand their physical implications as it is described in Appendix C. These processes, which are highly dependent on the microstructure of the host porous material need to be further investigated by means of observations.

The modelling approach adopted in this study relies on the elastoplastic constitutive laws. Using a dilation angle smaller than the friction angle (observed for most of porous rocks) can lead to a softening behaviour as presented in the present study. This softening behaviour can be potentially unstable (Vermeer and de Borst, 1984). This means that softening can cause a local loss of ellipticity of the differential equations and lead to results which are dependent on the mesh size and orientation. This issue has been well documented in the literature (Schaeffer, 1990; Vardoulakis and Sulem, 1995). Several regularisation techniques can be used to prevent the formation of mesh-dependent shear-enhanced compaction bands including Cosserat model (Cosserat and Cosserat, 1909; Sluys, 1992), gradient model (Pardoen et al., 2015) or introducing a viscous component (Perzyna, 1966; Wang et al., 1997; da Silva, 2004). The present study, using classical elastoplastic constitutive laws provided good agreement between observed and modelled deviatoric stress evolutions. However, I also emphasise the need of further research on integrating a regularisation technique in order to study the influence of the confining pressure on the width and orientation of the shear bands and insure mesh-independent results. Finally, motivated by the observations in the laboratory, an extension of the elastoplastic constitutive laws which were developed in the context of solid mechanics is required to account for reliable poroelastic impacts on the porosity distribution and evolution.

The concepts presented in this chapter could therefore be used as a possible extension of the current physical framework to account for the mechanical impacts of faults and fractures on the hydrothermal behaviour of a reservoir. I presented two concepts, aiming at capturing the microstructural processes responsible for localised deformation around faults and fractures and their macroscopic multiphysic behaviour. These concepts could be combine together to define a more realistic description of the micro- and macroscopic behaviour of fractures and fault zones, which is currently the topic on ongoing work.

Chapter 8

Summarising discussions, outlook and conclusions

8.1 Discussion

The main goal of this thesis is to establish a flexible, integrative porous media numerical framework, which can be used to tackle problems related specifically to reservoir applications. Efforts have been made to develop a scientific workflow, combining laboratory experiments, field data and numerical models to capture the details of the multiphysic nature of porous reservoirs and the interactions among the relevant processes across the different scales of interest, from the microscale of the pores to the mesoscale of field applications. To establish such a workflow, a number of interconnected research questions have been embraced, as summarised in Section 1.2.2. Each chapter of this thesis (from Chapter 2 to 7) presented in details how and to which degree all of these open questions have been addressed separately. For this reason, I make use of this final chapter to open an integrative discussion of the results presented earlier in this thesis, while I dedicate a second paragraph to describe the most significant steps that I envisage for future activities as supplementary to the work done so far. For the sake of clarity and easiness of reading, I subdivide the discussion into three main core topics, each one inspired by the open scientific questions listed in the Introduction to this work.

8.1.1 Physical processes and their couplings

The bulk of current studies on heat energy extraction from underground reservoirs often centre on investigating processes relevant to a better characterisation of the dynamics of reservoir fluids as well as to quantify, via integrative techniques, the heat content available in the underground. Extraction of heat from a reservoir is conducted by making use of a single or multiple set of boreholes drilled within the targeted horizon, where fluid is let to circulate (inject and extract) within the reservoir rocks. Therefore, the transport of the heat contained in the reservoir rocks as it is advected by a moving fluid under pressurised conditions is a crucial process that should be quantified in order to make any prediction about the level of productivity and long-term sustainability of geothermal operations. Based on this simplified picture of an operational campaign, most studies tend to neglect the additional feedback effects from rock mechanics on

the fluid and heat transport processes. In this regard, one of the main outcomes of this thesis is that it has clearly demonstrated, by applied study cases, the first order relevance that the processes controlling the deformation of porous rocks and their interrelationships with the fluid and heat transport dynamics have in providing a better understanding of the behaviour of a geothermal reservoir. The applications as discussed in separate chapters of this thesis have provided strong indications that such mechanical feedbacks are not negligible when addressing issues relating to successful operations and environmental safety.

Starting by discussing the relevance of hydromechanical coupling, I have demonstrated how changes in the pore pressure as induced by fluid injection and extraction can significantly alter the in-situ effective stress within the reservoir. Closely linked to what discussed above, is the study of potential (re)activation of natural major fault zones by geothermal operations, once again a result from a tight coupling among hydraulic and mechanical processes. It has been well established that increase in pore pressure may enhance slip movements along fault planes even at relatively high friction coefficients. Therefore, faults reactivation and induced seismic events, might occur under conditions unexpected if based on a classical Anderson-Byerlee approach (Anderson, 1905; Byerlee, 1978) and show a transient characteristic which cannot be reconciled by any steady state description.

A last point worth discussing is the solid to fluid hydromechanical coupling, where the deformation of the solid skeleton affects the dynamics of the fluid within the pores. Such a coupling has been so far mostly considered in laboratory experiments (Mandel, 1953; Cryer, 1963), being deemed of secondary relevance at the scale of the reservoir. However, as shown in Chapter 6 of this thesis, the influence of the solid deformation on the resulting hydrodynamics of a porous rock has a primary, though not well constrained so far, importance for field scale applications. Such coupling is of particular relevance in the context of hydraulic stimulations where the deformation of a volume of a rock by fracture opening induces instantaneous (poroelastic) variations in the pore pressure, thus affecting the hydromechanical state of the reservoir at distances of some hundreds of metres from the stimulation point. In the same study case, I also demonstrated that only by taking this effect into account, it was possible to provide an explanation to field observations (Zimmermann et al., 2010), which were left unexplained before.

A few studies considering the poroelastic impacts of the Biot consolidation theory have been carried out at the field scale (Verruijt, 2010; Slack et al., 2013; Vinci et al., 2014). One major breakthrough in this field was achieved when the Noordbergum

effect (field observations of reverse water-level fluctuation) was recognised as a result of the consolidation theory (Wolff, 1970; Rodrigues, 1983; Kim and Parizek, 1997). The results presented in Chapter 6 revealed another poroelastic effect resulting from the consolidation theory at the field scale during hydraulic stimulation together with its observations (Zimmermann et al., 2010). Observations of such a phenomenon can therefore be used to better characterise the hydraulic state of a reservoir during hydraulic stimulation.

In addition to hydromechanical coupling, attention has been also towards a quantification of the interactions between the thermal and mechanical state of porous media (Chapters 4 and 5). I have demonstrated that the relatively large thermal gradients building up in a reservoir at the interface between the injected cold fluid and the relatively warmer host rock affect the mechanical stability of a rock by the initiation of thermoelastic stress. Magnitudes of such volumetric stress show a linear dependency on the magnitudes of thermal gradients induced by geothermal operations, and they can affect the mechanical state to the same degree as the corresponding poroelastic stress (Chapter 4). In addition, when coupled to the hydrodynamics, the volumetric deformation can propagate at distances from the injection well, and might lead to an additional perturbation of the stress state nearby existing natural fault zones thus contributing to their potential reactivation, as discussed in Chapter 5.

The issue of induced reactivation of faults during reservoir operations has been the subject of several studies in the last decades (Jaeger et al., 2007; Cappa and Rutqvist, 2011; Rutqvist et al., 2013). However, most of these studies focused on the reactivation of fault zones due to changes in pore pressure and often neglected the impacts of changes in temperature. In this thesis (Chapter 5), I showed that the thermal state of a reservoir can be relevant to quantify the slip potential of a fault. This is particularly essential for deep geothermal reservoirs which can be subjected to large temperature changes. This was achieved by considering dynamic evolutions of the heat transport processes in addition of the fluid flow coupled altogether to the deformation of the reservoir rocks. The results of this thesis therefore raised awareness of the need of characterising dynamically the thermal state of a reservoir during geothermal operations to limit environmental impacts.

8.1.2 Strong overall coupling via structure properties relationships

Apart from describing the non-linear physics, porous media applications face the challenging task to deal with heterogeneous and complex structures. Indeed, observations done on the macroscopic behaviour of a reservoir result from interactions and superpo-

sition of processes that originate at the microscale rock framework across disparate spatial and temporal scales.

In this thesis I propose an approach that tries to bridge scales by establishing appropriate, non-linear state relationships between the microscopic structure of porous media as constrained by laboratory investigations and the resulting material properties which are used to describe the macroscopic behaviour of the porous system. The results of this thesis show that by integrating such state equations into a numerical modelling framework, it is possible to take such microscale processes into account while looking at the mesoscale of a reservoir. An example has been discussed in Chapter 3, where deformation of a porous medium has been recognised as the dominant process controlling the evolution of its mechanical and transport properties.

By considering the micro-defects of a porous medium (microcracks) in an appropriate physical model (crack closure theory), it is possible to account for the resulting non-linear elastic macroscopic behaviour at low effective stress. Using laboratory observations, detailed information about these microcracks can be obtained (distribution and aspect ratio) and therefore serve as constraints for numerical modelling. This non-linear mechanical behaviour combined with transport properties evolution, will likely affect the overall fluid and heat transport behaviour of a reservoir.

Spatial and temporal variations of porosity and permeability affect, if not control the overall productivity and recovery of reservoirs. Changes in pore pressure, temperature and stress state during injection or production of fluid can give rise to porosity and permeability alterations which result from the deformation of the microscopic structure of the porous rock. In order to take these effects into account, in this thesis I worked out a physical framework that considers the poro- and thermoelastic impacts on the porosity evolution.

The results presented in this thesis (Chapters 3 and 4) helped to quantify the changes in porosity due to pore pressure, temperature and induced deformation perturbations. It was therefore possible to assess a more realistic reservoir behaviour at the field scale and to quantify the productivity of geothermal operations. I was indeed able to emphasise that the predictions of the life time for a real case study geothermal reservoir was smaller than the one predicted by classical studies which do not consider the impacts of the microstructure on the transport properties of the reservoir rocks. The results presented in this thesis provide therefore valuable insights to better quantify the productivity of future geothermal operations.

Efforts will be needed in future studies to include in the derived physical framework an appropriate description of the microstructural control (geometry and organisation of the solid grains) on the resulting permeability of porous rock formations.

8.1.3 Multiphysic behaviour in the presence of geological discontinuities

In addition to having a complex microscopic structure, porous rocks show also complex and heterogeneous characteristics at the macroscale, mainly faults and fractures. Natural or engineered fractures and major fault zones can alter the hydraulic and mechanical properties of the host reservoir rocks due to their discontinuous nature and therefore affect if not control the overall productivity of a geothermal reservoir. Challenges are related to find best ways to integrate such discontinuities into numerical models, and, once done, to describe the interactions among the processes occurring in the porous rock volume, in the discontinuities and along and across their respective interfaces.

To integrate faults and fractures in the modelling framework in a way that would enable to predict their impact on the hydrothermal state of a reservoir, the numerical formulations have been extended to account for lower dimensional, zero thickness, single nodded finite elements representing such discontinuities embedded in the three-dimensional discretisation of the porous rock volume. More details about the mathematical formulation can be found in Chapter 2.

However, constraining the hydraulic properties and hydrothermal behaviour of faults and fractures is quite complex and few observations exist to constrain any model (Bense et al., 2003; Pili et al., 2002; Gébelin et al., 2011; Mulch et al., 2007). Their behaviour is usually assessed by estimating the normal and shear components of the stress acting on a fault plane and linking such ratios to a rather qualitative hydraulic behaviour of the corresponding fault. As discussed by Barton et al. (1995, 1997), faults which bear a shear to normal stress ration higher than their static friction resistance are considered to be critically stressed, and therefore are expected to be more hydraulically conductive. However, the hydraulic behaviour of fault zones is generally more complex than this simple description as faults represent heterogeneous and complex domains. This is schematically illustrated in Figure 8.1, where the overall hydraulic behaviour of fault zones is plotted as a function of the ratio of the fault damage zone to the fault core. Fault cores are structures located in the centre of fault zones where most of the displacements localised. The nature and composition of these fault cores highly depend on their deformation, pore pressure and temperature history. In particular microscopic processes such as grain size reduction, pore collapse or mineral precipitation

can occur in such localised structures and may cause the fault core to act as hydraulic barrier. Damage zones, surrounding the fault core consist of a network of geological discontinuities such as fractures, veins, cleavage or folds. These damaged structures are generally considered to increase the hydraulic conductivity of the fault zone and depend on the mechanical conditions (stress field) and their deformation history (Caine et al., 1996).

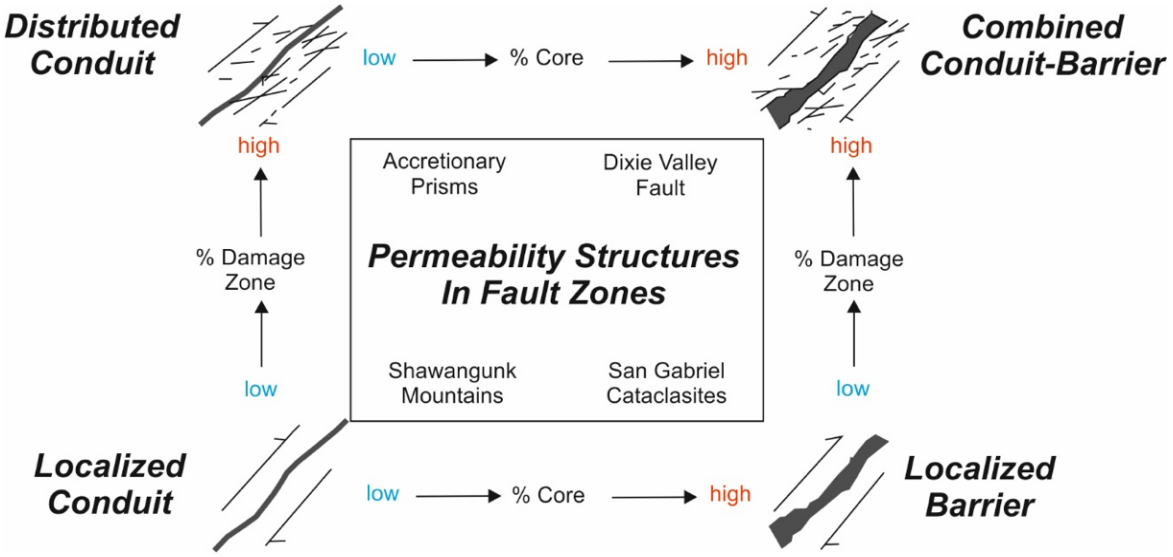

Fig. 8.1 Conceptual scheme for describing the hydraulic behaviour of fault zones (modified after Caine et al. (1996)).

From all stated above, a more complex picture of the properties and behaviour of fault zones comes out than could be simplified by any end-member cataloguing linking their hydraulic properties to the static stress state around them. While the approach presented in this thesis provides efficient results to integrate their geometric features and basic hydrothermal behaviour, additional work is required which should focus on a quantitative characterisation of the hydrothermal and mechanical behaviour of geological discontinuities and their dynamic evolution.

In this final discussion, I would like to emphasise the need for a multiscale approach in modelling the thermo-hydro-mechanical behaviour of geological discontinuities such as fractures and faults. As pointed out before, the macroscopic hydraulic behaviour of fault zones has been well recognised to control the far-field pore pressure and temperature distributions and to be linked to the deformation, pore pressure and temperature histories (Caine et al., 1996). The composition of the fault core is for example related to the occurrence of microstructural processes such as pore collapse and mineral precipitations (Faulkner et al., 2010). In this sense, the overall macroscopic

behaviour of a fault zone is not only related to the present-day heterogeneity in physical properties but also to the thermodynamic conditions at the time of its formation and its dynamic evolution over time. Studying the processes controlling the onset of localised deformation, at the origin of all geological discontinuities is therefore required to understand the transient impacts of fractures and faults on the THM behaviour of porous rocks. Formation of macroscopic discontinuities, such as major fault zones at the basin scale or hydraulic fractures at the reservoir scale arises as an assemble of microscopic discontinuities which aggregated over time due to driving microscopic processes. It is therefore required to account for these microscopic processes when dealing with modelling of fractures or faults initiation and propagation.

Localised deformation can occur at different scales within porous rocks. Whether in the context of microcracking due to compaction, initiation of hydraulic fractures in enhanced geothermal systems or large fault zone formation in natural systems, understanding the mechanisms responsible for initiation of localised deformation is anything but trivial. During the last decades, this topic has gained a great deal of attention, particularly in studies aiming at investigating the feedbacks between localised deformation and material properties, namely porosity and permeability in the context of engineered reservoir applications such as EGS (Gérard et al., 2006; Deichmann and Giardini, 2009). This is mainly because the geometry, shape and orientation with respect to the in situ stress field of natural and induced fractures have a strong control on the reservoir (secondary) permeability structure and therefore on its productivity.

Gradients in pore pressure, temperature and therefore in the mechanical state of a reservoir observed and monitored during heat extraction act in a way as to alter the shape (contracting or dilating) and geometry of existing fractures, leading possibly to the initiation of newly formed rupture planes. Under certain circumstances deformation as it accumulates in a rock volume could localise into bands of intense shear displacement, which, depending on their orientation with respect to the in-situ stress regime and history can either act as domains of increased permeability or as no flow contact areas.

The macroscopic behaviour of geological discontinuities is therefore the result of microscopic driving processes leading to a macroscopic alteration of the porous rocks (Caine et al., 1996; Faulkner et al., 2010). To model realistic behaviours, both the microscopic driving processes and the behaviour of the macroscopic discontinuity need to be considered. Modelling such multiscale behaviours is therefore not trivial and raises several challenges. In Chapter 7, I presented two concepts with their illustrative examples which can be further studied to overcome the challenge of scale dependency

inherent to the nature of these geological discontinuities. These concepts will be further discussed in the next section, particularly their combination to consider the miscroscopic-driven processes at the macroscopic scale.

An outlook of ideas collected from the work presented in this thesis will be presented in the section that follows.

8.2 Outlook

8.2.1 Bridging scales for modelling fracture and fault mechanics

I pointed out in the first part of these discussions that a continuous numerical approach is not sufficient for modelling macroscopic impacts of geological discontinuities. Discrete approach (such as XFEM presented in Chapter 7) need to be considered for representing these discontinuities in order to model reliable THM behaviours. This includes dynamic mechanical evolution and the far-field impacts of these discontinuities on the hydraulic and thermal state of the surrounding reservoir rocks. However, the driving mechanisms occurring in the process zone at the tips of discontinuities are likely to arise from microscopic processes as well. Propagation of fractures arises from microcracking and strain-softening behaviours at their tips which are similar to the ones controlling the onset of localised deformation.

The macroscopic behaviour of geological discontinuities has been recognised in these discussions as a result of microscopic driving processes leading to a macroscopic alteration of the porous rocks. The overview over the ongoing work presented in Chapter 7 (and in Appendix C) aims at considering the inelastic deformation occurring at large deformation which can lead to localisation of deformation and therefore nucleation of discontinuities or propagation of existing ones. Laboratory experiments, together with microscopic observations (EMP and 3D CT-scans) can be used to identify and quantify the microscopic processes controlling the initiation and propagation of localised deformation. They can also help to develop an appropriate physical formulation of the problem capturing the considered processes. Finally this physical framework can be used to extend the present XFEM formulation to consider the responsible processes for the THM behaviour of fractures and faults in a multiscale nature. Altogether, the improvement suggestions of this multiscale approach bear further challenges in the integration of new observations from the laboratory and in the numerical implementation of microscopic-based processes. Tackling these challenges can open new possibilities for future studies focusing on the fault rupturing process for example.

8.3 Further constraints of the physical framework and motivation for new experimental design

One advantage of the workflow developed in the frame of this thesis relies in its flexibility to integrate novel observations as constraints to the physical models. In this

final discussion, I present a serie of designs for laboratory experiments, which could help to extend the current physical framework and may therefore be the subject of future work.

The evolution of porosity as induced by thermal perturbations was recognised in Chapter 4 as quite complex. It depends mot only on the bulk properties (thermal expansion coefficient) as calculated by a mixture law but rather depends on the hydromechanical conditions, and a complex interaction between the solid grains and the contained fluid. Conceptual model developed in Chapters 2 and 4 indicates that the changes in temperature can induce both an increase or a decrease in porosity depending on the mechanical state and the nature of the rock (Biot coefficient and porosity). Novel laboratory experiments could therefore help to better constrain this relation by means of several rock types and further validate the physical framework. In the laboratory, continuous measurement of porosity can be conducted under different mechanical states (different confinements with an additional deviatoric component) combined together with thermal loading conditions (Pei et al., 2016). A catalogue of such experiments by varying mechanical conditions could further help to validate and constrain the physical framework. In addition, relevance of thermal processes for the onset of microcracking can be further investigated by means of laboratory experiments.

As already stated in the previous part of this discussion, quantifying the alterations of permeability is not trivial, especially within localised deformation features. Deformation can indeed localise in a preferential direction and therefore induce large anisotropy of the permeability tensor. From an Experimental perspective, it is often not possible to measure continuously both the porosity and the permeability during a triaxial test. In this thesis (Chapter 7 and Appendix C), I presented laboratory experiments investigating the evolution of porosity during the process of localisation of deformation. As further investigations, additional experiments could be conducted to record continuously the permeability in different directions (in the direction of the maximum or the minimum principal stress) during the onset and propagation of shear-enhanced compaction bands. Permeability does not only depend on porosity but rather on several parameters involving porosity, shape of the pores and their interconnectivity. Having a better constraint on these parameters could therefore be achieved by making use of novel laboratory experiments but also with high resolution CT-scans of the samples post-mortem (after failure) by measuring numerically its transport properties (Min et al., 2004; Mostaghimi et al., 2013).

8.4 Conclusions

In the frame of this thesis, a workflow for modelling multiscale physical THM processes for fractured geothermal reservoirs was developed and presented. Its applicability for field scale applications related to geothermal energy extraction has also been illustrated by means of a number of examples. Starting from a geological model, this workflow includes space discretisation of complex geometries and a powerful scalable numerical simulator based on the finite-element-method (FEM). It considers (1) the details of the multiphysics (THM coupling) nature of porous media applications; (2) It enable to quantify the strong coupling among these processes and relevant material properties, and linking them across the different relevant scales; and (3) it enables the full integration of the heterogeneous characteristic of geological systems, including macrofractures and fault zones.

By its applications to field case study cases, a number of first order conclusions have been derived. Processes controlling the deformation of a porous medium, which have been so far considered of secondary relevance, have been recognised as having an overall control on reservoirs performances, and on their long-term sustainability. Coupling among mechanical and hydrothermal flow is essential to assess the stability and sustainability of induced fractures and to predict and quantify potential detrimental effects from operations such as reactivation of pre-existing faults and induced seismicity.

To account for the multiscale nature of porous media, description of non-linear relations between the microscopic structure and the macroscopic properties have been developed and constrained by means of laboratory data. These considerations allow to account for processes which evolve within and from the microscopic framework of porous media, but have been often neglected while addressing the mesoscale dynamics of reservoirs. The relevance of deformation processes and their coupling with the fluid flow and heat transport was further emphasised as the main controlling processes driving these non-linear structure property relations.

The integration of the complex geometry of discrete geological structures has been combined in the present workflow with the description of their impacts on the hydrothermal flow. I have derived a physical description of fractures acting as preferential fluid pathways and therefore exerting a first order control on the overall reservoir hydrodynamics, especially for low porosity, low permeability rocks. In the outlooks to this thesis, I have also described in some details possible ways to extend the current numerical framework to account for additional processes related to fracture mechanics and to describe the physics responsible for spontaneous failure of rock samples.

The results presented in this thesis helped at improving the predictions for geothermal operations in three aspects. Multiphysic and dynamic modelling of the THM processes occurring in reservoir rocks, combined with non-linear relations between microstructure and macroscopic properties helped at improving the prediction of the life time and productivity of a geothermal reservoir. Thermal evolution of the reservoir state during operations has also been considered to constrain its impacts on potential thermal-induced fault reactivations, therefore providing more insights into the environmental safety of geothermal operations. Finally, a complete hydromechanical coupling has been used to characterise the hydraulic state of a geothermal reservoir during stimulation of a well which provided an explanation on the causative process behind field observations which were left unexplained before, consisting in instantaneous increases in pore pressure propagating at large distances from the stimulated well.

By combining laboratory experiments, field measurements and numerical techniques, and because of its flexibility to incorporate new information as available, the workflow presented in this study will provide an effective tool to help improving the predictive capabilities of any reservoir operation.

References

Al-Wardy, W. and Zimmerman, R. W. (2004). Effective stress law for the permeability of clay-rich sandstones. *Journal of Geophysical Research*, 109(October 2003):1–10.

Anderson, E. M. (1905). The dynamics of faulting. *Transactions of the Edinburgh Geological Society*, 8(3):387–402.

Bai, M., Meng, F., Roegiers, J. C., and Green, S. (2002). Improved determination of stress-dependent permeability for anisotropic formations. *Proceedings of SPE/ISRM Rock Mechanics Conference*.

Balay, S., Abhyankhar, S., Adams, M. F., Brown, J., Brune, P., Buschelman, K., Dalcin, L., Eijkhout, V., Gropp, W. D., Kaushik, D., Knepley, M. G., Curfman McInnes, L., Rupp, K., Smith, B. F., Zampini, S., and Zhang, H. (2016). Petsc users manual. Technical report, Argonne National Laboratory.

Barton, C. a., Hickman, S., Morin, R., Zoback, M. D., Finkbeiner, T., Sassj, J., and Benoit, D. (1997). Fracture permeability and its relationship to in-situ stress in the dixie valley, nevada, geothermal reservoir. *Twenty-Second Workshop on Geothermal Reservoir Engineering, Stanford University SGP-TR-155*, pages 147–152.

Barton, C. a., Zoback, M. D., and Moos, D. (1995). Fluid flow along potentially active faults in crystalline rock. *Geology*, 23(8):683–686.

Baud, P., Klein, E., and fong Wong, T. (2004). Compaction localization in porous sandstones: Spatial evolution of damage and acoustic emission activity. *Journal of Structural Geology*, 26(4):603–624.

Baud, P., Vajdova, V., and Wong, T. F. (2006). Shear-enhanced compaction and strain localization: Inelastic deformation and constitutive modeling of four porous sandstones. *Journal of Geophysical Research: Solid Earth*, 111(12):1–17.

Bear, J. (1988). *Dynamics of Fluids in Porous Media*. Dover, dover book edition.

Bense, V. F., Van den Berg, E. H., and Van Balen, R. T. (2003). Deformation mechanisms and hydraulic properties of fault zones in unconsolidated sediments; the roer valley rift system, the netherlands. *Hydrogeology Journal*, 11(3):319–332.

Bernabe, Y. (1986). The effective pressure law for permeability in chelmsford granite and barre granite. *International Journal of Rock Mechanics and Mining Sciences & Geomechanics Abstracts*, 23(3):267–275.

Biot, M. A. (1956). General solutions of the equations of elasticity and consolidation for a porous material. *Journal of Applied Mechanics*, 78:91–96.

Biot, M. A. (1973). Nonlinear and semilinear rheology of porous solids. *J Geophys Res*, 78(23):4924–4937.

Biot, M. A. and Willis, D. (1957). The elastic coefficients of the theory of consolidation. *J. appl. Mech*, pages 594–601.

Blöcher, G., Cacace, M., Reinsch, T., and Watanabe, N. (2015). Evaluation of three exploitation concepts for a deep geothermal system in the north german basin. *Computers & Geosciences*, 82:120–129.

Blöcher, G., Reinsch, T., Hassanzadegan, A., Milsch, H., and Zimmermann, G. (2014). Direct and indirect laboratory measurements of poroelastic properties of two consolidated sandstones. *International Journal of Rock Mechanics and Mining Sciences*, 67:191–201.

Blöcher, G., Reinsch, T., Henninges, J., Milsch, H., Regenspurg, S., Kummerow, J., Francke, H., Kranz, S., Saadat, A., Zimmermann, G., and Huenges, E. (2016). Hydraulic history and current state of the deep geothermal reservoir groß schönebeck. *Geothermics*, 63:27–43.

Blöcher, G., Zimmermann, G., and Milsch, H. (2009). Impact of poroelastic response of sandstones on geothermal power production. *Pure and Applied Geophysics*, 166:1107–1123.

Blöcher, G., Zimmermann, G., Moeck, I., Brandt, W., Hassanzadegan, A., and Magri, F. (2010). 3d numerical modeling of hydrothermal processes during the lifetime of a deep geothermal reservoir. *Geofluids*, 10(3):406–421.

Blöcher, G., Zimmermann, G., Moeck, I., and Huenges, E. (2012). Groß schönebeck (d) - moving forward on the learning curve: lessons learned from projects in the recent years from projects. In *International Conference on Enhanced Geothermal Systems*, Freiburg, Germany.

Broek, D. (1986). *Elementary engineering fracture mechanics*. Springer Netherlands, Dordrecht.

Brooks, A. N. and Hughes, T. J. R. (1982). Streamline upwind/petrov-galerkin formulations for convection dominated flows with particular emphasis on the incompressible navier-stokes equations. *Computer Methods in Applied Mechanics and Engineering*, 32(1):199–259.

Byerlee, J. (1978). Friction of rocks. *Pure and Applied Geophysics PAGEOPH*, 116:615–626.

Cacace, M. and Blöcher, G. (2015). Meshit - a software for three dimensional volumetric meshing of complex faulted reservoirs. *Environmental Earth Sciences*, 74(6):5191–5209.

Cacace, M., Blöcher, G., Watanabe, N., Moeck, I., Börsing, N., Scheck-Wenderoth, M., Kolditz, O., and Huenges, E. (2013). Modelling of fractured carbonate reservoirs: outline of a novel technique via a case study from the molasse basin, southern bavaria, germany. *Environmental Earth Sciences*, 70(8):3585–3602.

Caine, J. S., Evans, J. P., and Forster, C. B. (1996). Fault zone architechture and permeability structure. *Geology*, 24(11):1025–1028.

Cappa, F. and Rutqvist, J. (2011). Modeling of coupled deformation and permeability evolution during fault reactivation induced by deep underground injection of co2. *International Journal of Greenhouse Gas Control*, 5(2):336–346.

Carman, P. (1956). *Flow of Gases through Porous Media*. Butterworths Scientific Publications.

Carrol, M. M. and Katsube, N. (1983). The role of terzaghi effective stress in linearly elastic deformation. *Journal of Energy Ressources Technology*, 105:509–511.

Cherubini, Y., Cacace, M., Blöcher, G., and Scheck-Wenderoth, M. (2013). Impact of single inclined faults on the fluid flow and heat transport: results from 3-d finite element simulations. *Environmental Earth Sciences*, 70(8):3603–3618.

Cherubini, Y., Cacace, M., Scheck-Wenderoth, M., and Noack, V. (2014). Influence of major fault zones on 3-d coupled fluid and heat transport for the brandenburg region (ne german basin). *Geothermal Energy Science*, 2(1):1–20.

Chin, L. Y., Raghavan, R., and Thomas, L. K. (2000). Fully coupled geomechanics and fluid-flow analysis of wells with stress-dependent permeability. *SPE Journal*, 5(01):32–45.

Clauser, C., editor (2003). *Numerical Simulation of Reactive Flow in Hot Aquifers*. Springer Berlin Heidelberg, Berlin, Heidelberg.

Cosserat, E. and Cosserat, F. (1909). *Théorie des corps déformables (engl. translation by D. Delphenich 2007)*. Scientific Library A. Hermann and sons.

Crump, K. S. (1976). Numerical inversion of laplace transforms using a fourier series approximation. *Journal of the ACM*, 23(1):89–96.

Cryer, C. W. (1963). a comparison of the three-dimensional consolidation theories of biot and terzaghi. *The Quarterly Journal of Mechanics and Applied Mathematics*, 16(4):401–412.

da Silva, V. D. (2004). A simple model for viscous regularization of elasto-plastic constitutive laws with softening. *Communications in Numerical Methods in Engineering*, 20(7):547–568.

Dautriat, J., Gland, N., Guelard, J., Dimanov, A., and Raphanel, J. L. (2009). Axial and radial permeability evolutions of compressed sandstones: End effects and shear-band induced permeability anisotropy. *Pure and Applied Geophysics*, 166(5-7):1037–1061.

David, C., Wong, T. F., Zhu, W., and Zhang, J. (1994). Laboratory measurement of compaction-induced permeability change in porous rocks: Implications for the generation and maintenance of pore pressure excess in the crust. *Pure and Applied Geophysics PAGEOPH*, 143(1-3):425–456.

Deichmann, N. and Giardini, D. (2009). Earthquakes induced by the stimulation of an enhanced geothermal system below basel (switzerland). *Seismological Research Letters*, 80(5):784–798.

Doyen, P. M. (1988). Permeability, conductivity, and pore geometry of sandstone. *Journal of Geophysical Research*, 93(7):7729.

Durham, W. B. and Bonner, B. P. (1994). Self-propping and fluid flow in slightly offset joints at high effective pressures. *Journal of Geophysical Research*, 99(B5):9391–9399.

Ecomides, M. J. and Nolte, K. G. (2000). *Reservoir Stimulation*. Wiley and Sons Ltd., New York.

Elder, J. W. (1967). Transient convection in a porous medium. *Journal of Fluid Mechanics*, 27(03):609.

Fatt, M. A. and Davis, D. H. (1952). Reduction in permeability with overburden pressure. Technical report, California Research Corporation, La Habra.

Faulkner, D. R., Jackson, C. a. L., Lunn, R. J., Schlische, R. W., Shipton, Z. K., Wibberley, C. a. J., and Withjack, M. O. (2010). A review of recent developments concerning the structure, mechanics and fluid flow properties of fault zones. *Journal of Structural Geology*, 32(11):1557–1575.

Galeão, A. C., Almeida, R. C., Malta, S. M. C., and Loula, A. F. D. (2004). Finite element analysis of convection dominated reaction–diffusion problems. *Applied Numerical Mathematics*, 48(2):205–222.

Gaston, D., Newman, C., Hansen, G., and Lebrun-Grandié, D. (2009). Moose: A parallel computational framework for coupled systems of nonlinear equations. *Nuclear Engineering and Design*, 239(10):1768–1778.

Gébelin, A., Mulch, A., Teyssier, C., Heizler, M., Vennemann, T., and Seaton, N. C. A. (2011). Oligo-miocene extensional tectonics and fluid flow across the northern snake range detachment system, nevada. *Tectonics*, 30(5).

Geertsma, J. (1957). A remark on the analogy between thermoelasticity and the elasticity of saturated porous media. *Journal of the Mechanics and Physics of Solids*, 6(1):13–16.

Genter, A., Goerke, X., Graff, J.-j., Cuenot, N., Krall, G., Schindler, M., and Ravier, G. (2010). Current status of the egs soultz geothermal project (france). *World Geothermal Congress*, C(April):25–29.

Gérard, A., Genter, A., Kohl, T., Lutz, P., Rose, P., and Rummel, F. (2006). The deep egs (enhanced geothermal system) project at soultz-sous-forêts (alsace, france). *Geothermics*, 35(5-6):473–483.

Ghabezloo, S. and Sulem, J. (2009). Stress dependent thermal pressurization of a fluid-saturated rock. *Rock Mechanics and Rock Engineering*, 42:1–24.

Ghabezloo, S., Sulem, J., Guédon, S., and Martineau, F. (2009a). Effective stress law for the permeability of a limestone. *International Journal of Rock Mechanics and Mining Sciences*, 46(2):297–306.

Ghabezloo, S., Sulem, J., and Saint-Marc, J. (2008). The effect of undrained heating on a fluid-saturated hardened cement paste. *Cement and Concrete Research*, 39:54–64.

Ghabezloo, S., Sulem, J., and Saint-Marc, J. (2009b). Evaluation of a permeability–porosity relationship in a low-permeability creeping material using a single transient test. *International Journal of Rock Mechanics and Mining Sciences*, 46(4):761–768.

Guéguen, Y. and Boutéca, M. (2004). *Mechanics of Fluid-Saturated Rocks*. Academic Press, New York, internatio edition.

Haimson, B. and Fairhurst, C. (1969). Hydraulic fracturing in porous-permeable materials. *Journal of Petroleum Technology*, 21(07):811–817.

Han, G. and Dusseault, M. B. (2003). Description of fluid flow around a wellbore with stress-dependent porosity and permeability. *Journal of Petroleum Science and Engineering*, 40(1-2):1–16.

Hansbo, A. and Hansbo, P. (2004). A finite element method for the simulation of strong and weak discontinuities in solid mechanics. *Computer Methods in Applied Mechanics and Engineering*, 193(33-35):3523–3540.

Hassanzadegan, A., Blöcher, G., Zimmermann, G., and Milsch, H. (2012). Thermoporoelastic properties of flechtinger sandstone. *International Journal of Rock Mechanics and Mining Sciences*, 49:94–104.

Hassanzadegan, A. and Zimmermann, G. (2013). A poroelastic description of permeability evolution. *Pure and Applied Geophysics*, 171(7):1187–1201.

Heidbach, O., Rajabi, M., Reiter, K., and Ziegler, M. (2016). World stress map 2016.

Hertz, H. (1985). *Collected works*. J. A. Barth, Leipzig.

Holl, H., Moeck, I., and Schandelmeier, H. (2005). Characterisation of the tectonosedimentary evolution of a geothermal reservoir – implications for exploitation (southern permian basin , ne germany). In *Proceedings World Geothermal Congress*.

Hudson, J. A. and Harrison, J. P. (1997). Anisotropy and inhomogeneity. In *Engineering Rock Mechanics*, pages 163–172. Elsevier.

Huenges, E. and Hurter, S. (2002). In-situ geothermielabor groß schönebeck 2000/2001 : Bohrarbeiten, bohrlochmessungen, hydralik, formationsfluide, tonminerale. Technical report, GeoForschungsZentrum Potsdam.

IAPWS (2008a). Release on the iapws formulation 2008 for the thermodynamic properties of seawater. Technical report, The International Association for the Properties of Water and Steam.

IAPWS (2008b). Release on the iapws formulation 2008 for the viscosity of ordinary water substance. Technical report, The International Association for the Properties of Water and Steam.

Jacquey, A. B., Cacace, M., Blöcher, G., and Scheck-Wenderoth, M. (2015a). Numerical investigation of thermoelastic effects on fault slip tendency during injection and production of geothermal fluids. *Energy Procedia*, 76:311–320.

Jacquey, A. B., Cacace, M., Blöcher, G., Watanabe, N., Huenges, E., and Scheck-Wenderoth, M. (2016). Thermo-poroelastic numerical modelling for enhanced geothermal system performance: Case study of the groß schönebeck reservoir. *Tectonophysics*, 684:119–130.

Jacquey, A. B., Cacace, M., Blöcher, G., Watanabe, N., and Scheck-Wenderoth, M. (2015b). Hydro-mechanical evolution of transport properties in porous media : Constraints for numerical simulations roman symbols. *Transport in Porous Media*, 110(3):409–428.

Jaeger, J., Cook, N. G., and Zimmerman, R. W. (2007). *Fundamentals of Rock Mechanics*. Blackwell, Oxford.

James, O. (1999). *Fluid Mechanics for Chemical Engineering*. Wilkes Prentice Hal, Mew Jersey.

Khoei, A. R. (2014). *Extended Finite Element Method*. John Wiley & Sons, Ltd, Chichester, UK.

Kim, J. M. and Parizek, R. R. (1997). Numerical simulation of the noordbergum effect resulting from groundwater pumping in a layered aquifer system. *Journal of Hydrology*, 202(1-4):231–243.

Kirk, B. S., Peterson, J. W., Stogner, R. H., and Carey, G. F. (2006). libmesh : a c++ library for parallel adaptive mesh refinement/coarsening simulations. *Engineering with Computers*, 22(3-4):237–254.

Klein, E. and Reuschlé, T. (2003). A model for the mechanical behaviour of bentheim sandstone in the brittle regime. *Pure and Applied Geophysics*, 160(5):833–849.

Kolditz, O., Bauer, S., Bilke, L., Böttcher, N., Delfs, J. O., Fischer, T., Görke, U. J., Kalbacher, T., Kosakowski, G., McDermott, C. I., Park, C. H., Radu, F., Rink, K., Shao, H., Shao, H. B., Sun, F., Sun, Y. Y., Singh, a. K., Taron, J., Walther, M., Wang, W., Watanabe, N., Wu, Y., Xie, M., Xu, W., and Zehner, B. (2012a). Opengeosys: an open-source initiative for numerical simulation of thermo-hydro-mechanical/chemical (thm/c) processes in porous media. *Environmental Earth Sciences*, 67(2):589–599.

Kolditz, O., Görke, U.-J., Shao, H., and Wang, W. (2012b). Introduction. In Kolditz, O., Shao, H., Görke, U. J., and Wang, W., editors, *Thermo-Hydro-Mechanical-Chemical Processes in Fractured Porous Media*, pages 1–6. Springer, Berlin.

Kwiatek, G., Bohnhoff, M., Dresen, G., Schulze, A., Schulte, T., Zimmermann, G., and Huenges, E. (2010). Microseismicity induced during fluid-injection: A case study from the geothermal site at groß schönebeck, north german basin. *Acta Geophysica*, 58(6):995–1020.

Legarth, B., Huenges, E., and Zimmermann, G. (2005). Hydraulic fracturing in a sedimentary geothermal reservoir: Results and implications. *International Journal of Rock Mechanics and Mining Sciences*, 42:1028–1041.

Lisle, R. J. and Srivastava, D. C. (2004). Test of the frictional reactivation theory for faults and validity of fault-slip analysis. *Geology*, 32(7):569–572.

Lockner, D. A. (2002). Undrained poroelastic response of sandstones to deviatoric stress change. *Journal of Geophysical Research*, 107(B12):2353.

Lord, H. W. and Shulman, Y. (1967). A generalized dynamical theory of thermoelasticity. *Journal of the Mechanics and Physics of Solids*, 15(5):299–309.

Mandel, J. (1953). Consolidation des sols (étude mathématique). *Géotechnique*, 3(7):287–299.

McCartney, J. S., Sanchez, M., and Tomac, I. (2016). Energy geotechnics: Advances in subsurface energy recovery, storage, exchange, and waste management. *Computers and Geotechnics*, 75:244–256.

McTigue, D. F. (1986). Thermoelastic response of fluid-saturated porous rock. *Journal of Geophysical Research*, 91(B9):9533.

Mehrabian, A. and Abousleiman, Y. N. (2014). Generalized biot's theory and mandel's problem of multiple-porosity and multiple-permeability poroelasticity. *Journal of Geophysical Research: Solid Earth*, 119(4):2745–2763.

Milsch, H., Blöcher, G., and Engelmann, S. (2008). The relationship between hydraulic and electrical transport properties in sandstones: An experimental evaluation of several scaling models. *Earth and Planetary Science Letters*, 275(3-4):355–363.

Milsch, H., Seibt, a., and Spangenberg, E. (2009). Long-term petrophysical investigations on geothermal reservoir rocks at simulated in situ conditions. *Transport in Porous Media*, 77:59–78.

Min, K.-B., Rutqvist, J., Tsang, C.-F., and Jing, L. (2004). Stress-dependent permeability of fractured rock masses: a numerical study. *International Journal of Rock Mechanics and Mining Sciences*, 41(7):1191–1210.

Moeck, I. and Backers, T. (2006). New ways in understanding borehole breakouts and wellbore stability by fracture mechanics based numerical modelling. In *68th EAGE Conference and Exhibition incorporating SPE EUROPEC 2006*, pages 214–218.

Moeck, I., Kwiatek, G., and Zimmermann, G. (2009a). Slip tendency analysis, fault reactivation potential and induced seismicity in a deep geothermal reservoir. *Journal of Structural Geology*, 31:1174–1182.

Moeck, I., Schandelmeier, H., and Holl, H. G. (2009b). The stress regime in a rotliegend reservoir of the northeast german basin. *International Journal of Earth Sciences*, 98:1643–1654.

Moore, J. R. and Glaser, S. D. (2007). Self-potential observations during hydraulic fracturing. *Journal of Geophysical Research: Solid Earth*, 112(2):1–17.

Morlier, P. (1971). Description de l'état de fissuration d'une roche à partir d'essais non-destructifs simples. *Rock Mechanics*, 138.

Morris, A., Ferrill, D. a., and Henderson, D. B. (1996). Slip-tendency analysis and fault reactivation slip-tendency analysis and fault reactivation. *Geology*, 24(3):275–278.

Mostaghimi, P., Blunt, M. J., and Bijeljic, B. (2013). Computations of absolute permeability on micro-ct images. *Mathematical Geosciences*, 45(1):103–125.

Mulch, A., Teyssier, C., Cosca, M. A., and Chamberlain, C. P. (2007). Stable isotope paleoaltimetry of eocene core complexes in the north american cordillera. *Tectonics*, 26(4):1–13.

Mura, T. (1987). *Micromechanics of defects in solids*, volume 3 of *Mechanics of Elastic and Inelastic Solids*. Springer Netherlands, Dordrecht.

Norden, B., Förster, A., and Balling, N. (2008). Heat flow and lithospheric thermal regime in the northeast german basin. *Tectonophysics*, 460(1-4):215–229.

Norris, A. (1992). On the correspondence between poroelasticity and thermoelasticity. *Journal of Applied Physics*, 71(3):1138–1141.

Ogata, A. and Banks, R. B. (1961). A solution of the differential equation of longitudinal dispersion in porous media. Technical report, US Geological Survey.

O'Sullivan, M. J., Pruess, K., and Lippmann, M. J. (2001). State of the art of geothermal reservoir simulation. *Geothermics*, 30(4):395–429.

Pardoen, B., Levasseur, S., and Collin, F. (2015). Using local second gradient model and shear strain localisation to model the excavation damaged zone in unsaturated claystone. *Rock Mechanics and Rock Engineering*, 48(2):691–714.

Pei, L., Blöcher, G., Milsch, H., Deon, F., Zimmermann, G., Rühaak, W., Sass, I., and Huenges, E. (2016). Thermal strain in a water-saturated limestone under hydrostatic and deviatoric stress states. *Tectonophysics*, 688:49–64.

Perzyna, P. (1966). Fundamental problems in viscoplasticity. In *Advances in Applied Mechanics*, pages 243–377. Elsevier.

Peška, P. and Zoback, M. D. (1995). Compressive and tensile failure of inclined well bores and determination of in situ stress and rock strength. *Journal of Geophysical Research*, 100:12791.

Pili, É., Poitrasson, F., and Gratier, J. P. (2002). Carbon-oxygen isotope and trace element constraints on how fluids percolate faulted limestones from the san andreas fault system: Partitioning of fluid sources and pathways. *Chemical Geology*, 190(1-4):231–250.

Raghavan, R. and Chin, L. Y. (2004). Productivity changes in reservoirs with stress-dependent permeability. *Society of Petroleum Engineers*, 7(August).

Ramsay, J. G. and Lisle, R. L. (2000). Volume 3: Applications of continuum mechanics in structural geology. In *The Techniques of Modern Structural Geology*, page 560. Academic Press, London.

Reinicke, A., Zimmermann, G., Huenges, E., and Burkhardt, H. (2005). Estimation of hydraulic parameters after stimulation experiments in the geothermal reservoir groß schönebeck 3/90 (north-german basin). *International Journal of Rock Mechanics and Mining Sciences*, 42:1082–1087.

Richardson, C. L., Hegemann, J., Sifakis, E., Hellrung, J., and Teran, J. M. (2011). An xfem method for modeling geometrically elaborate crack propagation in brittle materials. *International Journal for Numerical Methods in Engineering*, 88(10):1042–1065.

Rinaldi, A. P., Rutqvist, J., and Cappa, F. (2014). Geomechanical effects on co2 leakage through fault zones during large-scale underground injection. *International Journal of Greenhouse Gas Control*, 20:117–131.

Rodrigues, J. D. (1983). The noordbergum effect and characterization of aquitards at the rio maior mining project. *Ground Water*, 21(2):200–207.

Rutqvist, J., Rinaldi, A. P., Cappa, F., and Moridis, G. J. (2013). Modeling of fault reactivation and induced seismicity during hydraulic fracturing of shale-gas reservoirs. *Journal of Petroleum Science and Engineering*, 107:31–44.

Rutqvist, J., Rinaldi, A. P., Cappa, F., and Moridis, G. J. (2015). Modeling of fault activation and seismicity by injection directly into a fault zone associated with hydraulic fracturing of shale-gas reservoirs. *Journal of Petroleum Science and Engineering*, 127:377–386.

Schaeffer, D. G. (1990). Instability and ill-posedness in the deformation of granular materials. *International Journal for Numerical and Analytical Methods in Geomechanics*, 14(4):253–278.

Schiffman, R. L. (1989). The finite element method in the deformation and consolidation of porous media (roland w. lewis and bernard a. schrefler). *SIAM Review*, 31(1):160–161.

Segall, P. and Fitzgerald, S. D. (1998). A note on induced stress changes in hydrocarbon and geothermal reservoirs. *Tectonophysics*, 289(1-3):117–128.

Segall, P. and Lu, S. (2015). Injection-induced seismicity: Poroelastic and earthquake nucleation effects. *Journal of Geophysical Research: Solid Earth*, 120:1–22.

Simo, J. C. and Hughes, T. J. R. (1998). *Computational Inelasticity*, volume 7 of *Interdisciplinary Applied Mathematics*. Springer-Verlag, New York.

Sisavath, S., Jing, X. D., and Zimmerman, R. W. (2000). Effect of stress on the hydraulic conductivity of rock pores. *Physics and Chemistry of the Earth, Part A: Solid Earth and Geodesy*, 25(2):163–168.

Slack, T. Z., Murdoch, L. C., Germanovich, L. N., and Hisz, D. B. (2013). Reverse water-level change during interference slug tests in fractured rock. *Water Resources Research*, 49(3):1552–1567.

Sluys, L. J. (1992). *Wave Propagation, Localisation and Dispersion in Softening Solids*. PhD thesis, Delft Technical University.

Soltanzadeh, H., Hawkes, C. D., and Smith, S. A. (2009). Poroelastic modelling of production and injection-induced stress changes in a pinnacle reef. In *Proceedings of RockEng09, Rock Engineering in Difficult Conditions*, pages 1–12, Toronto.

Somerton, W. H. (1992). *Thermal properties and Temperature Related Behaviour of Rock/Fluid Systems*. Elsevier, Amsterdam, developmen edition.

Souche, A., Medvedev, S., Andersen, T. B., and Dabrowski, M. (2013). Shear heating in extensional detachments: Implications for the thermal history of the devonian basins of w norway. *Tectonophysics*, 608:1073–1085.

Strack, O. D. L. (1982). Assessment of effectiveness of geologic isolation systems. analytic modeling of flow in a permeable fissured medium. Technical report, Pacific Northwest National Laboratory (PNNL), Richland, WA (United States).

Terzaghi, K. (1943). *Theoritical Soil Mechanics*. John Wiley & Sons.

Trautwein, U. and Huenges, E. (2005). Poroelastic behaviour of physical properties in rotliegend sandstones under uniaxial strain. *International Journal of Rock Mechanics and Mining Sciences*, 42:924–932.

Turner, a. K. (2005). Challenges and trends for geological modelling and visualisation. *Bulletin of Engineering Geology and the Environment*, 65(2):109–127.

Vardoulakis, I. and Sulem, J. (1995). *Bifurcation Analysis in Geomechanics*. Chapman & Hall.

Vermeer, P. A. and de Borst, R. (1984). Non-associated plasticity for soils, concrete and rock. *HERON*, 29(3):3–64.

Verruijt, A. (1969). Elastic storage of aquifers. In *Flow through porous media*, pages 331–376. Academic Press.

Verruijt, A. (2010). *An Introduction to Soil Dynamics*. Springer Netherlands, Dordrecht.

Vinci, C., Renner, J., and Steeb, H. (2014). A hybrid-dimensional approach for an efficient numerical modeling of the hydro-mechanics of fractures. *Water Resources Research*, 50(2):1616–1635.

Walder, J. and Nur, A. (1984). Porosity reduction and crustal pore pressure development. *Journal of Geophysical Research: Solid Earth ...*, 89.

Wang, W. and Kolditz, O. (2007). Object-oriented finite element analysis of thermo-hydro-mechanical (thm) problems in porous media. *International Journal for Numerical Methods in Engineering*, 69(May 2006):162–201.

Wang, W. M., Sluys, L. J., and De Borst, R. (1997). Viscoplasticity for instabilities due to strain softening and strain-rate softening. *International Journal for Numerical Methods in Engineering*, 40(20):3839–3864.

Warren, W. E. and Smith, C. W. (1985). In situ stress estimates from hydraulic fracturing and direct observation of crack orientation. *Journal of Geophysical Research*, 90(B8):6829.

Watanabe, N. (2011). *Finite element method for coupled thermo-hydro-mechanical processes in discretely fractured and non-fractured porous media*. PhD thesis, Dresden Technical University.

Watanabe, N., Wang, W., Taron, J., Görke, U. J., and Kolditz, O. (2012). Lower-dimensional interface elements with local enrichment : application to coupled hydro-mechanical problems in discretely fractured porous media. *International Journal for Numerical Methods in Engineering*, pages 1010–1034.

Wolff, R. G. (1970). Relationship between horizontal strain near a well and reverse water level fluctuation. *Water Resources Research*, 6(6):1721–1728.

Wu, R., Germanovich, L. N., Van Dyke, P. E., and Lowell, R. P. (2007). Thermal technique for controlling hydraulic fractures. *Journal of Geophysical Research: Solid Earth*, 112(5):1–15.

Yew, C. H. (1997). *Mechanics of Hydraulic Fracturing*. Gulf Publisching Co., Houston.

Zhao, J., Xiao, W., Li, M., Xiang, Z., Li, L., and Wang, J. (2011). The effective pressure law for permeability of clay-rich sandstones. *Petroleum Science*, 8:194–199.

Zimmerman, R. W. (1991). *Compressibility of Sandstones*. Elsevier, Amsterdam.

Zimmerman, R. W. (2000). Coupling in poroelasticity and thermoelasticity. *International Journal of Rock Mechanics and Mining Sciences*, 37(1-2):79–87.

Zimmermann, G., Blöcher, G., Reinicke, A., and Brandt, W. (2011). Rock specific hydraulic fracturing and matrix acidizing to enhance a geothermal system — concepts and field results. *Tectonophysics*, 503(1-2):146–154.

Zimmermann, G., Moeck, I., and Blöcher, G. (2010). Cyclic waterfrac stimulation to develop an enhanced geothermal system (egs)-conceptual design and experimental results. *Geothermics*, 39:59–69.

Zimmermann, G. and Reinicke, A. (2010). Hydraulic stimulation of a deep sandstone reservoir to develop an enhanced geothermal system: Laboratory and field experiments. *Geothermics*, 39:70–77.

Zimmermann, G., Tischner, T., Legarth, B., and Huenges, E. (2009). Pressure-dependent production efficiency of an enhanced geothermal system (egs): Stimulation results and implications for hydraulic fracture treatments. *Pure and Applied Geophysics*, 166:1089–1106.

Appendix A

Appendix related to Chapter 3

A.1 Specific surface area for a packed bed of spheres

This appendix presents the determination of the specific surface area coefficient used in the permeability determination. These equations are inspired from flow through packed fixed and fluidised beds model for chemical engineering (James, 1999). The grains of the sandstone are considered spherical and have all the same radius. Void between these spheres are considered to be all connected (tortuosity $\tau = 1$). The specific surface area S is defined as:

$$S = \frac{S_w}{V_b} \tag{A.1}$$

where S_w is the wetted surface of the grains and V_b the bulk volume. The wetted surface of the grains is equal to the total solid surface area. If there is N grains in a volume V:

$$S_w = NS_{grain} = N4\pi r_g^2. \tag{A.2}$$

The bulk volume V_b is linked to the pore volume by: $V_\phi = \phi V_b = \phi\left(V_\phi + V_s\right)$ which gives:

$$V_b = \frac{V_s}{1-\phi} \tag{A.3}$$

where V_s is the total volume of grains, $V_s = N\frac{4}{3}\pi r_g^3$. Substituting Equation A.2 and A.3 in Equation A.1, gives:

$$S = \frac{N4\pi r_g^2 v}{\frac{1}{1-\phi}N\frac{4}{3}\pi r_g^3} \tag{A.4}$$

which is simplified to:

$$S = \frac{3\left(1-\phi\right)}{r_s}. \tag{A.5}$$

Appendix B

Appendix related to Chapter 6

B.1 Analytical solution for the one-dimensional poroelastic effect during cycling hydraulic stimulation

With the model configuration presented in Section 6.2.3, the stress-strain relation (equation 2.12) can be simplified using the small-strain approximation (equation 2.11) as:

$$\sigma'_{xx} = \frac{E}{\left(1 - \frac{2\nu^2}{1-\nu}\right)} \frac{\partial u_x}{\partial x}. \tag{B.1}$$

Furthermore, the momentum balance equation in term of stress (equation 2.10) leads to:

$$\frac{\partial \sigma'_{xx}}{\partial x} = \frac{\partial p_f}{\partial x}. \tag{B.2}$$

Therefore, substituting equations B.1 and B.2 into equation 2.22, one obtains an equation in term of the horizontal displacement: u_x:

$$\frac{\partial}{\partial t}\left(\frac{\partial u_x}{\partial x}\right) = \gamma \frac{\partial^3 u_x}{\partial x^3} \tag{B.3}$$

where γ is a constant depending on the hydromechanical properties of the medium as: $\gamma = \frac{k}{\mu_f} \frac{E}{\left(1-\frac{2\nu^2}{1-\nu}\right)}$

Using the Laplace transform on equation B.3 and the initial condition ($u_x(x, t = 0) = 0$), on can obtain:

$$\frac{\partial^3 \bar{u}_x}{\partial x^3} - \frac{s}{\gamma} \frac{\partial \bar{u}_x}{\partial x} = 0. \tag{B.4}$$

Equation B.4 can be solved using the transformed boundary conditions imposed in terms of displacement and pore pressure ($u_x(x = L, t) = 0$ and $p_f(x = 0, t) = p_0$). This yields to the following solution:

$$\bar{u}_x(x,s) = \bar{f}(s)\frac{\sinh\left(\sqrt{\frac{s}{\gamma}}\,(L-x)\right)}{\sinh\left(\sqrt{\frac{s}{\gamma}}L\right)}, \tag{B.5}$$

$$\bar{\sigma}'_{xx}(x,s) = -\bar{f}(s)\frac{E}{\left(1-\frac{2\nu^2}{1-\nu}\right)}\sqrt{\frac{s}{\gamma}}\frac{\cosh\left(\sqrt{\frac{s}{\gamma}}\,(L-x)\right)}{\sinh\left(\sqrt{\frac{s}{\gamma}}L\right)}, \tag{B.6}$$

$$\bar{p}_f(x,s) = \frac{p_0}{s} + \bar{f}(s)\frac{E}{\left(1-\frac{2\nu^2}{1-\nu}\right)}\sqrt{\frac{s}{\gamma}}\frac{\left(\cosh\left(\sqrt{\frac{s}{\gamma}}L\right) - \cosh\left(\sqrt{\frac{s}{\gamma}}\,(L-x)\right)\right)}{\sinh\left(\sqrt{\frac{s}{\gamma}}L\right)} \tag{B.7}$$

where $\bar{f}(s)$ is the transformed boundary condition at $x = 0$ m for displacement defined in Equation 6.1 which has the form: $\bar{f}(s) = a\left(\frac{1}{s} - \frac{s}{s^2+\omega^2}\right)$. The values of the inverse of the Laplace transform of equations B.5 to B.7 is finally obtained using a Fourier series approximation algorithm (Crump, 1976).

Appendix C

Experimental study: triaxial experiments on Bentheim sandstone samples

C.1 Sample material

The behaviour of Bentheim sandstone during triaxial testing was investigated on three cylindrical sandstone samples (see samples SBS6-BB-01-01, SBS6-BB-01-02 and SBS6-BB-01-03 in Figure C.4) with a diameter of 5 cm and a length of 10 cm. Bentheim sandstone (Dautriat et al., 2009) is a Lower Cretaceous sedimentary rock that occurs as well-known outcrop sandstone from the Gildehausen quarry, near the village of Bentheim (Germany). The Bentheim sandstone is very homogeneous and is composed of quartz (95 %), kaolinite (3 %) and orthoclase (2 %) (Klein and Reuschlé, 2003; Baud et al., 2004). The initial porosity and permeability were measured to be 0.228 and approx. 800 mD, respectively. The porosity was measured by weighting the dry and saturated sample masses prior to the triaxial experiment. The permeability was measured during the saturation process but the obtained value was in the range of the apparatus limits (about 1 D) and therefore not considered in the following.

C.2 Experimental devices

The experiments were conducted in the triaxial mechanical testing system MTS 815 (Figure C.1). The confining pressure p_c ($0 - 140$ MPa) is applied by silicon oil pressurised by an external servo-controlled intensifier. The axial load ($0 - 1000$ kN) is generated by a servo-controlled loading piston.

Pore pressure was applied by four servo-controlled Quizix pumps. Two pumps each are connected to the upstream and downstream side, respectively. This allows continuous flow-through experiments at constant rates and pressures without interruption by refilling the pumps. The pumps have a resolution of fluid volumes as small as 1.35×10^{-5} mL and can operate at flow rates up to $200\,\mathrm{mL} \cdot \mathrm{min}^{-1}$. The maximum possible pore pressure is 68.9 MPa with a static accuracy of 0.06 % (Blöcher et al., 2014).

Two axial and one circumferential extensometers were attached to the rock specimens to detect their deformation. The circumferential extensometer enables displacement

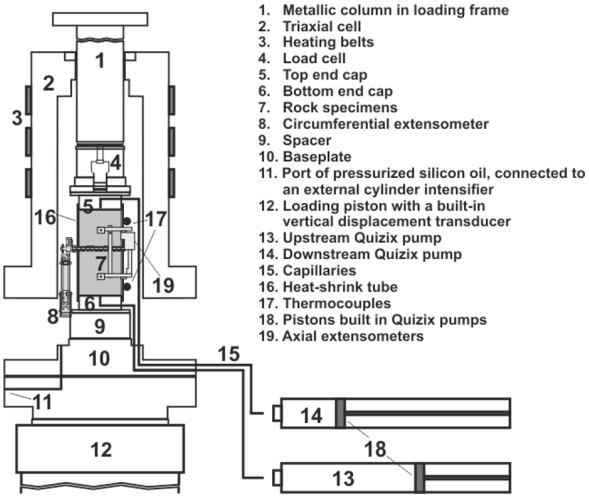

Fig. C.1 Sketch of the triaxial cell with connected pore fluid pump system (Pei et al., 2016).

measurements between $-2.5\,\mathrm{mm}$ and $8.0\,\mathrm{mm}$ with a resolution of $1 \times 10^{-3}\,\mathrm{mm}$ yielding a resolution of lateral strain of $6.0 \times 10^{-6}\,\mathrm{mm/mm}$. The axial extensometers enable displacement measurements between $-4.0\,\mathrm{mm}$ and $7.0\,\mathrm{mm}$ with a resolution of $1.0 \times 10^{-3}\,\mathrm{mm}$ yielding a resolution of axial strain of $2.0 \times 10^{-5}\,\mathrm{mm/mm}$. The aforementioned parameters were recorded in time intervals of 1 s.

C.3 Experimental procedure

The rock specimens were first oven dried at 60 °C before being jacketed using a heat-shrink tubing, equipped with the extensometers, and installed in the triaxial cell. Then a vacuum in the pore fluid system was applied and kept at a pressure of 6 mbar for approx. 1 day. Subsequently, a hydrostatic confining pressure of 1 MPa was applied followed by an increase in pore pressure to 0.1 MPa for sample SBS6-BB-01-01 and SBS6-BB-01-02 and to 0.5 MPa for sample SBS6-BB-01-03. Afterwards the pore pressure was kept constant at the downstream side and an appropriate flow rate at the upstream side was applied until the inflow rate equalised the outflow rate. Deionised water was used as the pore fluid. A pre-conditioning of the samples by cycling confining pressure was not conducted.

After saturation, a hydraulic short-circuit between the upstream and downstream sides of the sample was established. One downstream pump was filled with approximately 10 mL and was connected to the established short-circuit. The other three Quizix pumps were disconnected. A constant pore pressure of 0.1 MPa and 0.5 MPa was applied for the samples SBS6-BB-01-01, SBS6-BB-01-02 and SBS6-BB-01-03,

respectively. This pore pressure was kept constant during the first stage of the triaxial test. For the following stages the pore pressure was adjusted to 10 MPa. The pore volume change was recorded by the remaining Quizix pump. A pore volume change due to fluid compressibility was neglected. The following experimental stages were carried out (Figure C.2): (1) hydrostatic loading; (2) adjusting pore pressure to 10 MPa; (3) axial loading; (4) failure of the rock sample; and (5) post-failure measurements.

Stage (1) hydrostatic loading.
During this stage, the samples were hydrostatically loaded at a rate of $39\,\mathrm{MPa} \cdot \mathrm{h}^{-1}$ from the circum as well as from their end faces. No additional axial force was applied. For sample SBS6-BB-01-01, the confining pressure was increased from 1 to 40 MPa and the pore pressure was kept constant at 0.1 MPa. For sample SBS6-BB-01-02, the confining pressure was increased from 1 to 81 MPa and the pore pressure was kept constant at 0.1 MPa. For sample SBS6-BB-01-03, the confining pressure was increased from 1 to 100 MPa and the pore pressure was kept constant at 0.5 MPa.

Stage (2) adjusting pore pressure.
After hydrostatic loading, the pore pressure for all three samples was set to 10 MPa. This pressure change was performed by injecting fluid into the sample by the one connected Quizix pump. The required fluid volume to increase the pore pressure and the deformation of the sample were recorded during these adjustments. The confining pressure was kept constant at 40 MPa and 100 MPa for the samples SBS6-BB-01-01 and SBS6-BB-01-03, respectively. For sample SBS6-BB-01-02, the confining pressure was adjusted from 81 MPa to 70 MPa.

Stage (3) axial loading.
During this stage, the samples were axially loaded at a deformation rate of $1\,\mathrm{mm} \cdot \mathrm{h}^{-1}$. This deformation rate corresponds to a strain rate of $2.78 \times 10^{-6}\,\mathrm{s}^{-1}$. The pore pressure as well as the confining pressure were kept constant. The increase in axial force was measured by a build-in load cell. The deformation was recorded by the two axial and the one circumferential extensometers. The pore volume change was recorded by the one remaining Quizix pump connected to both sides of the sample.

Stage (4) failure of the rock sample.
The axial deformation was performed until a drop of the axial force could be monitored (Figure C.2). The drop in the axial force marks a failure of the rock sample. A

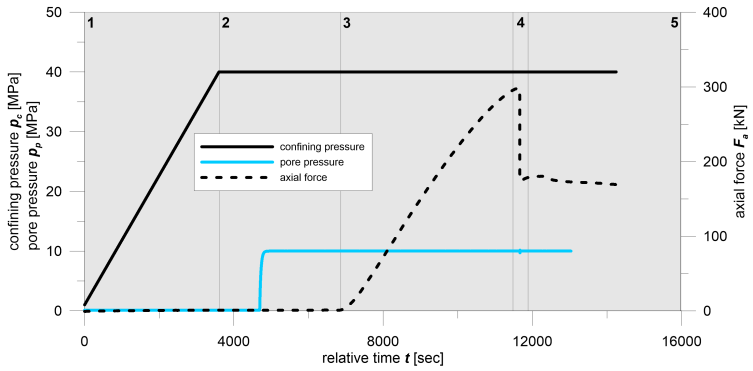

(a)

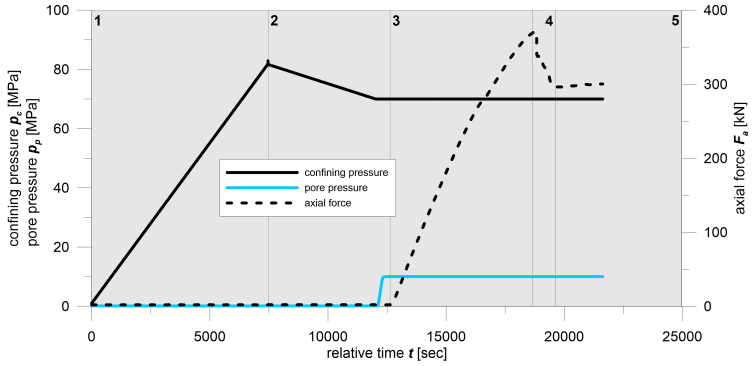

(b)

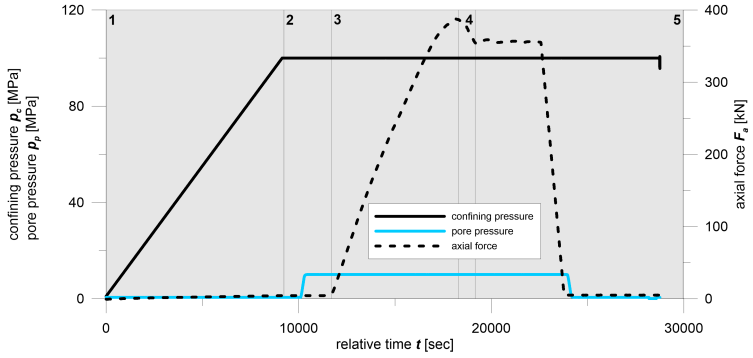

(c)

Fig. C.2 Design of three experiments (a) sample SBS6-BB-01-01; (b) sample SBS6-BB-01-02, (c) sample SBS6-BB-01-03 including the five stages: (1) hydrostatic loading; (2) adjusting pore pressure to 10 MPa; (3) axial loading; (4) failure of the rock sample; and (5) post-failure measurements.

continuous monitoring of deformation, pore volume change and axial force responses was performed.

Stage (5) post-failure measurements.
After the failure of the sample, the axial deformation ($1\,\mathrm{mm} \cdot \mathrm{h}^{-1}$) and strain rate

($2.78 \times 10^{-6}\,\mathrm{s}^{-1}$) were kept constant for approximately 1 h. During this time the pore pressure as well as the confining pressure were kept constant and a continuous monitoring of deformation, pore volume change and axial force responses was performed.

C.4 Data analysis

At the beginning of hydrostatic and axial loading the readouts of the two axial and the one circumferential extensometers were reset to 0. The average of the two axial extensometers was used as the axial strain ϵ_a and the lateral strain ϵ_l corresponds to the measurement of the circumferential extensometer. Finally the volumetric strain was calculated as $\epsilon_v = 2\epsilon_l + \epsilon_a$. In order to reduce the noise of the individual readouts, a sliding average of 40 data points (40 s) was performed for confining pressure, axial force, deviatoric stress, axial strain, lateral strain and volumetric strain. Based on these sliding averages the apparent Youngs's modulus E and Poisson's ratio ν were calculated.

In order to derive the porosity change, the fluid volume changes in the Quizix pump were recorded. The pore volume changes were assumed to be equivalent to the fluid volume changes in the pump. Based on the initial pore volume and the pore volume changes during the experiment, the current pore volume at any stage of the experiment can be calculated. The ratio between the current pore volume and the initial bulk volume expresses the Lagrangian porosity ϕ used in the experimental study.

C.5 Experimental results

In this contribution, only the experimental results obtained during axial loading are presented. The stress-strain relation and the dependency of the apparent Young's modulus, Poisson's ratio and porosity on axial strain were investigated (Figure C.3). All quantities show a linear dependency on axial strain until a value of $\epsilon_a = 4.0 \times 10^{-3}\,\mathrm{mm/mm}$. Until this strain, the quantities of the three experiments are similar and independent of the confining pressure level. Above an axial strain of $\epsilon_a = 4.0 \times 10^{-3}\,\mathrm{mm/mm}$ an individual non-linear dependency of the quantities on axial strain can be observed and be associated with non-elastic deformation.

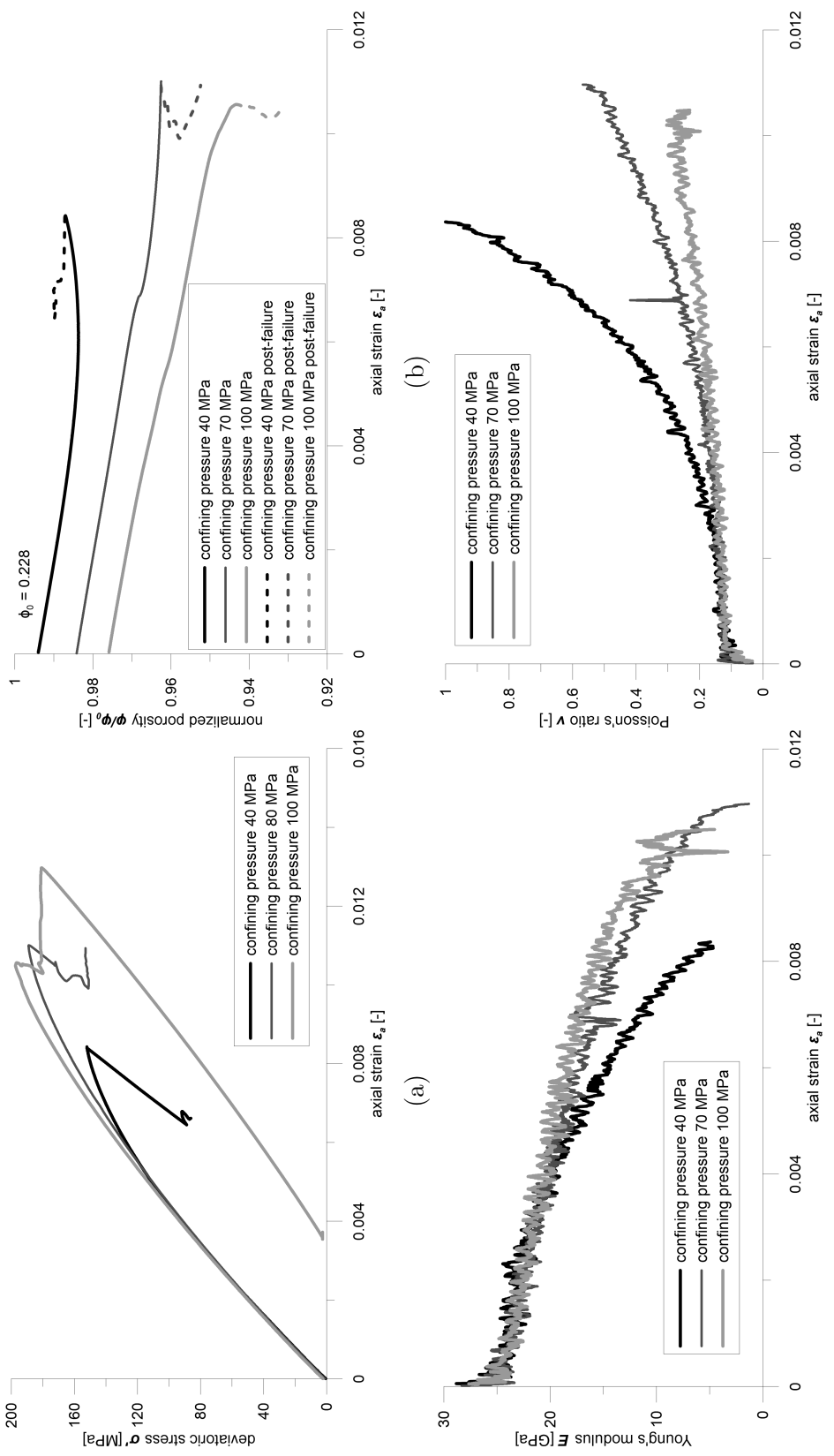

Fig. C.3 Results of the axial loading stage: (a) stress - strain relation, (b) porosity - axial strain relation, (c) Young's modulus - axial strain relation and (d) Poisson's ratio - axial strain relation.

The stress-strain curve (see Figure C.3a) indicates a linear elastic response for all tested samples until $\epsilon_a = 4.0 \times 10^{-3}$ mm/mm. Above this strain a flattening of the stress-strain curve can be observed which is most pronounced for a confining pressure of 40 MPa and less pronounced for a confining pressure of 100 MPa. Similar results were obtained in terms of the Young's modulus (see Figure C.3c). For all three samples the Young's modulus linearly decreased from 25 GPa to 20 GPa as strain increased to $\epsilon_a = 4.0 \times 10^{-3}$ mm/mm. Above this value for axial strain the Young's modulus decreased non-linearly. For the sample confined at 40 MPa, this decrease was more pronounced than for the 70 MPa and the 100 MPa confined samples.

The Poisson's ratio (see Figure C.3d) for all three samples was almost constant at 0.12 for axial strains between 0 and $\epsilon_a = 3.0 \times 10^{-3}$ mm/mm. Above this strain value, the Poisson's ratio increased non-linearly to almost 1 ($p_c = 40$ MPa), to 0.55 ($p_c = 70$ MPa), and to 0.25 ($p_c = 100$ MPa). These final values represent the sample state close to failure. The increase in the Poisson's ratio is most likely due to dilation.

The porosity at the beginning of axial loading varied for the individual samples due to its changes during hydrostatic loading (see Figure C.3b). For all samples to an axial strain of $\epsilon_a = 4.0 \times 10^{-3}$ mm/mm, porosity decreased by the same amount. Above, the three samples showed different inelastic behaviours. The porosity of the 40 MPa confined sample decreased and above an axial strain of $\epsilon_a = 6.0 \times 10^{-3}$ mm/mm started increasing. For the sample confined at 70 MPa the rate of porosity reduction remained almost constant. Finally, the sample confined at 100 MPa showed an enhanced porosity reduction for axial strains above $\epsilon_a = 1.0 \times 10^{-2}$ mm/mm.

C.6 Micro-structure observations

The microstructure observations gathered for this study comprise:

- Three-dimensional high resolution CT-scan of the samples were conducted at the Delft Technical University.
- 16 thin sections were cut for the three samples. Six for the sample SBS6-BB-01-01, six for SBS6-BB-01-02 and 4 for SBS6-BB-01-03.
- Electron Micro-Probe (EMP) images of the thin sections were taken and analysed.
- X-rax Powder Diffraction (XRD) analysis of the thin sections were conducted.

I present briefly here a selection of EMP images which helped to identify and understand the microstructural processes driving the localisation of deformation.

The thin sections have been observed at optical microscope in order to select the spot to be analysed a the EMPA. Secondary-electron (SE) images were collected with a JEOL JXA 8230 electron microprobe (15 kV accelerating voltage) at the Electron Microprobe Laboratory, Department of Inorganic and Isotope Geochemistry at the Helmholtz Centre Potsdam – German Research Centre for Geosciences (GFZ) in Potsdam, Germany. The analytical conditions include an accelerating voltage of 15 kV, a beam current of 10 nA, and a focused beam. The SE images have been acquired on polished in epoxy-embedded thin sections on quartz plagioclase grains which have been previously characterised by using well characterised standards crystals of plagioclase and quartz. The images have been systematically acquired throughout the pre-selected damaged-fractured portions of the thin sections.

Figure C.6 shows a selection of EMP images of sample SBS6-BB-01-01, where localised damage features with crushed grains can be identified in the vicinity of the main shear failure whereas the grain remain mostly undamaged far way from this shear failure. Figure C.7 shows a selection of EMP images of sample SBS6-BB-01-02 where the thickness of the damaged features with crushed grains are larger than in sample SBS6-BB-01-01. Finally Figure C.8 shows a selection of EMP images of sample SBS6-BB-01-03 where large regions of diffused damage were identified.

The analysis of these microstructural observations is still the subject of ongoing work, especially analysing the spatial distribution of damage and porosity reduction from the CT-scan observations (see Figure C.5).

Acknowledgements

In the frame of this experimental study, I would like to acknowledge a number of people and institutions who helped me to conduct these experiments. I would like to thank Guido Blöcher and Harald Milsch for their support and supervision during the triaxial experiments. I also want to thank Liane Liebeskind for her technical assistance.

I acknowledge the Aachen Institute for Advance Study in Computational Engineering Science (AICES) for their funding via the Experimental Funding program to conduct the microstructure analysis. I would like to thank the faculty of civil engineering and geosciences of the Technical University of Delft for providing me with the CT-scan measurements. Finally, I would like to thank Fiorenza Deon for her help and expertise for analysing the EMP images and Oona Appelt for her technical support.

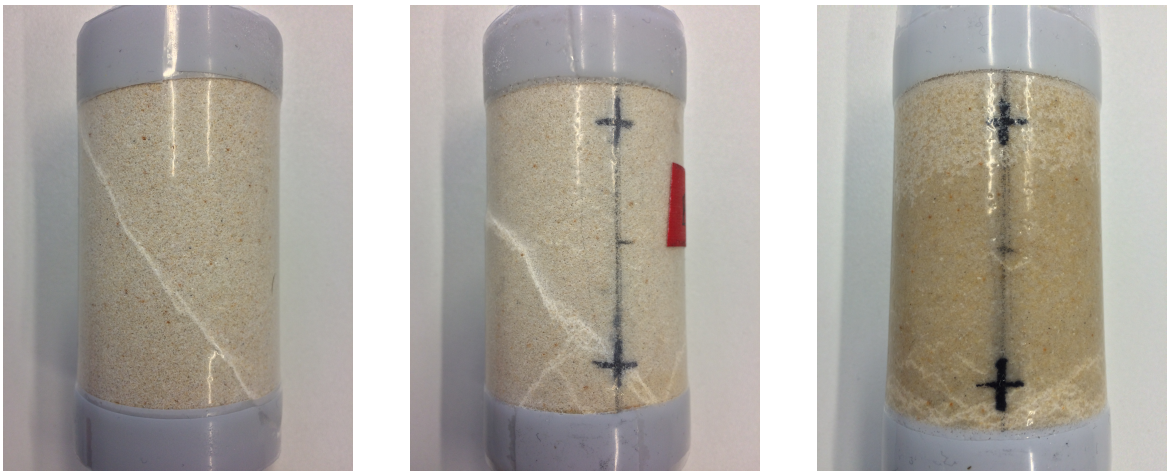

(a) SBS6-BB-01-01. (b) SBS6-BB-01-02. (c) SBS6-BB-01-03.

Fig. C.4 Pictures of the three samples after experiments. Panel (a) shows the sample SBS6-BB-01-01. Panel (b) the sample SBS6-BB-01-02 and panel (c) the sample SBS6-BB-01-03.

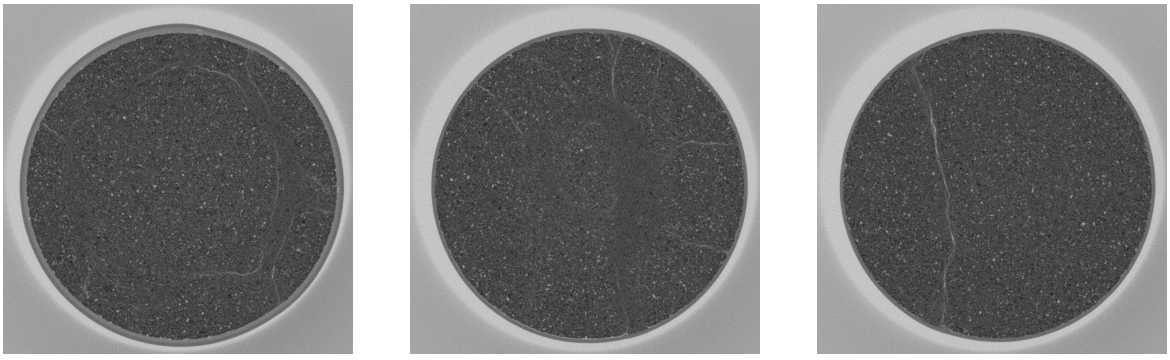

(a) (b) (c)

Fig. C.5 Slices in the CT-scan of sample SBS6-BB-01-01 at different heights.

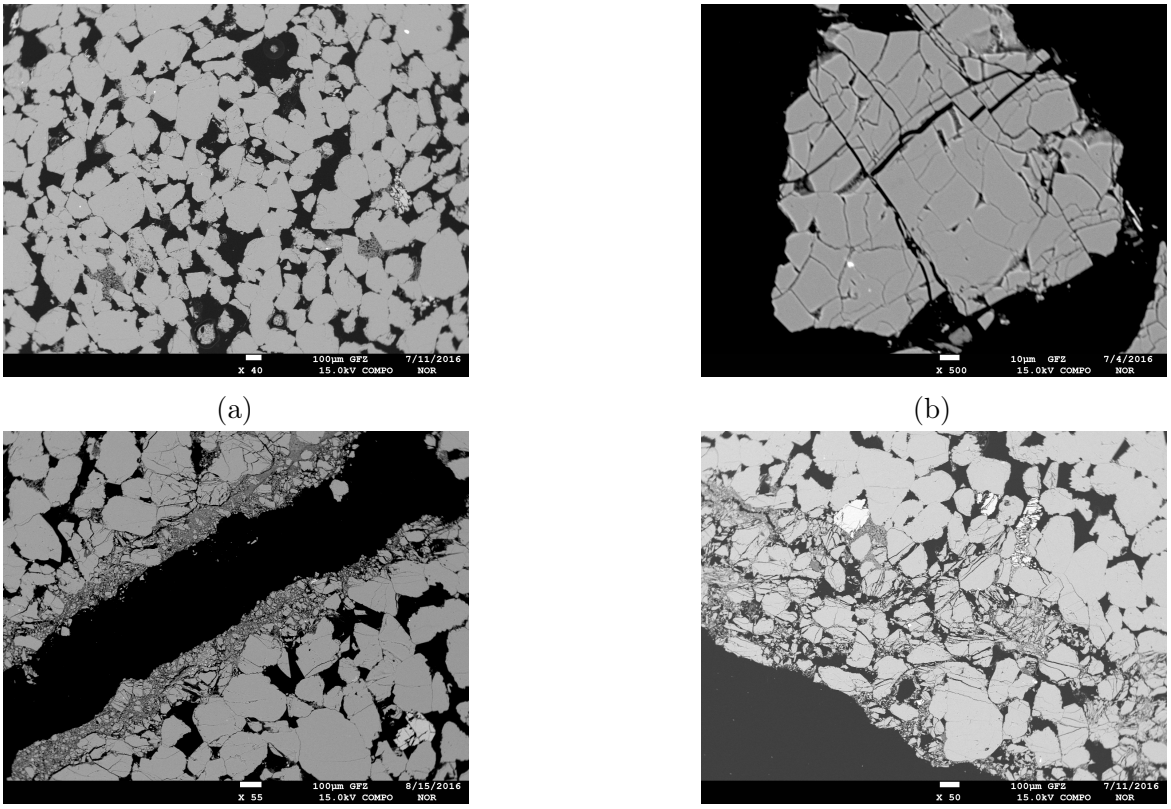

(a) (b)

(c) (d)

Fig. C.6 EMP images of a thin section from sample SBS6-BB-01-01. Panel (a) shows an undamaged grain organisation in a region far away from the main fracture. Panel (b) shows a damaged grain. Panel (c) shows the extend of the main shear failure. Panel (d) shows the damage zone around the main fracture.

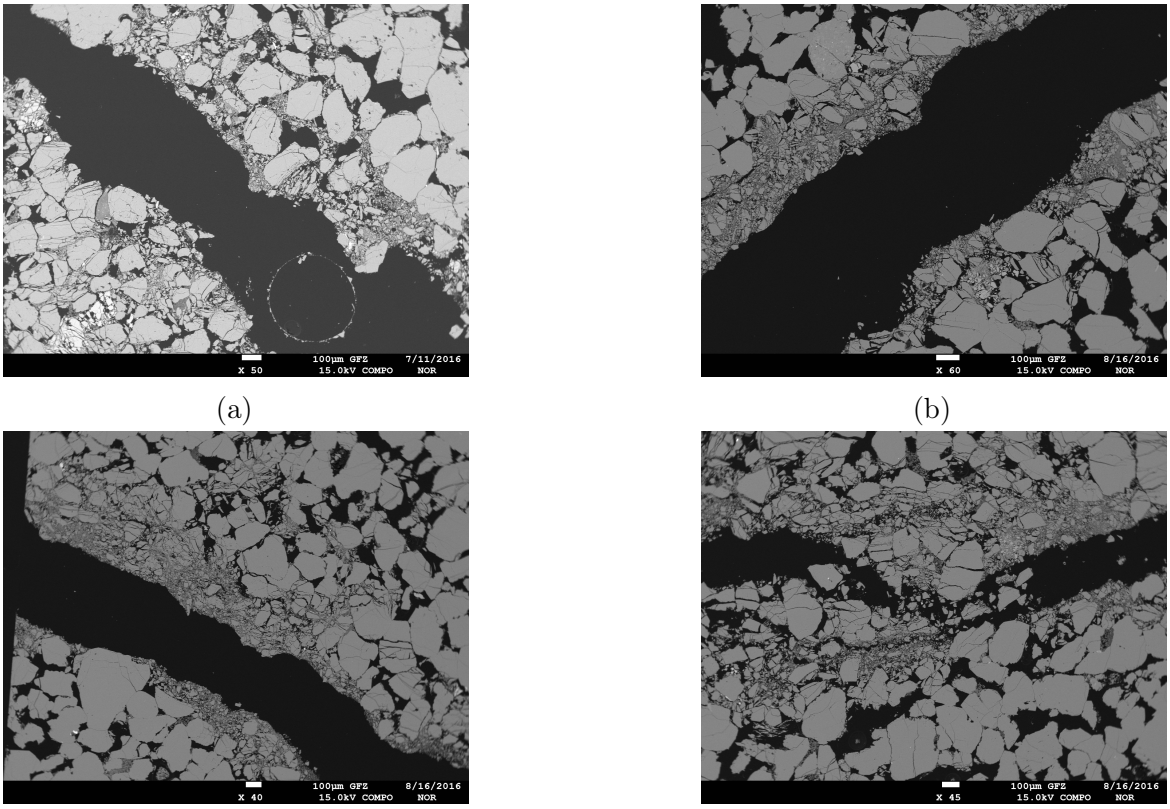

(a) (b)

(c) (d)

Fig. C.7 EMP images of a thin section from sample SBS6-BB-01-02. Panels (a), (b) and (c) show regions around fractures. Panel (d) shows a zoom into a damaged zone in the vicinity of a fracture.

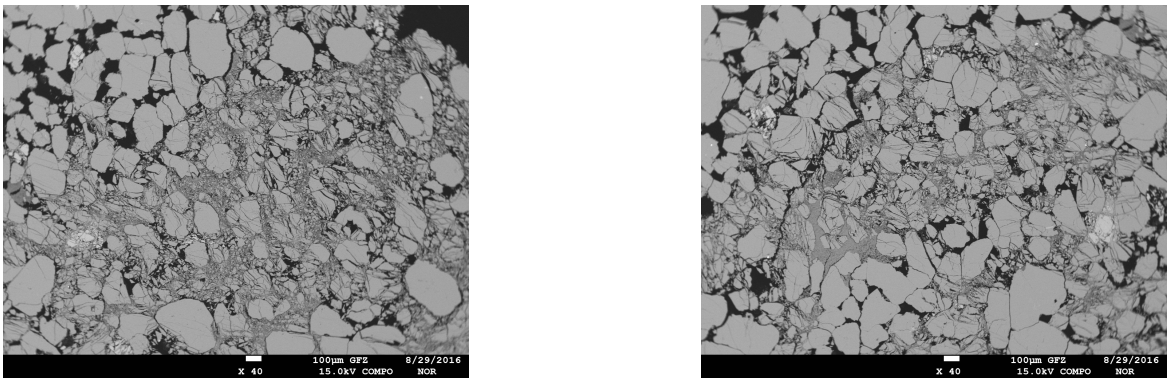

(a) (b)

Fig. C.8 EMP images of a thin section from sample SBS6-BB-01-03. Panels (a) and (b) show regions of diffused damaged grains.

Appendix D

List of publications and conferences attendances related to this thesis

Publications

Jacquey, A. B., Cacace, M., Blöcher, G., Milsch, H., Deon, F., and Scheck-Wenderoth, M., (accepted for publication). Processes Responsible for Localized Deformation within Porous Rocks: Insights from Laboratory Experiments and Numerical Modeling, 6^{th} *Biot Conference on Poromechanics, special issue*

Jacquey, A. B., Cacace, M., and Blöcher, (accepted for publication). Modelling coupled fluid flow and heat transfer in fractured reservoirs: description of a 3D benchmark numerical case, *Energy Procedia*

Jacquey, A. B., Urpi, L., Cacace, M., Blöcher, G., Zimmermann, G., and Scheck-Wenderoth, M., (under review). Poroelastic response of geothermal reservoirs to hydraulic stimulation treatment: theory and application to the Groß Schönebeck geothermal research facility, *Journal of Geohysical Research: Solid Earth*

Jacquey, A. B., Cacace, M., Blöcher, G., Watanabe, N., Huenges, E., and Scheck-Wenderoth, M., (2016). Thermo-poroelastic numerical modelling for enhanced geothermal system performance: Case study of the Groß Schönebeck reservoir, *Tectonophysics*, doi:10.1016/j.tecto.2015.12.020

Jacquey, A. B., Cacace, M., Blöcher, G., Watanabe, N., and Scheck-Wenderoth, M., (2015b). Hydro-Mechanical Evolution of Transport Properties in Porous Media: Constraints for Numerical Simulations, *Transport in Porous Media*, doi:10.1007/s11242-015-0564-z

Jacquey, A. B., Cacace, M., Blöcher, G., and Scheck-Wenderoth, M., (2015a). Numerical Investigations of Thermoelastic Effects on Fault Slip Tendency during Injection and Prodution of Geothermal Fluid, *Energy Procedia*, doi:10.1016/j.egypro.2015.07.868

Conference talks

Jacquey, A. B., Cacace, M., Blöcher, G., Milsch, H., and Deon, F., and Scheck-Wenderoth, M., (2017). Processes responsible for localized deformation within porous rocks - insights from laboratory experiments and numerical modelling, 6^{th} *Biot Conference on Poromechanics*, Paris, France

Jacquey, A. B., Cacace, M., Blöcher, G., Milsch, H., and Deon, F., (2017). From localized to homogeneous deformation of porous rocks - insights from laboratory experiments and numerical modelling, *GeoProc2017,* 6^{th} *International Conference on Coupled THMC Processes in Geosystems*, Paris, France

Jacquey, A. B., Urpi, L., Cacace, M., Blöcher, G., Zimmermann, G., and Scheck-Wenderoth, M., (2017). Poroelastic response of geothermal reservoirs during hydraulic stimulation treatment, *European Geosciences Union General Assembly (EGU) 2017*, Vienna, Austria

Jacquey, A. B., Cacace, M., Blöcher, G., Milsch, H., Deon, F., and Scheck-Wenderoth, M., (2016). Porous rock deformation: from localized brittle behavior to compaction bands formation – insights from laboratory experiments and numerical modeling, *GeoMod 2016*, Montpellier, France

Jacquey, A. B., Cacace, M., Blöcher, G., Milsch, H., and Scheck-Wenderoth, M., (2016). A visco-poroelastic damage model for modelling compaction and brittle failure of porous rocks, *European Geosciences Union General Assembly (EGU) 2016*, Vienna, Austria

Jacquey, A. B., Cacace, M., Blöcher, G., and Scheck-Wenderoth, M., (2015). Modelling of Thermo-Hydro-Mechanical coupled processes for faulted geothermal reservoirs, *European Geothermal Workshop 2015*, Strasbourg, France

Jacquey, A. B., Cacace, M., and Scheck-Wenderoth, M., (2015). Modelling of thermo-hydro-mechanical coupled processes for fluid-bearing reservoirs, *11th EURO-Conference on Rock Physics and Geomechanics*, Ambleside, UK

Jacquey, A. B., Cacace, M., Blöcher, G., Watanabe, N., and Scheck-Wenderoth, M., (2015). Thermo-Hydro-Mechanical numerical modelling for faulted geothermal reservoir systems: case study of the Groß Schönebeck reservoir, *GeoBerlin*, Berlin, Germany

Jacquey, A. B., Cacace, M., Blöcher, G., Huenges, E., and Scheck-Wenderoth, M., (2015). Hydro-mechanical Evolution of Transport Properties in Porous Media: Constrains for Numerical Modeling of Geothermal Systems, *European Geothermal Workshop 2014*, Karlsruhe, Germany

Jacquey, A. B., Cacace, M., Blöcher, G., and Scheck-Wenderoth, M., (2014). Modelling of fractured reservoirs: fluid-rock interactions within fault domains, *GeoMod 2014*, Potsdam, Germany

Conference posters

Jacquey, A. B., and Cacace, M., (2017). Modelling fully-coupled Thermo-Hydro-Mechanical (THM) processes in fractured reservoirs using GOLEM: a massively parallel open-source simulator, *European Geosciences Union General Assembly (EGU) 2017*, Vienna, Austria

Jacquey, A. B., and Cacace, M., (2016). Modelling fully-coupled Thermo-Hydro-Mechanical (THM) processes in fractured geothermal reservoirs using GOLEM: a massively parallel open-source simulator, *GeoMod 2016*, Montpellier, France

Cacace, M., Blöcher, G., Watanabe, N., **Jacquey, A. B.**, Wellmann, F., Huenges, E., and Scheck-Wenderoth, M., (2016). Coupled Thermo-Hydraulic (TH) modelling of geothermal systems – a review from the geothermal facility at Groß Schönebeck, North Germany, *GeoMod 2016*, Montpellier, France

Jacquey, A. B., Cacace, M., Blöcher, G., Milsch, H., and Scheck-Wenderoth, M., (2016). A damage mechanics approach for quantifying stress changes due to brittle failure of porous rocks, *European Geosciences Union General Assembly (EGU) 2016*, Vienna, Austria

Jacquey, A. B., Cacace, M., Blöcher, G., Huenges, E., and Scheck-Wenderoth, M., (2015). Thermo-Hydro-Mechanical numerical modelling for faulted geothermal reservoir systems: case study of the Groß Schönebeck reservoir, *3rd Aachen Conference on Computational Engineering Science (AC.CES)*, Aachen, Germany

Jacquey, A. B., Cacace, M., Blöcher, G., Watanabe, N., and Scheck-Wenderoth, M., (2016). Thermo-Hydro-Mechanical Evolution of Transport Properties in Porous Media: From Laboratory to the Groß Schönebeck Geothermal Reservoir, *European Geosciences Union General Assembly (EGU) 2015*, Vienna, Austria

Acknowledgements

This doctoral thesis presents results of a project which was funded by the Helmholtz Association, as part of the Helmholtz Portfolio Geo-Energy project. I therefore would like to thank the Helmholtz Association for giving me the financial and operational support to conduct this thesis. I also would like to thank the Aachen Institute for Advanced Study in Computational Engineering Science (AICES) for giving me the financial support to conduct a microstructure analysis via its experimental funding program.

I would like to thank Prof. Dr. Magdalena Scheck-Wenderoth from the German Research Centre for Geosciences GFZ and Prof. Dr. Florian Wellmann from the RWTH Aachen University for their supervision, their guidance and their sustained support during this project. You have both provided me with interesting feedbacks and additional motivation when needed and I am really grateful to you for that.

I also would like to deeply thank Dr. Mauro Cacace and Dr. Guido Blöcher for their scientific advices, their trust and mostly their positive attitude throughout this thesis. Without you, I would not have been able to achieve so much during these three years and I am really thankful for the time you invested in me.

I am grateful to all the members or former members of the section 6.1 of the GFZ, with whom I spent the time of this thesis and who helped to establish a friendly and pleasant working environment. Therefore, thank you Judith, Jessica, Leni, Anna, Lew, Mauro, Max and Christian. Especially I would like to thank Ingo and Peter, who gave me the necessary distractions from my research and made my stay in Germany memorable.

Finally, my deep and sincere gratitude goes to my parents, my sister and Kerstin for their continuous and unconditional love and support. This journey would not have been possible if not for them, and I dedicate this achievement to them.

Abstract

Motivated by the increasing need of carbon-free energy supply, development of concepts related to geothermal energy production has gained increasing attention in the last decades. Production of geothermal energy consists in the extraction of the heat stored in the Earth's crust for direct use or electricity production. One or several borehole doublets are usually drilled to gain access to the targeted geological formations and the heat stored within the reservoir rocks is extracted by producing and injecting the geothermal fluid. It has also become a standard practice to use well stimulation or enhancement treatments in order to create secondary permeability and enhance the productivity of medium to low enthalpy reservoirs. The main challenges to guarantee a productive, sustainable and environmental safe geothermal operational campaign are to capture the details of the geology of the reservoir structures (geological formations, fractures and faults) and to quantify in time and space the dynamics of the relevant physical processes and their interactions with the geological environment where they occur.

Continuous production and injection of geothermal fluids lead to changes in the thermodynamic conditions of a reservoir, where significant variations in pore pressure and temperature induce local gradients in the stress acting on the porous rock, thus affecting reservoir's performance. The transport properties of a porous medium, which are porosity and permeability are indeed sensitive to the deformation of the bulk and pore volume and can alter if not control the overall reservoir productivity. Furthermore, changes in the stress acting on a geological discontinuity such as a fracture or a fault, as induced by geothermal operations can compromise the mechanical stability of such structures. This can result in the propagation or closing of existing fractures but it can also induce slip along fault planes which is usually accompanied by induced seismicity.

This thesis aims at quantifying the impacts of the dynamics of coupled thermo-hydro-mechanical processes on the transport properties of the reservoir rocks. The goal is to provide a working framework which will assist field scientists in assessing the reservoir behaviour during operations in the light of increasing the productivity of such operations by limiting related hazards. For this purpose, a multiphysic and multiscale workflow has been developed which combines data obtained from laboratory-based rock deformation experiments and field operations and an accurate description of the main physical processes and their coupling into a novel numerical framework.

A poroelastic framework capturing non-linear processes related to the closure of microcracks at low confining pressure during hydrostatic loading in drained conditions has been constrained and validated using published laboratory data on two different

sandstones. It was therefore possible to capture the non-linear decrease of porosity during hydrostatic loading in numerical simulation as monitored in the laboratory. The resulting poroelastic framework was later extended to account for thermal feedbacks in a thermo-poroelastic model. The impacts of temperature changes on the mechanical behaviour and as well as on the porosity and permeability distributions were analysed and quantified by means of a generic model and a field case application, the Groß Schönebeck geothermal research facility, located north of Berlin, Germany. The results predicted a decrease of approximatively 14 % in the life time of the reservoir with respect to previous estimates based on studies neglecting such deformation feedbacks. This thermo-poroelastic framework has also been used to study the impacts of pore pressure and temperature changes on the slip tendency of major faults zones in the vicinity of an operating well. The results showed that gradients in temperature can contribute to the increase of slip movements along major fault zones, with the magnitude of such movement correlating with magnitudes of induced thermal gradients by fluid injection and faults geometry with respect to the in situ stress field. Finally, a complete hydromechanical model formulation has been used to provide an explanation on the causative process behind field observations which were left unexplained before. These consist in instantaneous increases in pore pressure propagating at large distances ($\sim$ 500 m) from a stimulated well which has been observed during a stimulation campaign at the Groß Schönebeck geothermal field. These observations can be explained as the results from a poroelastic effect in relation to a solid to fluid hydromechanical coupling, similar to the Mandel-Cryer effect triggered by compressional deformation as induced by the opening of a hydraulic fracture.

In summary, this thesis demonstrates the importance of mechanical processes and multiscale non-linear relations between transport properties and the microstructure of the reservoir rocks for assessing the hydrothermal state of a geothermal reservoir and ultimately the productivity, sustainability and safety of geothermal operations. By means of complementary laboratory- and field-based observations, the outcomes of this thesis provide a complete workflow including space discretisation of complex geometries of a geological model and a powerful scalable numerical simulator capable of integrating new information as available. The tool developed during the course of this thesis is intended to help at improving the predictive capabilities of geothermal operations and could be extended to any reservoir operation in the future.

Zusammenfassung

In Zeiten wachsender Nachfrage nach CO_2-freier Energieversorgung steht besonders die Entwicklung von Konzepten im Bereich der erneuerbaren Energien im Fokus. Eine dieser regenerativen Energien ist die Erdwärme. Bei der geothermischen Energiebereitstellung wird die in der Erdkruste gespeicherte Wärme entweder direkt für Heizzwecke oder zur Erzeugung von elektrischem Strom genutzt. Üblicherweise wird eine Produktions- und Injektionsbohrung (Doubletten-System) in die Zielformationen abgeteuft um heißes Wasser aus der Tiefe zu produzieren, Wärme an der Oberfläche zu extrahieren und das abgekühlte Wasser zu re-injizieren. Sind die hydraulischen Eigenschaften des Reservoirs nicht ausreichend für eine wirtschaftliche Energiebereitstellung, gehört es mittlerweile zur Standartprozedur, dass das Reservoir stimuliert wird, um die Permeabilität und somit die Produktivität zu erhöhen. Ein solches stimuliertes Reservoir wird auch Enhanced Geothermal System (EGS) genannt. Um die Produktivität, Nachhaltigkeit und Umweltverträglichkeit eines EGS bewerten zu können, ist die größte Herausforderung die geologische Struktur des Reservoirs (Störungszonen, geologische Schichten, hydraulisch induzierte Risse, Bohrungen) abzubilden, um relevante physikalische Prozesse in Raum und Zeit quantifizieren zu können.

Die Produktion und Injektion von geothermischem Fluid ändert die thermodynamischen Bedingungen im Reservoir. Hauptsächlich wird eine Änderung des Porendrucks und der Temperatur induziert. Diese Änderungen führen wiederum zu einer Veränderung des Spannungsfeldes. Die damit verbundene Deformation verändert die Transporteigenschaften des Reservoirs (Porosität und Permeabilität) und somit die Reservoirperformanz. Darüber hinaus kann ein verändertes Spannungsfeld zur Reaktivierung von Störungszonen und zur Öffnung oder Schließung von Klüften und führen, was wiederum seismische Aktivität auslösen kann.

Im Rahmen dieser Doktorarbeit wird der Einfluss von gekoppelten thermo-hydro-mechanischen Prozessen auf die Transporteigenschaften des Reservoirs quantifiziert. Ziel ist es, während laufender Feld-Operationen die Reaktionen des Reservoirs zu bewerten und mögliche Arbeitsschritte zu definieren, welche die Förderleistung maximieren und gleichzeitig Risiken minimieren. Dafür wurde ein neuer Workflow für verschieden Skalen einschließlich der relevanten physikalischen Prozesse entwickelt. Dieser Arbeitsablauf basiert auf Daten zur Gesteinsdeformation aus Laborexperimenten und Feldstudien. Darauf aufbauend wurde ein neuer numerischer Simulator entwickelt, indem die wichtigsten physikalischen Prozesse und deren Kopplung implementiert sind.

Das poro-elastische Verhalten von porösen Sandsteinen wurde in diesem Simulator integriert. Diese poro-elastische Implementierung beinhaltet die nicht-linearen

Prozesse, welche bei der Schließung von Mikro-Rissen bei geringem Umgebungsdruck, hydrostatischer Belastung und konstanten Porendruck auftreten. Der numerische Simulator wurde anhand von Laborexperimenten an zwei verschiedenen Sandsteinen (publizierte Daten) validiert. Es war möglich, das im Labor beobachtete nichtlineare Abnehmen der Porosität bei hydrostatischer Belastung auch numerisch erfolgreich zu simulieren. Eine spätere Erweiterung des Simulators hinsichtlich thermischer Prozesse macht es möglich, das thermo-poro-elastische Verhalten abzubilden. Der Einfluss der Temperaturveränderungen auf das mechanische Verhalten sowie auf die Porositäts- und Permeabilitätsverteilung wurde in einem generischen Modell und in einem Fallbeispiel (Geothermie-Forschungsplattform Groß Schönebeck) analysiert und quantifiziert. Die Ergebnisse zeigen eine um ungefähr 14 % verkürzte Nutzbarkeit des Reservoirs im Vergleich zu früheren Studien, welche das thermo-poro-elastische Verhalten vernachlässigten. Der thermo-poro-elastische Ansatz wurde weiterhin genutzt, um den Einfluss des Porendrucks und der Temperaturveränderung auf mögliche Bewegungen entlang von Störungen zu untersuchen. Die Ergebnisse zeigen, dass die Temperaturverringerung an der Injektionsbohrung dazu beitragen kann, die Wahrscheinlichkeit einer Störungsreaktivierung zu erhöhen. Abschließend wurde das hydro-mechanische Modell genutzt, um für Feldbeobachtungen die verursachenden Prozesse zu ermitteln. Während der Stimulation einer Bohrung am Standort Groß Schönebeck wurde ein unmittelbarer Porendruckanstieg an der Beobachtungsbohrung, welche 500 m vom Reservoir entfernt ist, beobachtet. Diese bis dato nicht erklärbare Beobachtung kann durch einen poroelastischen Effekt ähnlich dem Mandel-Cryer Effekt erklärt werden. Dieser Effekt beruht auf der Kompression des umliegenden Gesteins beim Öffnen eines hydraulischen Risses.

Diese Doktorarbeit zeigt, dass mechanische Prozesse - der nichtlineare Zusammenhang zwischen Transporteigenschaften und Mikrostruktur des Reservoirgesteins - wichtige Parameter zur Beurteilung des hydrothermalen Zustands eines geothermischen Reservoirs und dessen nachhaltige Förderleistung sind. Die Verwendung von Labordaten und Beobachtungen aus dem Feld erlauben erstmals die Erstellung eines Bewertungstools für geothermische Standorte, das die Abbildung von räumlich komplexen geologischen Strukturen sowie einen skalierbaren numerischen Simulator umfasst. Es erlaubt neu gewonnene Daten direkt zu integrieren. Die Arbeitsschritte sind dazu ausgelegt, bessere Voraussagen für geothermische Reservoire während operativer Maßnahmen zu treffen, können jedoch auch auf andere Untergrundnutzungen erweitert werden.